Advanced FEs for the micropolar and geometrical nonlinear analyses of composite structures

ScuDo

Scuola di Dottorato ~ Doctoral School

WHAT YOU ARE, TAKES YOU FAR

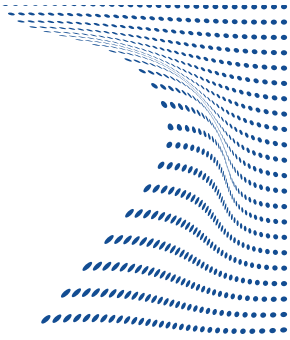

Riccardo Augello

Scuola di Dottorato

Department of Mechanical and Aerospace Engineering

Politecnico di Torino

Supervisors:

Prof. Erasmo Carrera

Prof. Alfonso Pagani

January 2021

A zio Gerlando

Declaration

I hereby declare that, the contents and organization of this dissertation constitute my own original work and does not compromise in any way the rights of third parties, including those relating to the security of personal data.

Riccardo Augello
January 2021

Acknowledgements

First, i would like to extend my deepest gratitude to my advisors, Prof. Erasmo Carrera and Prof. Alfonso Pagani for their continuous guidance and timely supervision during the Ph.D. course. Prof. Erasmo Carrera's priceless insigth into mechanics and the passion and dedication he put on his work has inspired me on my research activities. Prof. Alfonso Pagani has provided me a constant help during every step of my activities and has encouraged me with his devotion to research. I am also deeply greateful to Prof. Marco Petrolo, Prof. Maria Cinefra, Dr. Enrico Zappino and Dr. Matteo Filippi for their constant and kind support. I want to express my gratitude to the whole MUL2 group and it is an honor for me to be a member of such a successful team. In particular, i want to thank Daniele, Andrea, Tommaso, Rodolfo, Daniel and Michele for their constant support as officemates. I would also like to thank Prof. C. W. Lim for hosting me during my academic visit to City University of Hong Kong. Finally, i would like to acknowledge the joint project with City University of Hong Kong, which is funded under a Compagnia di San Paolo grant.

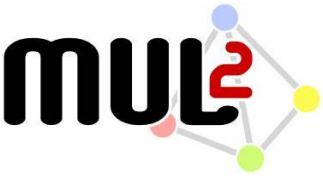

My biggest recognition is dedicated to my family for their encouragment and for cherishing every small milestone on the way.

Abstract

The numerical simulation of composite structures requires the implementation of sophisticated and efficient models in order to overcome the restrictions of established finite element method codes for metallic components. The heterogeneous nature of laminated structures has always represented a challenging modelling issue and has cut down the trust of engineers on the simulation codes. As a consequence, high safety margins are employed in the industry for this kind of applications. However, the adoption of innovative tools for the correct prediction of the mechanical behavior of composite structures has become less attractive. Moreover, during working conditions, the external forces which act on composite components may induce large deflection on them. Consequently, an accurate and efficient solution able to predict the nonlinear behavior of such structure should be needed. Addressing this issue, this thesis aims to develop a solid and general formulation for a geometrical nonlinear static and dynamic structural analysis of laminated structures. In addition, the microstructure of such components may have a crucial role on the global mechanical behavior, and its contribution has to be considered. In order to address this problem, the micropolar elasticity is investigated, which represents a theory accounting for the microstructural properties of structures.

In this thesis, the development of geometrical nonlinear and micropolar elasticity-based refined beam, plate, and shell models are built in the framework of Carrera Unified Formulation (CUF). Taylor series and Lagrange polynomials are introduced in either equivalent-single-layer or layer-wise approach and numerically validated. For the solution of the governing relations of static and dynamic analyses the finite element method is adopted. The developed nonlinear beam and shell models are used to investigate the mode change of structures in the large deflection and post-buckling field, and the process is validated through comparison with literature and experimental evidences. The proposed results show how the change of the dynamic properties of composite structure is not negligible in the geometrical nonlinear field and must be considered in the design process. Moreover, the degree of accuracy of popular nonlinear strain models, such as the well-known von Kármán assumptions, is evaluated for various one-dimensional and two-dimensional problems and the results show when this nonlinear approximation theory can be employed or not. Three-dimensional stress distributions

in the nonlinear regime are shown as well, proving the capability of the proposed model to evaluate them with ease. Finally, beam and plate models are built in the framework of the micropolar elasticity and they are adopted for the analysis of real structures. The employed finite element approaches lead to results matching well with the available reference and three-dimensional solutions.

Table of contents

List of figures

List of tables

Chapter 1

Introduction

1.1 Motivation

Composite structures have encountered a wide success for a reliable design of advanced working components. Due to their outstanding performances in terms of mechanical properties, the aerospace industry continues to rely on composite materials applications, which demand for an accurate technological and structural verification. Consequenlty, scientific researches have been encouraged to develop refined theories for an accurate description of the behavior of composite laminates during their working conditions. In fact, the typical models employed for the analysis of metallic structures have revealed to be obsolete and not applicable for composite ones. Carrera [27] and Kapania and Raciti [91, 92] presented an exhaustive review regarding the mathematical modeling of the behavior of laminated one-dimensional (1D) and two-dimensional (2D) structures. Among the widely investigated topics in the mechanics field, the geometrical nonlinear problems have demonstrated to cover a great importance. It is clear that the large deflections may significantly afflict the static and dynamic behavior response of structures and it is common that external forces can induce those conditions on typical working components, such as space antennas, robotic arms, rotor blades and wing structures. As a matter of fact, the literature about this topic is vast and some significant contributions on nonlinear models on history are presented hereafter. Regarding structure which cross-section does not play a primary role on the whole behavior, i.e. in case of thin and solid cross-section, the so-called elastica [123, 68, 178] represents a reliable model. It takes its assumptions based on the classical Euler–Bernoulli beam theory [62], and, in particular, the local curvature is considered proportional to the bending moment. It is clear how this approximation can not be applied when dealing with composite structures, where the shear effects plays a crucial role on the whole behavior. Consequently, most of the literature works rely on the Timoshenko beam theory [176]. It

considers a constant shear distribution over the cross-section of the 1D structure of thickness of the 2D components. The pioneering work by Reissner [159] demonstrated how this theory was largely used for the nonlinear analysis of metallic structures. He solved the analysis of thin curved 1D structures via the principle of virtual work. In [160, 161] the problem of the bending and torsion effects on beams is discussed. The First-order Shear Deformation Theory (FSDT) represents the evolution of the Timoshenko beam model for the modelling of composite structures. This model has turned to be very effective for the analysis of composite structures in the linear and geometrical nonlinear static domain. As an example, Kapania and Raciti [93] presented a 1D model of FSTD to deal with twisting and shear deformation of symmetryc and unsymmetric laminated beams. Agarwal et al. [2] studied the influence of the geometrical nonlinear phenomena on the static and dynamic response of beams, made of isotropic, composite and functionally graded material. A post-buckling investigation of composite beams was proposed by Gupta et al. [72] and Lanc et al. [110]. In the latter, under the assumption of the classical lamination theory, the cross-section was supposed to not show any shear strain. However, when higher-order phenomena occur within the structures, for instance in case of coupling of bending and torsion/axial deformation, when an accurate evaluation of the stress distribution in the large displacement field is demanded, more refined kinematics must be exploited. For instance, Obst and Kapania [141] developed a geometrical nonlinear model with a parabolic distribution of the shear strain components. The stress-free condition at the top and bottom surfaces were satisfied. Chandrashekhara and Bangera [43] developed bending analyses of laminated 1D structures through a refined shear distribution formulation. Another approach could be the use of more Degrees Of Freedom (DOFs) in the thickness direction, so that the shear distribution results to be more accurate. This approach is described by Singh et al. [170], who analyzed unsymmetric composite beams with von Kármán assumptions and twelve DOFs per node. Moreover, the Variational Asymptotic Beam Sectional (VABS) analysis was used for the analysis of laminated beams with cross-section with any geometrical and material characteristics, adopting a generalized Vlasov theory (see [188] for instance). Other important contributions are recalled hereafter. Krawczyk et al. [102] and Krawczyk and Rebora [101] developed a Layer-Wise (LW) model for the geometrical nonlinear analysis of laminated 1D structures, assuming a FSDT theory for each layer. Hamilton's principle was exploited by Emam [58] for the post-buckling analysis of 1D structures and a sinus distribution of the shear components was employed by Vidal and Polit [180] for the development of a three-noded beam finite element. A cosine distribution for the shear component of the strain was assumed and the continuity between adjacent layers was ensured.

Two-dimensional shelll structures are also prone to suffer geometrical deformations. Their application is very popular in mechanical and aerospace engineering mainly for their outstanding characteristics of supporting external forces with high efficiency. This capability is due to their curvature, which implies the coupling between the membrane and flexural strength. Furthermore, shell models are capable of undergoing large displacements and rotations when external loadings become extreme. For the same reason, the assumptions of linear geometrical relations hold for a narrow range of applications. Indeed, thin shells exhibit large rotations even for moderate loadings and, therefore, geometrical nonlinear relations must be generally considered [66].
The literature about theories of shells constructions dates back to the 40s [138, 23, 135]. This topic was developed in many research works to obtain efficient shell formulations to perform static and dynamic analyses. Lately, considerable importance was focused on the development of accurate theories to implement the effects of shear deformation and normal transverse stress in composite shells. The classical formulations are represented in literature from the studies by Poisson [150], Love [122], Mindlin [130], Kirchhoff [98], Reissner [157] and Cauchy [40]. Commercial codes adopt these classical theories in their two-dimensional (2D) elements. Recently, different higher-order 2D formulations were implemented to overcome the assumptions made in classical studies. These improvements become fundamental when composite structures are analyzed, and whenever the through-the-thickness stresses need to be evaluated with a reliable accuracy.
As reported by Kapania [90], shell structures made of composite material have a crucial use in different branches of engineering, in particular in aerospace. Composite materials provide an attractive possibility to more traditional construction types thanks to their resistance to corrosion, high strength-to-weight ratio, ease of formability, excellent fatigue strength, and tailoring ability. However, the study of the behaviour of laminated materials is not a simple task because of the anisotropy nature of the material, and it turns to be a challenging issue for scientists and researchers. A large number of higher-order shell theories were developed over the years and some of those are described here. Reddy [155] developed a refined through-the-thickness kinematic, including a higher-order shear deformation to study composite shell structures. The same author reported the mechanics of laminated plate and shell structures in [153]. A refined shear-deformation model based on finite-rotations formulation with seven independent displacement variables to study arbitrary multilayered composite shells was implemented by Başar *et al.* [13]. Mashat *et al.* [126] provided an assessment of the relevance of displacement variables in refined theories for isotropic and multilayered shells using an axiomatic/asymptotic technique. A refined approach for analyzing the effect of shear deformation in thick laminated anisotropic shell structures was described by Jing and Tzeng

[87]. Shu [164] performed different refined analyses to derive a refined formulation accounting for a higher-order transverse shear deformation to study composite shell structures. The refined theories of shell models were unified by Carrera in his early works, e.g., [26]. Cinefra and Carrera [46] provided several linear static analyses of composite structures adopting a finite element shell model with different through-the-thickness kinematics. Petrolo and Carrera [149] developed a useful review of methods and guidelines for the selection of shell models. Other significant works on refined shell theories can be found in [47, 116].
As reported by Liew *et al.* [121], laminated composite models show a very complex behaviour if subjected to extreme external loads, which induce large rotations. In most of the studies, the solution is obtained through approximated computational methods [179, 156]. A large variety of studies has been performed on the nonlinear static and dynamic analysis of laminated shells. As an example, Han *et al.* [73] presented a 2D model with a shear distribution of a first-order type to perform geometrical nonlinear analyses of composite shell structures with large displacement field, in the case of small strains only. Amabili and Reddy [9] formulated a theory of first-order thickness stretching with higher-order shear strain using 6 independent parameters. All nonlinear terms are considered in the middle plane, while those relating to rotations and deformations are neglected. Amabili and Reddy [10] adopted a third-order thickness and shear deformation theory to perform both nonlinear static and dynamic analyses of doubly-curve composite shell structures. A new third-order thickness and shear deformation theory, including nonlinearities in rotation, by using 8 parameters was developed by Amabili [6]. This proposed theory, also considering geometric imperfections, was used to investigate laminated shells' static and dynamic behaviors. Rivera *et al.* [162] implemented a new 12 independent parameters shell FE using third-order thickness stretch kinematics to analyze large deflection of laminated shell structures. A detailed description of the nonlinear shell theories and more recent advances on these composite structures and their nonlinear vibrations was presented by Amabili [7]. The same auhor [5] discussed both the theoretical and experimental peculiarities of nonlinear vibrations and the stability of shells and plates. Boutagouga and Djeghaba [22] proposed an investigation on the proper FE to use in linear and nonlinear static and dynamic analyses. A 3D shell element for nonlinear analyses of composite structures was provided by Klinkel *et al.* [99]. A geometrical nonlinear shear deformation formulation for laminated shells was presented by Dennis and Palazotto [55]. Sze *et al.* [175] suggested different nonlinear benchmark problems of shells.
This thesis work aims to describe a unified 1D and 2D formulation for the geometrical nonlinear analysis of beam- and shell-like composite structures. Isotropic structures are analyzed as well, to demonstrate the general applicability of such models. The Carrera Unified Formulation (CUF) [33, 29] represents the theoretical basis for the development of

the geometrical nonlinear formulation adopted. The geometrical nonlinear unified model was first developed by Pagani and Carrera [144, 143] for the nonlinear analysis of metallic and composite beams. The topic was further expanded by De Pietro [53, 83] and Hui [82, 84] to deal with multi-stable and multi-scale problems.

In the geometrical nonlinear approach, the Classical Elasticity (CE) is adopted. CE assumes the material to be continuous and homogeneous whithin the body, which intrinsic microstructure is not considered. However, any body is made of mass of grains at microstructural level. In addition, the material should be considered to contain microflaws, grain boundaries and dislocations. These tremendous defects al microlevel have huge effects on the behavior of a body at macrolevel. Experiments [173, 109, 65] have been conducted to investigate the influence of the microstructure on the structural macro-scale response. The results show that when the size of the structures become comparable to the microstructure, the microlevel gains an influence which could not be negligible. The trend of miniaturization in engineering, i.e. ultra-thin films, electronic materials and Micro-Electro-Mechanical Systems (MEMS), requires a comprehensive study of the microstructure.
CE can not describe such scale-dependent phenomena. In fact, it is well-known that constitutive models of theories which rely on CE do not account for any length-scale parameters. To overcome this issue, many theories have been developed in history to account for the micro-structural properties of structures. Among these, Micropolar Elasicity (ME) deserves particular attention. The assumptions at the basis of ME are the following:

A Each material point can rotate indipendently of its translations;

B The interactions between adjacent material points occur not only through translational forces (as in CE), but also by means of couple stresses.

Assumption [A] makes each point of a micropolar media to be considered to have six degrees of freedom, three classical translational forces and three micropolar rotations, which are called as microrotations. Moreover, thanks to assumption [B], the asymmetry of the stress tensors can be achieved. This guarantee the applicability of ME to the simulation of porous and granular solid and fibrous materials, as well as in correspondence of holes, notches and cracks.
In the second part of this thesis, the applicability of ME is considered. Unified models based on CUF, FEM and ME are built for the analysis of 1D and 2D structures.

1.2 Outline

The present thesis is divided into two parts. Part I focuses on the formulation of a unified model accounting for the geometrical nonlinear analysis. Then, micropolar unified models are built within the scheme of 1D and 2D CUF and presented in Part II.

1.2.1 Part I

Chapter 2 presents the higher-order 1D and 2D models adopted in this thesis. Such unified models are formulated within the FEM framework via the principle of virtual work. The capabilities of CUF models to deal with geometrical nonlinear analysis are demonstrated via some numerical examples dealing with large deflection and post-buckling evaluation of isotrpoic and composite beams and shells. The chapter intends to describe the formulation of the higher-order nonlinear models and their applicability for a large number of cases. In chapter 3, a step further is taken, and the effectiveness of the models to deal with modal analysis over the nonlinear equilibrium path is shown. At each equilibrium condition, the dynamic properties are evaluated in terms of modal shapes and natural frequencies, by an opportune linearization of the geometrical nonlinear equations. Numerical results for isotropic and composite beams and shells, along with comparison with experimental results of a reinforced panel, are presented. The results are compared with those obtained by analyzing the trivial states of the equilibrium, showing that nonlinear stiffness matrixes have to be included in order to accurately predict the mode aberration of structures, especially in the post-buckcling regime. Chapter 4 presents a geometrical nonlinear platform formulated within the scheme of CUF to undertake analyses for various nonlinear approximations, including the well-known von Kármán strain approximation. The ability of nonlinear CUF models to easily deal with different nonlinear theories is demonstrated. Compact to thin-walled isotropic and composite beams and shells are analyzed. Chapter 5 proposes an analysis on the effects of geometrical nonlinearities on the static response using low- to higher-order kinematics model. In other words, the chapter aims to enstablish if the geometrical nonlinear analysis have to be accomplished by a refined kinematics. Chapter 6 proposes an accurate description of the through-the-thickness distribution of stresses, in isotropic and composite shell structures in the large deflection field. Finally, chapter 7 proposes an alternative approach for the geometrical nonlinear analysis of structure with complex geometries, with 1D model and only cross-sectional geometrical nonlinearities.

1.2.2 Part II

Chapter 8 introduces the basis of the ME, including the choice of the additional material parameters, typical for this applications. The framework exploits the refined 1D model based on CUF to model a human bone specimen in Chapter 9. Moreover, in the same chapter, the effeciency of the proposed 1D model is tested through comparison with literature results. Finally, an extension to 2D models is explained and considered in Chapter 10.

Part I

Geometrical nonlinear unified formulation

Chapter 2

CUF-based finite element for the static geometric nonlinear analysis

2.1 Carrera unified formulation

This Section intends to enstabilish the formulation of 1D and 2D shell models. Figure 2.1 shows a shell-type structure modelled using 1D and 2D models. Let us now focus on the former. It is supposed to have its cross-section laying on a x,z-plane of a cartesian reference system. Consequently, the beam axis is placed along the y direction. The 3D displacement vector can be written as follows:

$$\mathbf{u}(x,y,z) = \left\{ \begin{array}{ccc} u_x & u_y & u_z \end{array} \right\}^T \tag{2.1}$$

where u_x, u_y and u_z are the displacement component and T is the transpose operator. The stress, σ, and strain, ε, components are expressed in vectorial form with no loss of generality,

$$\begin{aligned} \sigma &= \{\sigma_{xx} \quad \sigma_{yy} \quad \sigma_{zz} \quad \sigma_{xz} \quad \sigma_{yz} \quad \sigma_{xy}\}^T, \\ \varepsilon &= \{\varepsilon_{xx} \quad \varepsilon_{yy} \quad \varepsilon_{zz} \quad \varepsilon_{xz} \quad \varepsilon_{yz} \quad \varepsilon_{xy}\}^T \end{aligned} \tag{2.2}$$

On the other hand, the 2D model requires the introduction of two geometrical parameters, the curvature radius R_α and R_β. A one-curvature cylindrical shell is depicted in Fig. 2.1 and the R_α is highlighted in red. Moreover, an orthogonal curvilinear system is employed, so that α and β describe the in-plane directions, whereas z the through-the-thickness one. Whitin a

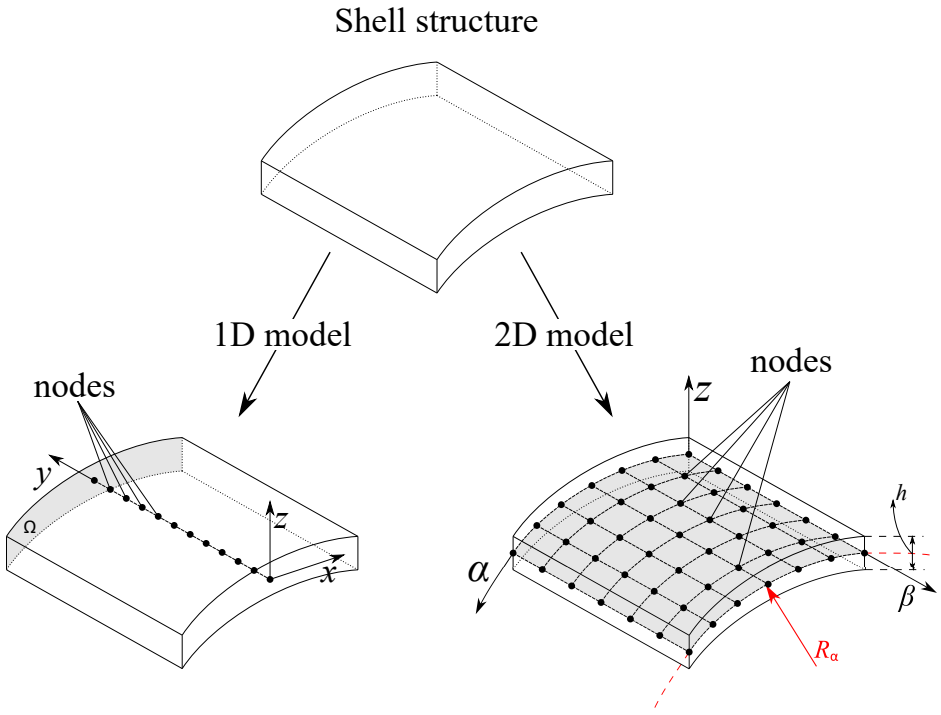

Fig. 2.1 A shell structure modelled via 1D and 2D unified theories.

continuum shell, the displacement components of a generic point are introduced hereafter:

$$\mathbf{u}(\alpha,\beta,z) = \left\{ \begin{array}{ccc} u_\alpha & u_\beta & u_z \end{array} \right\}^{\mathrm{T}}, \tag{2.3}$$

Finally, the transposed vectors of the strains and stresses reads as:

$$\begin{aligned} \sigma &= \{\sigma_{\alpha\alpha} \quad \sigma_{\beta\beta} \quad \sigma_{zz} \quad \sigma_{\alpha z} \quad \sigma_{\beta z} \quad \sigma_{\alpha\beta}\}^T, \\ \varepsilon &= \{\varepsilon_{\alpha\alpha} \quad \varepsilon_{\beta\beta} \quad \varepsilon_{zz} \quad \varepsilon_{\alpha z} \quad \varepsilon_{\beta z} \quad \varepsilon_{\alpha\beta}\}^T \end{aligned} \tag{2.4}$$

2.1.1 Geometrical relations

Regarding the geometrical relations, the Green-Lagrange strains are taken into consideration. In this manner, the relation between the strains and the displacement can be expressed as

$$\varepsilon \quad = \quad (\mathbf{b}_l + \mathbf{b}_{nl})\mathbf{u} \tag{2.5}$$

where $\mathbf{b}_l$ is the linear differential operator and $\mathbf{b}_{nl}$ is the nonlinear one. Due to the differences highlighted in the previous Section, the complete form of these two matrices are different for

1D and 2D models. For 1D models, they are:

$$\mathbf{b}_l = \begin{bmatrix} \partial_x & 0 & 0 \\ 0 & \partial_y & 0 \\ 0 & 0 & \partial_z \\ \partial_z & 0 & \partial_x \\ 0 & \partial_z & \partial_y \\ \partial_y & \partial_x & 0 \end{bmatrix}, \qquad \mathbf{b}_{nl} = \begin{bmatrix} \frac{1}{2}(\partial_x)^2 & \frac{1}{2}(\partial_x)^2 & \frac{1}{2}(\partial_x)^2 \\ \frac{1}{2}(\partial_y)^2 & \frac{1}{2}(\partial_y)^2 & \frac{1}{2}(\partial_y)^2 \\ \frac{1}{2}(\partial_z)^2 & \frac{1}{2}(\partial_z)^2 & \frac{1}{2}(\partial_z)^2 \\ \partial_x\partial_z & \partial_x\partial_z & \partial_x\partial_z \\ \partial_y\partial_z & \partial_y\partial_z & \partial_y\partial_z \\ \partial_x\partial_y & \partial_x\partial_y & \partial_x\partial_y \end{bmatrix} \tag{2.6}$$

where ∂_x stands for the derivative along the x direction, so that $\partial_x = \dfrac{\partial(\cdot)}{\partial x}$. Tha same symbol is assumed for y and z directions. For the 2D model, the complete expressions of $\mathbf{b}_l$ and $\mathbf{b}_{nl}$ are:

$$\mathbf{b}_l = \begin{bmatrix} \frac{\partial_\alpha}{H_\alpha} & 0 & \frac{1}{H_\alpha R_\alpha} \\ 0 & \frac{\partial_\beta}{H_\beta} & \frac{1}{H_\beta R_\beta} \\ 0 & 0 & \partial_z \\ \partial_z - \frac{1}{H_\alpha R_\alpha} & 0 & \frac{\partial_\alpha}{H_\alpha} \\ 0 & \partial_z - \frac{1}{H_\beta R_\beta} & \frac{\partial_\beta}{H_\beta} \\ \frac{\partial_\beta}{H_\beta} & \frac{\partial_\alpha}{H_\alpha} & 0 \end{bmatrix},$$

$$\mathbf{b}_{nl} = \begin{bmatrix} \frac{1}{2H_\alpha^2}\left[(\partial_\alpha)^2 + \frac{2u_z\partial_\alpha}{R_\alpha} + \frac{u_\alpha}{R_\alpha^2}\right] & \frac{(\partial_\alpha)^2}{2H_\alpha^2} & \frac{1}{2H_\alpha^2}\left[(\partial_\alpha)^2 - \frac{2u_\alpha\partial_\alpha}{R_\alpha} + \frac{u_z}{R_\alpha^2}\right] \\ \frac{(\partial_\beta)^2}{2H_\beta^2} & \frac{1}{2H_\beta^2}\left[(\partial_\beta)^2 + \frac{2u_z\partial_\beta}{R_\beta} + \frac{u_\beta}{R_\beta^2}\right] & \frac{1}{2H_\beta^2}\left[(\partial_\beta)^2 - \frac{2u_\beta\partial_\beta}{R_\beta} + \frac{u_z}{R_\beta^2}\right] \\ \frac{1}{2}(\partial_z)^2 & \frac{1}{2}(\partial_z)^2 & \frac{1}{2}(\partial_z)^2 \\ \frac{1}{H_\alpha}\left(\partial_\alpha\partial_z + \frac{u_z\partial_z}{R_\alpha}\right) & \frac{\partial_\alpha\partial_z}{H_\alpha} & \frac{1}{H_\alpha}\left(\partial_\alpha\partial_z - \frac{u_\alpha\partial_z}{R_\alpha}\right) \\ \frac{\partial_\beta\partial_z}{H_\beta} & \frac{1}{H_\beta}\left(\partial_\beta\partial_z + \frac{u_z\partial_z}{R_\beta}\right) & \frac{1}{H_\beta}\left(\partial_\beta\partial_z - \frac{u_\beta\partial_z}{R_\beta}\right) \\ \frac{1}{H_\alpha H_\beta}\left(\partial_\alpha\partial_\beta + \frac{u_z\partial_\beta}{R_\alpha} + \frac{u_\beta}{R_\alpha R_\beta}\right) & \frac{1}{H_\alpha H_\beta}\left(\partial_\alpha\partial_\beta + \frac{u_z\partial_\alpha}{R_\beta}\right) & \frac{1}{H_\alpha H_\beta}\left(\partial_\alpha\partial_\beta - \frac{u_\alpha\partial_\beta}{R_\alpha} - \frac{u_\beta\partial_\alpha}{R_\beta}\right) \end{bmatrix} \tag{2.7}$$

where $H_\alpha = (1 + \frac{z}{R_\alpha})$, and $H_\beta = (1 + \frac{z}{R_\beta})$.

2.1.2 Constitutive equation

In this reasearch thesis, a linear elastic monoclinic material with orthotropic properties is supposed for each layer. The fiber angle only rotate around the z coordinate (for both 1D and 2D models). Hence, Hooke's law can be written at lamina level:

$$\sigma = \mathbf{C}\varepsilon \tag{2.8}$$

where $\mathbf{C}$ consists in the matrix of the material.

$$\mathbf{C} = \begin{bmatrix} C_{11} & C_{12} & C_{13} & 0 & 0 & C_{16} \\ & C_{22} & C_{23} & 0 & 0 & C_{26} \\ & & C_{33} & 0 & 0 & C_{36} \\ & & & C_{44} & C_{45} & 0 \\ & & & & C_{55} & 0 \\ sym & & & & & C_{66} \end{bmatrix} \tag{2.9}$$

where the coefficients depend on the Young moduli E, the Poisson ratios ν, the shear moduli G and the fiber angle orientation.

2.2 Finite Element Formulation of 1D and 2D CUF

2.2.1 1D beam elements

The Carrera Unified Formulation (CUF) is hereafter recalled for the definition of the 3D displacement field. It can be evaluated through expansion functions in the cross-sectional x, z plane of the unknowns evaluated over the beam axis in y. It can be stated that:

$$\mathbf{u}(x,y,z) = F_s(x,z)\mathbf{u}_s(y), \qquad s = 1,2,....,M \tag{2.10}$$

where F_s represent the expansion functions, $\mathbf{u}_s$ is the vector of the displacements along the y direction and M indicates the order of expansion in the thickness direction. The indexes s stand for the summing convention. The choice of F_s is purely arbitratry and determines the theory of structure adopted for a given problem. In this work both Lagrange and Taylor

polynomials are adopted to discretize the displacement field over the cross-section and they allow for the Layer-wise (LW) and Equivalent Single Layer (ESL) approaches, respectively. As far as the LW approach is concerned, the cross-section of the laminated beam is discretized with a set of Lagrange Points (LP), opportunely subdivided into Lagrange Elements (LE). The grade of the interpolation is defined by the number of the LP of the LE. For instance, a 4 points LE (L4) ensures a linear interpolation, a 9 points LE (L9) a quadratic interpolation and a 16 point LE (L16) a cubic interpolation. When dealing with composite structures, each layer may be modelled indipendently by using a dedicated F_τ polynomial set, bringing to a LW description of the laminate. A comprehensive review about LW theories was made by Carrera [25]. This theory treats each layer individually and both displacement and transverse shear stress continuity may be satisfied between each layer; therefore, it yields results compatible to 3D elasticity solutions. According to the LW approach, each layer has its own kinematic described by its own set of Lagrange polynomials. Multiple Lagrange polynomials can be assembled above the cross-section imposing the displacement continuity at the interface nodes, so any type of cross-section, from compact to thin-walled shapes, can be analyzed. For the sake of completeness, the complete expression of the displacement field of a generic point "A" within the cross-section, using an L9 polynomial, is reported hereafter:

$$\begin{aligned}
u_x(x,y,z) &= F_1(x,z)u_{x_1}(y) + F_2(x,z)u_{x_2}(y) + \ldots + F_9(x,z)u_{x_9}(y) \\
u_y(x,y,z) &= F_1(x,z)u_{y_1}(y) + F_2(x,z)u_{y_2}(y) + \ldots + F_9(x,z)u_{y_9}(y) \\
u_z(x,y,z) &= F_1(x,z)u_{z_1}(y) + F_2(x,z)u_{z_2}(y) + \ldots + F_9(x,z)u_{z_9}(y)
\end{aligned} \tag{2.11}$$

where the F_τ can be found in in [29].
The ESL approach allows to treat the multi-layered structure as a single-layered one, through an appropriate homogenization of the cross-section properties. The complete expression for a TE of order two (TE2) is reported in Eq. 2.12:

$$\begin{aligned}
u_x(x,y,z) &= u_{x_1}(y) + x\,u_{x_2}(y) + z\,u_{x_3}(y) + \\
&\quad x^2\,u_{x_4}(y) + xz\,u_{x_5}(y) + z^2\,u_{x_6}(y) \\
u_y(x,y,z) &= u_{y_1}(y) + x\,u_{y_2}(y) + z\,u_{y_3}(y) + \\
&\quad x^2\,u_{y_4}(y) + xz\,u_{y_5}(y) + z^2\,u_{y_6}(y) \\
u_z(x,y,z) &= u_{z_1}(y) + x\,u_{z_2}(y) + z\,u_{z_3}(y) + \\
&\quad x^2\,u_{z_4}(y) + xz\,u_{z_5}(y) + z^2\,u_{z_6}(y)
\end{aligned} \tag{2.12}$$

where x, y and z are the coordinates of a generic point "A". The number of the Degrees Of Freedom (DOFs) is equal to the displacement and derivatives of the TE and, for the case of a TE2, they are 18.
For the discretization along the y beam axis, the Finite Element Method (FEM) is employed. The unknowns over the beam axis can, then, be written as:

$$\mathbf{u}_s(y) = N_j(y)\mathbf{q}_{sj} \qquad j = 1,2,\ldots,p+1 \tag{2.13}$$

where N_j are the 1D finite element shape functions, p stands for the order of the shape functions, the repeated index j indicates summation over the number of nodes and $\mathbf{q}_{sj}$ is the vector of the Finite Element (FE) nodal parameters:

$$\mathbf{q}_{sj} = \left\{ \begin{array}{ccc} q_{x_{sj}} & q_{y_{sj}} & q_{z_{sj}} \end{array} \right\}^T \tag{2.14}$$

The complete expression of the shape functions can be found in many reference texts, for instance in Bathe [14]. It has to be pointed out that the type of the cross-section discretization (i.e. the order of the shape function F_s) does not depend on the choice of the shape function N_j. In this thesis, four noded 1D FEs (B4) are adopted, i.e. a cubic approximation along the y axis is assumed.

2.2.2 2D shell elements

Regarding the 2D models, according to CUF, the 3D displacement field of a shell structure can be evaulated as a generic through-the-thickness z expansion of FE nodal unknowns which lay on the α-β surface. It reads as:

$$\mathbf{u}(\alpha,\beta,z) = F_s(z)\mathbf{u}_s(\alpha,\beta), \qquad s = 0,1,\cdots,N, \tag{2.15}$$

where N determines the the order of the through-the-thickness expansionn. In this thesis the same LW and ESL approaches as described in the previous Section are used. For the latter, Taylor expansions are employed, for the former linear two noded (LD1), quadratic three noded (LD2), and cubic four noded (LD3) Lagrange expansion functions are adopted. Finally, FEM is used to approximate the shell component in the α-β surface, as follows:

$$\mathbf{u}_s(\alpha,\beta) = N_j(\alpha,\beta)\mathbf{q}_{sj}, \qquad j = 1,2,\ldots,p+1, \tag{2.16}$$

The vector of the FE nodal unknowns $\mathbf{q}_{sj}$ reads as

$$\mathbf{q}_{sj} = \left\{ \begin{array}{ccc} q_{\alpha_{sj}} & q_{\beta_{sj}} & q_{z_{sj}} \end{array} \right\}^{\mathrm{T}} \tag{2.17}$$

In the present thesis, 2D nine noded quadratic FEs (Q9) will be adopted for the shape function in the α-β surface. Figure 2.2 summarises the described process. In Fig. 2.2(a), the 1D model is described, where the cross-section expansion function are higligthed in red and lays on the x,z plane, and the shape function, in blue, approximate the beam axis. On the other hand, Fig. 2.2(b) shows the 2D shell model, where the red F_s describe the thickness z coordinate, whereas N_j approximate the displacemens over the reference surface.

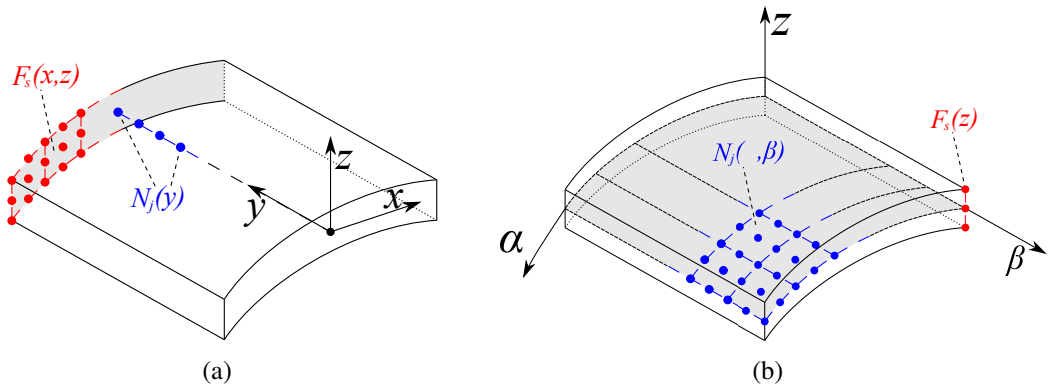

Fig. 2.2 CUF and FEM 1D (a) and 2D (b) models of the shell structure.

Finally, with the CUF ((Eqs. (2.10) and (2.15))) and FEM ((Eqs. (2.13) and (2.16))) equations into Eq. (6.1), the strain vector can be evaluated as:

$$\varepsilon \quad = \quad (\mathbf{B}_l^{sj} + \mathbf{B}_{nl}^{sj})\mathbf{q}_{sj} \tag{2.18}$$

where $\mathbf{B}_l^{sj}$ is the linear contribution and $\mathbf{B}_{nl}^{bsj}$ the nonlinear one. Refs. [144] and [186] report the complete expression of these matrixes for 1D and 2D models, respectively.

2.3 Stiffness matrices

The equation of an elastic body can be obtained by the principle of virtual work. Neglecting the work made by the inertial loads, it can be written as follows:

$$\delta L_{\text{int}} - \delta L_{\text{ext}} = 0 \tag{2.19}$$

where L_{int} is the strain energy, the work by the external loads is represented by L_{ext}, and δ denotes a virtual variation. The first term of Eq. (2.19) can be written as:

$$\delta L_{\text{int}} =< \delta\varepsilon^T \sigma > \tag{2.20}$$

In Eq. (2.20) and in every subsequent equation, $< (\cdot) >= \int_V (\cdot)\, dV$, where V is the volume of the structure.

2.3.1 Secant stiffness matrix

Given the geometrical (Eq. (2.18)) and constitutive relations (Eq. (2.8)), one has:

$$\begin{aligned}
\delta L_{\text{int}} &= \delta \mathbf{q}_{\tau i}^T < \left(\mathbf{B}_l^{\tau i} + 2\mathbf{B}_{nl}^{\tau i}\right)^T \mathbf{C} \left(\mathbf{B}_l^{sj} + \mathbf{B}_{nl}^{sj}\right) > \mathbf{q}_{sj} \\
&= \delta \mathbf{q}_{\tau i}^T \mathbf{K}_0^{ij\tau s} \mathbf{q}_{sj} + \delta \mathbf{q}_{\tau i}^T \mathbf{K}_{lnl}^{ij\tau s} \mathbf{q}_{sj} + \delta \mathbf{q}_{\tau i}^T \mathbf{K}_{nll}^{ij\tau s} \mathbf{q}_{sj} + \delta \mathbf{q}_{\tau i}^T \mathbf{K}_{nlnl}^{ij\tau s} \mathbf{q}_{sj} \\
&= \delta \mathbf{q}_{\tau i}^T \mathbf{K}_S^{ij\tau s} \mathbf{q}_{sj}
\end{aligned} \tag{2.21}$$

where $\mathbf{K}_S^{ij\tau s}$ is the secant stiffness matrix and it is equal to $\mathbf{K}_0^{ij\tau s} + \mathbf{K}_{lnl}^{ij\tau s} + \mathbf{K}_{nll}^{ij\tau s} + \mathbf{K}_{nlnl}^{ij\tau s}$. In Eq. 2.21, $\mathbf{K}_0^{ij\tau s}$ is the linear contribution of $\mathbf{K}_S$, $\mathbf{K}_{lnl}^{ij\tau s}$ and $\mathbf{K}_{nll}^{ij\tau s}$ are the nonlinear components of order 1, and $\mathbf{K}_{nlnl}^{ij\tau s}$ represents the nonlinearities of order 2. These contitute the *so-called* fundamental nuclei (FN), and are 3×3 matrices that can be arbitrarily expanded by opportunely expanding the indexes τ, s, i and j in order to achieve any desired theory and FE approximation order. Basically, any refined theory can be implemented in the model in an automatic manner by the expansion functions (F_τ and F_s) and the shape expansions (N_i and N_j).
The L_{ext}, right term of the Eq. (2.19), ca be expressed as:

$$\delta L_{\text{ext}} = \delta \mathbf{q}_{sj}^T \, \mathbf{p}_{sj} \tag{2.22}$$

The mathematical steps behind Eq. (2.22) can be found in Carrera *et al.* [33]. Given the Eqs. (2.21) and (2.22) into Eq. (2.19) becomes:

$$\mathbf{K}_S^{ij\tau s} \mathbf{q}_{\tau i} - \mathbf{p}_{sj} = 0 \tag{2.23}$$

Any arbitrary theory can be obtained by expanding Eq. (2.23), by using the values for τ, s, i and j. It reads:

$$\mathbf{K}_S \, \mathbf{q} - \mathbf{p} = 0 \tag{2.24}$$

where $\mathbf{K}_S$, $\mathbf{q}$, and $\mathbf{p}$ are the assembled, finite element matrices and vectors of the global structure.

2.3.2 Tangent stiffness matrix

As far as the tangent stiffness matrix, $\mathbf{K}_T^{ij\tau s}$, is concerned, the linearization of the equilibrium equations has to be performed. Conservative loadings are assumed in this work, so that the linearization of the work made by the external loads is null. As a consequence, the linearization of the internal loads is required:

$$\begin{aligned} \delta(\delta L_{\text{int}}) &= \int_V \delta(\delta\varepsilon^T \sigma)\, dV \\ &= \int_V (\delta\varepsilon^T \delta\sigma) + (\delta(\delta\varepsilon^T)\sigma)\, dV \end{aligned} \tag{2.25}$$

where the left term is evaluated as follows:

$$\int_V \delta\varepsilon^T \delta\sigma dV = \delta\mathbf{q}_{\tau i}^T \int_V (\mathbf{B}_l^{\tau i} + 2\mathbf{B}_{nl}^{\tau i})^T \mathbf{C}\,(\mathbf{B}_l^{sj} + 2\mathbf{B}_{nl}^{sj}))\, dV \delta\mathbf{q}_{sj} \tag{2.26}$$

Equation 2.26 can be expanded in terms of the FN, as the following system suggests:

$$\begin{cases} \int_V \mathbf{B}_l^{\tau i} \mathbf{C} \mathbf{B}_l^{sj}\, dV = \mathbf{K}_0^{ij\tau s} & \textit{linear contribution} \\ \int_V \mathbf{B}_l^{\tau i} \mathbf{C} 2\mathbf{B}_{nl}^{sj}\, dV = 2\mathbf{K}_{lnl}^{ij\tau s} & \textit{nonlinear contribution of order 1} \\ \int_V 2\mathbf{B}_{nl}^{\tau i} \mathbf{C} \mathbf{B}_l^{sj}\, dV = \mathbf{K}_{nll}^{ij\tau s} & \textit{nonlinear contribution of order 1} \\ \int_V 2\mathbf{B}_{nl}^{\tau i} \mathbf{C} 2\mathbf{B}_{nl}^{sj}\, dV = 2\mathbf{K}_{nlnl}^{ij\tau s} & \textit{nonlinear contribution of order 2} \end{cases} \tag{2.27}$$

where $\mathbf{K}_0^{ij\tau s}$, $\mathbf{K}_{lnl}^{ij\tau s}$, $\mathbf{K}_{nll}^{ij\tau s}$, and $\mathbf{K}_{nlnl}^{ij\tau s}$ are the same FNs as presented in Eq. 2.21.

The right term of the Eq. 2.25 is:

$$\int_V \delta(\delta\varepsilon^T)\sigma \, dV \quad = \quad \delta\mathbf{q}_{\tau i}^T \mathbf{K}_\sigma^{ij\tau s} \delta\mathbf{q}_{sj} \tag{2.28}$$

where $\mathbf{K}_\sigma^{ij\tau s}$ is the FN of the geometrical stiffness matrix. It is a diagonal matrix and it is given in the following for the sake of completeness:

$$\begin{aligned}
\mathbf{K}_\sigma^{ij\tau s} \quad = \quad & \int_V (\sigma_{xx} F_{\tau,x} F_{s,x} F_\tau N_j + \sigma_{yy} F_\tau F_s N_{i,y} N_{j,y} + \sigma_{zz} F_{\tau,z} F_{s,z} N_i N_j + \sigma_{xy} F_{\tau,x} F_s N_i N_{j,y} \\
+ \quad & \sigma_{xy} F_\tau F_{s,x} N_{i,y} N_j + \sigma_{xz} F_{\tau,x} F_{s,z} N_i N_j + \sigma_{xz} F_{\tau,z} F_{s,x} N_i N_j + \sigma_{yz} F_{\tau,z} F_s N_i N_{j,y} \\
+ \quad & \sigma_{yz} F_\tau F_{s,z} N_{i,y} N_j) \mathbf{I} \mathrm{d}V
\end{aligned} \tag{2.29}$$

where $\mathbf{I}$ is the 3×3 identity matrix. As for the elemental linear stiffness matrix, and given the cross-sectional functions F_τ and the 1D shape functions F_τ, the fundamental nucleus of the geometric stiffness matrix can be expanded in an automatic way by employing CUF to give the elemental matrix for any desired beam theory.

2.4 Nonlinear governing equations

2.4.1 Newton-Raphson linearization

Equation (2.24) represents the starting condition for the solution of the geometrical nonlinear problems. Typically, an incremental scheme of linearizing type is employed, and the one adopted in this thesis is the Newton-Raphson method (or *tangent method*). According to it, the equations can be written as:

$$\varphi_{res} \equiv \mathbf{K}_S \mathbf{q} - \mathbf{p} = 0 \tag{2.30}$$

where φ_{res} can be represented as the *residual nodal forces* (unbalanced nodal force vector). Taylor's series can now be adopted to linearize the previous equation. Around a known

condition $(\mathbf{q}, \mathbf{p})$ and with the first order terms, it reads:

$$\varphi_{res}(\mathbf{q}+\delta\mathbf{q}, \mathbf{p}+\delta\mathbf{p}) = \varphi_{res}(\mathbf{q}, \mathbf{p}) + \frac{\partial \varphi_{res}}{\partial \mathbf{q}}\,\delta\mathbf{q} + \frac{\partial \varphi_{res}}{\partial \mathbf{p}}\,\delta\lambda\,\mathbf{p}_{ref} = 0 \tag{2.31}$$

where $\dfrac{\partial \varphi_{res}}{\partial \mathbf{q}} = \mathbf{K}_T$ represents the tangent stiffness matrix, and $-\dfrac{\partial \varphi_{res}}{\partial \mathbf{p}}$ stands for the matrix $\mathbf{I}$. Equation (2.31) assumes the proportionality between the external load $\mathbf{p}$ and the reference one $\mathbf{p}_{ref}$, and the rate equals λ, which can be called as the load parameter . Basically, one has:

$$\mathbf{p} = \lambda\,\mathbf{p}_{ref} \tag{2.32}$$

If the load parameter λ is considered as a variable, an additional equation need to be included. Usually, it is represented by a constraint equation $c(\delta\mathbf{q}, \delta\lambda)$. The final system reads as:

$$\begin{cases} \mathbf{K}_T\,\delta\mathbf{q} = \delta\lambda\,\mathbf{p}_{ref} - \varphi_{res} \\ \\ c(\delta\mathbf{q}, \delta\lambda) = 0 \end{cases} \tag{2.33}$$

Different constraining equations can be implemented. For instance, one can impose the condition $\delta\lambda = 0$ or $\delta\mathbf{q} = 0$, corresponding to the load-control and displacement-control methods. in the present thesis, a method of a path-following type is implemented, and the contraint condition involves both displacement and load parameter. Differences between the aforementioned contraint equations are described in Fig. 2.3 and more details can be found in [154, 24, 52].

2.4.2 Path-following constraint

The path following constraint used in this thesis in the framework of CUF was first developed by Pagani and Carrera [144]. Figure 2.4 shows the details, along with the adopted notation, of the path-following contraint employed in this thesis. In the figure:

- $\delta^n_m(\cdot)$ denotes a finite variation, where m indicates the number of reached load step and n the iteration within the m^{th} load step. It can be stated that $\delta^n_m(\cdot) = (\cdot)^n_m - (\cdot)^{n-1}_m$ and $(\cdot)_m = (\cdot)_{m-1} + \sum_n \delta^n_m(\cdot)$;
- $n = 0$ is the initial condition, so that $\delta^0_m\mathbf{q}$ is the initial linear solution and $\delta^0_m\lambda$ is the initial increment of the load parameter;
- $\varphi^n_{m_{res}}$ is the vector of the residual nodal forces at the n^{th} iteration (of the m^{th} load step).

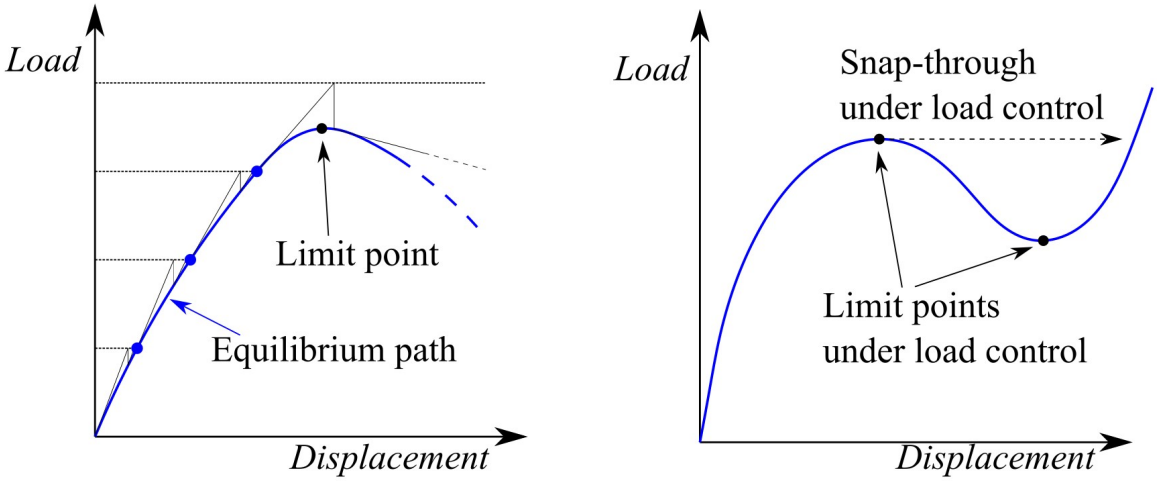

(a) Load-control method

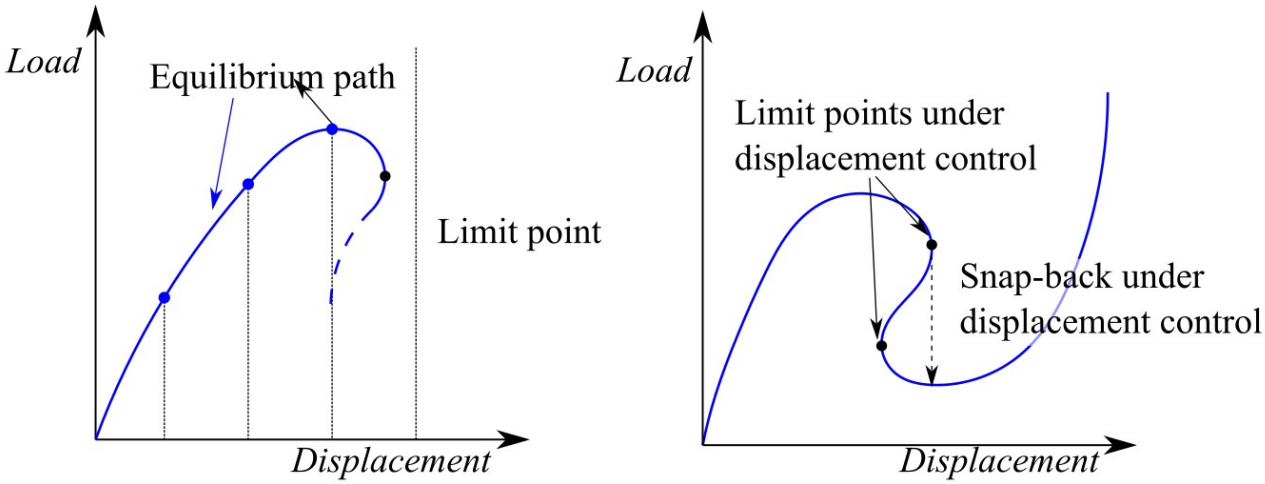

(b) Displacement-control method

Fig. 2.3 Contraint methods.

- $\mathbf{t}_m^n = \mathbf{t}_m^{n-1} + \delta_m^n \mathbf{t} = \mathbf{t}_m^{n-1} + (\delta_m^n \mathbf{q} + \delta_m^n \lambda \, \mathbf{p}_{ref})$ relates the current solution to the previous one.

As a consequence, the equilibrium reached at each iteration is given by the intersection of the linearized governing equation and the constraint equation $c(\delta\mathbf{q}, \delta\lambda) = 0$. The arc-length method as developed by Criesfield [50, 51] is employed. Thus, the initial arc-length value Δl_m^0 is equal to the radius of a sphere, which represent the constraint relationship. It means that $|\mathbf{t}_m^n|$ is equal to the square of the arc-length. The system of equation expressed in Eq. (2.33)

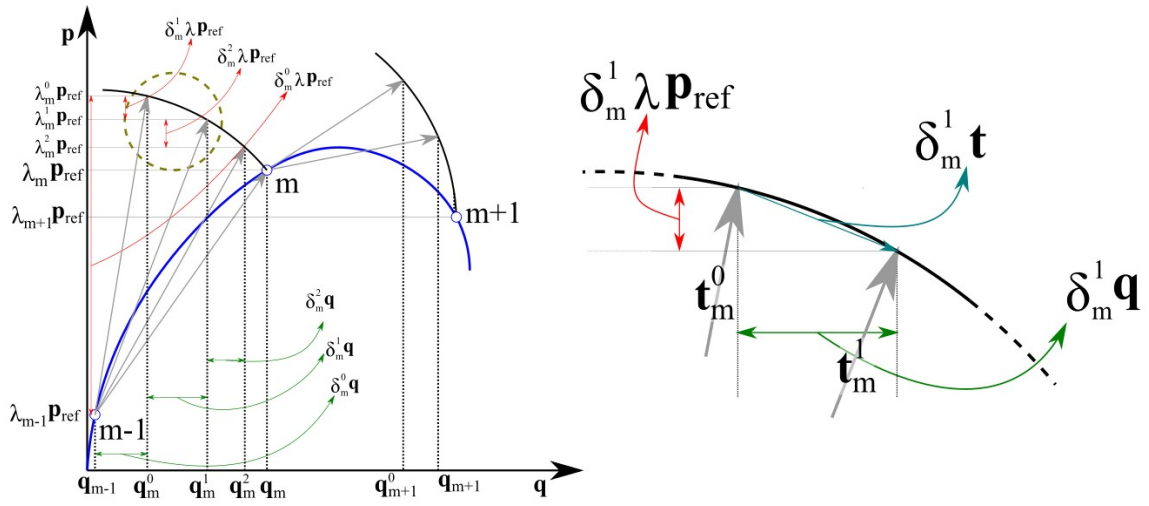

Fig. 2.4 Contraint method of arc-length type.

becomes:

$$\begin{cases} \mathbf{K}_T \, \delta^n_m \mathbf{q} = \delta^n_m \lambda \, \mathbf{p}_{ref} - \varphi^n_{m_{res}} \\ \\ \mathbf{t}^{n^T}_m \mathbf{t}^n_m = (\Delta l^0_m)^2 \end{cases} \tag{2.34}$$

This procedure would require the inversion of the tangent stiffness matrix, which could be computationally heavy. For this reason, the Batoz and Dhatt [16] approach is adopted, and the finite displacement vector could be written as:

$$\delta^n_m \mathbf{q} = \delta^n_m \lambda \, \bar{\mathbf{q}}^n_m + \delta^n_m \hat{\mathbf{q}} \tag{2.35}$$

where $\bar{\mathbf{q}}^n_m$ and $\delta^n_m \hat{\mathbf{q}}$ are the solutions of the linear systems below:

$$\begin{cases} \mathbf{K}_T \, \bar{\mathbf{q}}^n_m = \mathbf{p}_{ref} \\ \\ \mathbf{K}_T \, \delta^n_m \hat{\mathbf{q}} = -\varphi^n_{m_{res}} \end{cases} \tag{2.36}$$

Thus, introducing Eq. (2.35) into the system Eq. (2.34), the following equation can be written as:

$$a \, (\delta^n_m \lambda)^2 + 2 \, b \, \delta^n_m \lambda + c = 0 \tag{2.37}$$

where

$$\begin{aligned} a &= \bar{\mathbf{q}}_m^{n^T}\,\bar{\mathbf{q}}_m^n + \mathbf{p}_{ref}^T\,\mathbf{p}_{ref} \\ b &= (\mathbf{q}_m^{n-1} - \mathbf{q}_{m-1})^T\,\bar{\mathbf{q}}_m^n + \bar{\mathbf{q}}_m^{n^T}\,\delta_m^n\hat{\mathbf{q}} + (\lambda_m^{n-1} - \lambda_{m-1})\,\mathbf{p}_{ref}^T\mathbf{p}_{ref} \\ c &= \left((\mathbf{q}_m^{n-1} - \mathbf{q}_{m-1}) + \delta_m^n\hat{\mathbf{q}}\right)^T\left((\mathbf{q}_m^{n-1} - \mathbf{q}_{m-1}) + \delta_m^n\hat{\mathbf{q}}\right) + \\ &\quad (\lambda_m^{n-1} - \lambda_{m-1})^2\,\mathbf{p}_{ref}^T\mathbf{p}_{ref} - (\Delta l_m^0)^2 \end{aligned} \tag{2.38}$$

Equation (2.37) returns two solutions of the load parameter $\delta_m^n\lambda$, so the problem of which of the solutions has to be chosen, arises. The solution which gives a positive angle is the one to be chosen. In the case both solutions gives positive angles, the appropriate one is the closest to the linear solution of Eq. (2.37), i.e. $\delta_m^n\lambda = -\frac{c}{b}$. In this thesis, the closest solution to the one of the linearized constraint equation, $\delta_m^n\lambda_{\text{cl}}$. $\delta_m^n\lambda_{\text{cl}}$ is calculated by linearizing the constraint relationship $c(\delta\mathbf{q}, \delta\lambda) = 0$, as done for the equilibrium equations. [24] reported the explicit linearization of the constraint equation.

2.5 Examples

2.5.1 Beams subjected to bending

An cantilever isotropic beam is considered as a first example. The beam is subjected to a transverse force and the material properties involve the Young modulus E equal to 75 GPa and Poisson ratio $\nu = 0.33$. The geometric properties and discretization details are shown in Fig. 2.5. Two length-to-side ratios are considered, $L/h = 10$ and $L/h = 100$. One L9 and 20 B4 are employed for the cross-section and beam axis approximations, respectively. The results are shown in Fig. 2.6 for both slenderness ratios. A comparison with the results from [21] is proposed, to highlight the validity of the proposed approach. The steps evaluated with the arc-length method are highlighted, and for some of those the deformed structure is shown.

2.5.2 Compressed isotropic square beam

The second analysis case regards the post-buckling of a cantilever beam. The same structure as the one presented in the previous analysis case with $L/H = 100$ slenderness ratio is considered. The discretization for both cross-section and beam axis domains is the same. It must be higlighted that the structure shows symmetric at geometric, material and boundary

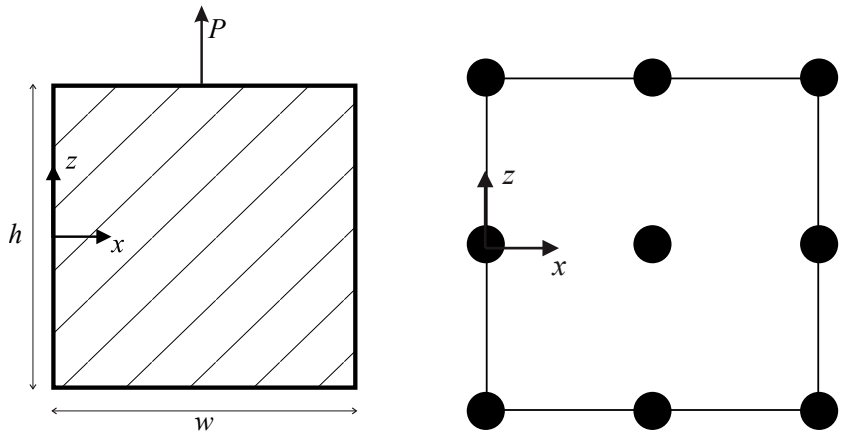

(a) (b)

Fig. 2.5 Geometric properties (a) and cross-sectional discretization details (b) of a cantilever isotropic beam.

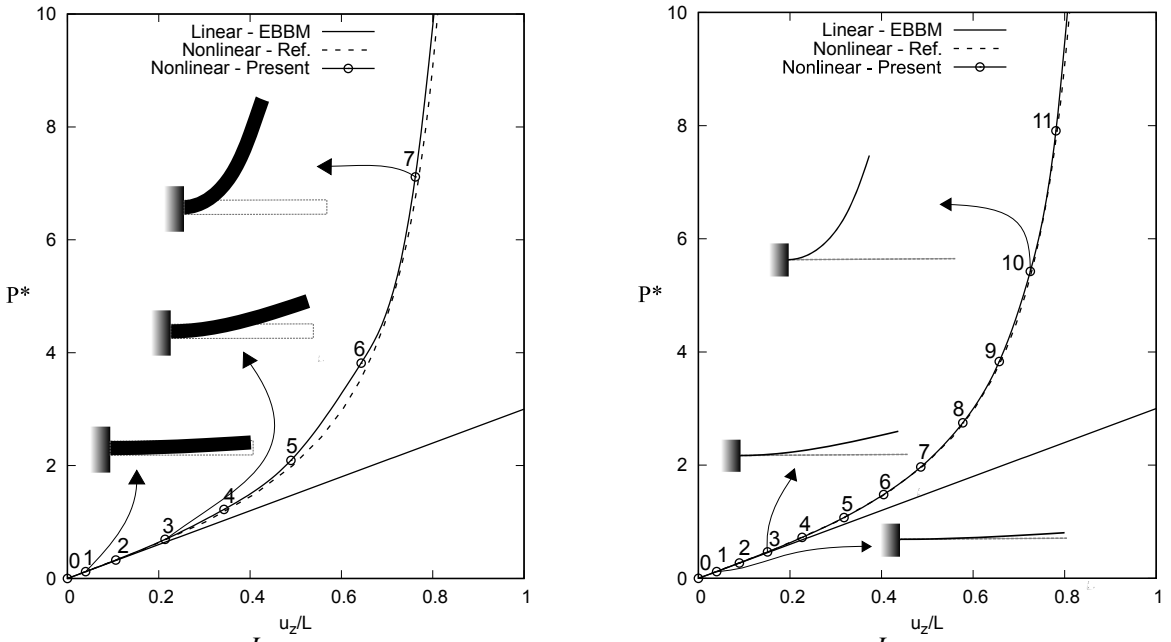

(a) $\frac{L}{h} = 10$ (b) $\frac{L}{h} = 100$

Fig. 2.6 Nonlinear equilibrium static curves of the cantilever isotropic beam, considering two slenderness ratios. Reference solution [21]. $P^* = \frac{l^2}{EI}$

level. For this reason, the post-buckling solution has to be enforced by imposing some imperfections. The solution adopted in this thesis is to impose a very small perturbation load (compared to the external one) to induce the solution branch. The static solution is reported in Fig. 2.7, where some of the deformed configurations are reported.

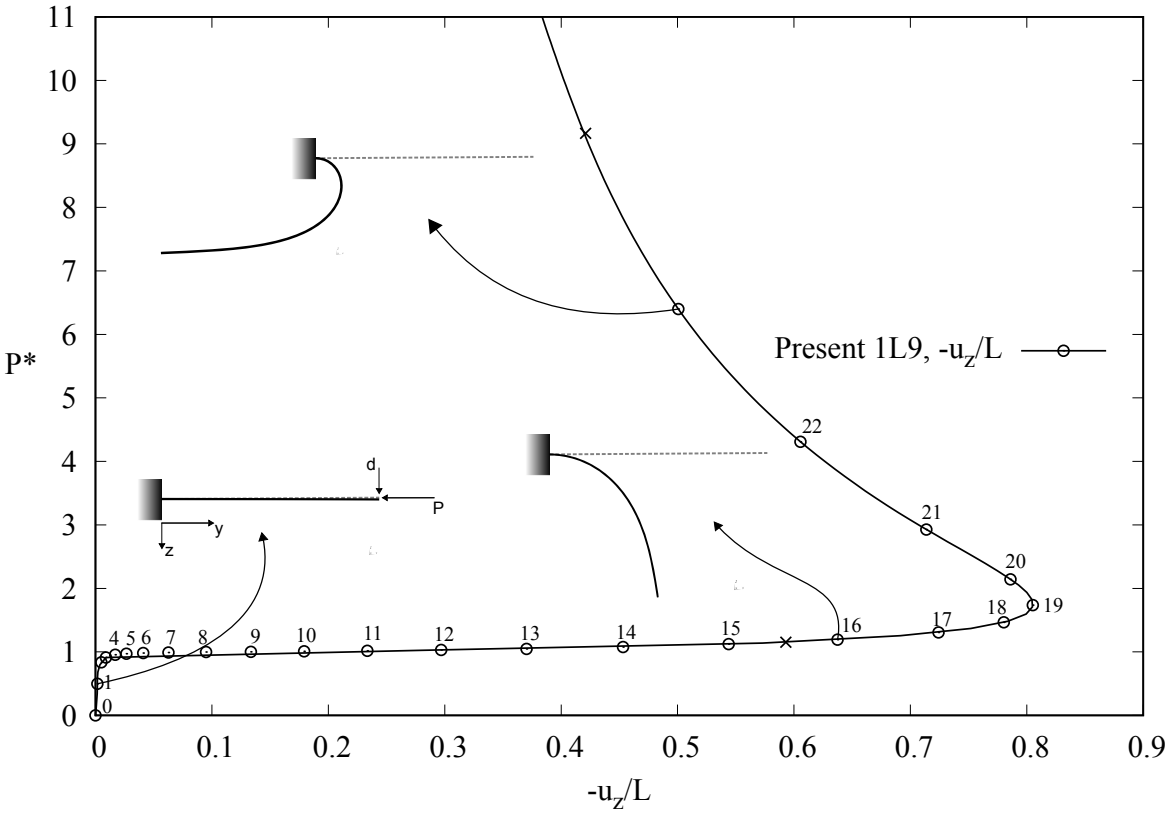

Fig. 2.7 Nonlinear equilibrium static curve for a compressed isotropic beam. $P^* = \frac{4L^2}{\pi^2 EI}$

2.5.3 Pinched thin-walled cylinder

The capability of the proposed model to deal with the analysis of shell structure using 2D model is demonstrated in this Section. A pinched cylinder is analyzed, and the material properties, along with the geometrical properties, are taken from the well-known problem analyzed by Flügge [66]. The geometric and loading condition are shown in Fig. 2.8, where $L = 600$ in, radius $r = 300$ in and thickness $t = 3$ in. The Young modulus is $E = 3 \times 10^6$ psi and Poisson ratio $\nu = 0.3$. The transverse displacement of the loading point was evaluated using both 1D and 2D models of the structure. Figure 2.9 shows both models and, for the symmetric nature of the study case, only 1/8 of the entire model is analyzed. Regarding the 1D model, 10L9, 20L9, and 30L9 Lagrange polynomials were adopted for the cross-section discretization, whereas 1, 2 and 3 B4 for the beam axis one. As far as the 2D model is concerned, from 12Q9 up to 600Q9 described the in-plane displacement field, expanded by 1LD2 in the thickness direction. Figure 2.10 shows the quasi-static equilibrium nonlinear curve of the transverse displacement of the loading point A (see Fig. 2.9). These converged analyses show the model to be taken for the comparison between the two models, i.e. the 30L9 - 10B4 solution for the 1D model and 600Q9 - 1LD2 for the 2D one. In addition, a

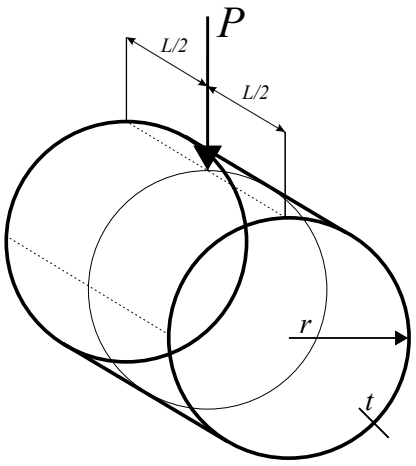

Fig. 2.8 Pinched isotropoic cylinder. Geometry and loading conditions.

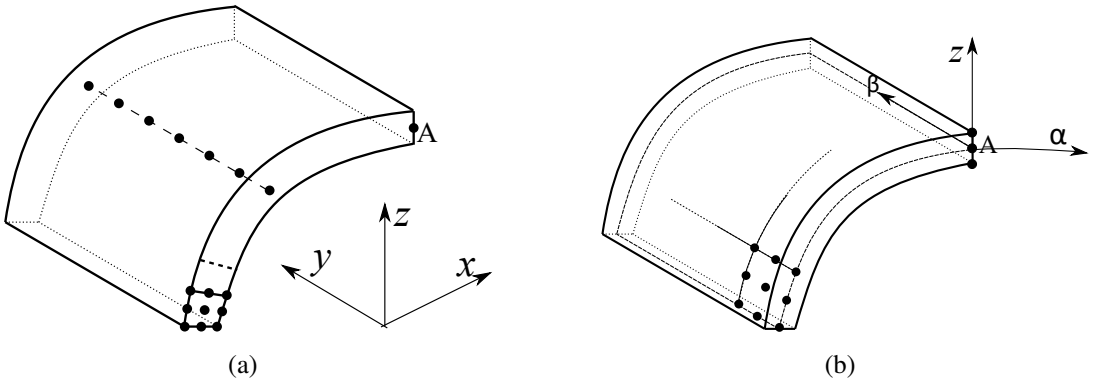

Fig. 2.9 1D and 2D models of a pinched cylinder.

2D shell and 3D solid discretizations with Nastran were built for comparison purposes. The adopted Nastran models are shown in Fig. 2.11. 5400 shell elements were emploued for the 2D shell model (90×60). For the 3D solid solution, 12600 solid elements were used ($315 \times 200 \times 2$). The results of the considered models are reported in Table 4.1, which show the validity of the proposed 2D shell model and, in addition, a DOF reduction compared with the 1D model. The converged 1D and 2D unified models are compared with the Nastran ones in Fig. 2.12, showing an almost perfect match between the solutions. Finally, the convergence properties of the two models (with the 3D Nastran solution as reference) are reported in Fig. 2.13. Clearly, the 1D beam models shows a faster convergence then the 2D model. $P = 1000$ klb was fixed for the convergence analysis. As a final analysis, a 1D model with different sizes of the FEs is proposed. In fact, for the results previously shown, a homogeneous discretization for the beam axis is adopted, so that every B4 element has the same size. This choice was made to make the proposed model as generic as possible

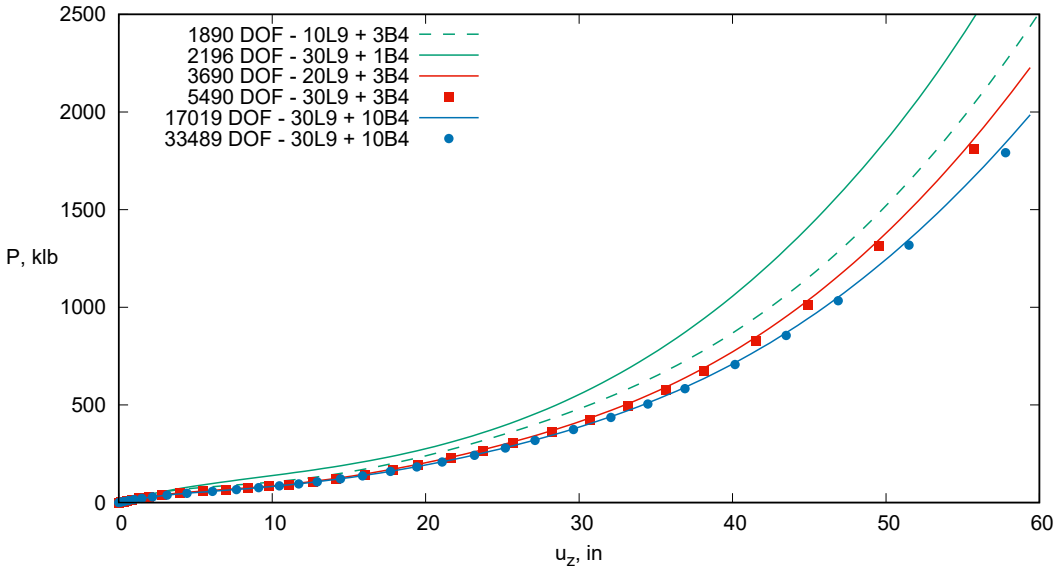

(a) 1D Beam CUF model

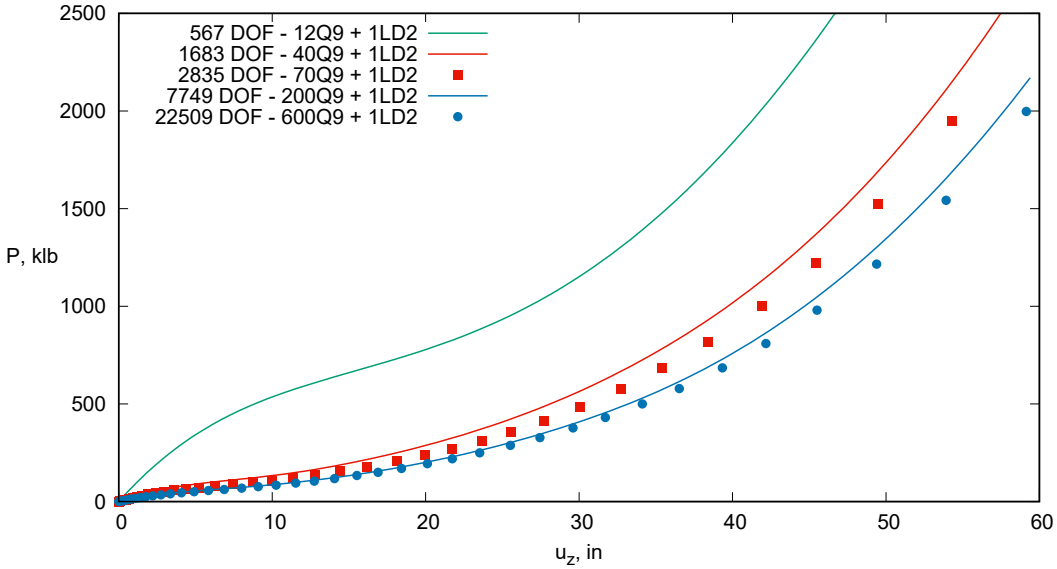

(b) 2D Shell CUF model

Fig. 2.10 Equilibrium curves and convergence anaylses for the pinched isotropic cylinder via 1D (a) and 2D (b) models.

and suitable for every loading and boundary condition. However, one of the main features of the proposed unified 1D model is the possibility to refine the mesh in certain zones of interest within the structure. As depicted in Fig. 2.15, one can add more FEs in the proximity of interested areas (for example, the external force) without any mesh problems. For the 2D models, the refinement is not possible without resorting to external and time-consuming techniques. Fig. 2.15(b) shows a finer mesh, and some red nodes are not connected. Next,

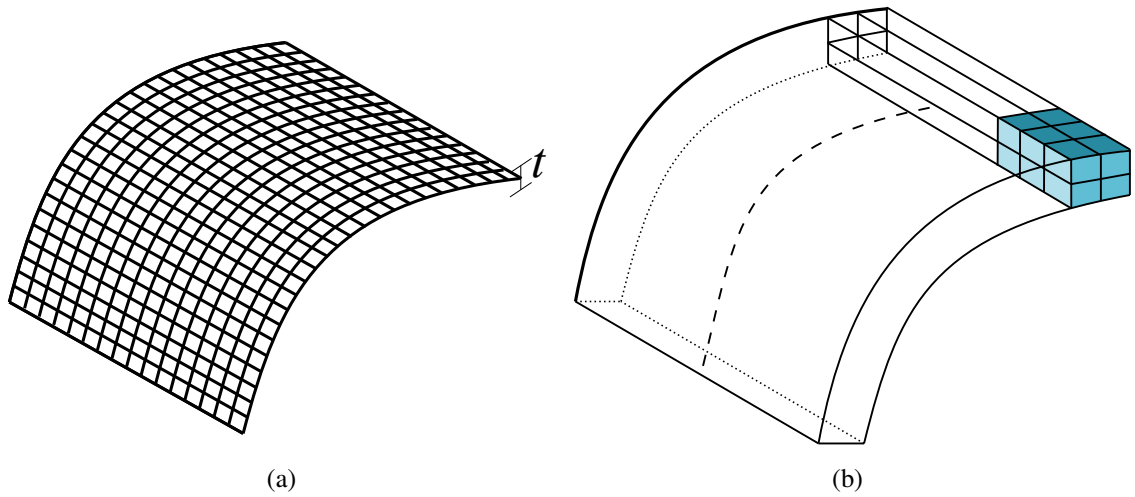

Fig. 2.11 Nastran 2D (a) and 3D (b) models of the pinched isotropic cylinder.

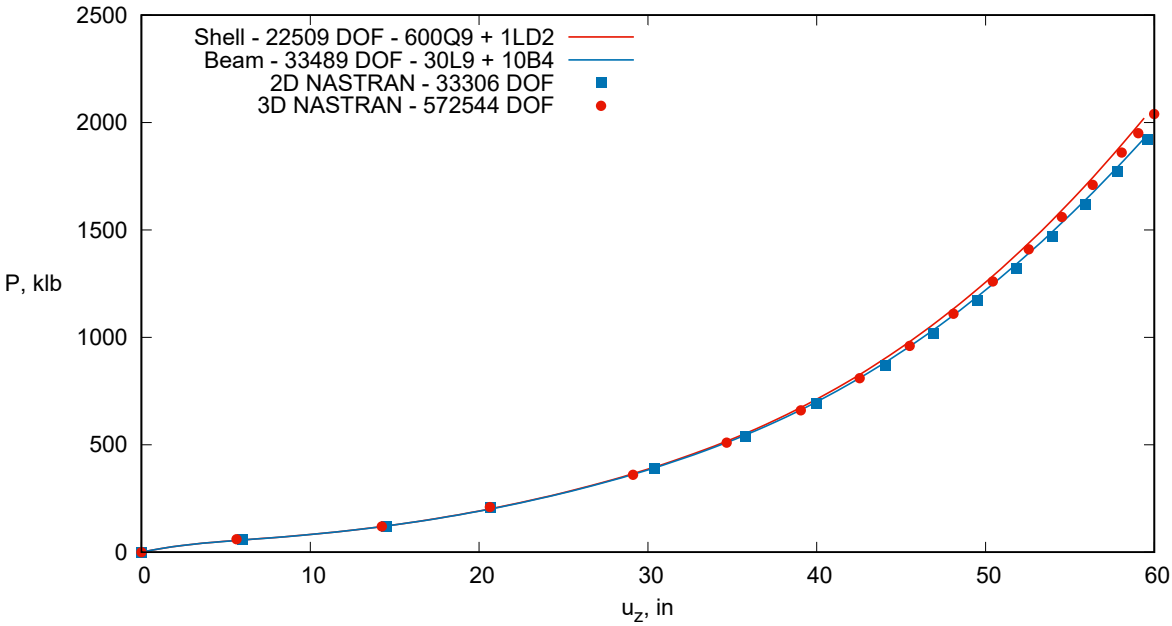

Fig. 2.12 Solution of the converged unified models and the Nastran 2D shell and 3D solid models.

a 15B4 1D model with a different size of the FEs is considered in the next analysis. To distinguish this analysis from the other, an apex is used, so that 15B4* means that the FEs are not equi-sized. The displacement trend is shown in Fig. 2.14. Clearly, the results are slightly different from the equi-sized FE mesh, and the 15B4* solution is closer to the previously shown with 20B4, with a significant loss of DOFs. Correspondent values are reported in Table 2.2.

Model	Approximation	DoFs	P = 500.0	P = 1000	P = 1500	P = 2000
			u_{zA}	u_{zA}	u_{zA}	u_{zA}
1D Beam	10L9 + 3B4	1890	30.64	42.35	49.63	55.15
	30L9 + 1B4	2196	28.38	39.00	45.91	51.23
	20L9 + 3B4	3690	32.97	44.30	51.38	57.02
	30L9 + 3B4	5490	33.35	44.72	51.86	57.57
	30L9 + 10B4	17019	34.13	45.86	53.58	59.50
	30L9 + 15B4	25254	34.26	46.14	53.73	59.82
	30L9 + 20B4	33489	**34.49**	**46.89**	**54.21**	**59.92**
2D Shell	12Q9 + 1LD2	567	8.865	26.70	35.71	41.74
	40Q9 + 1LD2	1683	28.08	39.61	47.08	52.70
	70Q9 + 1LD2	2835	30.48	41.85	49.18	54.79
	200Q9 + 1LD2	7749	33.16	44.61	51.99	57.62
	600Q9 + 1LD2	22509	**34.35**	**46.11**	**53.68**	**59.15**
3D NASTRAN	200 × 315	571644	**34.36**	**46.23**	**54.76**	**59.58**

Table 2.1 Transverse displacement of the loading point of the pinched isotropic ctlinder using different models and theories. P is expressed in klb, u_{zA} in inches.

Model	Approximation	DoFs	P = 500.0	P = 1000	P = 1500	P = 2000
			u_{zA}	u_{zA}	u_{zA}	u_{zA}
1D Beam	30L9 + 10B4	17019	34.13	45.86	53.58	59.50
	30L9 + 15B4	25254	34.26	46.14	53.73	59.82
	30L9 + 15B4*	25254	34.32	46.32	54.26	60.43
	30L9 + 20B4	33489	34.49	46.89	54.21	59.92
3D NASTRAN	200 × 315	571644	**34.36**	**46.23**	**54.76**	**59.58**

Table 2.2 Transverse displacement for the 1D model of a pinched thin-walled cylinder evaluated at the middle of the thickness of the structure (see point A in Fig. 2.9). P is expressed in klb, u_{zA} in inches. 15B4* means that elements along the beam axis do not have the same size, but they are finer near the external force.

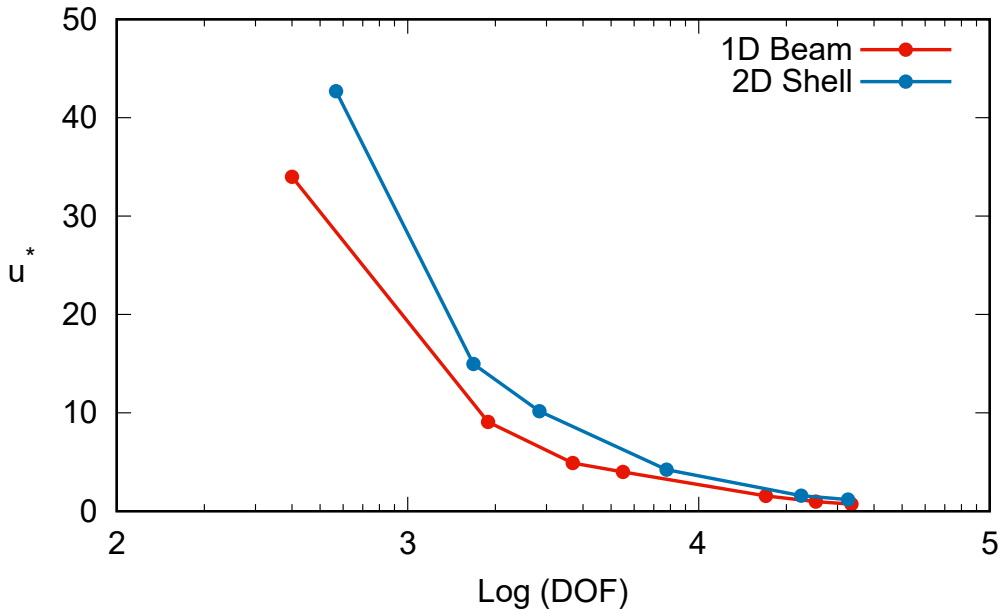

Fig. 2.13 Convergence properties of the 1D and 2D models for the pinched isotropic cylinder. Reference results taken from 3D analysis with NASTRAN. $u^* = \dfrac{u_z - u_{zRef.}}{u_{zRef.}}$ and $P = 1000$ N.

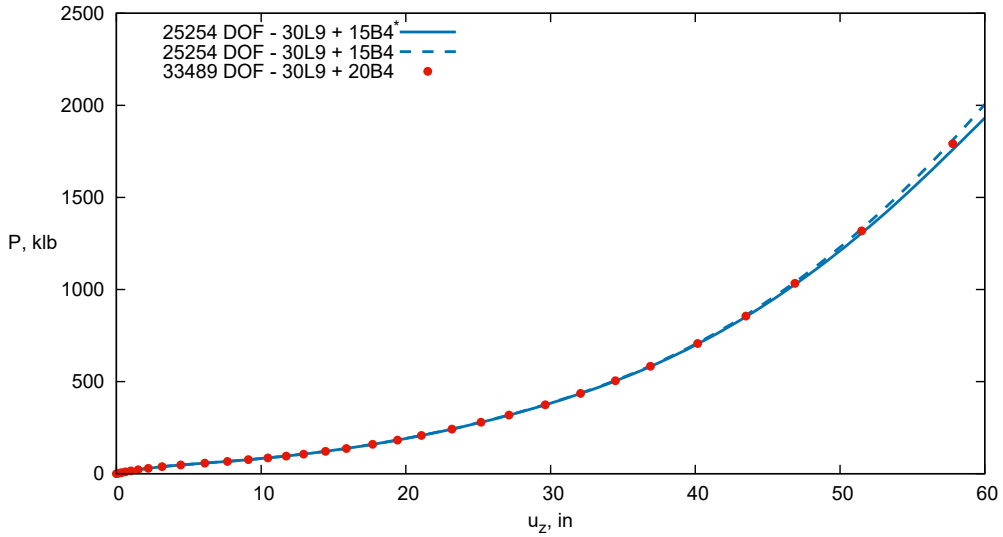

Fig. 2.14 Nonlinear equilibrium curves of the pinched thin-walled cylinder using 1D models. Transverse displacement valuated at the middle of the thickness of the structure (see point A in Fig. 2.12). 15B4* means that elements along the beam axis do not have the same size, but they are finer near the external force.

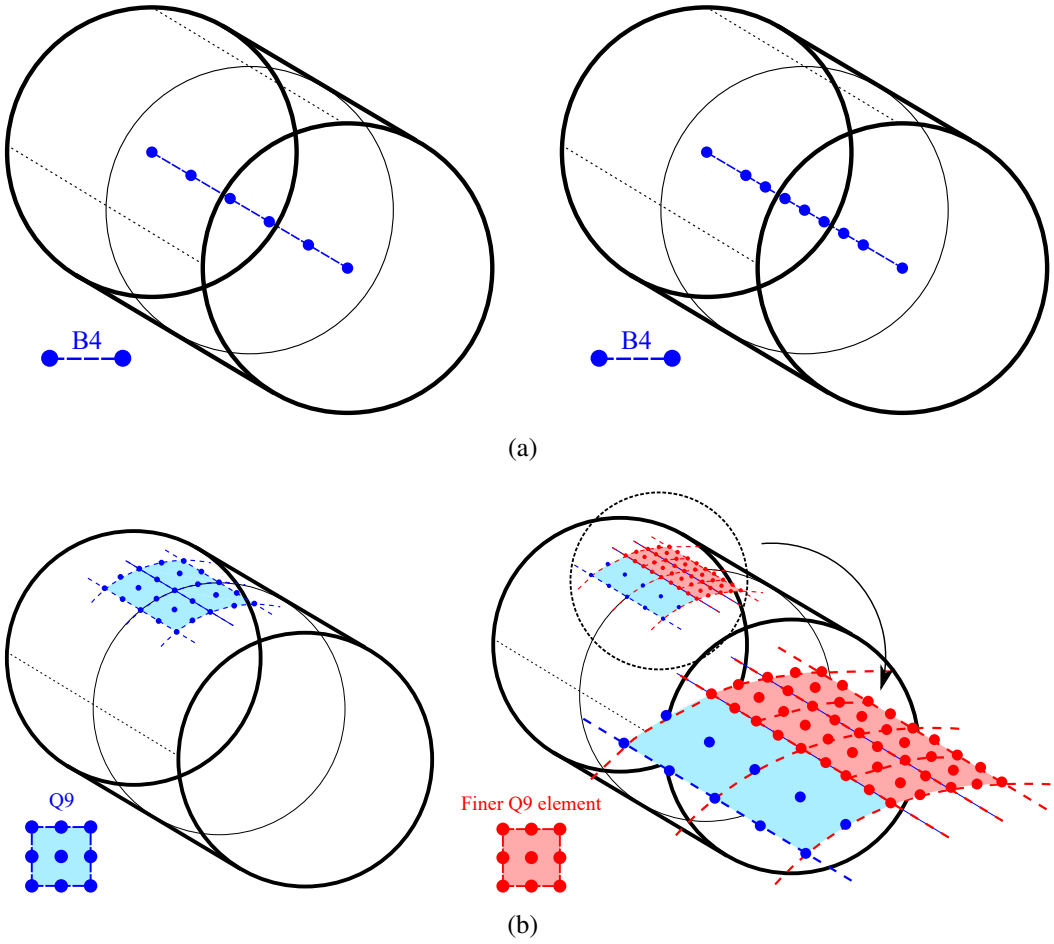

Fig. 2.15 1D elements (a) allow for the refinment of the model without any mesh incongruence. 2D elements (b) present lack of nodes connectivity if a finer mesh is employed in portions of the structure.

Chapter 3

Trivial-linearized and nonlinear free vibration

3.1 Natural frequencies in nonlinear equilibrium states

An accurate evaluation of the dynamic behavior (i.e. modal shapes and natural frequencies) is demanded for a reliable design and verification of working structure. In addition, it can be pointed out that the equilibrium state and the pre-stress condition of a structure highly affect its modal characteristic. When large displacement and rotations occur within a working service of a component, its equilibrium conditions change, so it is expected that its dynamic properties change as well. For this reason, it is important to evaluate the changing of modal shapes and natural frequencies in the case of geometrical nonlinear situations, i.e. when the equilibrium condition is far from the trivial state.

Biot [18] developed a nonlinear theory accounting for both first and second order terms to describe the evolution of static and dynamic properties of a structure subjected to high pre-stress states. A similar approach was used by Abkarov [3] and Akbarov and Ozisik [4], where the latter analyzed a pre-stressed nonlinear layer. Moreover, Ogden and Roxburgh [142] and Herrmann [78] studied the influence of initial stress on the dynamic response of isotropic plates, whereas Sun and Whitney [174] of composite ones. A similar approach can be found in a real application, see Abramovich *et al.* [1] and Arbelo *et al.* [12], who developed the so-called Vibration Correlation Technique (VCT). It consists in a not-destructive method for the evaluation of critical buckling load of metallic structure by interpolating until singularity the natural frequencies calculated experimentally at progressive loadings.

The free vibration characteristic of composite structures were analyzed for the evaluation of their dynamic properties by scientists and engineers. The literature about vibration of

structures is vast, and only a few are mentioned here for the sake of completeness. Virgin [182] presented a deep analysis of the vibration properties of slender structures subjected to compressive loadings. Moreover, based on Timoshenko beam theory [176], Ke *et al.* [94] analyzed the dynamic characteristic of functionally graded nanocomposite beams using Foppl-von Kármán geometrical nonlinear approximation, while Zhu *et al.* [192] conducted comparable analyses in the case of carbon nanotube-reinforced composite plates. Leissa [113, 114] and Leissa and Qatu [115] proposed a description of classical plate and shell theories, considering different geometrical and material characteristics. Regarding composite beams, Hodges *et al.* [80] showed methods for the evaluation of the natural frequencies and the associated modal shapes, using the Finite Element Method (FEM) to solve the equations of motion. Moreover, free vibrations of composite beams were investigated by Chandrashekhara *et al.* [44], considering rotary inertia and first-order shear deformations, and by Chandrashekhara and Bangera [42], using a refined higher-order shear deformation theory. Both works showed the effect of geometric and material properties and boundary conditions on dynamic properties of composite beams. Moreover, Song and Librescu [171] analyzed the free vibration of anisotropic beams with thick - and thin-walled cross-sections, whereas Lee [111] studied delaminated composite beams, adopting a layerwise approach. Regarding plates, Kant and Swaminathan [89] used a higher-order theory to develop a refined model for the free vibration analysis of laminated sandwich plates. Besides, simply-supported multilayered composite plates were studied by Noor and Burton [136]. Amabili and Farhadi [8] studied forced nonlinear vibrations of both isotropic and laminated plates adopting classical and higher-order theories. A comprehensive review of nonlinear vibrations of composite plates was proposed by Amabili [7].

The present chapter intends to investigate the change of natural frequency and associated mode shapes in the case of large displacements/rotations of composite beam and shell structures. The adopted nonlinear model is the same as the one presented in the previous chapter and, here, the formulation is further extended to deal with vibrations.

3.2 Mass matrix

The principle of wirtual work is recalled hereafter. For an un-damped eleastic body, neglecting the external forces and considering the inertia forces, it reads:

$$\delta L_{\text{int}} = -\delta L_{\text{ine}} \tag{3.1}$$

where L_{int} is the work made by the internal forces, L_{ine} stands for the work made by the inertial loads, whereas the virtual variation is expressed by δ. A linearization of the equilibrium of motion is required for the evaluation of nonlinear vibrations around equilibrium states. This assumption is allowed since the nonlinear vibration are supposed to have low amplitude. The linearized form of Eq. (3.1) yields:

$$\delta(\delta L_{\text{int}}) = -\delta(\delta L_{\text{ine}}) \tag{3.2}$$

In the previous Section, the linearization of the internal strain energy was described and, hereafter, is briefly recalled.

$$\begin{aligned}
\delta(\delta L_{\text{int}}) &= \int_V \delta\left(\delta\varepsilon^T \sigma\right) \mathrm{d}V \\
&= \int_V \delta\varepsilon^T \delta\sigma \,\mathrm{d}V + \int_V \delta\left(\delta\varepsilon^T\right)\sigma \,\mathrm{d}V \\
&= \delta\mathbf{q}_{\tau i}^T \left(\mathbf{K}_0^{ij\tau s} + \mathbf{K}_{T_1}^{ij\tau s}\right) \delta\mathbf{q}_{sj} + \delta\mathbf{q}_{\tau i}^T \mathbf{K}_\sigma^{ij\tau s} \delta\mathbf{q}_{sj}
\end{aligned} \tag{3.3}$$

where $\mathbf{K}_T^{ij\tau s}$ represents the FN of the tangent stiffness matrix. Note that $\mathbf{K}_T^{ij\tau s} = \mathbf{K}_0^{ij\tau s} + \mathbf{K}_{T_1}^{ij\tau s} + \mathbf{K}_\sigma^{ij\tau s}$. $\mathbf{K}_0^{ij\tau s}$ is the linear contribution, $\mathbf{K}_{T_1}^{ij\tau s}$ equals to $2\mathbf{K}_{lnl}^{ij\tau s} + \mathbf{K}_{nll}^{ij\tau s} + 2\mathbf{K}_{nlnl}^{ij\tau s}$, and $\mathbf{K}_\sigma^{ij\tau s}$ represents the so-called geometric stiffness [193]. It takes into account both linear and nonlinear pre-stress states. The explicit form of the tangent stiffness matrix is given in [144]. In the next step - by using the aforementioned relations, assuming constant mass, neglecting higher-order nonlinearities, and after opportune manipulations - the linearization of the virtual variation of the inertia loadings is expressed as follows:

$$\begin{aligned}
\delta(\delta L_{\text{ine}}) &= \delta\left(\int_V \delta\mathbf{u}^T \rho\, \ddot{\mathbf{u}} \,\mathrm{d}V\right) = \delta\left(\delta\mathbf{q}_{sj}^T \mathbf{M}^{ij\tau s} \ddot{\mathbf{q}}_{\tau i}\right) \\
&= \delta\mathbf{q}_{sj}^T \mathbf{M}^{ij\tau s} \delta\ddot{\mathbf{q}}_{\tau i}
\end{aligned} \tag{3.4}$$

where $\mathbf{M}^{ij\tau s}$ is the FN of the elemental, linear mass matrix. Substituting Eqs. (3.3) and (3.4)

Eq. (3.2), one has:

$$\delta \mathbf{q}_{\tau i}^{T} \mathbf{K}_{T}^{ij\tau s} \delta \mathbf{q}_{sj} = -\delta \mathbf{q}_{\tau i}^{T} \mathbf{M}^{ij\tau s} \delta \ddot{\mathbf{q}}_{sj} \tag{3.5}$$

Given the nature of the problem at hand and the hypothesis made, it is reasonable to assume harmonic motion around linearized states along the nonlinear equilibrium path. Thus, one has:

$$\begin{aligned} \delta \mathbf{q}_{sj}(t) &= \delta \bar{\mathbf{q}}_{sj} e^{i\omega t} \\ \delta \ddot{\mathbf{q}}_{sj}(t) &= -\omega^2 \delta \bar{\mathbf{q}}_{sj} e^{i\omega t} \end{aligned} \tag{3.6}$$

where omega is the circular frequency and $\bar{\mathbf{q}}_{sj}$ is the static solution. Finally, substituting Eq. (3.6) into Eq. (3.5), the equations of motion take the form of a linear eigenvalue problem:

$$\left(\mathbf{K}_{T}^{ij\tau s} - \omega^2 \mathbf{M}^{ij\tau s} \right) \delta \bar{\mathbf{q}}_{sj} = \mathbf{0} \tag{3.7}$$

3.3 Mode changing

The equations of motion for free vibrations hold the form of a linear eigenvalue problem, which in unified form reads:

$$(\mathbf{K}_{T}^{ij\tau s} - \omega^2 \mathbf{M}^{ij\tau s}) \, \mathbf{q}_{\tau i} = 0 \tag{3.8}$$

where ω is a natural period and $\mathbf{q}_{\tau i}$ the related amplitude eigenvector.

The proposed method is able to identify bifurcations, elastic instabilities or buckling phenomena as those conditions which render the tangent stiffness matrix singular, see Fig. 3.1.

Essentially, given a loading condition, pre-stresses σ are evaluated by means of nonlinear static response analysis into the geometric stiffness matrix $\mathbf{K}_{\sigma}^{ij\tau s}$. The modal characteristics of the deformed structure are calculated by solving the following linearized eigenproblem:

$$(\mathbf{K}_{0}^{ij\tau s} + \mathbf{K}_{T_1}^{ij\tau s} + \mathbf{K}_{\sigma}^{ij\tau s} - \omega^2 \mathbf{M}^{ij\tau s}) \, \mathbf{q}_{\tau i} = 0 \tag{3.9}$$

Intrinsically, critical buckling loads can be determined as those initial stress states σ which render the tangent stiffness matrix singular; i.e., $|\mathbf{K}_{0}^{ij\tau s} + \mathbf{K}_{T_1}^{ij\tau s} + \mathbf{K}_{\sigma}^{ij\tau s}| = 0$.

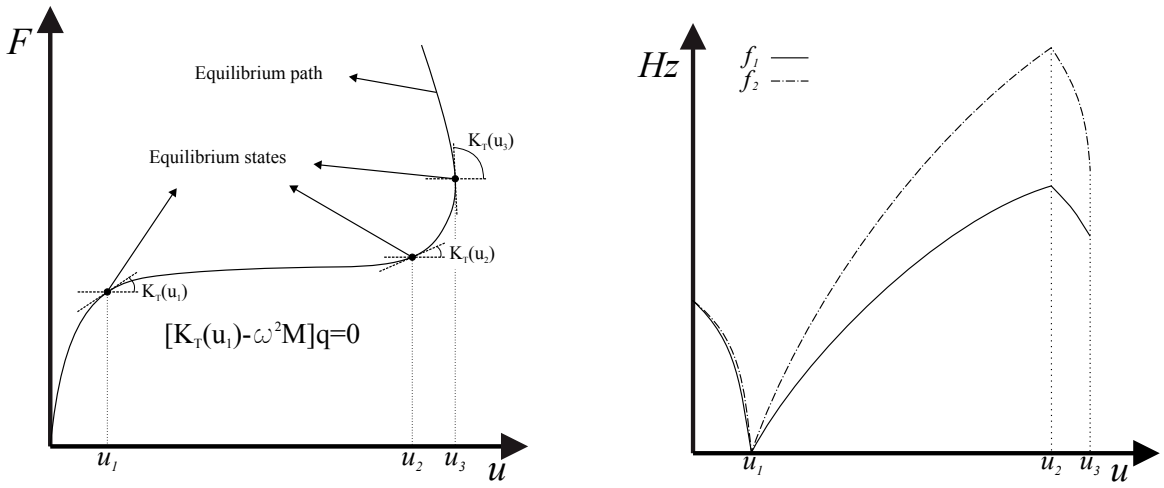

(a) Eigenvalue problem at equilibrium states (b) Natural frequencies trend

Fig. 3.1 Natural frequencies evaluation from eigenvalue problems solving about some equilibrium states of nonlinear equilibrium path.

3.3.1 Vibration Correlation Technique

The evaluation of the post-buckling behavior of structure is of a crucial importance in real applications. In particular, the modal characteristics can drastically change in the post-buckling regime, and a numerical simulation relying on linear models could lead to not accurate results. For this reason, a geometrical nonlinear model must be employed for the calculation of natural frequencies in the pre- and post-buckling of structures. Moreover, as already described in the previous Section, the equilibrium states change, and as they change, the modal properties are affected as well. In particular, in the case of a compression case, as the external load increases, the $\mathbf{K}_{\sigma}^{ij\tau s}$ norm decreases. As a matter of fact, since the norm of the stiffness matrix $|\mathbf{K}_0^{ij\tau s} + \mathbf{K}_{T_1}^{ij\tau s} + \mathbf{K}_{\sigma}^{ij\tau s}|$ decreases, the natural frequencies decreases as well. When the bucklind load is reached, the singularity of the stiffness matrix occurs, and the first natural frequency goes to zero. Scientists and reasearchers have built an experimental way to investigate the first critical buckling load based on this assumption. Such method is called Vibration Correlation Technique (VCT) and introduced by many authors, see Abramovich *et al.* [1] and Lurie [124]. This approach consists in a nondestructive way to estimate the first critical buckling load. Basically, the structure is subjected to an external and increasing compressive force and for each force value, the first natural frequencies are evaluated. Since this method is nondestructive, the external force does not usually exceed the 70% of an estimated buckling load. Then, the buckling load is evaluated by interpolating those values until the frequency equals zero.

3.4 Examples

3.4.1 Vibration of cantilever beams subjected to flexure

The first analysis case on the modal change in the nonlinear field takes its basis from the first analysis case shown in the previous chapter. The natural frequencies are evaluated at each equilibrium state, highlighted with circles in Fig. 2.6. Table 3.1 and Table 3.2 report the values of the first two bending and torsional frequencies for both slenderness ratios considered (i.e. $L/h = 10$ and $L/h = 100$). In both cases the two bending modes are the first naural frequencies, whereas the torsional shape is the 5^{th} mode, in the case of short beam and the 13^{th} mode for the slender one. It can be noticed that, in both cases, the increase of

$L/h = 10$				
		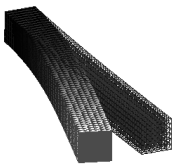	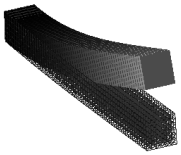	
$Step$	u_z/L	f_1	f_2	f_3
0	0.000	42.56	42.56	403.9
1	0.040	42.66	42.80	406.3
2	0.106	43.31	43.98	415.6
3	0.214	43.41	44.41	410.7
4	0.343	44.92	47.08	414,5
5	0.489	48.11	52.09	418.8
6	0.643	54.67	61.15	420.9
7	0.762	65.78	74.49	421.4
8	0.851	88.39	95.89	521.6

Table 3.1 Natural frequencies (Hz) of the first two bending and torsion modal shapes of the short beam.

the natural frequency associated to bending modal shape in the same direction as the external force is higher than the frequency associated to the other bending mode shape. The reason is that in the first case the bending geometrical stiffness matrix $\mathbf{K}_\sigma$ is affected by contribution of both modal shape and external loading (they have the same direction), whereas in the other case, they have different direction. This aspect is explained in Fig. 3.2.

Moreover, the trend of the first 10 natural frequencies versus the tip transverse deflection is addressed in Fig. 3.3. The change of the natural frequency can be clearly appreciated, for both considered cases. Of particular interest is the behavior of the torsional mode shape (5^{th}

$L/h = 100$				
				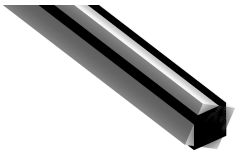
Step	u_z/L	f_1	f_2	f_3
0	0.000	0.427	0.427	40.39
1	0.039	0.427	0.427	40.41
2	0.089	0.428	0.430	40.43
3	0.151	0.431	0.435	40.47
4	0.227	0.437	0.445	40.53
5	0.318	0.448	0.462	40.54
6	0.405	0.463	0.486	40.56
7	0.487	0.484	0.519	40.77
8	0.577	0.525	0.573	42.27
9	0.657	0.613	0.670	51.63
10	0.725	0.720	0.789	65.33
11	0.781	0.839	0.921	79.48
12	0.827	0.943	1.035	79.95

Table 3.2 Natural frequencies (Hz) of the first two bending and torsion modal shapes of the slender beam.

frequency) for the short beam. It remains almost constant during the nonlinear analysis, and suddenly increases around a u_z/L value between 0.7 and 0.8. The same can be seen for the slender case in Fig. 3.4. Here, the natural frequencies from the 11^{th} to the 20^{th} modes are displayed, and the torsional mode highligthed.

For a better comprehension of the given problem, some MAC (Modal Assurance Criterion) values are reported in Fig. 3.5. The three MAC graphical rappresentation relate the undeformed configuration with a nearly linear, moderate nonlinear and highly nonlinear solution. As a consequense in the first graphs, the black boxes are concentrated in diagonal, which suggests the there is no an evident change on the modal characteristics. Going on the other graphs, light black and gray boxes start spreading within the graphs, which suggests a nonlinear behavior of the problem.

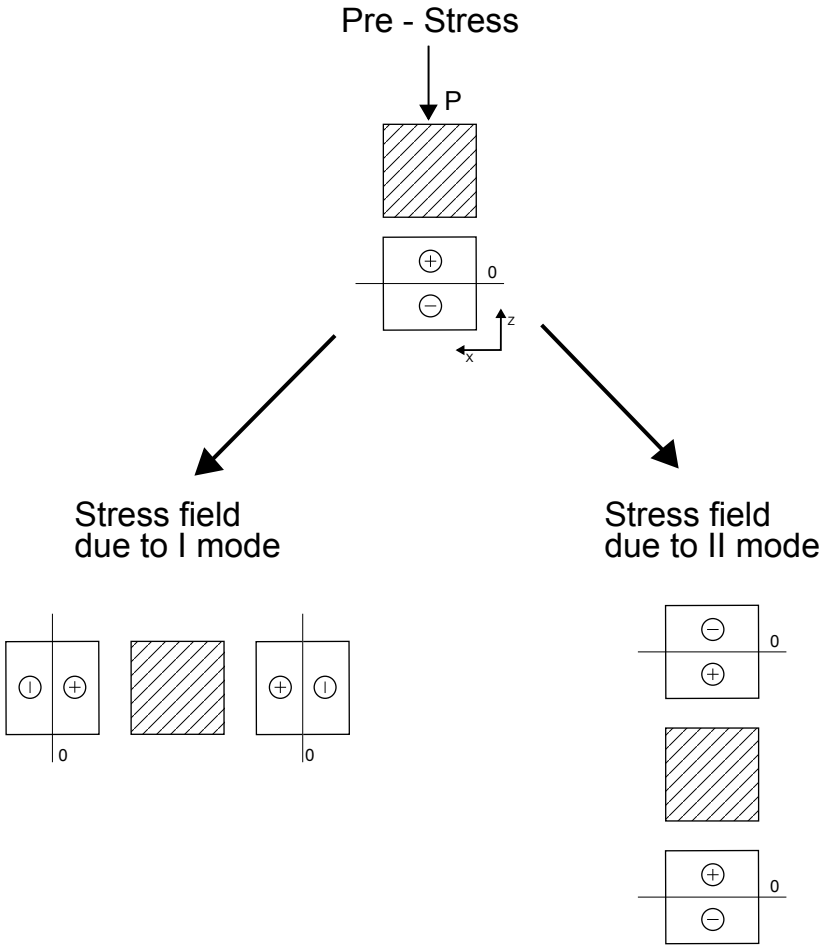

Fig. 3.2 Stress conditions of the first two bending modes and due to external load.

3.4.2 Nonlinear vibration of unsymmetric laminated beam-column and comparison with trivial linearized solution

As a further example, the modal change behavior of unsymmetric laminated cantilever beams is addressed. The beam is made of two layers and 3 stacking sequences are considered, i.e.[0°/45°], [0°/90°] and [15°/−45°]. The material is orthotropic with the following characteristics, E_1 = 144.8 GPa, $E_2 = E_3$ = 9.65 GPa, $G_{12} = G_{13}$ = 4.14 GPa, G_{23} = 3.45 GPa and ν_{12} = 0.3. The loading condition, as well as the geometric properties are shown in Fig. 3.6, with L/w = 9, t/w = 0.6. Layers are supposed to have the same thickness. The LW approach is employed, along with L16 kinematics for each layer. The nonlinear static curve is shown in Fig. 3.7. As in the previous example, the modal characteristics are evaluated at each equilibrium point using the tangent stiffness matrix. The results are shown in Fig. 3.8, for each stacking sequence considered. The first four modes are evaluated. Clearly, a crossing phenomena occurs for the [0°/90°] between the first and second modes, whereas

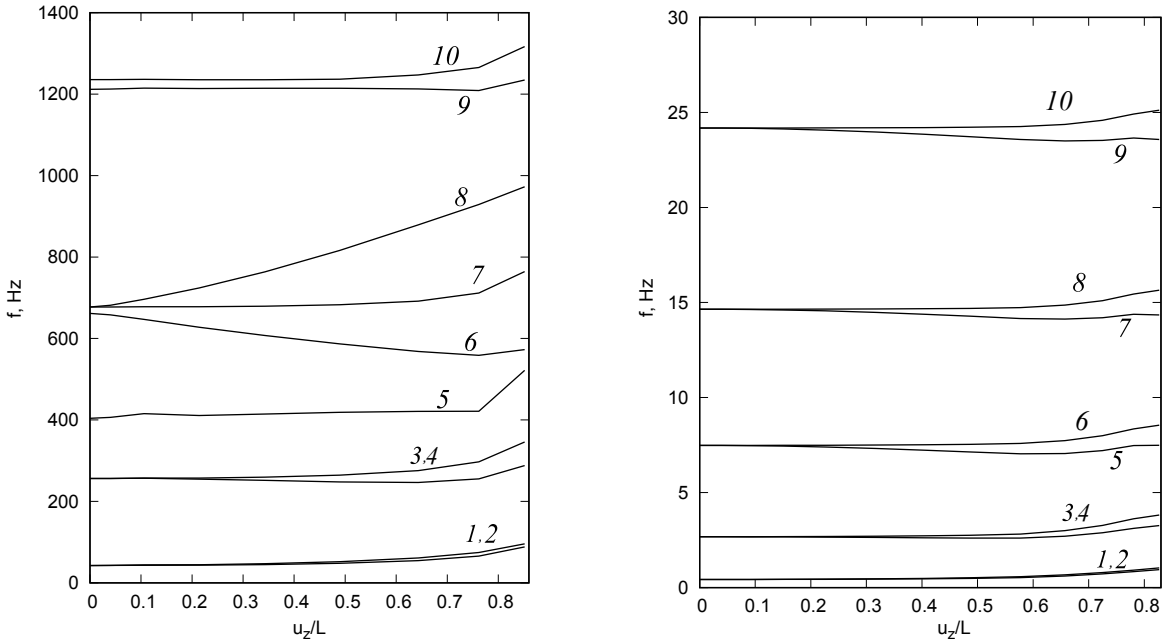

(a) $\frac{L}{h} = 10$ (b) $\frac{L}{h} = 100$

Fig. 3.3 Trend of the 10 natural frequencies for the short (a) and slender (b) beam.

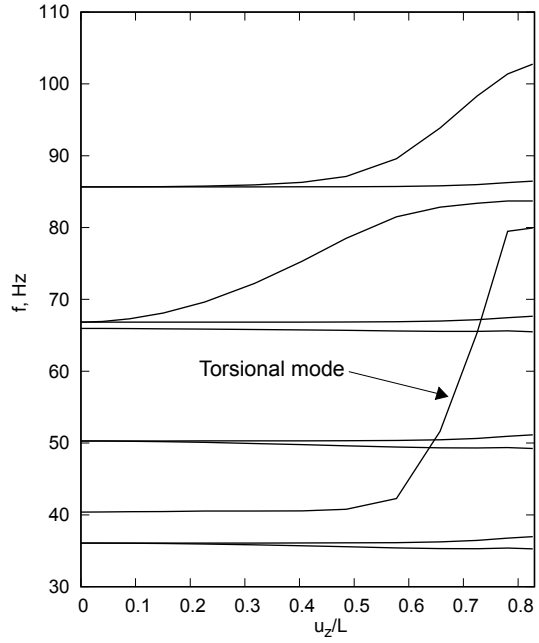

Fig. 3.4 Trend of the natural frequencies of the modes from 11 to 20 of the slender beam.

a veering phenomenon occurs for the [15°/−45°]. The modal shapes are reported in Figs.

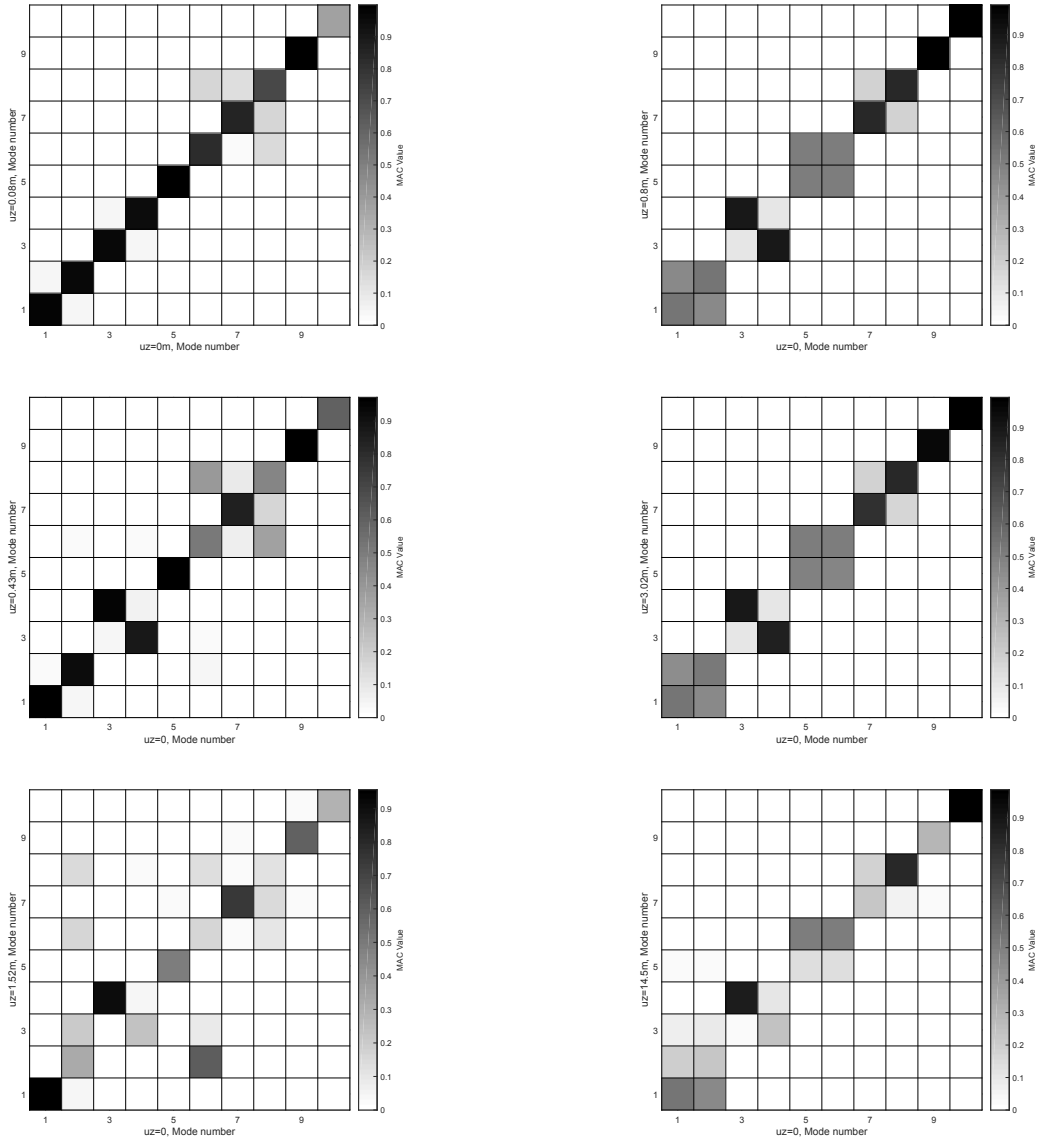

(a) $\frac{L}{h} = 10$ (b) $\frac{L}{h} = 100$

Fig. 3.5 MAC values of the short (a) and slender (b) beam.

3.9, 3.10 and 3.11. They are the same for each stacking sequence. The first, second and third modes are bending modes and the fourth is a torsional mode.

3.4.3 Numerical simulation of VCT: compressed reinforced panel case

This numerical example intends to enstabilish a numerical simulation of the VCT, considering the nonlinear relations. For this purpose, a comparison with experimental results was

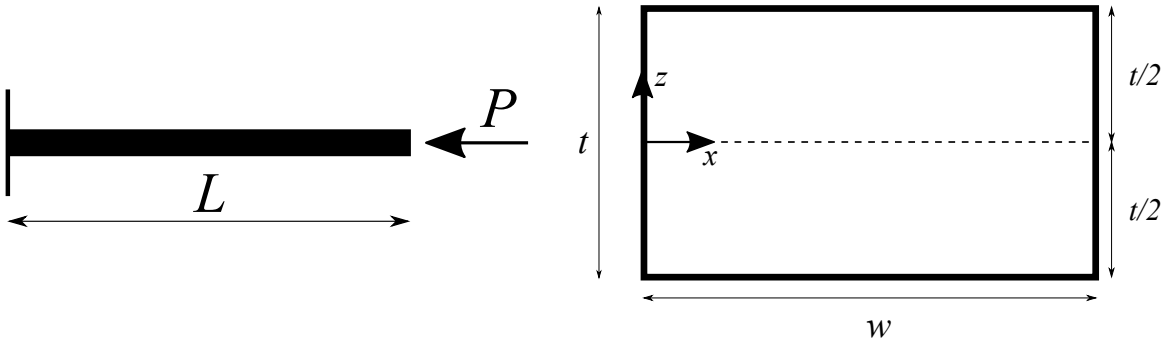

Fig. 3.6 Loading condition and cross-section geometry for the compressed composite beam.

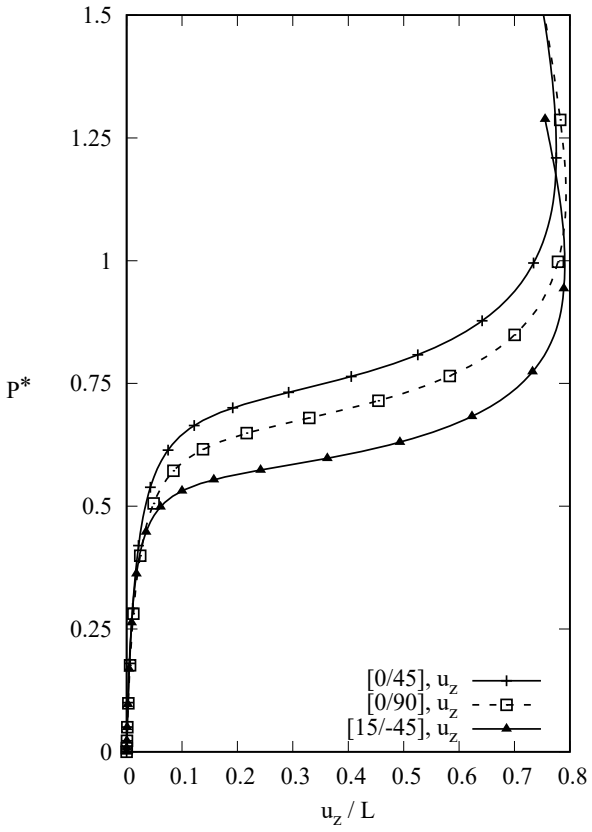

Fig. 3.7 Equilibrium curve of the compressed composite beam. $P^* = \dfrac{PL^2}{E_2 b h^3}$.

conducted. In particular, a reinforced panel, designed by Embraer and manufactured and tested by the laboratory of TU Delft, is considered. Figures 3.12 and 3.13 show the boundary and geometric condition of the stiffened panel. In the experimental setup, the panel is axially compressed by a press, and this load is simulated by a pressure (in red in Fig. 3.12). Moreover, the panel is joint to the press and top the ground through two 50 mm resin blocks,

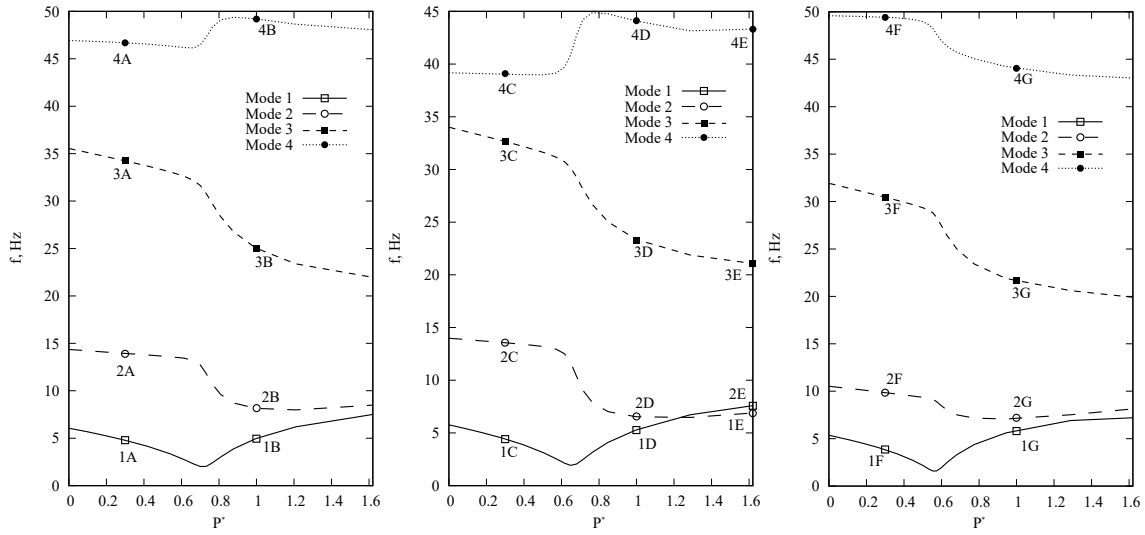

(a) (b) (c)

Fig. 3.8 Natural frequency trends of the first 4 modes for the cantilever asymmetric cross-ply beam subjected to compression. (a) [0°/45°], (b) [0°/90°], (c) [15°/−45°]. $P^* = \dfrac{PL^2}{E_2 b h^3}$.

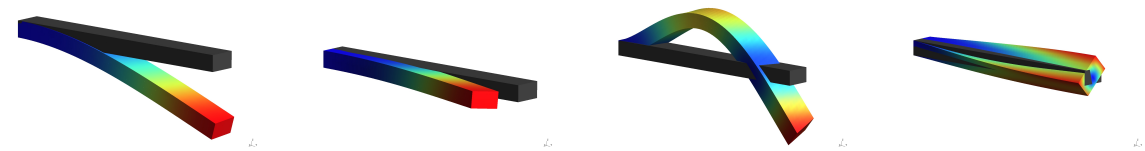

(a) Mode 1A. $P^* = 0.292$ (b) Mode 2A. $P^* = 0.292$ (c) Mode 3A. $P^* = 0.292$ (d) Mode 4A. $P^* = 0.292$

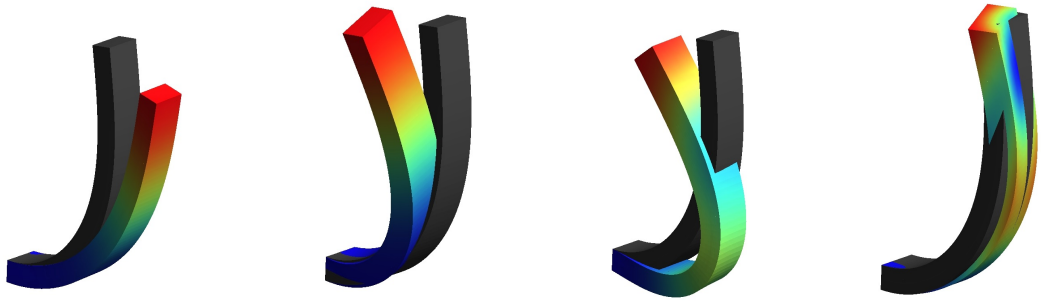

(e) Mode 1B. $P^* = 0.995$ (f) Mode 2B. $P^* = 0.995$ (g) Mode 3B. $P^* = 0.995$ (h) Mode 4B. $P^* = 0.995$

Fig. 3.9 Modal shapes of the first 4 modes for the compressed composite beam. Numbers refer to Fig. 3.8(a). $P^* = \dfrac{PL^2}{E_2 b h^3}$.

simulated by a stiffer material. Finally, the kinematic boundary condition are shown in the

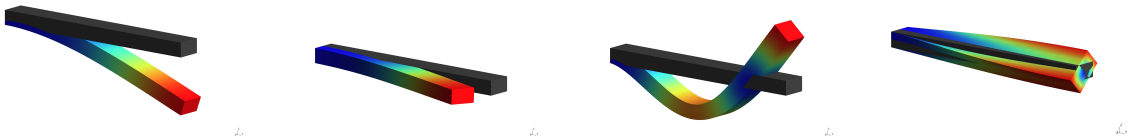

(a) Mode 1C. $P^* = 0.292$ (b) Mode 2C. $P^* = 0.292$ (c) Mode 3C. $P^* = 0.292$ (d) Mode 4C. $P^* = 0.292$

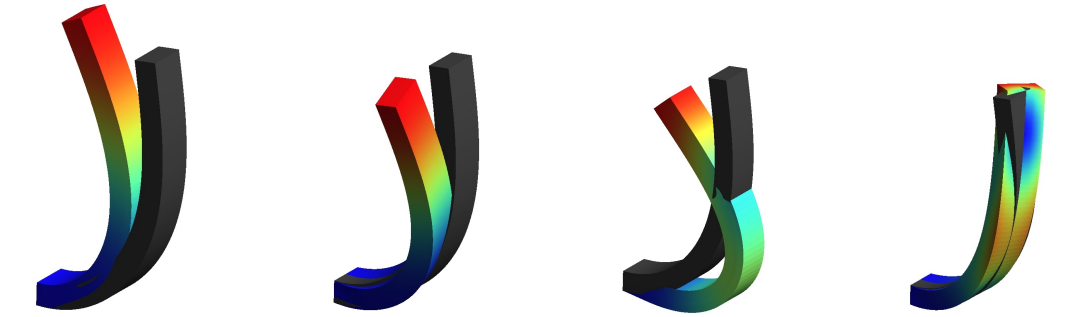

(e) Mode 1D. $P^* = 0.995$ (f) Mode 2D. $P^* = 0.995$ (g) Mode 3D. $P^* = 0.995$ (h) Mode 4D. $P^* = 0.995$

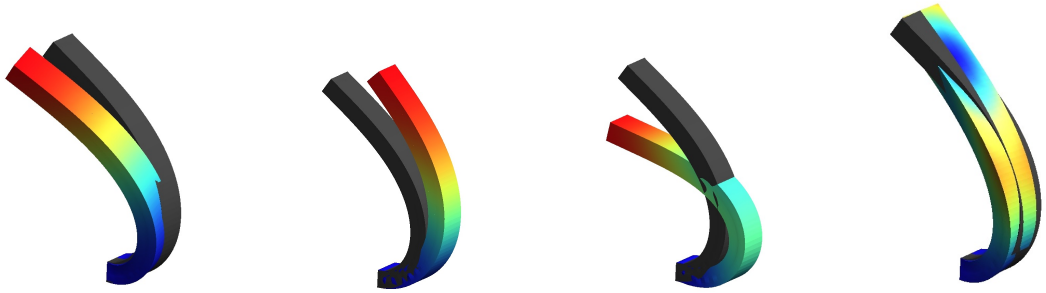

(i) Mode 1E $P^* = 1.630$ (j) Mode 2E. $P^* = 1.630$ (k) Mode 3E. $P^* = 1.630$ (l) Mode 4E. $P^* = 1.630$

Fig. 3.10 Modal shapes of the first 4 modes for the compressed composite beam. Numbers refer to Fig. 3.8(b). $P^* = \dfrac{PL^2}{E_2 b h^3}$.

same figure. The geometric properties are shown in Fig. 3.13, where h = 39.3 mm, h_1 = 9.52 mm, h_2 = 3.66 mm, t = 7.32 mm, b = 270 mm and the total length is 790 mm. The stacking sequence is shown in Fig. 3.12 and the material properties are $E_1 = 1.19 \times 10^5$ GPa, $E_2 = E_3 = 9.80 \times 10^3$ GPa, $G_{12} = G_{13} = G_{23} = 4.70 \times 10^3$ GPa, $\nu_{12} = \nu_{13} = \nu_{23} = 0.316$ and $\rho = 1580$ kg/m^3. Finally, the proposed numerical solution compared to the VCT performed experimentally are shown in Fig. 3.15. Clearly, the present numerical simulation has demonstraed its capabilities on capturing the mode change effects. The first buckling shape is the fourth frequency.

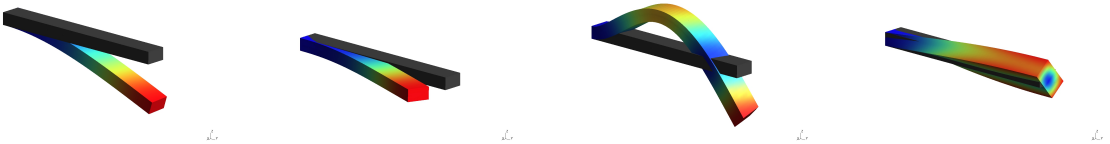

(a) Mode 1F. $P^* = 0.292$ (b) Mode 2F. $P^* = 0.292$ (c) Mode 3F. $P^* = 0.292$ (d) Mode 4F. $P^* = 0.292$

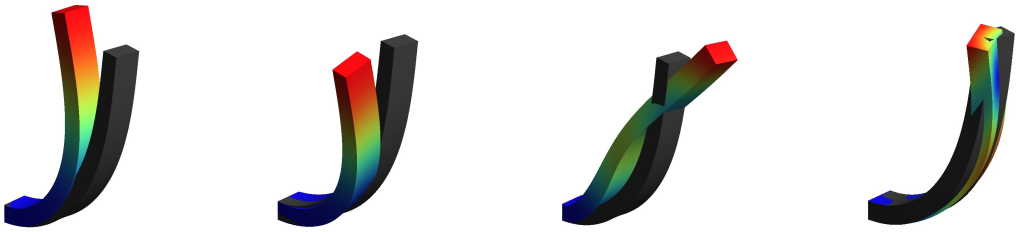

(e) Mode 1G. $P^* = 0.995$ (f) Mode 2G. $P^* = 0.995$ (g) Mode 3G. $P^* = 0.995$ (h) Mode 4G. $P^* = 0.995$

Fig. 3.11 Modal shapes of the first 4 modes for the compressed composite beam. Numbers refer to Fig. 3.8(c). $P^* = \dfrac{PL^2}{E_2 b h^3}$.

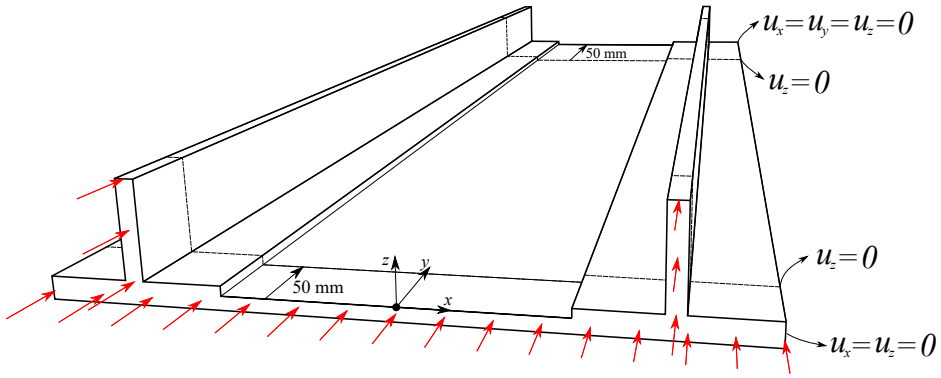

Fig. 3.12 Geometric properties and kinematic constraints of the composite reinforced panel. Red arrows indicate the external axial pressure.

3.4.4 Mode change of a pinched cylinder

As an example of an application of 2D shell models for the modal analysis of structures, a pinched cylindrical shell is analyzed. Both metallic and composite materials are considered. For the former, E= 2.0685×10^7 N/m^2, ν= 0.3, whereas for the latter E_L= 2068.5×10^4 N/m^2, E_T= 517.125×10^4 N/m^2, shear moduli G_{LT}= 795.6×10^4 N/m^2 and Poisson's ratio ν_{LT}=ν_{TT}= 0.3, where L stands for "longitudinal" and T for "transversal". In addition, for the composite structure case, the $[90°, 0°, 90°]$ is considered. The structure is clamped at one side and undergoes a vertical load at the other side. The longitudinal edges are constrained

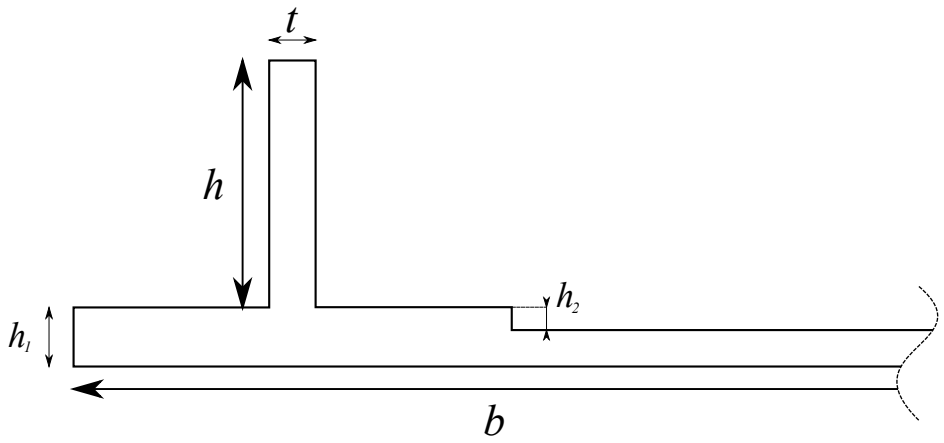

Fig. 3.13 Geometric properties of the cross-section of the composite reinforced panel.

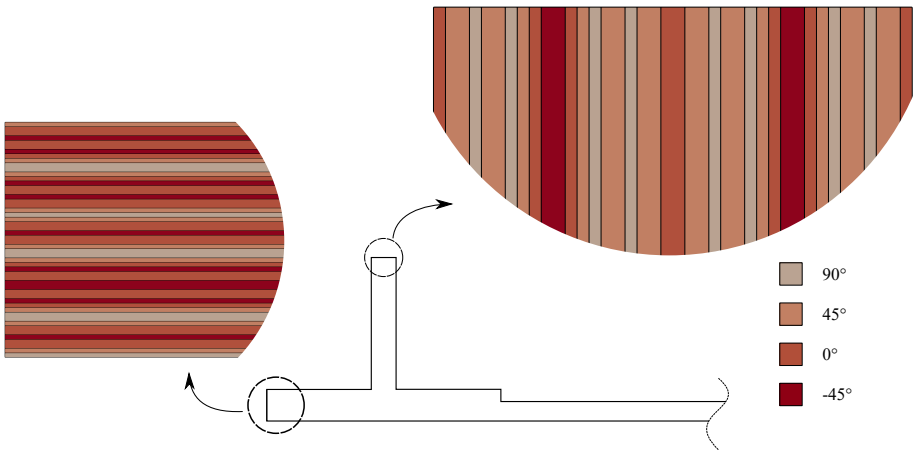

Fig. 3.14 Stacking sequence of the composite reinforced panel.

in their vertical deflection and rotation around the β-axis. The geometry of the structure is reported in Fig. 3.16 and L= 3.048 m, R_α= 1.016 m, and thickness (h) equal to 0.03 m. The present analysis case is taken from [175] where the nonlinear static behavior of the structure is evaluated. The static results of both cases (metallic and composite are reported in Fig. 3.17. In the present model, 32×32 quadratic elements are used for the in-plane discretization, whereas LD3 is adopted in the thickness direction. For the composite case, the LW approach is employed. Some of the most relevant deformed configurations are depicted, as well. Clearly, the results perfectly match the reference ones, so these models are subsequently used for the modal shapes and natural frequencies evaluation. In correspondence of each equilibrium step, the modal shape are evaluated, along with the associated natural frequencies. The local stiffness matrix of the deformed configuration is used. The results are reported in Table 3.3, where the natural frequencies are reported for some u_z values, for both material

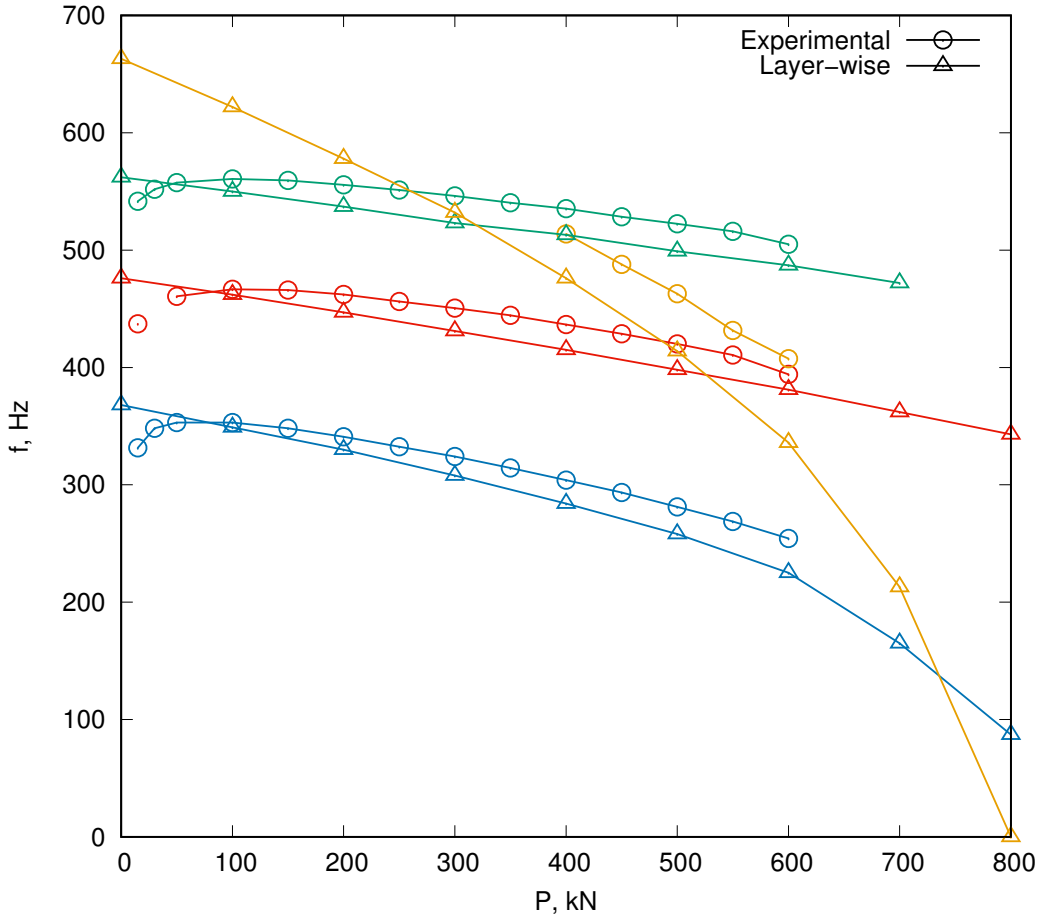

Fig. 3.15 Mode aberration results from experimental test and numerical simulation.

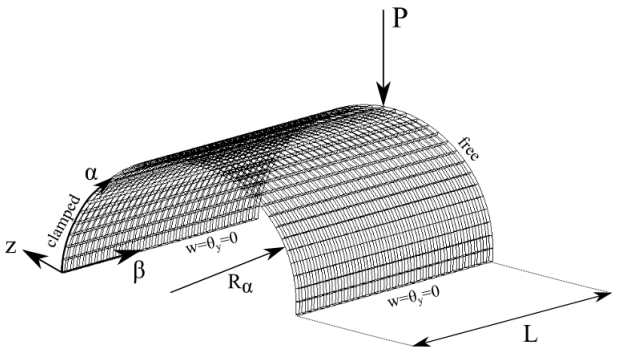

Fig. 3.16 Geometric and loading condition of a pinched cylinder.

cases. Moreover, the trend of the first six frequencies is reported in Fig. 3.18. A generic decrease of every natural frequency can be observed. The most relevant result concerns a crossing phenomenon between 5^{th} and 6^{th} mode and veering phenomenon between 4^{th} and 5^{th} for the isotropic structure. As far as the composite case is concerned, crossing

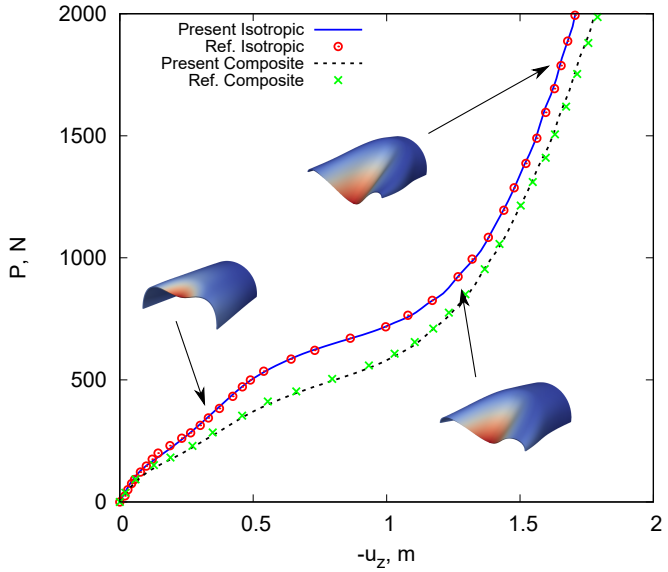

Fig. 3.17 Nonlinear static solution of both metallic and composite pinched cylinder.

Isotropic				Composite			
$-u_z$	$f_1/\sqrt{\rho}$	$f_2/\sqrt{\rho}$	$f_3/\sqrt{\rho}$	$-u_z$	$f_1/\sqrt{\rho}$	$f_2/\sqrt{\rho}$	$f_3/\sqrt{\rho}$
0.00	56.82	56.55	95.44	0.00	44.05	51.77	90.76
0.24	47.59	50.32	86.43	0.13	40.78	48.38	82.61
0.57	29.99	44.38	81.90	0.63	21.16	37.75	65.98
1.11	16.89	39.11	59.14	1.12	20.41	42.85	48.93
1.36	24.43	44.54	52.44	1.46	21.13	42.04	48.06
1.48	22.68	45.23	52.63	1.58	20.77	37.84	48.39

Table 3.3 Natural frequencies [Hz/(kg/m^3)] of the isotropic and composite pinched cylinder.

phenomena arise between 4^{th}, 5^{th} and 6^{th}. A decrease of every frequqncy appears in this case too, except for the 2^{nd} and 4^{th} modes. For a better comprehension of the problem, the first three mode shapes are reported in Fig. 3.19 for isotropic and composite cases. Moreover, some significant MAC values are calculated for the composite structure and they are reported in Fig. 3.20. The modes of the unloaded structure ($u_z = 0$) is compared with itself (Fig. 3.20(a)), with $u_z = 0.38$ (Fig. 3.20(b)), with $u_z = 0.97$ (Fig. 3.20(c)) and with $u_z = 1.48$ (Fig. 3.20(d)). Clearly, in the first figure all black dots are located in the diagonal, but when increasing the u_z value (i.e. the external load), grey and light grey boxes start spreading all over the grid.

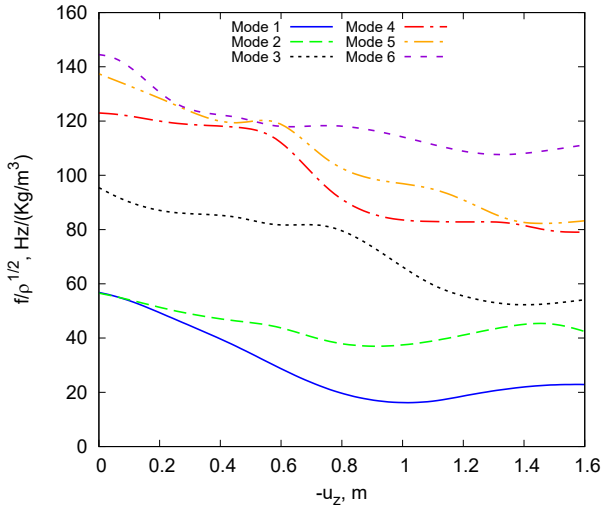

(a)

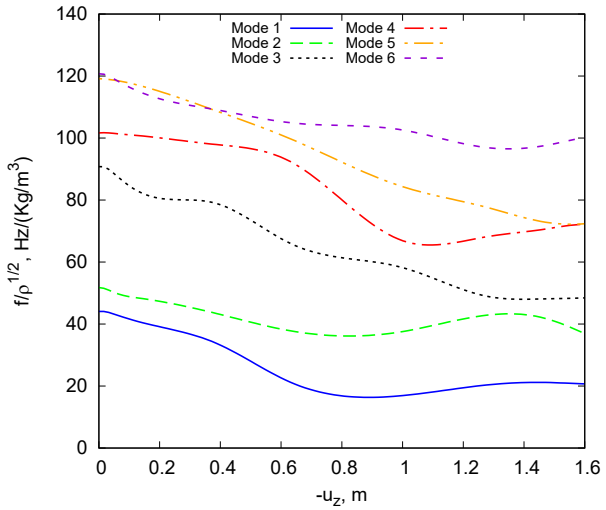

(b)

Fig. 3.18 Natural frequencies evolution of the first six modes for both isotropic and composite pinched cylinder.

3.4.5 Vibrations of a composite compressed pinched cylinder

As a second case, a uniform longitudinal pressure is added to the previous analysis case, considering the composite cylinder. The compression-transverse load rate equals 66. The geometric and loading conditions are shown in Fig. 3.21(a), whereas in Fig. 3.21(b) the static equilibrium curve is reported, along with some deformed configuration. The dynamic properties are evaluated on each nonlinear equilibrium states. The trend of the first 5 frequencies is reported in Fig. 3.22. More crossing phenomena arise compared to the

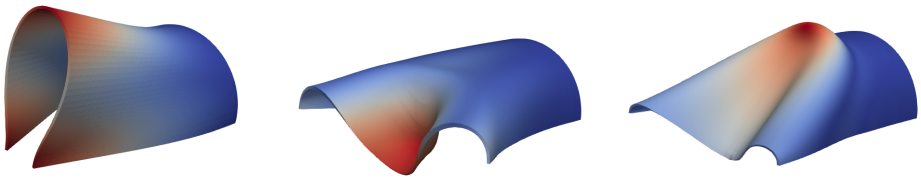

(a) $u_z = 0\,m$ (b) $u_z = 0.63\,m$ (c) $u_z = 1.58\,m$

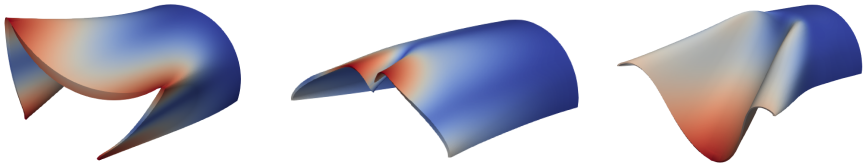

(d) $u_z = 0\,m$ (e) $u_z = 0.63\,m$ (f) $u_z = 1.58\,m$

Fig. 3.19 First three modal shapes of the isotropic (a, b, c) and composite (d, e, f) pinched cylinder.

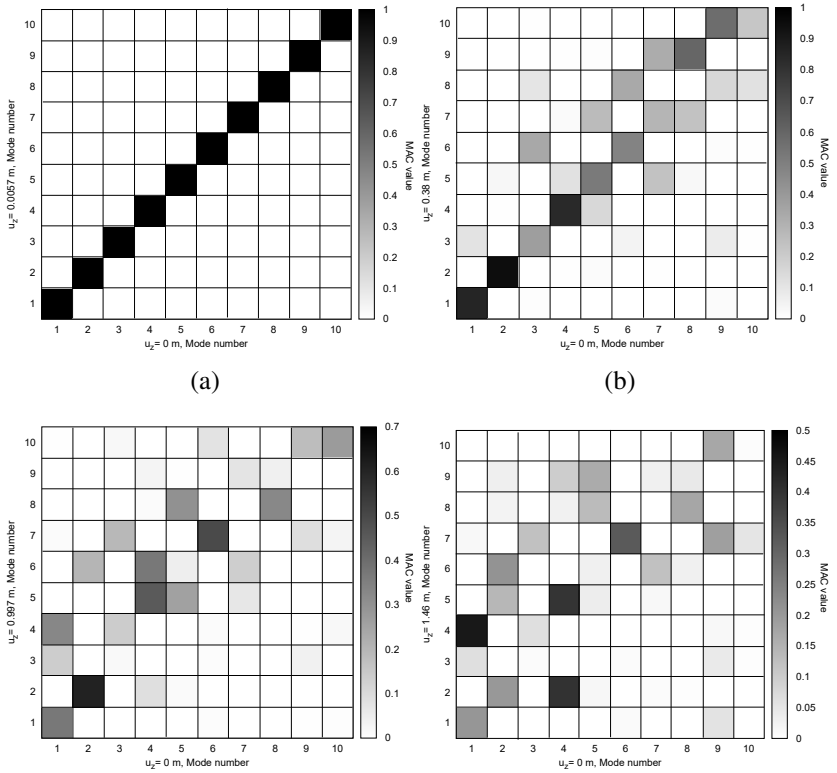

Fig. 3.20 MAC values of some configuration for the composite pinched cylinder.

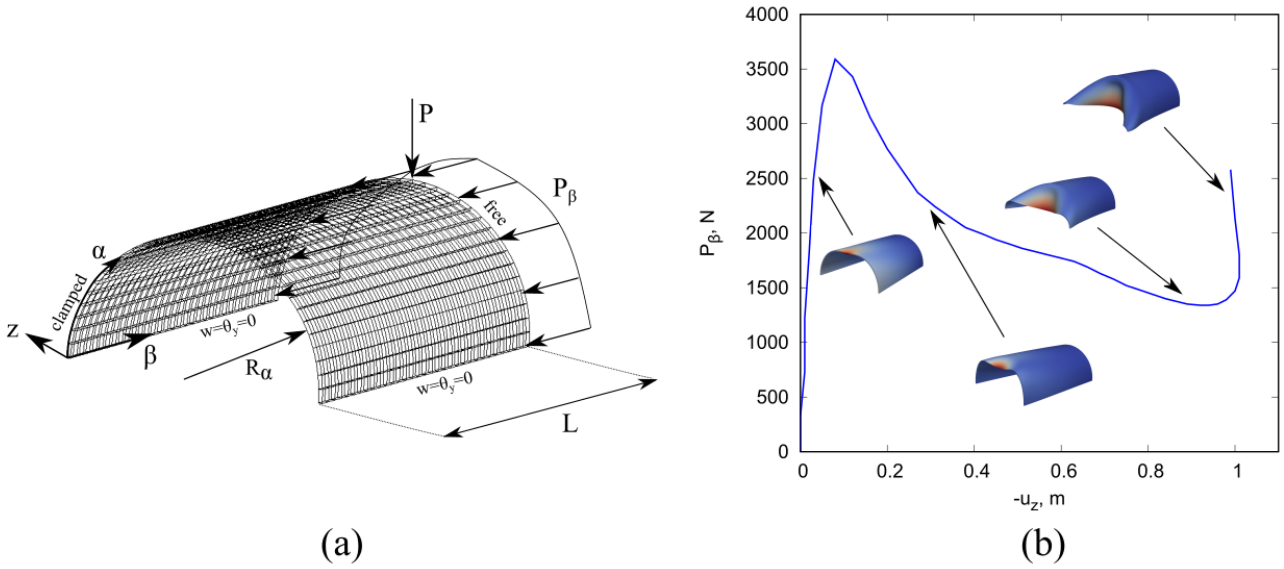

Fig. 3.21 Geometric properties (a) and static equilibrium curve (b) for the compressed composite cylinder.

previous analysis case. In particular 3^{rd}, 4^{th} and 5^{th} intersect each other in the early static curve, whereas 1^{st} and 2^{nd} in the advanced nonlinear regime. As a final investigation, Fig.

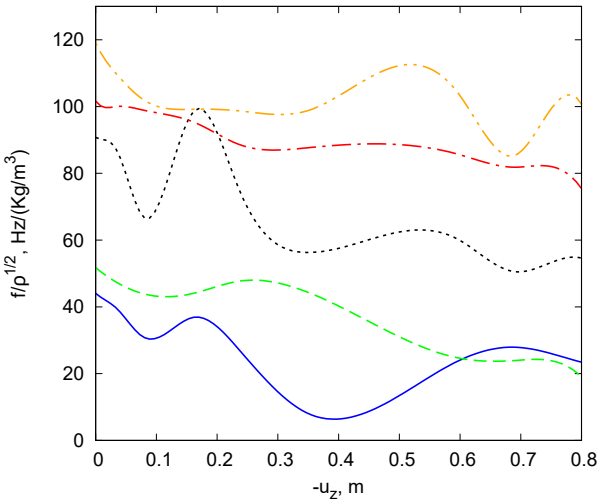

Fig. 3.22 First 5 natural frequencies evolution of the composite compressed pinched cylinder.

3.23 reports some relevant MAC values. The same conclusion can be drawn as those made for the previous MAC values, although not-white boxes seem to be more spread, which indicates a more rigorous change of the modal characteristics.

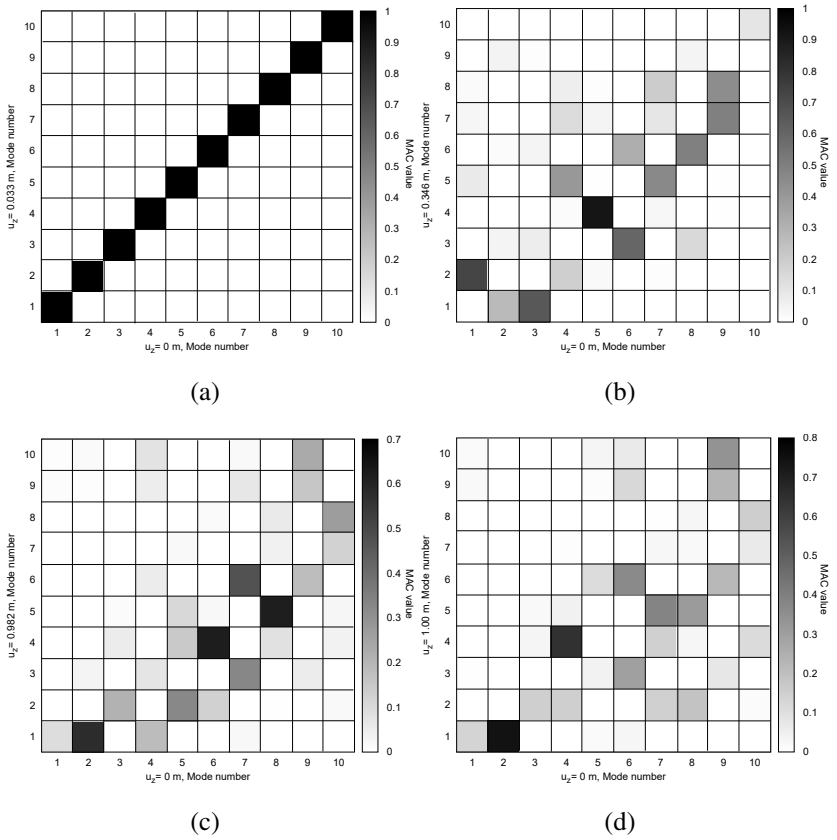

Fig. 3.23 MAC values of the composite compressed pinched cylinder.

Chapter 4

Effect of various geometrical nonlinear terms on the large-deflection response

4.1 Nonlinear approximation theories

In engineering applications, a large number of structures are designed to undergo large rotations and deflections, without encountering any plastic deformation. This is the case of components with high flexibility, like cables, space antennas, parachutes and wings [146]. For this reason, an accurate evaluation of the behavior of such structures in the geometrical nonlinear regime is of fundamental importance for a reliable design process. This constitues a challenge for scientific researchers. In the previous chapter, the history of the adopted solutions for the resolution of the geometrical nonlinear problem was described. The geometrical nonlinear models were based on the classical approaches of Euler [62] and Timoshenko [176] beam theories. The former assumed the curvature to be proportional to the bending moment, whereas the latter proposed a constant shear-components distribution along the thickness of a structure, see for example Refs. [147, 71, 131]. Both theories were demonstrated to be valid for a large number of applications but limited to thin and slender structures, i.e. when the cross-section (for 1D structures) or thickness (for 2D structures) does not play an important role on the static and dynamic overall behavior. Nevertheless, when higher-order phenomena occur and for thick and short structures, refined theories must be considered in order to achieve reliable results. This led to the development of several nonlinear refined theories, as deeply described in the previous chapters. Many of these theories, makes use of the well-known von Kármán nonlinear strain approximation. This approximation is used for the evaluation of the load-carrying capability of flexible structures, which easily undergo large deflections. The von Kármán nonlinear approximation

was studied by Carrera and Parisch [35], and it was demonstrated to lead to accurate results in those cases where the displacements are of the same magnitude order as the thickness of the given structure. However, the same accuracy is not guaranteed when dealing with thick components. Moreover, the error made by the von Kármán approximation is even more evident when rotations are large. The same results were obtained, some years later, by Kim and Chaudhuri [96], when studing laminated panels. The von Kármán strains are not applicable especially in the advanced nonlinear states and they overall yield to an overestimation of the displacements. In general, several nonlinear theories and nonlinear strains assumptions can be formulated for the resolution of a given problem. Although they can provide good results for that application, it may lack the ability to accurately predict the nonlinear behavior if the problem is different. What this chapter intends to focus on is the evaluation of the effectiveness of various nonlinear theories for the geometrical nonlinear analysis of 1D and 2D problems. This is possible thanks to the scalable nature of CUF, which allows to implement the full Green-Lagrange strain-displacement relation, and which terms could be omitted to lead to reproduce the various nonlinear strains assumptions, including the von Kármán ones.

4.2 The von Kármán assumptions

An accurate strain-displacement relation definition is required for a reliable evaluation of the geometrical nonlinear behavior of structures. However, when dealing with large displacements and rotations and post-buckling conditions, the issue of characterizing the strain tensor is not trivial, see [125].

When dealing with geometrical nonlinear study cases, it can be supposed that the structure will return in its undeformed state if unloaded. For this reason, the *Lagrangian* formulation is usually employed, which describes the strains in terms of its undeformed configuration. This approach leads to a number of advantages, as declared in [146]:

- Strain and stress components do not require any coordinate transformation;
- Theoretically, the error is null, since the current step solution does not depend on the previous step;
- If the iteration method is convergent, large steps can be implemented, without losing any degree of accuracy.

In this framework, the Green-Lagrange strains are employed, since they are work-conjugate with the second Piola-Kirchoff stresses.

The Green-Lagrange strains were already defined in Chapter 2, and they are briefly recalled:

$$\mathbf{b}_{nl} = \begin{bmatrix} \frac{1}{2}(\partial_x)^2 & \frac{1}{2}(\partial_x)^2 & \frac{1}{2}(\partial_x)^2 \\ \frac{1}{2}(\partial_y)^2 & \frac{1}{2}(\partial_y)^2 & \frac{1}{2}(\partial_y)^2 \\ \frac{1}{2}(\partial_z)^2 & \frac{1}{2}(\partial_z)^2 & \frac{1}{2}(\partial_z)^2 \\ \partial_x\partial_z & \partial_x\partial_z & \partial_x\partial_z \\ \partial_y\partial_z & \partial_y\partial_z & \partial_y\partial_z \\ \partial_x\partial_y & \partial_x\partial_y & \partial_x\partial_y \end{bmatrix} \tag{4.1}$$

This approach allows for the complete definition of coupling phenomena (bending, shear and torsion) which may be activated in the large displacement field. For simplification purspose and to reduce the computational cost, many nonlinear theory approximation developed for 1D and 2D models.

A popular nonlinear theory was developed by von Kármán in the case of plates (see [69]). In fact, when dealing with thin 2D structures undergoing small rotations, von Kármán states only the in-plane partial derivatives of the transverse displacement need to be considered, and thus, not neglected. Basically, the von Kármán relations read as:

$$\begin{aligned} \varepsilon_{xx_{nl}} &= \frac{1}{2}(u_{z,x})^2 \\ \varepsilon_{yy_{nl}} &= \frac{1}{2}(u_{z,y})^2 \\ \varepsilon_{xy_{nl}} &= u_{z,x}u_{z,y} \end{aligned} \tag{4.2}$$

When dealing with 1D structures (beams and columns) according to the von Kármán approximations, the component of the nonlinear strain tensor is:

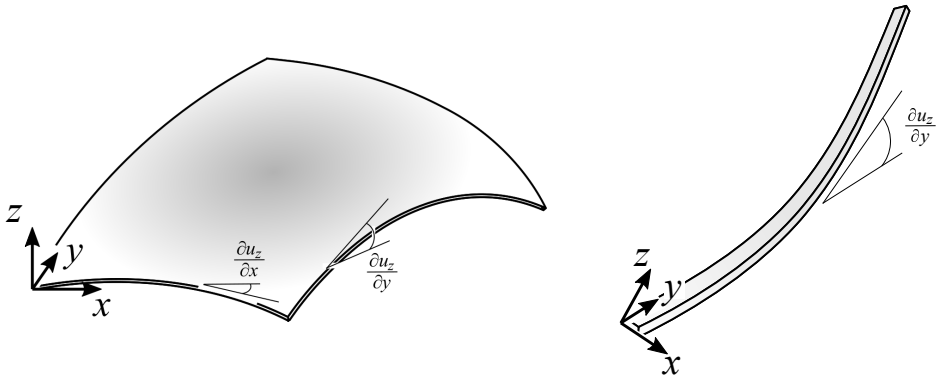

Fig. 4.1 Notation of a plate and a beam in the large displacement field.

$$\varepsilon_{yy_{nl}} = \frac{1}{2}(u_{z,y})^2 \tag{4.3}$$

Figure 4.1 shows the notation adopted to write Eqs. (4.2) and (4.3). It proposes a plate and a beam undergoing large displacements, where the plate is placed so that the thicness coordinate is the z and the y is the direction of the beam axis. The application and validity of the von Kármán assumptions is limited to small rotations, whereas for even moderate rotations it leads to not reliable results (see [146]).

This chapter wants to evaluate the effect of various nonlinear approximation on the static behavior of beams and shells. This is possible thanks to the scalable nature of CUF. In fact, the terms of the Green-Lagrange strain tensor could be neglected (or included in the analysis) in an automatic manner and without developing an *ad-hoc* formulation for each nonlinear theory. The FN (presented in Chapter 1) are evaluated using the Green-Lagrange strains as input, so any desired nonlinear set can be achieved.

4.3 Nonlinear approximation theories for 1D and 2D CUF

In history, scientific researchers have built many geometrical nonlinear models for 1D and 2D structures, as simplifications of the Green-Lagrange strains Eq. (4.1), which is recalled in this chapter as *full geometrical nonlinear model*.

For 1D models, the nonlinear Green-Lagrange strains Eq. (4.1) can be easily modified to consider various nonlinear theories. For instance, when dealing with the von Kármán assumption shown in Eq. (4.3) and introducing CUF and FEM (with the same approach described in Chapter 2), the nonlinear algebraic matrix becomes:

$$\mathbf{B}_{nl}^{sj^{1DVK}} = \frac{1}{2}\begin{bmatrix} 0 & 0 & 0 \\ 0 & 0 & u_{z,y}F_sN_{j,y} \\ 0 & 0 & 0 \\ 0 & 0 & 0 \\ 0 & 0 & 0 \\ 0 & 0 & 0 \end{bmatrix} \tag{4.4}$$

As described in the previous Section, in this Chapter, higher-order models are employed. For this reason and for compatibility purposes between the kinematic and the geometrical nonlinear model, the shear effect has to be considered. Thus, the shear term can be considered as follows:

$$\mathbf{B}_{nl}^{sj^{1DVK_s}} = \frac{1}{2}\begin{bmatrix} 0 & 0 & 0 \\ 0 & 0 & u_{z,y}F_sN_{j,y} \\ 0 & u_{y,z}F_{s,z}N_j & 0 \\ 0 & 0 & 0 \\ 0 & 0 & 0 \\ 0 & 0 & 0 \end{bmatrix} \tag{4.5}$$

This nonlinear set is recalled as 1DVK$_S$ in the numerical results.

As far as the 2D models are concerned, the von Kármán strain theory for shells, see [69], are reported in Eq. 4.2, where the in-plane partial derivatives of the transverse displacement are not neglected. Introducing CUF and FEM in (4.1), it becomes:

$$\mathbf{B}_{nl}^{sj^{2DVK}} = \frac{1}{2}\begin{bmatrix} 0 & 0 & u_{z,x}F_{s,x}N_j \\ 0 & 0 & u_{z,y}F_sN_{j,y} \\ 0 & 0 & 0 \\ 0 & 0 & 0 \\ 0 & 0 & 0 \\ 0 & 0 & u_{z,x}F_sN_{j,y} + u_{z,y}F_{s,x}N_j \end{bmatrix} \tag{4.6}$$

This nonlinear algebraic matrix is recalled as 2DVK. When the shear effects have to be considered within the given mathematical model (2DVK$_S$), algebraic nonlinear matrix becomes:

$$\mathbf{B}_{nl}^{sj^{\text{2DVK}_s}} = \frac{1}{2}\begin{bmatrix} 0 & 0 & u_{z,x}F_{s,x}N_j \\ 0 & 0 & u_{z,y}F_sN_{j,y} \\ u_{x,z}F_{s,z}N_j & u_{y,z}F_{s,z}N_j & 0 \\ 0 & 0 & 0 \\ 0 & 0 & 0 \\ 0 & 0 & u_{z,x}F_sN_{j,y} + u_{z,y}F_{s,x}N_j \end{bmatrix} \tag{4.7}$$

Finally, Fig. 4.2 reports a schematic rappresentation of the nonlinear matrices evaluated, along with the adopted notation. If a parameter is included within the analysis, it is marked by a black dot, otherwise by a white dot.

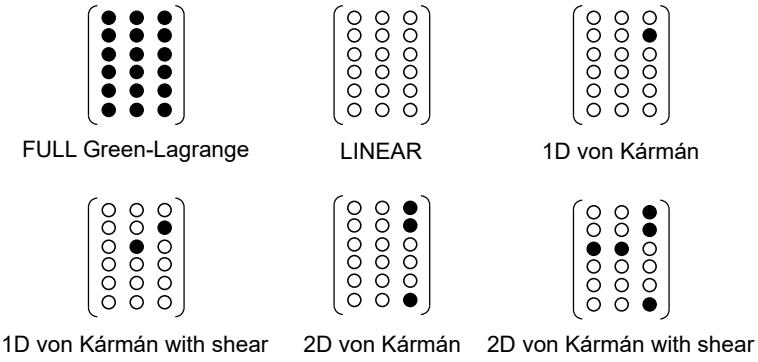

Fig. 4.2 Schematic rappresentation of the geometrical nonlinear matrix.

4.4 Examples

4.4.1 Inefficacy of VK for the post-buckling of square cross-section beam

The capability of the present geometrical nonlinear model is demonstrated with a cantilever isotropic beam. The geometric properties and cross-sectional discretization are reported in Fig. 4.3. The cross-section has a square shape, and the length-to-side ratio equals 100. The 1D mathematical model involves a single L9 over the cross-section and 20 B4 for the beam axis discretization. The material has the following properties: Young modulus E equal to 75 GPa and Poisson ratio $\nu = 0.33$. Finally, the beam is subjected to a compressive loading, and as already seen in previous examples, due to the symmetry of the beam, a small defect load d is applied in the negative z direcrtion.

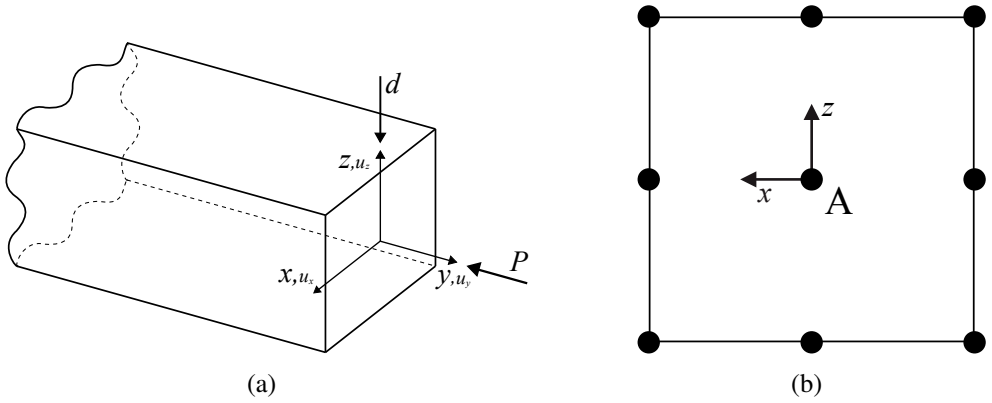

Fig. 4.3 Loading condition (a) and discretization (b) of the cantilever beam.

Static results using different nonlinear approximations are reported in Fig. 4.4. Every curve is denoted by a number, which refers to a specfic nonlinear matrix reported in the same figure. As already explained, if a parameter is marked by a black circle, it means that that parameter is included within the analysis. For instance, the first matrix is full of black dots, meaning that a full geometrical nonlinear analysis is employed (i.e. the full Green-Lagrange) strains are adopted). Matrix 4 does not include any nonlinear parameter, so a linear analysis is performed. The matrices denoted by number 1 include every parameter but the 1^{st} column and the 1^{st}, 4^{th} and 6^{th} rows, meaning that the nonlinearities in the x and u directions are neglected. The respective results are the same as the full nonlinear analysis. This is clear since the load and deformation are acting on the yz plane. The strain set 2 makes use of the von Kármán assumptions of 1D beams and leads to an almost constant value of P/P_{cr} increasing the displacement value. It must be pointed out that higher-order model, accounting for shear effects, are employed in this work. Accordingly, the nonlinear effects of shear strain must be included in the analysis due to the fact that an higher-order kinematic model is adopted (3^{rd} case in Fig. 4.4).

The 5 case is addressed to show how the results can change if a different nonlinear theory is employed. Compared to the full nonlinear one, this analysis shows a great accuracy until the normalized displacement value of 0.4. Then, they start differing and in the advanced geometrical nonlinear regime the two solutions are completely different. Some of the most relevant displacement and load values are reported in Table 4.1.

4.4.2 Bending of a thin-walled channel section beam

As a second analysis case, an unsymmetric channel section is addressed. The cross-section is thin-walled and the geometry is shown in Fig. 4.5(a), where $h_1 = 48$ mm, $h_2 = 40$ mm,

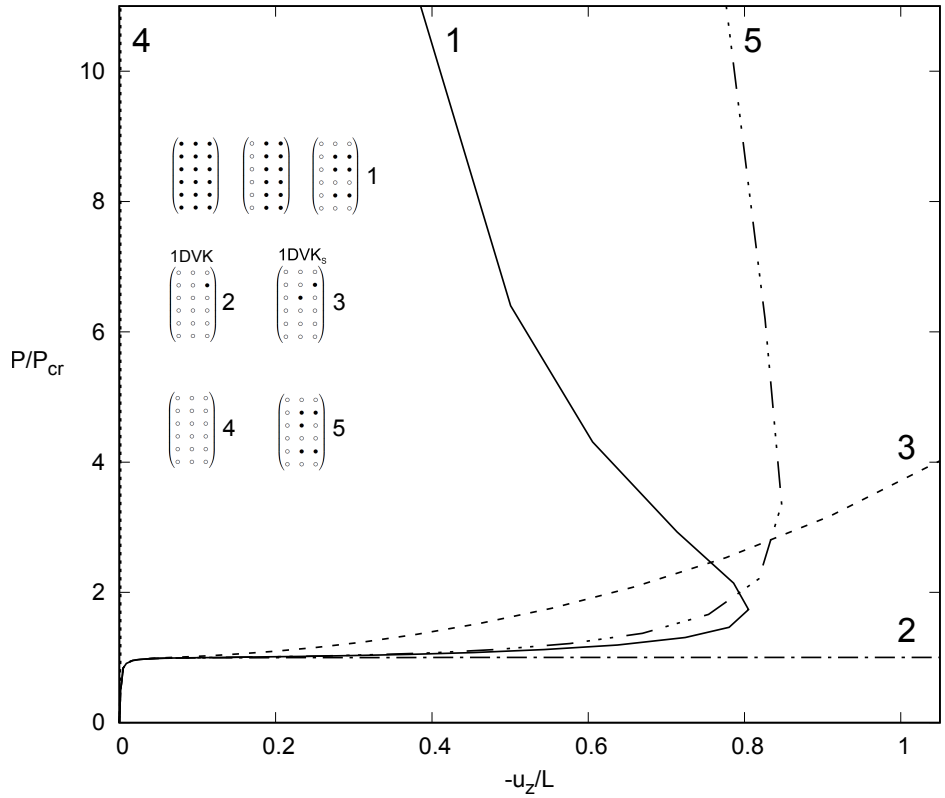

Fig. 4.4 Static curves for the cantilever beam using different strains approximations. $P_{cr} = \frac{4L^2}{\pi^2 EI}$

$-u_{zA}/L$		P	
0.2	61.42	63.58	61.61
0.4	62.38	67.62	62.43
0.6	63.70	76.27	64.24

Table 4.1 Values of P and displacement for the cantilever beam subjected to axial loading.

$t = 10$ mm and $b = 100$ mm. The cross-section is approximated with 44 Lagrangian points, which pattern is shown in Fig. 4.5(b). The material is the same as the previous analysis case, and it is subjected to a transverse force. Finally, 20 B4 finite elements are placed on the y direction to approximate the axis of the beam.

Static curves are depicted in Fig. 4.6, employing different nonlinear approximations. On the contrary of the previous analysis case, the u_x component has a strong infleunce, since a

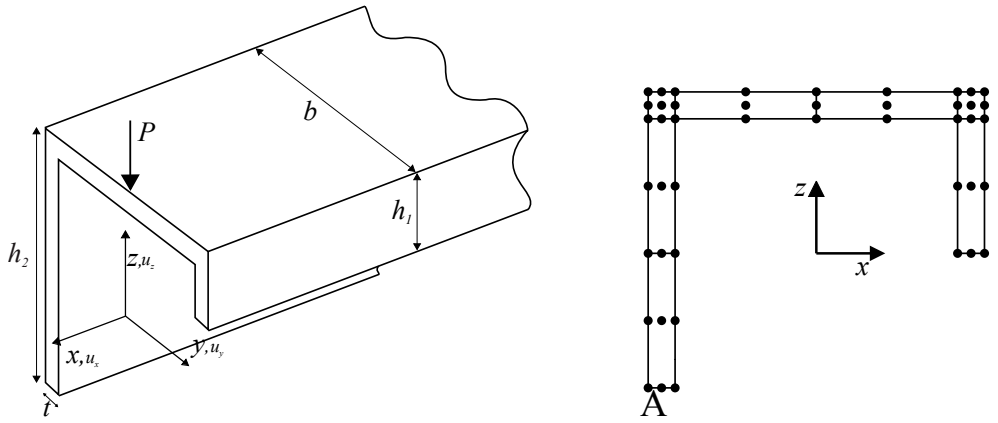

Fig. 4.5 Geometric characteristics and loading condition (a) and discretization (b) of the unsymmetric thin-walled cantilever beam.

torsion phenomenon occurs along with the bending one. For this reason, nonlinear sets 1 and 2 lead to different results.

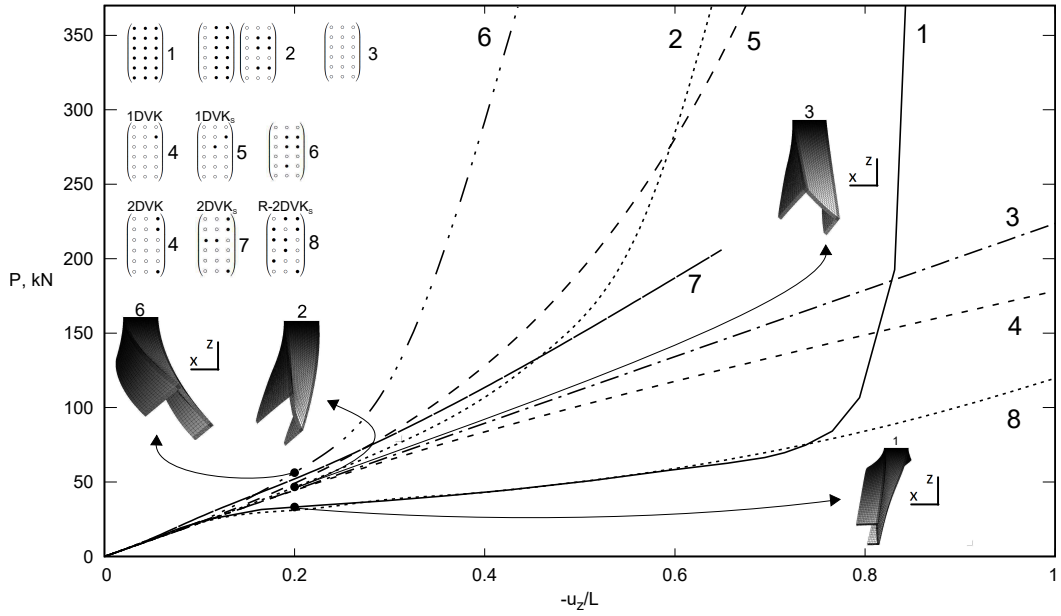

Fig. 4.6 Static nonlinear solution of the unsymmetric channe cantilever beam.

The analysis 3 shows the linear solution, since no parameters are involved in the analysis. The 4 and 5 analysis shows the 1D nonlinear theory of von Kármán excludling and including the shear term, respectively. The difference between the two analyses shows the importance of including the shear term. The same discussion can be extended to the cases number 4 and 7, which use the 2D von Kármán theories, but now, not even the shear terms are

sufficient to achieve the accurate results. The reason is that, due to the unsymmetric geometry of the cross-section, during the bending, a rotation occurs. When the rotation terms are included (analysis case 8, which is denoted as R-2DVK$_S$), the solution is very close to the full geometrical nonlinear one. Finally, the case 6 shows an additional nonlinear theory, which leads to a hardening static behaior of the structure.

4.4.3 Consistency of the nonlinear approximations on the pinched thin-walled cylinder via 1D model

As a final example, a pinched cylinder is considered. The problem is taken from Flügge [66]. The material properties are Poisson ratio $\nu = 0.3$ and Young modulus $E = 3 \times 10^6$. Fig. 4.7(a) reports the geometric characteristics, where L is the length of the cylinder and equals 600 in, the radius r is equal to 300 in and thickness $t = 3$ in. The cross-sectional mathematical model involves 30L9 elements. the discretization pattern is shown Fig. 4.7(b), where more lagrangian elemenents are near the loading point, so that $A_1/A_2 = 10$.

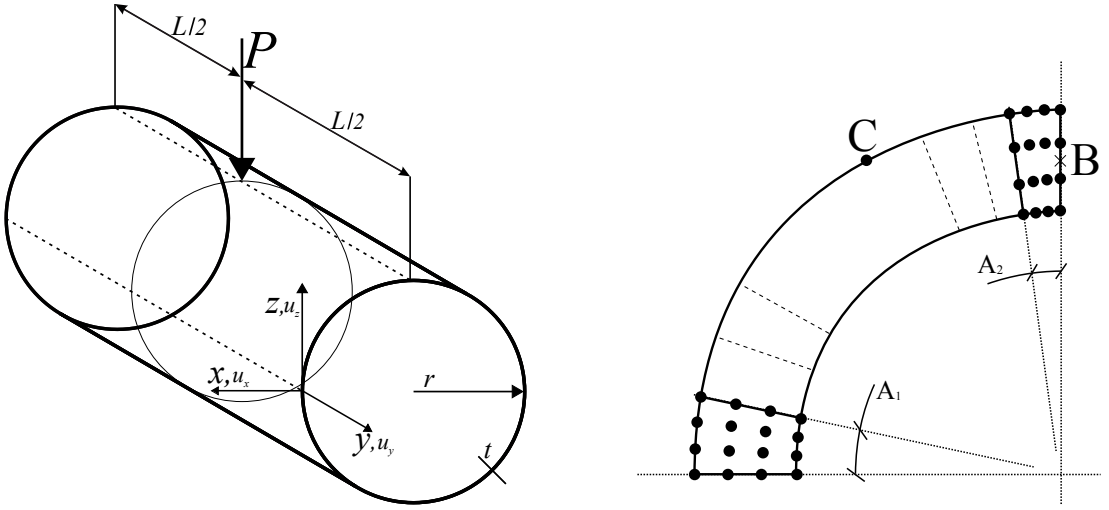

Fig. 4.7 Geometric and loading condition (a) and discretization (b) of the pinched cylinder.

The transverse displacement of the point B is reported in Figure 4.8. Nonlinear approximation 1 demonstrates that first and second column of the full nonlinear matrix do not have any influence on the nonlinear behavior, since their results is the same as the full nonlinear one. Analysis 2 shows the linear solution, since any nonlinear terms is excluded. Analyses 3 and 4 report two additional nonlinear approximations which lead to not accurate results. The former lead to an almost horizontal line, the latter a result near the linear solution. Analyses 5, 6 and 7 show the solution of von Kármán theories including the shear terms, where the

analysis 7 is almost equal to the full nonlinear analysis. Some deformed structures are reported in the same figure. The transverse displacement of point *C* is reported in Fig. 4.9 using the same approximation sets presented in the previous figure. The most relevant results, in terms of values of load P and displacements, are reported in Tables 4.2 and 4.3.

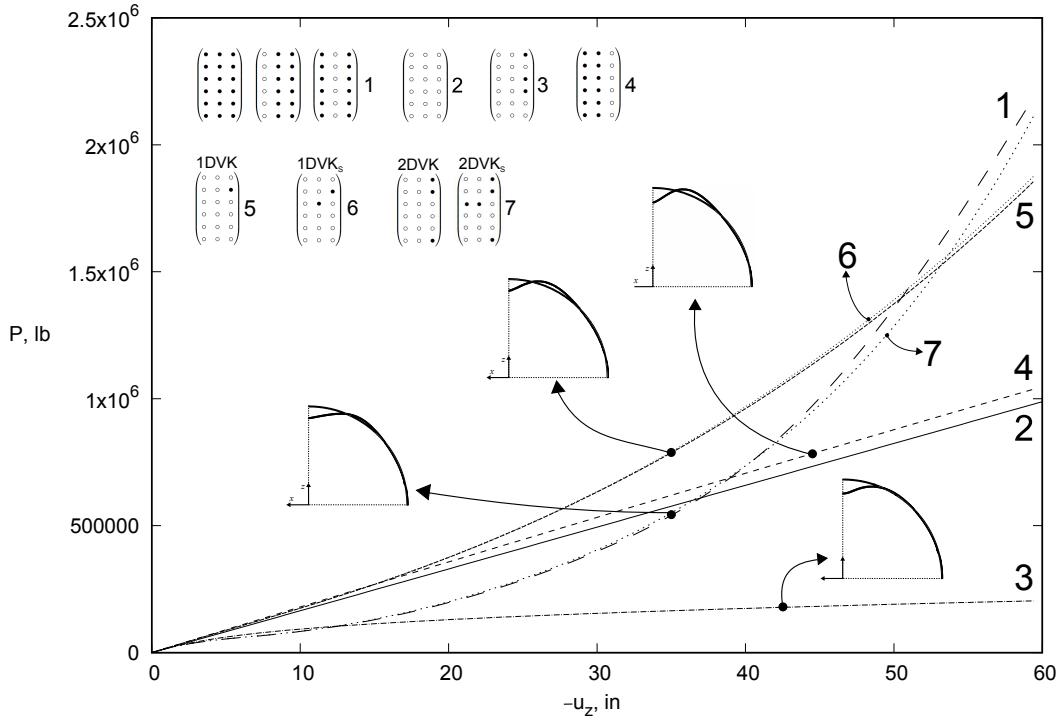

Fig. 4.8 Static curves using different nonlinear approximations for the pinched cylinder. The displacement is the transverse component of point *B*.

P	$-u_{zB}$	$-u_{zB}$	$-u_{zB}$	$-u_{zB}$	$-u_{zB}$
250.0	22.83	15.18	22.91	13.98	-
750.0	39.10	45.53	38.37	42.56	-
1800	54.03	109.3	54.86	108.3	-

Table 4.2 Relevant values of the displacement of point *B* for the pinched cylinder. P is expressed in lb $\times 10^3$, u in inches.

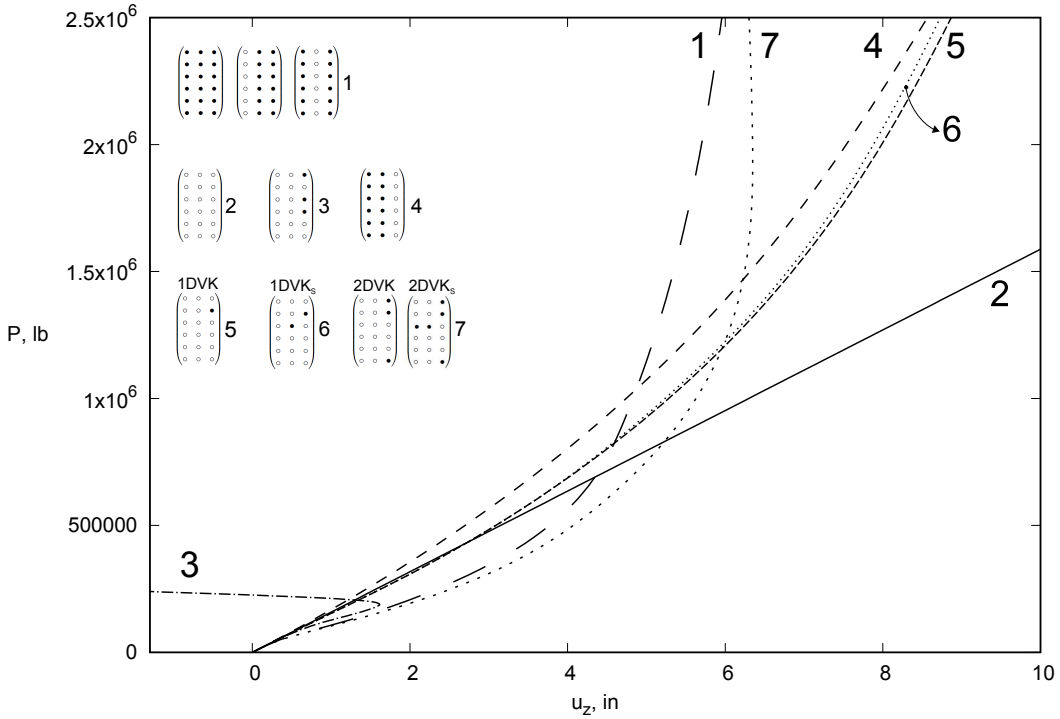

Fig. 4.9 Static curves using different nonlinear approximations for the pinched cylinder. The displacement is the transverse component of point C.

P	u_{zC}	u_{zC}	u_{zC}	u_{zC}	u_{zC}
250.0	2.304	1.575	2.530	1.424	-
750.0	4.247	4.724	4.603	3.775	-
1800	5.378	11.34	6.020	6.978	-

Table 4.3 Relevant values of the displacement of point C for the pinched cylinder. P is expressed in lb $\times 10^3$, u in inches.

4.4.4 Consistency of the nonlinear approximations on the pinched thin-walled cylinder via 2D shell model

The same pinched cylinder case as in the previous example is analyzed via a 2D shell model. The geometric, loading, material and boundary conditions are the same, only the mathematical model is different. Figure 4.10 shows the structural case, along with the cylindrical reference system α, β and z.

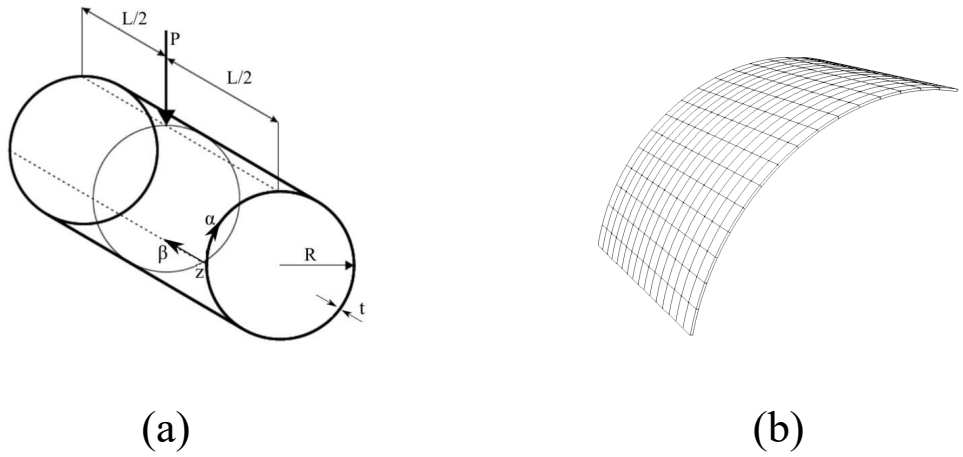

Fig. 4.10 Representation of (a) the entire pinched thin-walled cylindrical under transverse load and (b) in-plane mesh approximation of the model studied.

The first analysis regards a convergence investigation to establish the mathematical model for the subsequent analyses. The in-plane finite element discretization is evaluated first, then the converged theory for the thickness direction is evaluated. From 64 to 256 quadratic Q9 finite elements are employed for the surface approximations, using the LD2 kinematics for the thickness expansion. Then, on the converged in-plane mathematical model, the thickness function analyzed are LD1, LD2 and LD3. The static results are shown in Figure 4.11. Clearly, the converged mathematical model is represented by the 16x16Q9 + LD2. The solutions taken as reference are those shown in the previous example and described in Pagani *et al.* [145].

Moreover, the transverse displacement values for various models and loads, along with the total degrees of freedom (DOFs), are tabulated in Table 4.4. As evident from Fig. 4.11

Model	DOFs	$-u_z$ [in]	
		2.5×10^5 lb	15×10^5 lb
8 x 8Q9 + LD2	2601	18.5	48.1
12 x 12Q9 + LD2	5625	21.8	50.8
16 x 16Q9 + LD2	9801	22.9	52.0
20 x 20Q9 + LD2	15129	22.9	52.1
Ref. [145]	10920	23.1	52.4

Table 4.4 Values of transverse displacements of the loading point for various mathematical models.

and Table 4.4, to carry out an accurate static response analysis, showing the various nonlinear

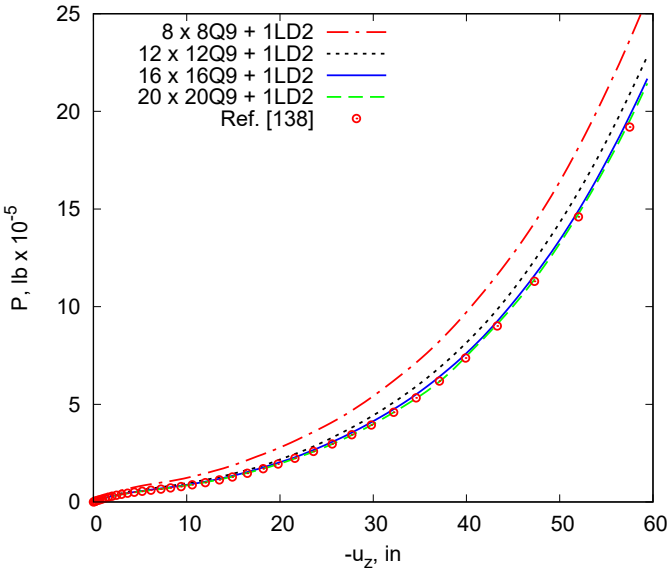

(a) Mesh size

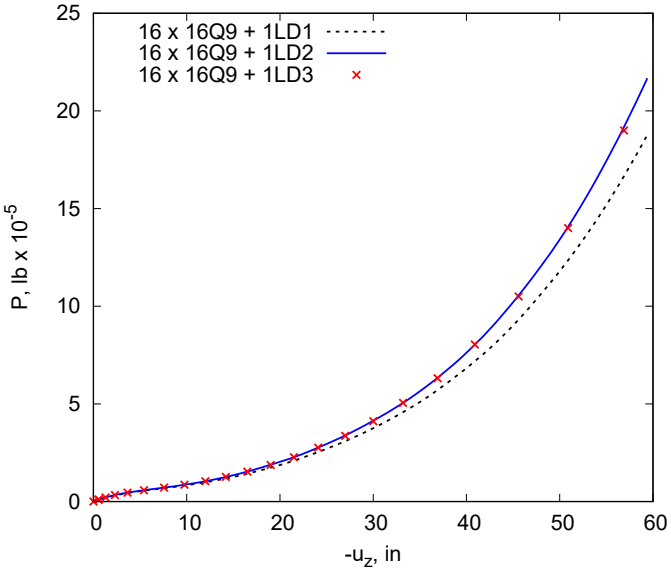

(b) Theory approximation

Fig. 4.11 Convergence study of the nonlinear solutions. Comparison of (a) various surface approximations and (b) kinematic expansion over the thickness.

terms effects, the structure is modelled employing 16×16Q9 for the surface approximation and only one LD2 in the thickness direction. Figure 4.12 depicts the equilibrium curves of the pinched cylindrical shell for various geometrical nonlinear models at the load point. In addition, some deformed configurations are illustrated in the same figure. Basically, different nonlinear terms of the operator $\mathbf{b}_{nl}$ are activated in each geometrical nonlinear theory. In essence, black dots in Fig. 4.12 denote the nonlinear terms that are active. For example, the

analysis with all nonlinear terms involved (i.e., full 3D nonlinear Green-Lagrange strains) is abbreviated as “Full”, whereas that with all nonlinear terms excluded indicates “linear" analysis. “1DVK” and “2DVK” analyses represent the von Kármán assumptions to 1D and 2D models. Instead, analysis including nonlinear shear effects will be referred to as “1DVKs" and “2DVKs". Analysis case number 4 points out that neglecting the higher-order derivatives

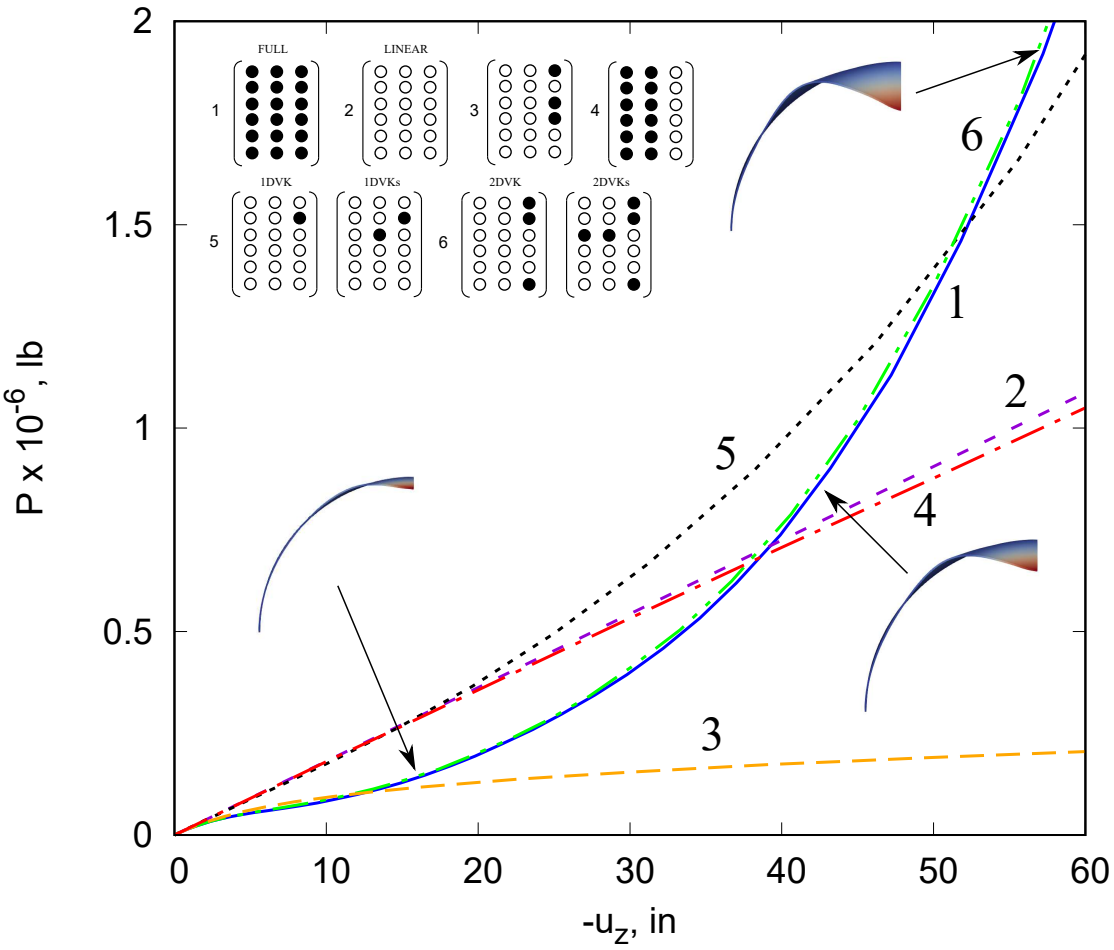

Fig. 4.12 Static nonlinear solution performed at loading point for different approximation theories.

of the displacement component u_z (third column of matrix b_{nl}) affects the accuracy of the solution. In fact, the trend is very similar to that of linear analysis (case number 2).

Chapter 5

Geometrical nonlinear effects due to large cross-sectional deformations

5.1 Large cross-sectional displacements in beam structural elements

Beam theories are an important means for the study of a large number of structural problems in many engineering fields, such as mechanical, civil and aerospace engineering . Compared to two-dimensional (2D) and three-dimensional (3D) models, one-dimensional (1D) theories provide a great advantage in terms of computational costs when dealing with slender structures. Early theories include the classical models of Eulero-Bernoulli [63], Saint-Venant [54] and Timoshenko [177]. According to these models, the three-dimensional problem is reduced into a one-dimensional one, which depends only on the axial coordinate along the beam length (axis). A detailed analysis and discussion of these classical theories have been provided in many works, for example by Mucichescu [133].
In general, classical models consider the cross-section as rigid. However, the investigation of more complicated structures, such as thin-walled ones, and the need to detect in-plane and out-of-plane phenomena, such as distortion or warping, may require the adoption of refined beam theories, and various are available in literature. In particular, this chapter focuses on the evaluation of the effects of cross-sectional deformations. The effects of the geometrical nonlinear equations on the static behavior of this kind of structures is investigated. The need to include a 3D model to evaluate every local effect that may appear within the structure is demonstrated by Bažant and Cedolin [17]. Moreover, Bathe and Bolourchi [15] developed beam model based on an updated Lagrangian and a total Lagrangian formulation, highligthing its efficiency in terms of computational cost. As shown by Simo and Vu-Quoc

[168], when dealing with local effects and higher-order warping phenomena, the introduction of refined beam theories in the geometrically nonlinear relations is needed. The authors analyzed a 3D beam structure, able to detect torsional warping. Frey [85] and Ibrahimbegović used finite element analysis to evaluate the geometrical nonlinear one on the behavior of beams, considering the Reissner theory of shear deformation [158]. Other relevant nonlinear analyses were performed by Kang and Yoo [88] and Chan and Kitipornchai [41]. The former analyzed the post-buckling field of circular beams made by circular cross-sections, the latter evaluated geometrical nonlinear governing equations for thin structures.

5.2 Modeling of complex thin-walled structure

The development of refined models has been encouraged by the need of enstabilish accurate design procedures of sophisticated structures undergoing large deflections and rotations. A vast number of components can show nonlinear behavior during their working service, in many engineering fields, such as aerospace and civil engineering. Given the complex geometry of such components, refined models are mandatory for an accurate geometrical nonlinear analysis. In the previous Chapter, the historical evolution of geometrical nonlinear models has been proposed, including the novel outcomes on higher-order theories. Hereafter, just a few are recalled, for the application of refined theories of complex structures. Obst and Kapania [141] employed a parabolic stress distribution for the analysis of beam structures. Singh et al. [169] studied asymmetric laminated composite structures, in the geometrical nonlinera domain, using the von Kármán strains and the same approach was conducted by Chandrashekhara and Bangera [43]. The Variational Asymptotic Beam Sectional (VABS) is widely adopted to formulate geometrical nonlinear analyses in various works [188]. The 3D configuration is considered as a combination of a linear cross-sectional contribution, and a nonlinear one, i.e. the beam axis. Krawczyk et al. [100] considered a first-order shear distribution for each layer, in a Layer-Wise (LW) scenario. The nonlinear issue was evaluated by introducing a three-noded FE 1D model by Vidal and Polit [181]. They evaluated the situation of composite beams with a sinusoidal strain distribution, avoiding the employment of mathematical techniques like shear factors. Li and Qiao [119] adopted the Reddy's high-order shear deformation beam theory for the thermal post-buckling analysis of laminated 1D structures, adopting the von Kármán approximations. Components with initial cracks and of laminated circular components were further investigated by the same authors in [118, 120]. Mororo et al. [132] recently introduced a total Lagrangian approach for the geometrical nonlinear investigation of laminated 1D structures with thin cross-sections.

The adoption of 1D models found applications mainly when dealing with slender and compact cross-section beams, which do not show complex geometry in the three dimensions, which is clearly not valid for lattice structures. In the last years, they attracted much attention due to their outstanding properties. Lattice components are made of repetitions of elements in the space, and their production was made possible due to the achivements in additive manufacturing techniques [70]. They are capable to: (1) reduce the material in the production process, (2) decrease the manufacturing time, (3) reduce the energy during the production process, (4) show high optimization in terms of strength/weight ratio [77]. In the case of sophisticated structures, various techniques were proposed to consider 1D systems made of beam structures, oriented in the 3D space in a generic way. Rotational joint springs were developed by Lee and Nikolaidis [112]. The stiffness of those was evaluated by the static behavior of the structure. El-Sayed [57] evaluated the 3D problem for the joint portion to calculate the spring stiffness. A new approach for the joint connection was developed by Jang et al. [86], avoiding the usage of artificial springs. The Guyan reduction was adopted by Donders et al. [56] to report a FE model of a joint beam elements. The static and modal solutions were evaluated [134]. The adoption of these theories gets harder when dealing with the geometrical nonlinear behavior, including post-buckling behaviour. For this reason, it is needed to implement a technique that solves complex structures with a straightforward procedure, to overcome the aforementioned problems. This chapter investigates and develop an alternative approach, based on CUF, to analyze the geometrical nonlinear analysis of complex beam structures. Fig. 5.1(a) shows the basics of this approach. Consider a generic 1D structure, whose length is L, width is b and thickness is h. According to classical 1D theories, it is needed to consider the beam axis placed on the y coordinate, along the beam length L, as depicted in Fig. 5.1(b), whereas Ω_c is the cross-section, in the $b \times h$ coordinates (in red). On the contrary, regarding the present CUF-based approach, the y coordinate can be put on any direction, like the width b. In particular, in the present modeling technique, Ω_p lays along the $L \times h$ directions, and the beam axis y is placed on the width direction b. If the Finite Element Method (FEM) is employed, its approximation is evaluated along the 1D axis, which is much shorter when the present technique is adopted. On the contrary, many DOFs are needed for the evaluation of the displacement over the cross-section, which is a popular approach of many refined 1D models. Despite this aspect, numerical issues, such as the shear locking, can be mitigated with this approach, since they usually afflict FEs, which field of application is much more limitated compared to classical approaches. Finally, the nonlinear governing relations are less complex, especially when dealing with curved geometries.

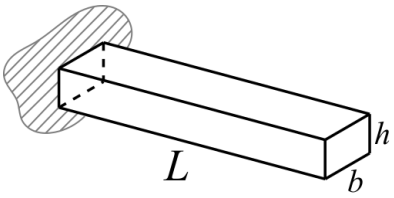

(a) Generic 1D structure

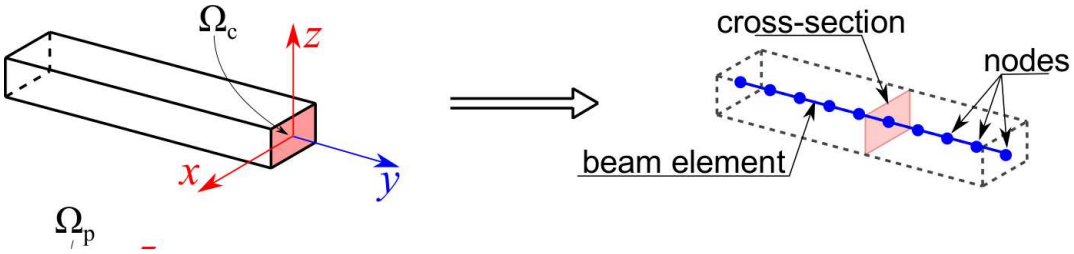

(b) Classical beam model: the axis "y" lays along the length "*L*".

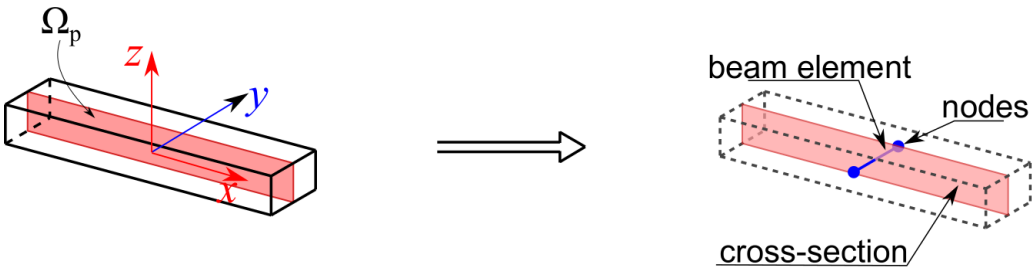

(c) Present approach: the axis "y" lays along the "b" length.

Fig. 5.1 1D-modeling techniques for a generic beam.

5.3 Importance of nonlinear geometrical relations when using nonlinear kinematics

In this chapter, large cross-sectional deformations and rotations are evaluated by an opportune higher-order model in a geometrical nonlinear scenario. Fig. 5.2 reports typical phenomena which can occurr in thin sections. It can exhibit rigid rotations (5.2(a)) that can be evaluated by classical beam theories. On the contrary, the deformations and rotations of Figure 5.2(b) can be evaluated only through higher-order beam theories. The issue we want to discuss in this chapter regards the effectiveness of an higher-order *kinematic* model on the geometrical nonlinear *structural* behavior of structures. The accuracy in these situations is, then, evaluated. The results show that the displacement-strain nonlinear relations have to be considered, even if kinematically higher-order models are employed. For completeness purpose, Eq. (5.1) reports the linear and nonlinear strains along the three cartesian beam axis directions y and

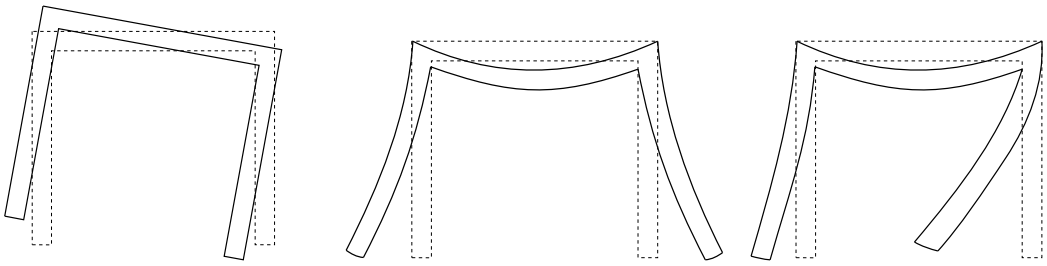

(a) Rigid cross-section - classical models

(b) Deformations and rotations - higher-order models

Fig. 5.2 Deformations of classical and higher-order beam models.

cross-section coordinates x and z.

$$\begin{aligned}
\varepsilon_{xx} &= u_{x_{,x}} + \frac{1}{2}\left(u_{x_{,x}}{}^2 + u_{y_{,x}}{}^2 + \overbrace{\boxed{u_{z_{,x}}{}^2}}^{(Section)}\right) \\
\varepsilon_{yy} &= u_{y_{,y}} + \frac{1}{2}\left(u_{x_{,y}}{}^2 + u_{y_{,y}}{}^2 + \overbrace{\boxed{u_{z_{,y}}{}^2}}^{(Flexure)}\right) \\
\varepsilon_{zz} &= u_{z_{,z}} + \frac{1}{2}\left(\overbrace{\boxed{u_{x_{,z}}{}^2}}^{(Section)} + u_{y_{,z}}{}^2 + u_{z_{,z}}{}^2\right)
\end{aligned} \tag{5.1}$$

where u_x, u_y, u_z represent the displacements, which are shown in Fig. 5.3, along with the adopted notation.

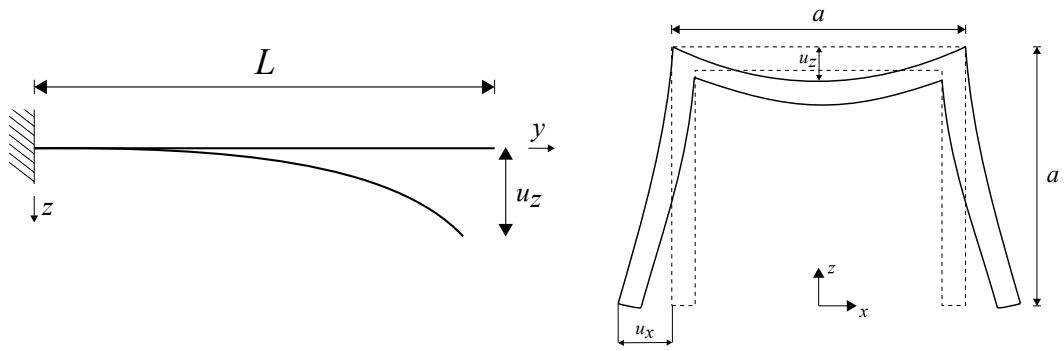

(a) Axis

(b) Cross-section

Fig. 5.3 Adopted notation for the directions and displacements.

5.4 Geometrical nonlinear model of cross-sections

The 3D displacements of an arbitrary 1D structure in a cartesian reference system x, y and z, as depicted in Fig. 5.1(a), can be evaluated in a vectorial form, and it reads:

$$\mathbf{u}(x,y,z) = \left\{ \begin{array}{ccc} u_x & u_y & u_z \end{array} \right\}^T \tag{5.2}$$

Consider y as the coordinate of the 1D axis, whereas x and z are the in-plane directions of the cross-section. Fig. 5.1(b) shows the classical technique, in which the cross-section Ω_c (in red) is placed on the plane, and the beam axis (in blue) lays along the length L direction. On the contrary, the proposed present approach, depicted in (Fig. 5.1(c)), assumes the cross-section Ω_p in the $L \times h$ domain, and, consequently, the axis is placed along the width direction. It should be pointed out that the cartesian reference system, in both tenchiques, is built so that the cross-section is on the $x-z$ plane and the beam axis lays in the y direction.
CUF and FEM allow the 3D displacement field to be written as:

$$\mathbf{u}(x,y,z) = F_\tau(x,z) N_i(y) \mathbf{u}_{\tau i}, \qquad \tau = 1,2,\ldots,M \quad i = 1,2,\ldots,N \tag{5.3}$$

where $F_\tau(x,z)$ are the cross-section expansion functions in x and z directions, N_i represents the i-th shape function in the y direction, M represents the number of the terms used in the expansion, N stands for the number of the nodes on the beam axis and $\mathbf{q}_{\tau i}$ is the vector of the nodal unknowns. Note that the Lagrange polynomials could be adopted in both classical and present modeling techniques, as explained in Fig. 5.1(a). Since only one FE is used in the present approach, numerical locking issues, such as the shear locking, appear to be less evident.
The classical approach and the proposed modeling technique is described in Fig. 5.4. L4 Lagrange elements are adopted. A more popular case of thin-walled 1D structure is shown in Fig. 5.5. It can be pointed out that the nonlinearities along the axis direction correspond to the nonlinearities on the cross-sectional domain in the present modeling approach. In addition, the approach described herein, allows the analysis of complex geometry, which would require the implementation of various 1D elements, adopting the classical approach. Thus, one of the most interesting difference between the two approaches is the behavior in the geometrical nonlinear field. In fact, as described in Fig. 5.6(a), full nonlinear behavior can be achieved by considering only cross-sectional nonlinearities. This approach appears to be more effective when adopted on complex and thin-walled geometries, as it is clear from the proposed results.

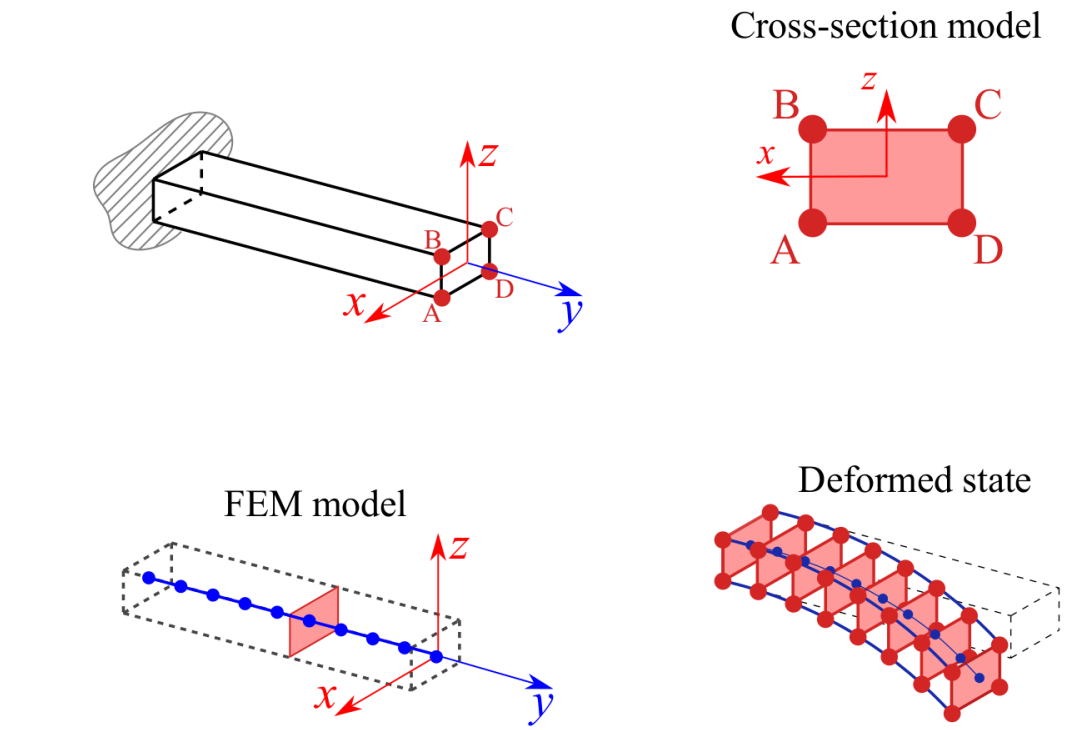

(a) Classical beam formulation.

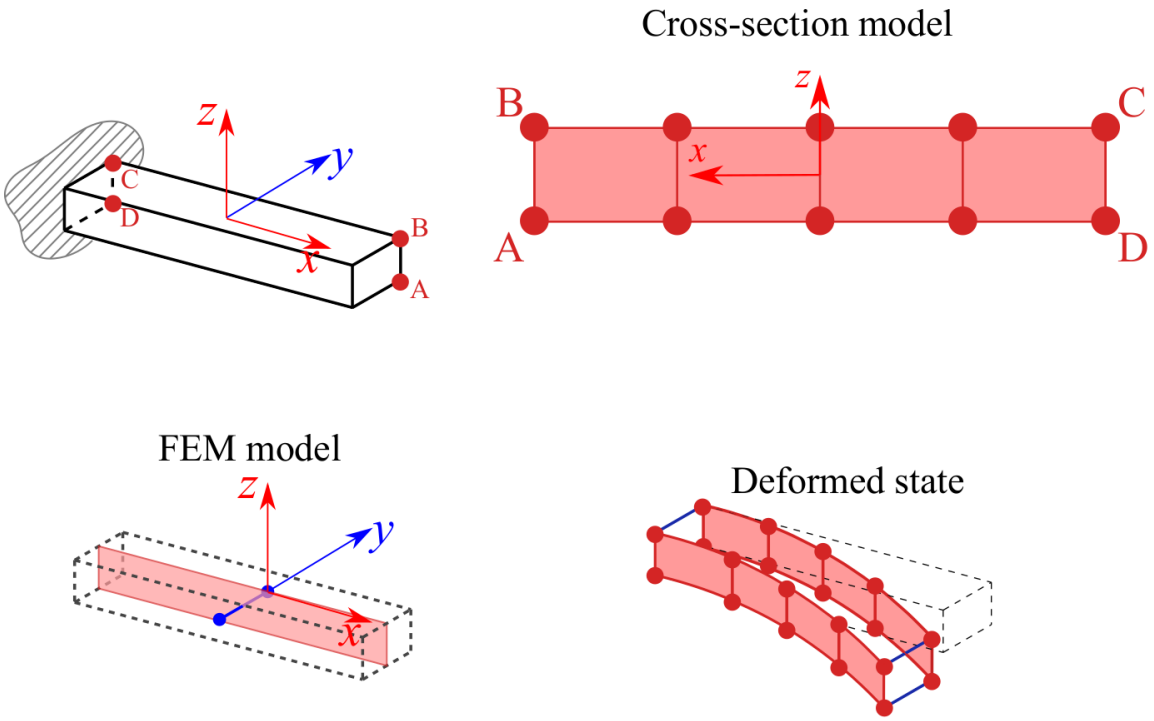

(b) Present model with large deformation.

Fig. 5.4 Modeling approaches of the FE CUF-based.

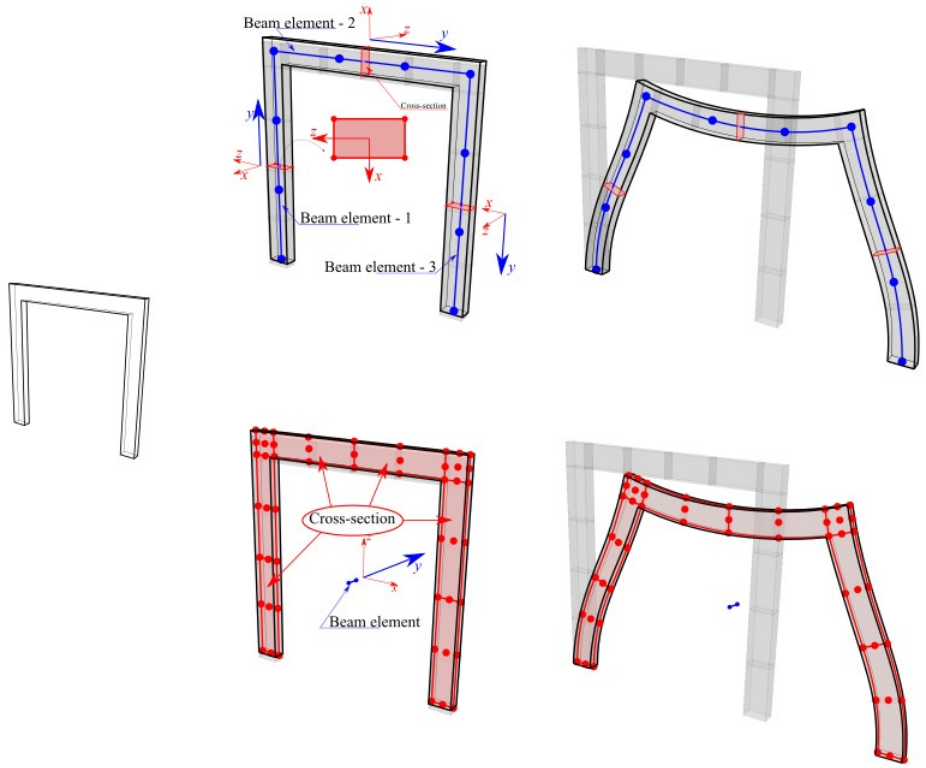

Fig. 5.5 Classical and present modeling techniques for a complex thin-walled structure.

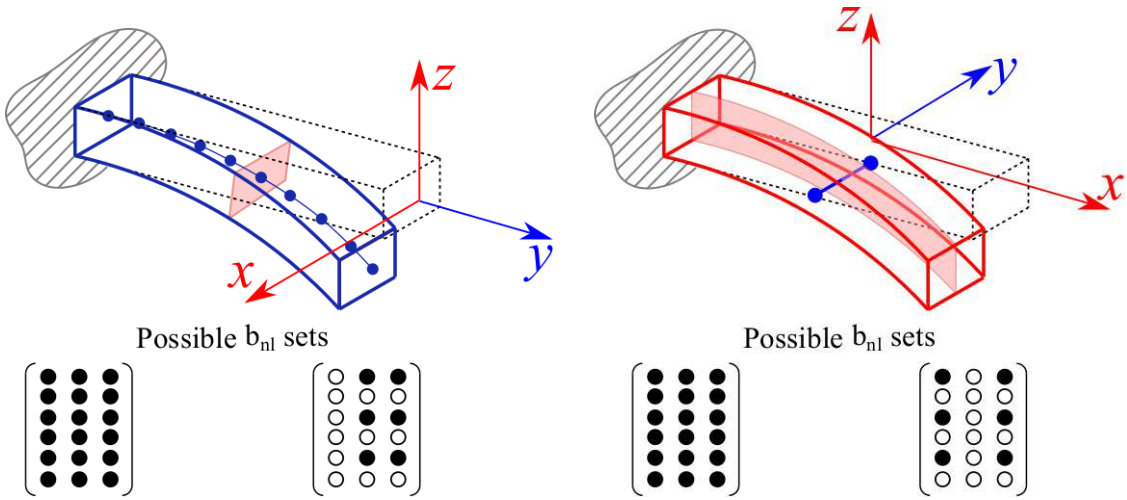

(a) Classical (b) Present

Fig. 5.6 Nonlinear terms for the modelling tenchiques.

5.5 Examples

5.5.1 Geometric nonlinearities effects on isotropic composite structures

The first analysis case regards a compact isotropic cross-section beam. The material has E equal to 75 GPa and Poisson ratio $\nu = 0.33$, which represents an aluminum alloy. Figure 5.7 shows the square cross-section, with side equals 0.1 m and subjected to pinched opposite forces and the boundaries involve clamped-free conditions. Three kinematic models are

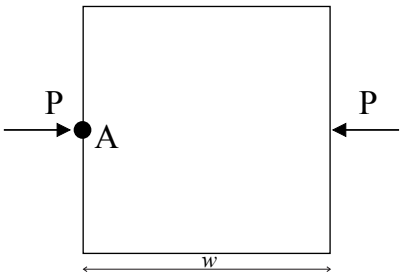

Fig. 5.7 Square cross-section geometry of the isotropic cantilver beam.

employed for this problem, as depicted in Fig. 5.8. They involve a bilinear L4 (Fig. 5.8(a)), a quadratic L9 (Fig. 5.8(b)) and a cubic L16 (Fig. 5.8(c)) interpolation functions. Finally, increasing forces are used until the stress reaches the yield one, which is 503 MPa. Linear

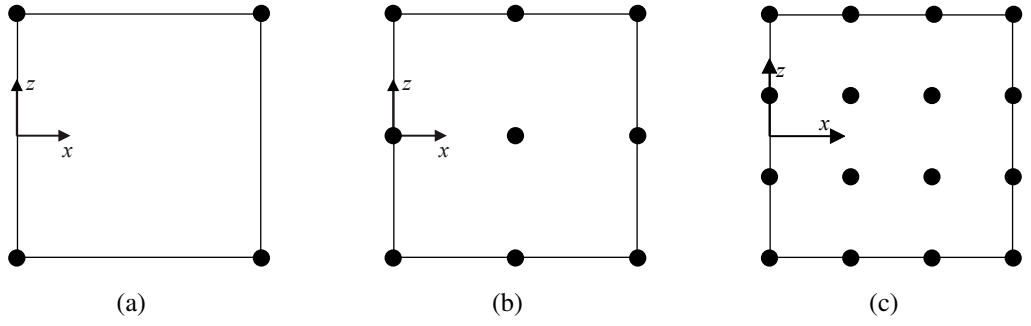

Fig. 5.8 Kinematic models of a compact isotropic beam.

and geometrical nonlinear solutions are evaluated for every kinematic models, for the lateral displacement of point "A" in Fig. 5.7. Figure 5.9 shows the percentage differences between the two solutions. Two main conclusions can be drawn from the results:

- The higher-order kinematics reports greater differences;
- Even for the most refined L16 kinematic theory reports negligible differences.

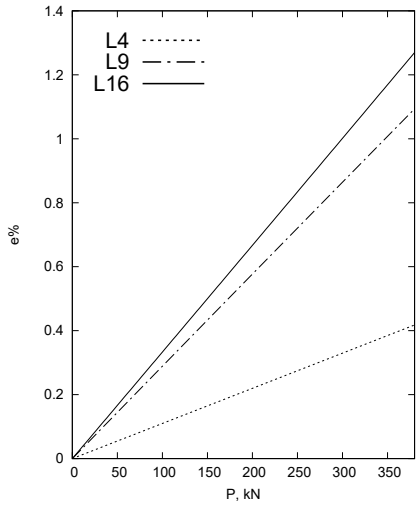

Fig. 5.9 Difference between linear and nonlinear solutions.

The numerical values are shown in Table 5.1, for many values of P.

	*L*4			*L*9			*L*16		
P	$-u_{xl}$	$-u_{xnl}$	$e_{\%}$	$-u_{xl}$	$-u_{xnl}$	$e_{\%}$	$-u_{xl}$	$-u_{xnl}$	$e_{\%}$
9.997	0.004	0.004	0.011	0.010	0.010	0.029	0.008	0.008	0.033
52.68	0.020	0.020	0.058	0.051	0.051	0.152	0.044	0.044	0.175
128.3	0.048	0.048	0.141	0.123	0.124	0.370	0.106	0.107	0.427
256.7	0.097	0.096	0.097	0.246	0.248	0.740	0.213	0.215	0.857
392.4	0.149	0.148	**0.431**	0.376	0.381	**1.129**	0.325	0.329	**1.311**

Table 5.1 Displacement values for many load P. P is expressed in kN, the displacements are in $mm \times 10^3$.

A thin-walled beam is addressed as a second analysis case. The geometry is reported in Fig. 5.10, where $w = 0.1$ m, $h = 0.1$ m, $t = 0.01$ m and $L = 2$ m. The material characteristics are those described in the previous case.

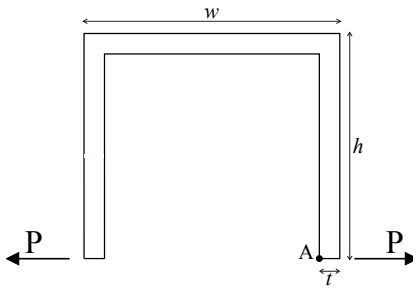

Fig. 5.10 Geometry and loading conditions of thin-walled cross-section.

Kinematic higher-order models are employed to evalulate the 3D displacement field, according to the number of elements used on the cross-sectional discretization. Figure 5.11 show the 8L4, 8L9 and 8L16 that are implemented.

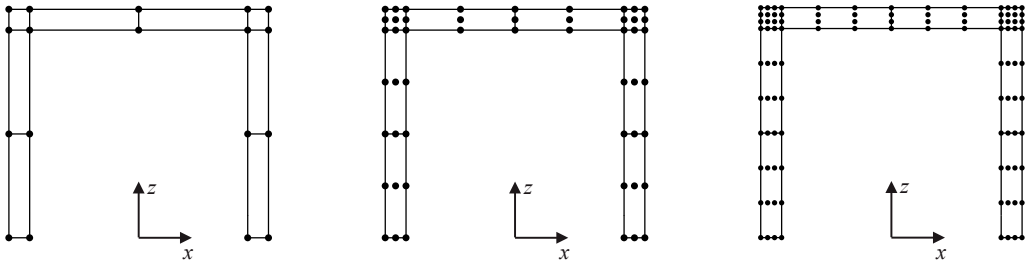

(a) 8L4 discretization (b) 8L9 discretization (c) 8L16 discretization

Fig. 5.11 Kinematics theories employed for the thin-walled cross-section.

Lateral forces are used until the stress reaches the yield limit and both linear and nonlinear solutions are evaluated and the lateral displacement of point “A”. The difference between the two solutions is evaluated in Fig. 5.12.

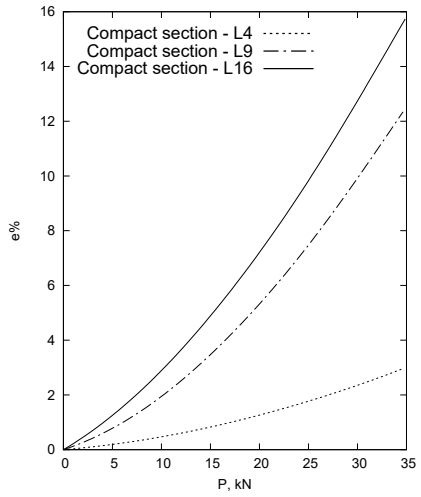

Fig. 5.12 Difference between linear and nonlinear solutions.

On the contrary of the previous analysis case, the difference is more evident, reaching higher values. Those values are reported in Table 5.2. The highest value is for a cubic kinematic model, 15.7%. It is clear that the employment of geometrical nonlinear equations is mandatory in case of thin-walled structures.

		L4			L9			L16	
P	$-u_{xl}$	$-u_{xnl}$	$e_{\%}$	$-u_{xl}$	$-u_{xnl}$	$e_{\%}$	$-u_{xl}$	$-u_{xnl}$	$e_{\%}$
1.503	0.498	0.498	0.049	1.314	1.311	0.193	1.363	1.358	0.335
6.377	2.099	2.094	0.258	5.571	5.512	1.064	5.776	5.681	1.665
16.94	5.564	5.626	1.017	14.80	14.21	4.157	15.31	14.49	5.735
25.62	8.338	8.508	1.888	22.38	20.77	7.764	23.13	21.00	10.12
35.08	11.29	11.64	**3.044**	30.63	27.21	**12.57**	31.60	27.30	**15.74**

Table 5.2 Displacement values for many P level. P is expressed in *kN*, the displacements are reported in $mm \times 10^3$.

5.5.2 Geometric nonlinearities effects on composite structures

In the following analysis case, a square cross-section of a cantilever beam is addressed. The structure is made of three layers of a composite material, having Poisson's ratios $\nu = 0.25$, Young moduli $E_1 = 155$ GPa, $E_2 = E_3 = 15.5$ GPa, and shear moduli $G_{12} = G_{13} = 9.3$ GPa, $G_{12} = G_{23} = 7.75$ GPa. Figure 5.13 reports the loadings and the geometry of the section. The thinkess of each layer is same $t/3$, where t is the side of the square, and the aspect ratio is 10. 10 cubic elements were used for the beam axis discretization. Figure 5.14 reports the

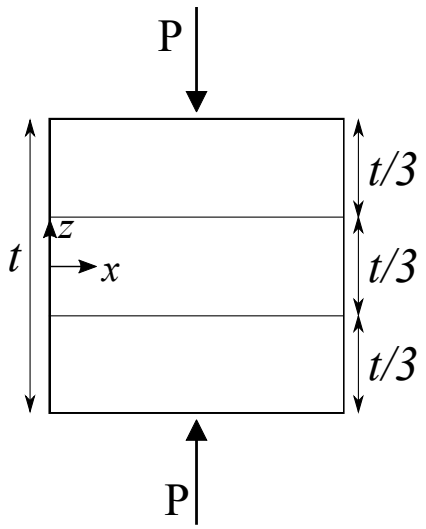

Fig. 5.13 Square cross-section geometry and loading condition.

approximation employed for each layer, i.e. L4, L9 and L16 Lagrange polynomials. Two stacking sequences are considered, [0°/90°/0°] and [0°/45°/0°].

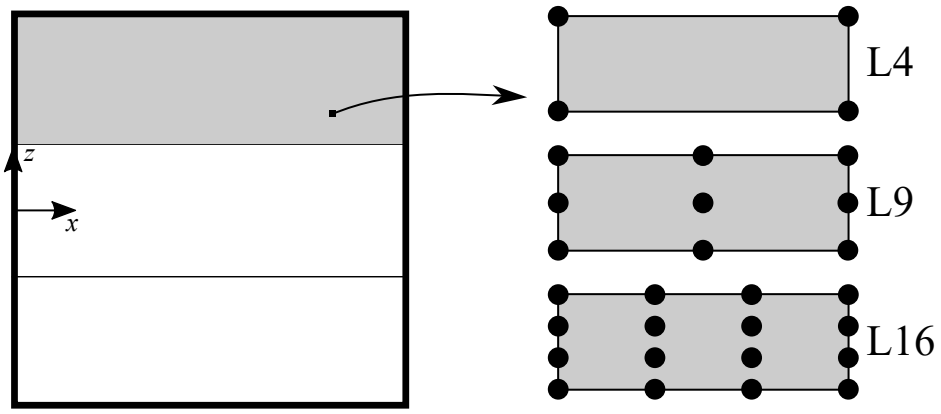

Fig. 5.14 Compact cross-section approximation.

Figure 5.15 reports the linear and nonlinear static curves for the [0°/90°/0°] stacking sequence, where the transverse displacement of the loading point is calculated. Then, the percent difference between the two solutions is shown in Fig. 5.15(b). The results show greater values for higher order theory and the L9 and L16 curves show very close solutions. Despite the results shown for a compact isotropic case, Fig. 5.15 proved that the values of the linear and nonlinear differences are not negligible when composite materials are taken into account. For this reason, linear analyses could not be enough for an accurate evaluation of the given problem. For the L4 kinematics the percentage difference value is near 5%. The same conclusions can be discussed from the [0°/45°/0°] lamination, whose result is reported in Fig. 5.16. The differences reaches 20% for the L16 approximation between linear and nonlinear solutions.

The next analysis dealt with a thin-walled channel-section beam. The geometry is shown in Fig. 5.17, and w=h, h/t = 10 and length-to-side ratio is 20. The material adopted is orthotropic, with E_1=155 GPa, E_2 =E_3 =15.5 GPa, $\nu_{12} = 0.25$, G_{12} =G_{13} = 9.3 GPa and G_{12} =G_{23} = 7.75 GPa. Two different stacking sequences were considered, [0°/90°/0°] and [0°/45°/0°]. Three different higher-order models were used to define the channel-section and to approximate the displacement field. In detail, as shown in Fig. 5.18, 18L4, 18L9 and 18L16 Lagrange polynomials were implemented. Increasing forces were applied as shown in Fig. 5.17, and in this scenario, static analysis using linear and nonlinear strain-displacement relations were performed, and the displacement of the point “A” along the x-axis and of the point “C” along the z-axis were calculated. Then, the difference between linear and nonlinear solutions was calculated.

In Fig. 5.19, both linear and nonlinear solutions are displayed, using the L4, L9 and L16 Lagrange polynomials. The percentage difference for the [0°/90°/0°] stacking sequence is shown too, along with some of the deformed configurations. It can be noticed that increasing

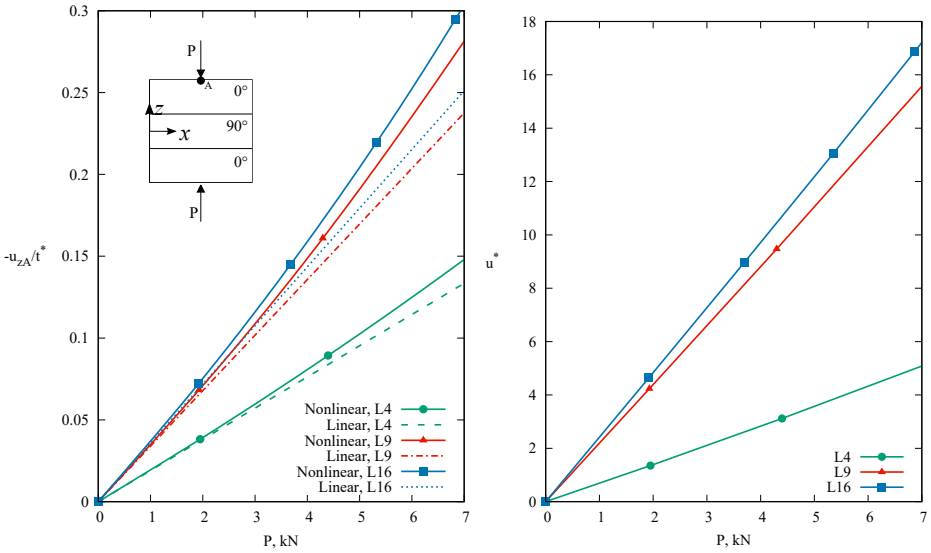

(a) (b)

Fig. 5.15 (a) Static linear and nonlinear equilibrium conditions for the transverse displacement of the loading point for the composite structure. (b) Percentage difference. Percentage difference $u^* = \dfrac{u_{nl} - u_l}{u_{nl}} \times 100$. $t^* = \dfrac{t}{3}$. [0°/90°/0°].

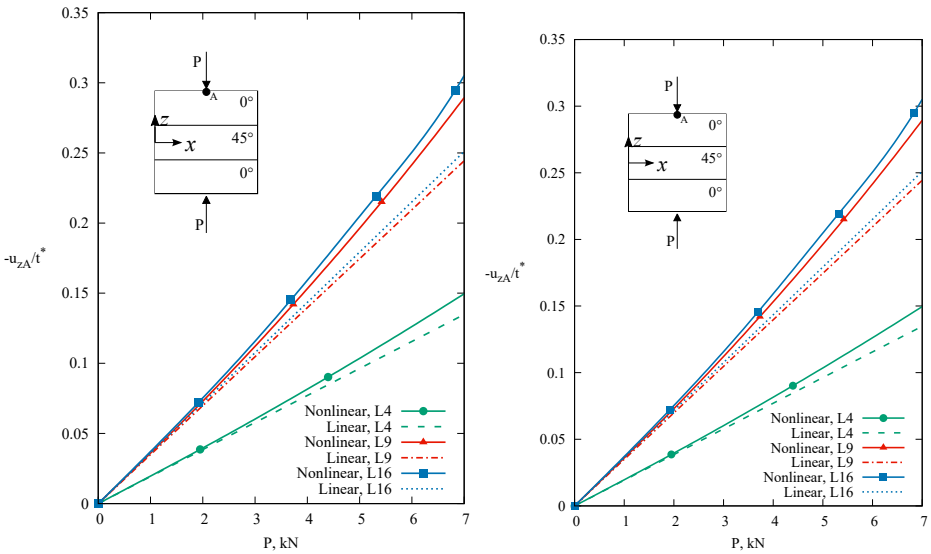

(a) (b)

Fig. 5.16 (a) Static linear and nonlinear equilibrium conditions for the transverse displacement of the loading point for the composite structure. (b) Percentage difference. Percentage difference $u^* = \dfrac{u_{nl} - u_l}{u_{nl}} \times 100$. $t^* = \dfrac{t}{3}$. [0°/45°/0°].

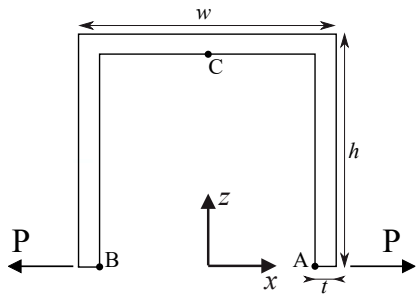

Fig. 5.17 Geometry and loading conditions of the composite thin-walled beam.

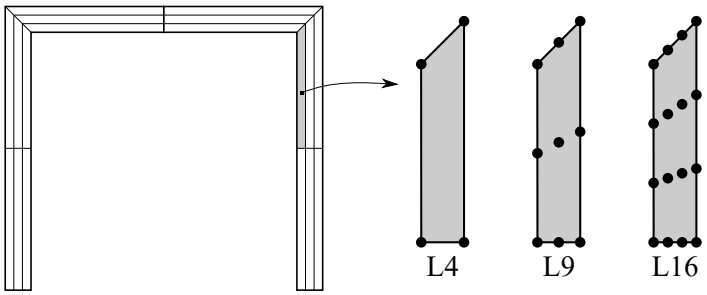

Fig. 5.18 Kinematic approximations of the thin-walled composite structure.

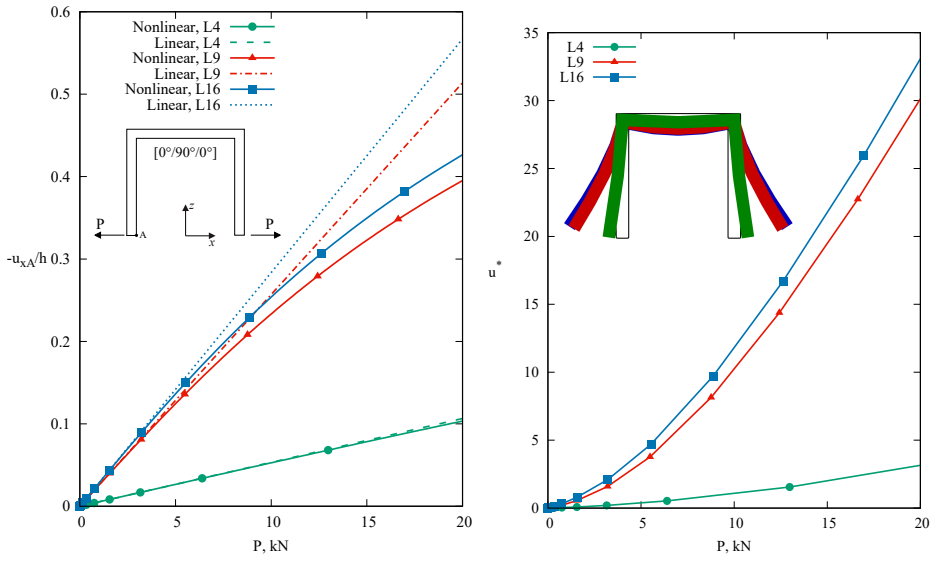

(a) (b)

Fig. 5.19 (a) Static linear and nonlinear equilibrium conditions for the lateral displacement of the "A" point for the composite structure. (b) Percentage difference. Percentage difference $u^* = \dfrac{u_{nl} - u_l}{u_{nl}} \times 100$.

			*L*4			*L*9			*L*16
P	$-u_{xl}$/h	$-u_{xnl}$/h	$e_{\%}$	$-u_{xl}$/h	$-u_{xnl}$/h	$e_{\%}$	$-u_{xl}$/h	$-u_{xnl}$/h	$e_{\%}$
5.000	0.027	0.027	-0.39%	0.128	0.124	-3.300%	0.142	0.136	-4.100%
10.00	0.053	0.053	-1.09%	0.257	0.232	-10.25%	0.284	0.253	-11.81%
15.00	0.080	0.078	-2.01%	0.385	0.321	-19.48%	0.425	0.348	-21.76%
20.00	0.106	0.103	**-3.15%**	0.514	0.394	**-30.12%**	0.567	0.425	**-33.08%**

Table 5.3 Values of the lateral displacement and percentage difference of the composite [0°/90°/0°] cross-section, for various kinematic theories.

the external loading, the percentage difference increases as well. The greater the order of the beam theory is, the higher the differences between linear and geometrical nonlinear analyses are. This behavior can be assessed in Table 5.3, where some values of both linear and nonlinear solution are reported. The highest values of the difference percentages are reported in bold in the table, going from 3.15 mm for a first order beam model to 30.12 mm for a quadratic beam model and to 33.08 mm for a cubic theory. It is clear that the adoption of geometrical nonlinear relations is required for thin-walled problems. Figure 5.20 shows the results of the same analyses for the point "C". A hardening behavior of the nonlinear analysis can be noticed until a certain load, and then a softening trend appears. For example, for the cubic interpolation mathematical model, the percentage difference changes the sign after a load P=16 kN, as clearly reported in Table 5.4. The same trend is evident for the L9 solution, but in this case, the load of the changing trend is higher, near 20 N. Finally, the L4 solution leads to a hardening behavior.

			*L*4			*L*9			*L*16
P	$-u_{xl}$/t	$-u_{xnl}$/t	$e_{\%}$	$-u_{xl}$/t	$-u_{xnl}$/t	$e_{\%}$	$-u_{xl}$/t	$-u_{xnl}$/t	$e_{\%}$
5.000	0.046	0.046	0.88%	0.177	0.184	3.95%	0.197	0.203	2.85%
10.00	0.092	0.093	1.56%	0.353	0.369	4.50%	0.394	0.404	2.60%
15.00	0.138	0.141	2.77%	0.530	0.544	2.79%	0.592	0.592	0.25%
20.00	0.184	0.189	**2.47%**	0.706	0.702	**-0.35%**	0.789	0.761	**-3.39%**

Table 5.4 Values of the transverse displacement and percentage difference of the composite [0°/90°/0°] cross-section, for various kinematic theories.

As far as the [0°/45°/0°] cross-ply is concerned, Fig. 5.21 shows the percentage difference between linear and nonlinear solutions, along with both static solutions for point "A". As noticed in the previous case, it can be observed that the percentage difference increases with the external loading. The values of the percentage difference are greater than the ones of the [0°/90°/0°] stacking sequence case. Table 5.5 reports values of the displacement for points point "A" and in bold are quoted the highest values. For the point "A", they go from 1.99 for

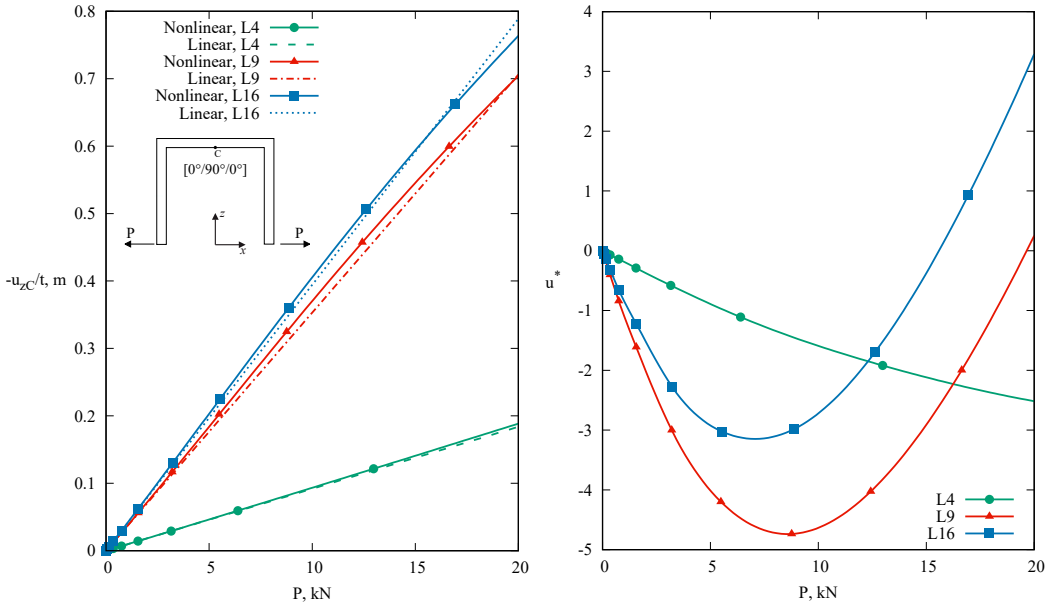

(a) (b)

Fig. 5.20 (a) Static linear and nonlinear equilibrium conditions for the transverse displacement of the loading point for the composite structure. (b) Percentage difference. Percentage difference $u^* = \dfrac{u_{nl} - u_l}{u_{nl}} \times 100$.

a first order beam model to 25.30 for a quadratic beam model and to 29.63 for a cubic theory. It results evident that for the thin-walled problems, the adoption of geometrical nonlinear relations is needed. Finally, the z-displacement of the point "C" is analyzed as well. The curves and values are reported in Fig. 5.22 and Table 5.6, respectively and they show a similar trend of those of the "C" point for the [0°/90°/0°] stacking sequence case.

	L4			*L9*			*L16*		
P	$-u_{xl_A}$/h	$-u_{xnl_A}$/h	$e_{\%}$	$-u_{xl_A}$/h	$-u_{xnl_A}$/h	$e_{\%}$	$-u_{xl_A}$/h	$-u_{xnl_A}$/h	$e_{\%}$
5.000	0.026	0.026	0.88%	0.128	0.127	-1.15%	0.143	0.141	-1.91%
10.00	0.051	0.051	-0.24%	0.257	0.240	-6.89%	0.287	0.263	-8.84%
15.00	0.077	0.076	2.77%	0.385	0.397	-15.26%	0.430	0.362	-18.47%
20.00	0.103	0.101	**-1.99%**	0.514	0.409	**-25.30%**	0.574	0.442	**-29.63%**

Table 5.5 Values of the lateral displacement and percentage difference of the composite [0°/45°/0°] cross-section, for various kinematic theories.

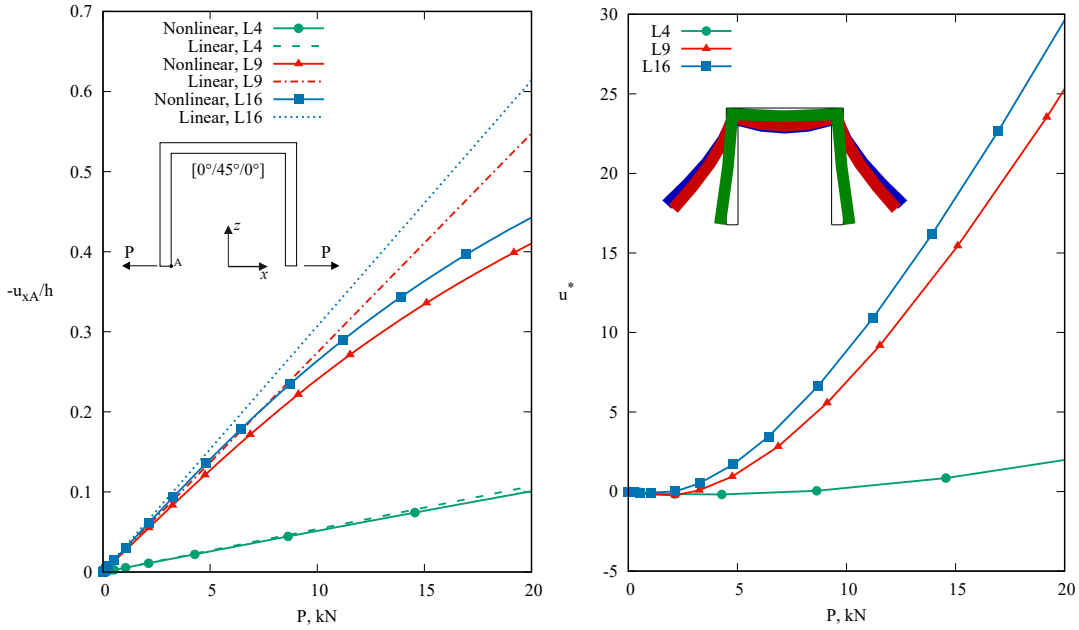

(a) (b)

Fig. 5.21 (a) Linear and nonlinear equilibrium solutions for the lateral displacement of the point "A" for the composite structure. (b) Percentage difference.

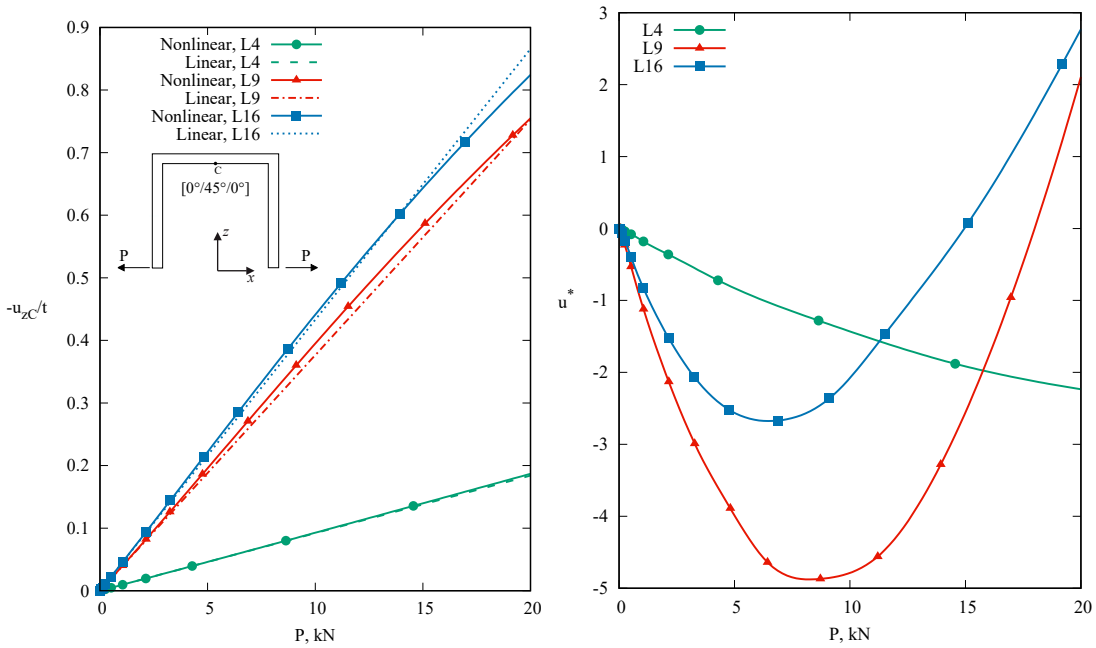

(a) (b)

Fig. 5.22 (a) Linear and nonlinear equilibrium solutions for the transverse displacement of the point "A" for the composite structure. (b) Percentage difference.

	L4			*L9*			*L16*		
P	$-u_{xl_C}$/t	$-u_{xnl_C}$/t	$e_{\%}$	$-u_{xl_C}$/t	$-u_{xnl_C}$/t	$e_{\%}$	$-u_{xl_C}$/t	$-u_{xnl_C}$/t	$e_{\%}$
5.000	0.046	0.046	0.81%	0.188	0.196	3.97%	0.216	0.222	2.54%
10.00	0.091	0.093	1.42%	0.376	0.395	4.75%	0.432	0.440	1.90%
15.00	0.137	0.140	1.91%	0.564	0.583	3.32%	0.648	0.642	-0.85%
20.00	0.183	0.187	**2.21%**	0.752	0.754	**0.35%**	0.865	0.824	**-4.90%**

Table 5.6 Values of the transverse displacement and percentage difference of the composite [0°/45°/0°] cross-section, for various kinematic theories.

5.5.3 Large deflection and post-buckling of cantilever beams with cross-section nonlinearities

The nonlinear behavior of a cantilver beam is considered as first investigation case. The beam is made of a material with Young modulus E equal to 75 GPa and Poisson ratio ν = 0.33. The structure is shown in Fig. 5.23(a), and it is the same as the one analyzed in the Section 2. The proposed technique adopts a different approximation, and in particular, the length of the beam is treated as the cross-section of the model. Quadratic and cubic theories are adopted for the cross-section, as shown in Fig. 5.23(b). Table 5.7 describes the transverse displacement at the free edge, changing the aspect ratio and the loading condition. Given the convergence of Tab. 5.7, a cubic element along with a quadratic (10L16) theory are used for the following analyses. In this thesis, convergence results are obtained with 20B4 finite elements and a nine-points Lagrange polynomial for the cross-section. Given the present approach with only section nonlinearities, convergence results are evaluated with a DOFs gain. Figure 5.24(b) describes the equilibrium condition for a bending load and the results of the present 1D model are compared with those from linear and nonlinear reference solutions. Clearly, the proposed approach, taking into account only cross-section nonlinearities, can evaluate the large deflections of cantilever beams, in agreement with reference results. The

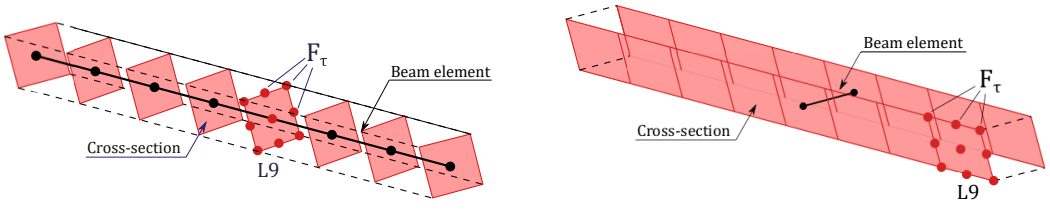

(a) Classical beam model (b) Present beam model

Fig. 5.23 Classical and present modeling tecnhiques for the static analysis of the clamped-free structure undergoing transverse and axial loadings.

post-buckling behaviour of the same beam structure as considered in the previous analysis

case, is addressed. Fig. 5.24 reports the transverse displacements versus the normalized loading P. Also, in this case, the post-buckling trend is comparable with the reference.

Table 5.7 Transverse displacement of the compact cantilever beam for $\frac{PL^2}{EI} = 3$. Ref. [144], $u_z/L = 0.599$ with 1647 DoFs. Number of DoFs in brackets.

Beam elements	**Cross-section elements**						
Reference	**1L9**			**1L16**			
5B4	$0.594^{(432)}$			$0.594^{(768)}$			
10B4	$0.597^{(837)}$			$0.597^{(1488)}$			
20B4	$0.599^{(1647)}$			$0.599^{(2928)}$			
Present approach	**10L9**	**15L9**	**20L9**	**9L16**	**10L16**	**15L16**	**20L16**
1B2	$0.567^{(378)}$	$0.585^{(558)}$	$0.589^{(738)}$	-	$0.591^{(744)}$	$0.592^{(1104)}$	$0.592^{(1464)}$
1B3	$0.573^{(567)}$	$0.592^{(837)}$	$0.597^{(1107)}$	$0.597^{(1008)}$	$0.599^{(1116)}$	$0.599^{(1656)}$	$0.599^{(2196)}$
1B4	$0.573^{(756)}$	$0.592^{(1116)}$	$0.597^{(1476)}$	-	$0.598^{(1488)}$	$0.599^{(2208)}$	$0.599^{(2928)}$

5.5.4 Thin-walled U-shaped structures wih cross-section nonlinearities

This section focuses on the investigatation of the geometrical nonlinear effects within a cantilever thin-walled channel-section beam. In Fig. 5.25 the structural properties are described, with w = 0.1 m, h = 0.1 m, and t = 0.01 m. The beam has Young modulus equal to 75 GPa and Poisson ratio $\nu = 0.33$. The load P is applied in the free side of the cross-section, as depicted in figure 5.25. As far as the finite element approximation is concerned, the structure is discretized by using a B4 beam element. Three cross-section discretizations are employed to approximate the displacement field, and they differ for the number of lagrangian domains for the section discretization. The approximation 5.26(a) adopts 8 LEs, the discretization 5.26(b) uses twice the elements on each side and the discretization 5.26(c) is the most refined one. Bilinear, quadratic and cubic Lagrange polynomials are used for the discretization of each cross-section, as described in Fig. 5.26(d). For each kinematic theory, both linear and nonlinear solutions were evaluated. The static curves are presented in Fig. 5.27(a), 5.28(a) and 5.29(a), where the lateral displacement of point A is calculated. In Fig. 5.27(a) the equilibrium solutions for L4, L9 and L16 elements are shown with the discretization 5.26(a). As predictable, with L4 model, the structure has a higher stiffness that leads to decreased displacements. Moreover, the nonlinear trend is similar to the linear one. When higher-order theories are used, the differences between linear and nonlinear solutions are not negligible. The percent difference between those solutions is shown in Fig. 5.27(b). A bilinear description is not accurate, thus the cases with L4 elements were not adopted for

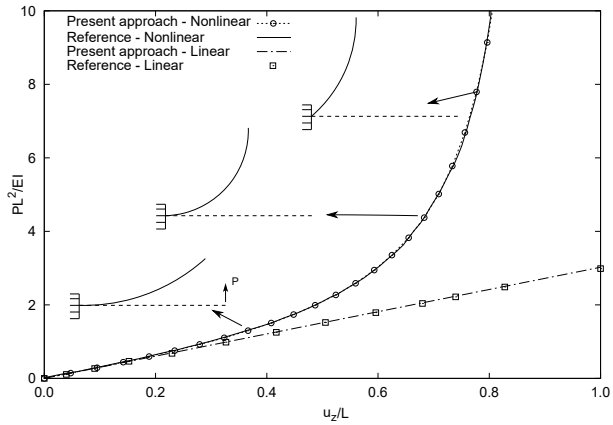

(a) Equilibrium solution of the cantilever beam subjected to bending loading. Reference solution from Ref. [144].

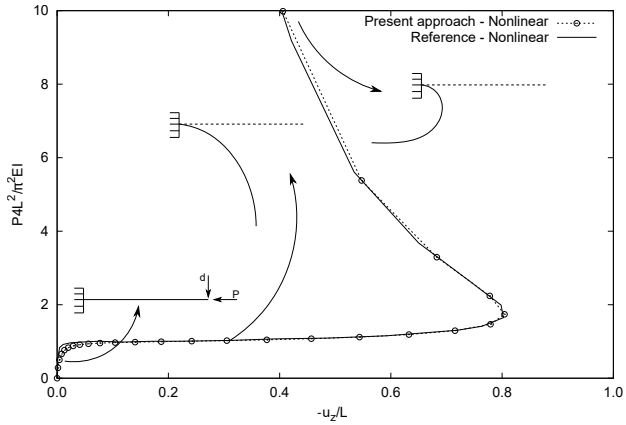

(b) Equilibrium solution of the cantilever beam subjected to compressive loading. Reference solution from Ref. [144].

Fig. 5.24 Static nonlinear solutions of the cantilever beam.

the following analyses. In Figs. 5.28(a) and 5.29(a) the L9 and L16 solutions are similar for both discretizations. Further analyses on computational costs show that the approximation 5.26(c) has similar results as those from the 5.26(b) set. Thus, the case 5.26(b) guarantees the best compromise between DOFs gain and accuracy. Taking the displacements of the most refined approximation with L16 elements as the reference solution, the percent difference is evaluated and listed in Tab. 5.8. The second L16 discretization elements leads to negligible error, and the computational gain is evident. MAPE (Mean Absolute Percentage Error) indicates the accuracy of a approximation compared to the reference L16 one. A 3D model is built in Nastran, with 1695 3D HEXA elements and 5095 DoFs. The percent difference between CUF and 3D model is negligible, but the proposed technique uses less than 40% of the DoFs.

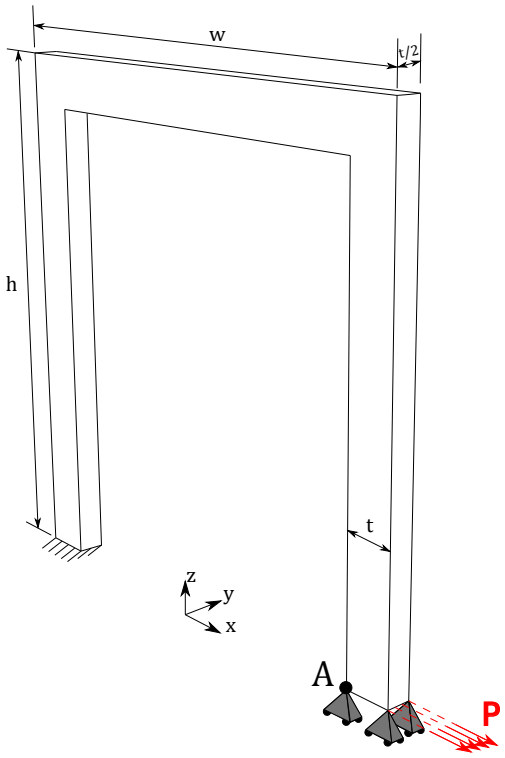

Fig. 5.25 Geometry, loading and boundary condition of the thin-walled beam.

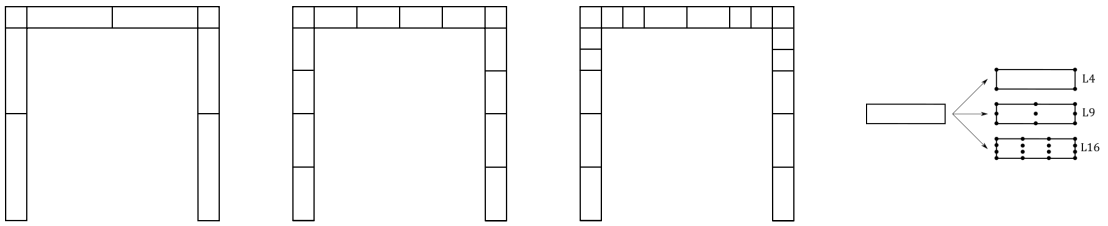

(a) LE model 1 (b) LE model 2 (c) LE model 3 (d) LE polynomials

Fig. 5.26 Approximations of the cross-section of the thin structure.

The next study case analyzes the capability of many nonlinear strain assumptions in the static behavior of thin structures. The approximation 5.26(b) elements is used along with cubic interpolations to evaluate the three displacement field. Different types of structures are considered, as described in Fig. 5.30. The results of the static response analysis based on the proposed technique are shown in Fig. 5.31, where some of the deformed configuration are displayed. In general, the same approach as the one applied in Chapter 4 is adopted hereafter, and different nonlinear approximations are adopted. Black dots in the matrixes in Fig. 5.31 shows that the nonlinear term of the Green-Lagrange matrix is included in the correspondent analysis. The nonlinear set 1 shows that the nonlinearities in the y direction do not show

Table 5.8 Values of errors of the static solution compared to the L16 reference one. Nastran model: 1695 HEXA elements.

	Discretization 1		**Discretization 2**		**Discretization 3**		**3D***
P [kN]	**L9**	**L16**	**L9**	**L16**	**L9**	**L16 - u_x [mm]**	**HEX elements**
1	-10.29%	-1.91%	-3.07%	-0.31%	-2.46%	4.39	0.68%
5	-13.04%	-2.08%	-3.33%	-0.30%	-2.68%	39.77	0.83%
25	-16.56%	-2.86%	-3.78%	-0.29%	-3.17%	115.37	0.75%
50	-13.66%	-3.01%	-3.32%	-0.02%	-2.96%	141.73	2.26%
100	-9.82%	-2.46%	-2.61%	0.00%	-2.18%	159.97	2.27%
500	-5.77%	-0.65%	-0.37%	-0.16%	-0.36%	210.81	1.19%
1000	-0.65%	0.11%	0.16%	-0.12%	0.23%	234.63	-
1500	-0.46%	0.06%	0.05%	-0.12%	0.18%	254.30	-
2000	-0.40%	-0.04%	-0.06%	-0.21%	0.02%	271.39	-
MAPE	-7.85%	-1.43%	-1.81%	-0.17%	-1.49%	-	1.33%
DoFs	612	1200	1044	2064	1332	2640	5085

any impact in the static nonlinear behavior of the structure. In fact, its trend is the same as the full nonlinear solution. The curve 2 trend equals to the case in which $(\partial_x \partial_z)$ terms are involved. Indeed, the shear effects have no significant influence on the static solution of the structure. The cases from 3 to 9 show some other nonlinear approximations. They show a general hardening behavior, except curves 4 and 7 which indicate a softening solution. The comparison between the matrixes shows that $(\partial_x u_x)^2$ and $(\partial_z u_z)^2$ have no any influence on the accuracy of the static solution. The curve number 4 leads to a nonlinear solution where only parameters $(\partial_x u_z)^2$ and $(\partial_z u_x)^2$ included. Clearly, the distribution is similar as the full nonlinear one. The cases 8 and 9, with only $(\partial_x u_z)^2$ or $(\partial_z u_x)^2$ included, demonstrate a linear solution. In Fig. 5.32 the deformed configuration for three different multiple arches structure are depicted for the nonlinear approximations 1, 5 and 7. Increasing the total length of the structures, the differences between a full nonlinear solution and a reduced one are greater. The displacements of points A and B for different geometries at P = 20 kN are shown in Tab. 5.9. The shortest structure leads to lower displacement, compared to its length. Indeed this geometry shows a greater stiffness compared to the other cases. Regarding the point A, the displacement is greater as the length of the structure increases. The differences between a full and approximated nonlinear analysis increase as the number of arches increase. However, the difference between a full and a reduced nonlinear analysis changes when other points of the structure are considered. This behavior does not allow to univocally establish the capability of a nonlinear approximation when only one point of the structure is considered. Clearly,

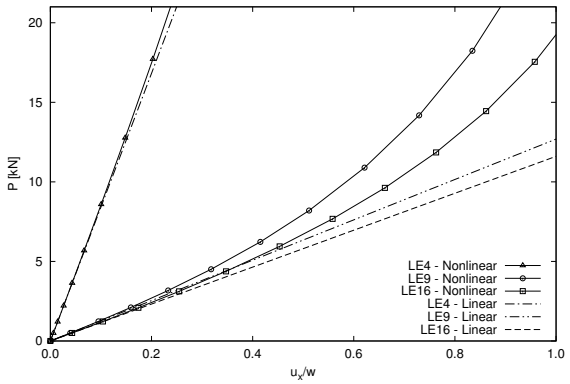

(a) Equilibrium curves of the thin-walled cross-section.

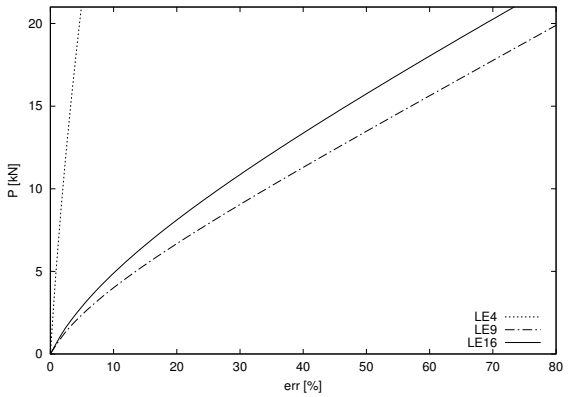

(b) Percentage difference between linear and nonlinear analyses.

Fig. 5.27 Nonlinear static solution and percentage difference with linear solution of the thin structure shown in 5.26(a).

a periodicity of the displacements for the different structures arises. In fact, the number of arches influence the displacement of point A. From the Tab. 5.9 it is possible to note that the displacements of the two arches and five arches are twice and five times the single arch one. Further comparisons are evaluated adopting 3D models analysed with Nastran. As previously shown the 3D models of more complex structures show a greater amount of DoFs necessary for the solution with the same accuracy. In Fig. 5.33, the static solutions for a axial load are reported. For these studies, the considered geometry is depicted in Fig. 5.30(b). The structure is subjected to an axial load at the same point as in the previous cases. Solutions 3, 6, 7, and 9 show a hardening behavior compared to the full nonlinear case. They are described by the missing of the term $(\partial_x u_x)^2$, therefore not including the variations along the x-axis leads to underestimate the deformation of the structure. Curves 5 and 8 show a softening behavior and they lead to a considerably greater deformation compared to the full case. Cases 2 and 4

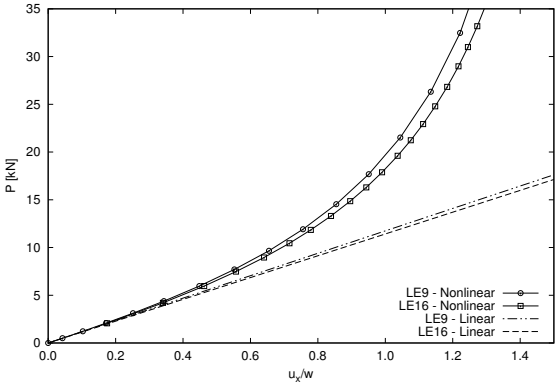

(a) Equilibrium curves of the thin-walled cross-section.

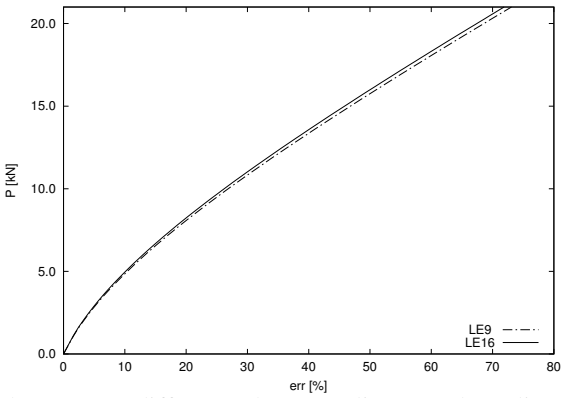

(b) Percent difference between linear and nonlinear analyses.

Fig. 5.28 Nonlinear static solution and percentage difference with linear solution of the thin structure shown in 5.26(b).

show an accurate description of the behavior of the geometry, and the trends are comparable to curve 1. Case 7 including $(\partial_x u_z)^2$ and $(\partial_z u_x)^2$ terms is not enough to accurately evaluate the nonlinear behavior of the structure. This phenomenon is due to the higher length of the structure, as demonstrated in the previous analysis. Parameter $(\partial_x u_x)^2$ is also demanded for a compression load analyses. Clearly, the set of nonlinear parameters described by curve 4 shows an hardening behavior until $-u_x/x = 1,7$, and then softening. Therefore it is important to consider the proper configuration of the nonlinear matrix according to which load level the structure is wanted.

Finally, a structure very similar to that described in Fig. 5.25 is analyzed, the edges were rounded. In Fig. 5.34. the geometry of the approximation with 1 and 2 arches is presented, with R = 0.03 m. The methodology described in this thesis, allows the development of a computational model by only describing the cross-section and no ad-hoc theory is demanded

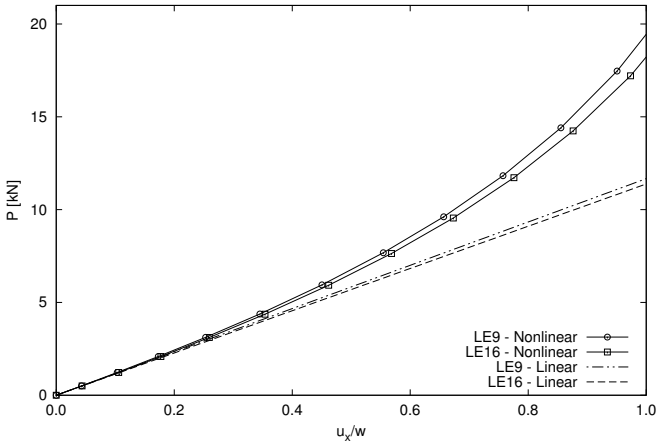

(a) Equilibrium curves of the thin-walled cross-section.

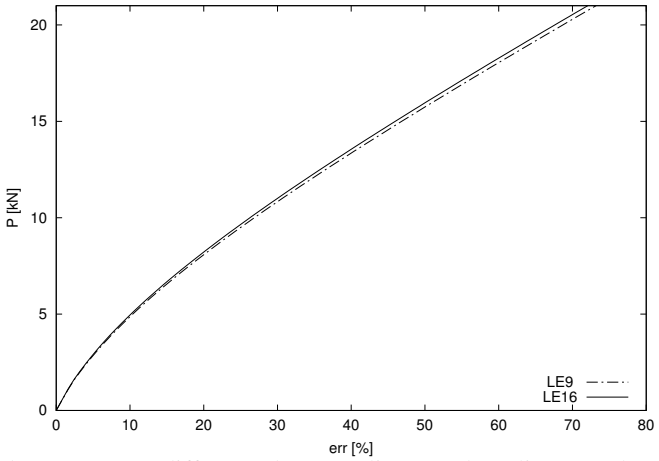

(b) Percentage difference between linear and nonlinear analyses.

Fig. 5.29 Nonlinear static solution and percentage difference with linear solution of the thin structure shown in 5.26(c).

for the modelling of the curved part of the structure. In Fig. 5.35 the equilibrium curves for different sets of parameters of the nonlinear matrix for 1 arch configuration are shown. It is interesting to note that curve 4 follows the trend of case 1 almost perfectly, adding the parameter $(\partial_z u_z)^2$ gives a greater evident error. This indicates that the different parameters have a very different influence on the nonlinear behaviour of the structure, and the addition of one or more parameters can lead to a lower accuracy of the solution. The equilibrium curves for 2 arches configuration are shown in Fig. 5.36. Curve 4 represents the configuration most similar to the full nonlinear matrix case and, also in this case, the addition of the parameter $(\partial_z u_z)^2$ compromises the accuracy of the solution. By comparing the trends of curve 7 between the one and two-arch configurations, it is possible to note that for the structure with

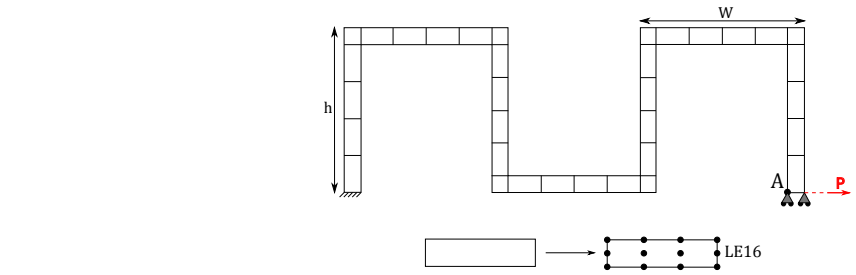

(a) 2 arches

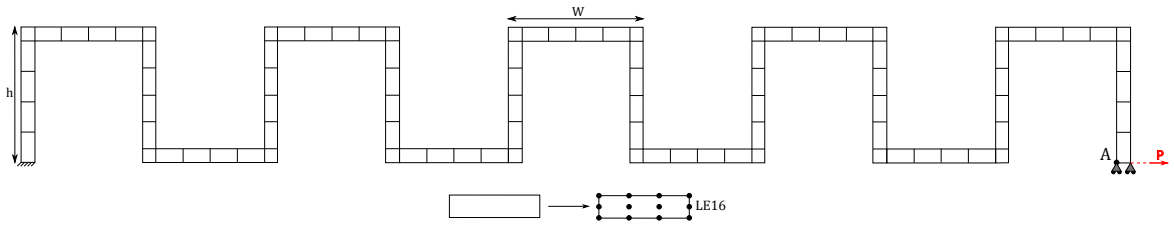

(b) 5 arches

Fig. 5.30 Description of multiple arches thin structure (geometry, loading and approximation).

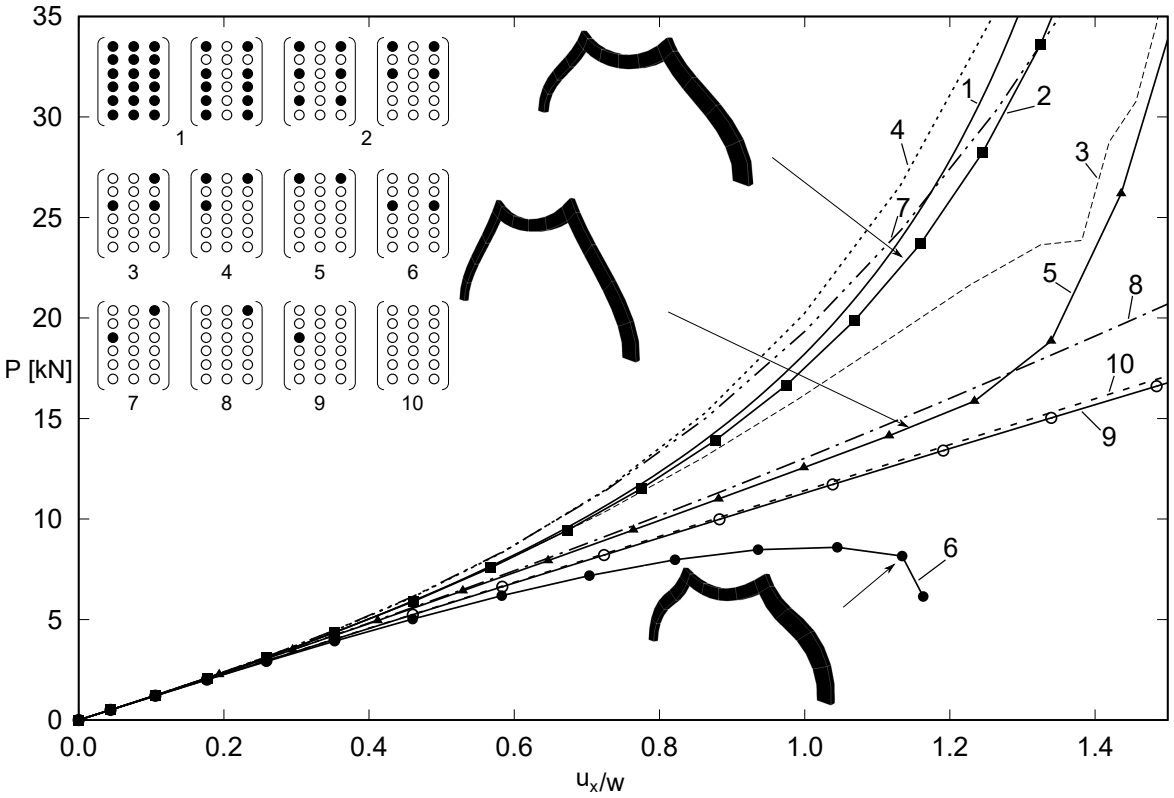

Fig. 5.31 Nonlinear static solution of the thin structure with one arch adopting different nonlinear theories.

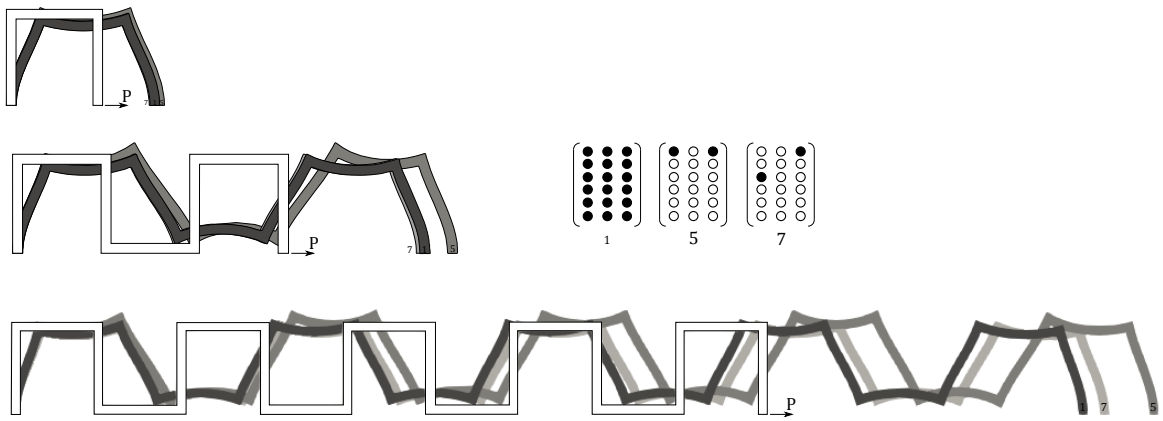

Fig. 5.32 Structural deformation of the thin structure with multiple arches. $P = 8$ kN.

Table 5.9 Values of lateral displacement of the full nonlinear solution, nonlinear approximation and 3D Nastran model.

	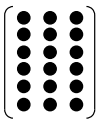	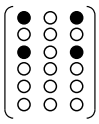	**3D* - HEXA**	**DoFs**
	105.32 mm	1.49 %	0.21%	CUF: 2640 3D: 5085
	118.58 mm	3.75 %	1.13%	CUF: 4944 3D: 11565
	118.93 mm	3.35 %	0.77%	CUF:13584 3D: 31005
	207.82 mm	4.28 %	9.67%	-
	535.74 mm	6.33 %	11.18%	-

a greater span, the approximation errors are higher. As in the previous case, this phenomenon is probably due to the higher displacements detected for the structure with two arches, which leads to less accuracy of results.

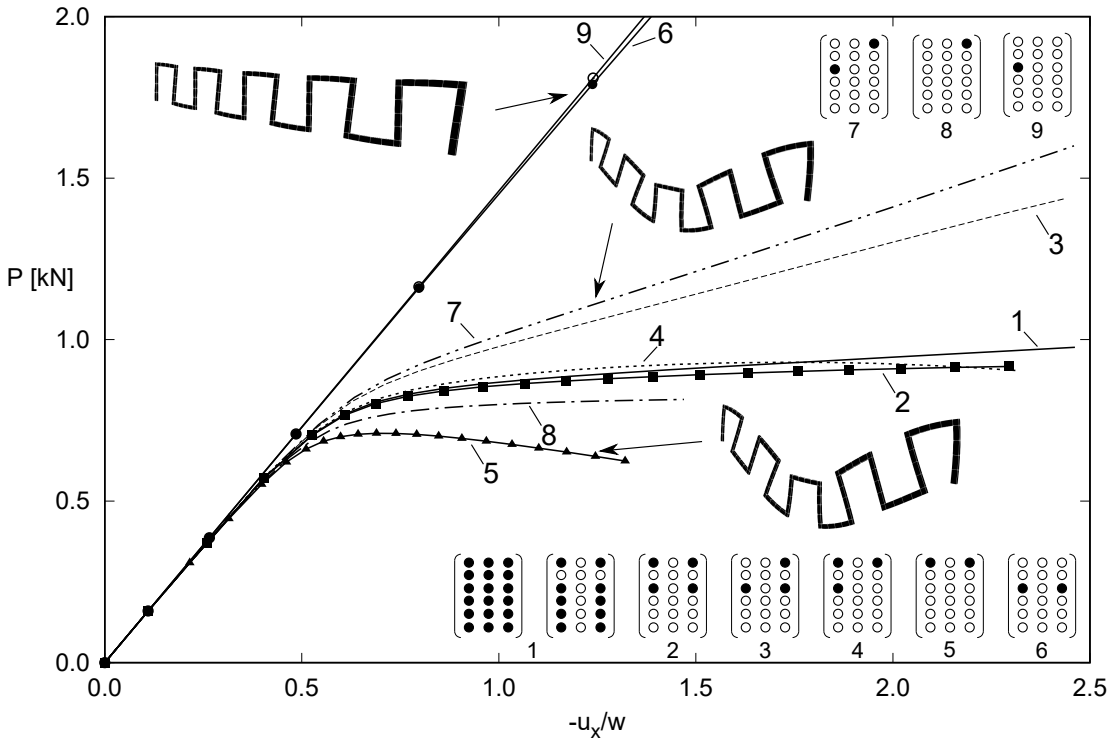

Fig. 5.33 Nonlinear static solution of the thin structure with five arches adopting different nonlinear theories. Compression case.

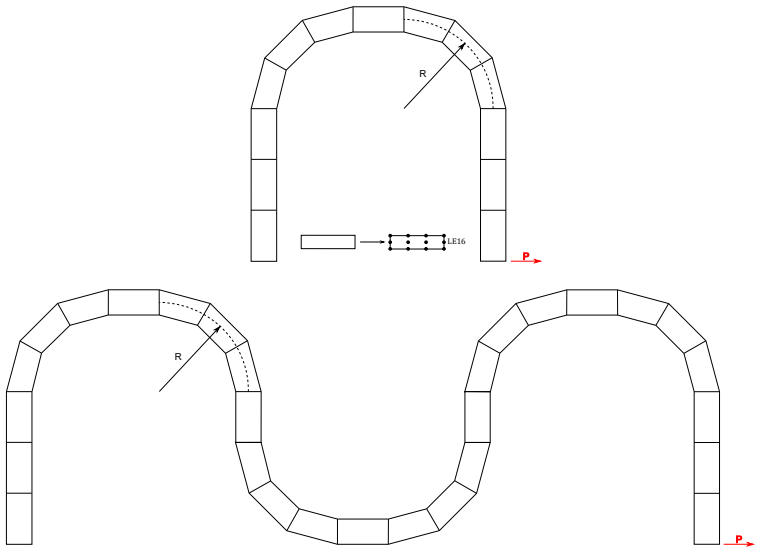

Fig. 5.34 Description of multiple arches thin curved structure (geometry, loading and approximation).

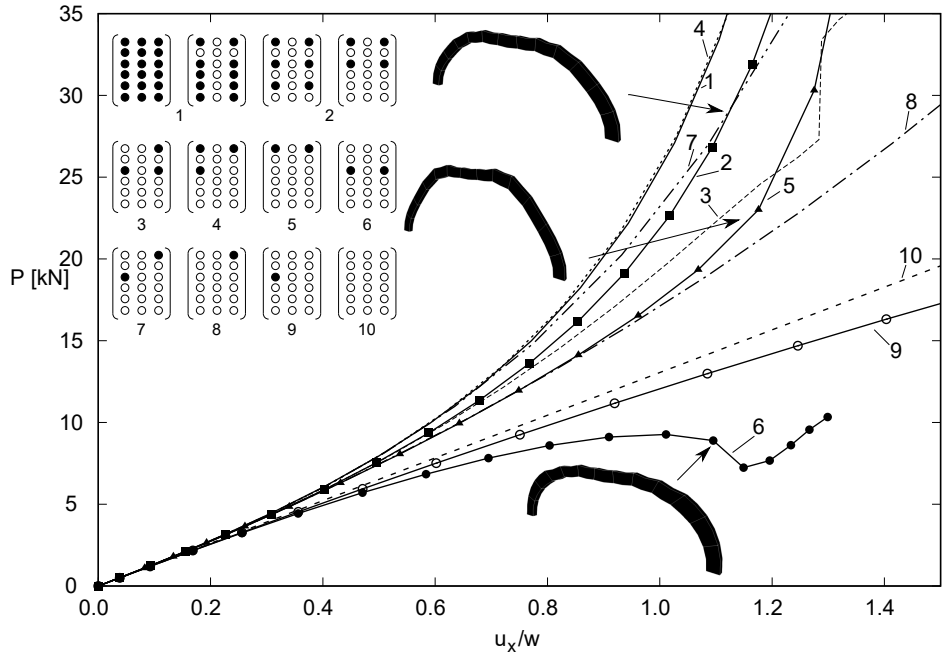

Fig. 5.35 Nonlinear static solution of the thin structure with curved arch adopting different nonlinear theories. Compression case.

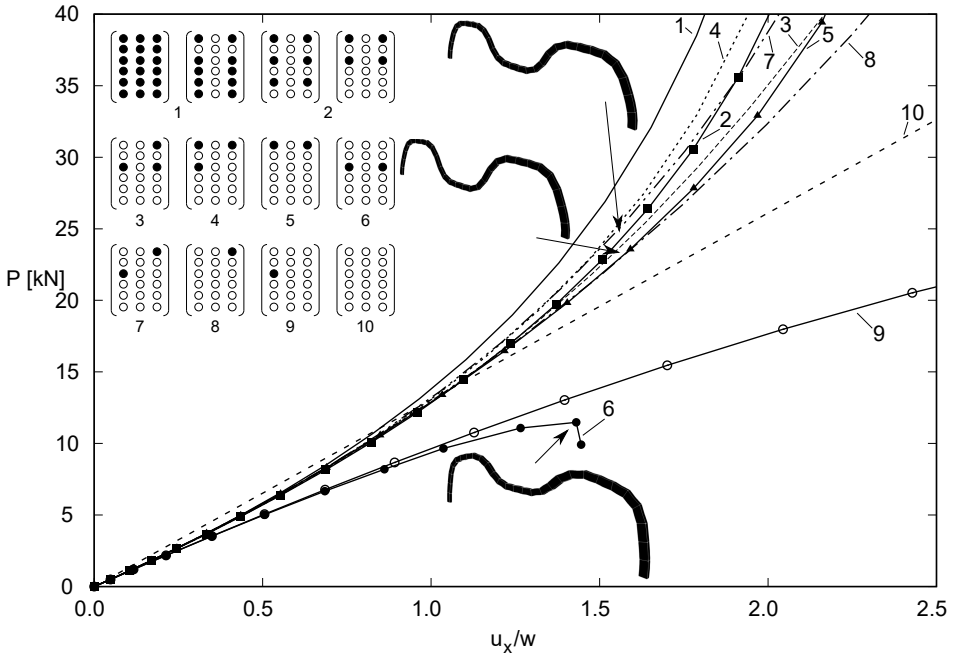

Fig. 5.36 Nonlinear static solution of the thin structure with two curved arches adopting different nonlinear theories. Compression case.

Chapter 6

Evaluation of 3D stress distributions of beams and shells in a large deflection field

6.1 Stress evaluation models

In the literature, most of the works make use of the nonlinear von Kármán approximation. Furthermore, an Updated Lagrangian (UL) approach is often used with the assessment of corotational Cauchy stresses [15]. Stresses referred to the deformed configuration have a simpler physical interpretation because equilibrium equations express the balancing of internal stresses of the deformed state.
Pai [146] described how the total Lagrangian formulation is typically employed in geometrical nonlinear analyses because the structure returns to its original mechanical configuration, once unloaded. When dealing with nonlinear analyses, strain and stress formulations must be work-conjugate. Thus, a total Lagrangian approach is more used than a updated lagrangian formulation, since the accuracy of each equilibrium condition does not rely on the previous state. In addition, the displacements evaluated, strains and, consequently, stresses do not need any coordinate transformation. For this reason, the Green–Lagrange strains and the second Piola-Kirchhoff stresses are perfectly formulated in the total Lagrangian approach. In addition, in order to develop stress analyses of geometrical nonlinear components, Second Piola-Kirchhoff stresses are sometimes transformed into true Cauchy's stresses, which are physically meaningful. Since the deformed configuration of various problems, especially those involving solids, is unknwon, it is not convenient to deal with stress tensor, which is expressed in terms of spatial coordinates. In some cases, it is needed to work with stress ten-

sors that is referred to the undeformed configuration. The goal of this chapter is to accurately evaluate the 3D stress distributions of composite shells in the large displacement/rotation field.

6.2 Node-dependent kinematic model for the stress distributions evaluation

When higher-order phenomena arise, an accurate evaluation of the stress distribution may be necessary, so that theories based on classical approaches might be inappropriate and lead to wrong conclusions. For this reason, refined kinematics were suggested by researchers.
Stephen and Levinson [172] developed a higher-order theory starting from the Timoshenko beam equation and taking into account the shear curvature, through the introduction of new coefficients. As further examples of higher-order beam models proposed in the past, Vlasov [183] introduced warping functions to capture the deformations of beam cross-sections. This approach found a great success between scientists, see the works by Ambrosini *et al.* [11], Mechab *et al.* [129] and Friberg [67], who made use of warping functions for thin-walled structures. A combination of the refined Vlasov model and the classical Euler-Bernoulli model was adopted by Kim and Lee [97] to analyze thin-walled beams made of functionally graded materials. The so-called Generalized Beam Theory (GBT) was suggested by Schardt [163]. This theory allows the displacement field to be expressed as a linear combination of cross-section deformation modes. GBT found many applications in the literature, for example by Peres *et al.* [148] for the analysis of curved thin-walled beams, and by Silvestre [165] for buckling problems. GBT was also adopted for the analysis of laminated materials, as presented by Silvestre and Camotim [166, 167].
Particular attention must be given to local phenomena when structures are subjected to large deformation, e.g. large displacements and large rotations. In fact, for an accurate design of structures undergoing extreme loading conditions, a geometrical nonlinear analysis must be carried out. The contributions of scientists about the nonlinear analysis of 1D structures are uncountable. Most of the geometrical nonlinear models developed in the past are based on the Timoshenko beam theory, see, for example, Refs. [147, 71, 131]. The works by Hodges [79] and Chia [45] presented an overview of the geometrically nonlinear behaviour of composite beams and plates, respectively. The literature of works about the behaviour of composite structures in the large displacement and rotation field is vast, indeed. As an example, the work by Zhang and Kim [191] is mentioned. It proposes a quadrilateral plate element for the geometrical nonlinear analysis of laminated composite plate. The model is based on FSDT

and Foppl-von Kármán geometrical nonlinearities, within a total Lagrangian approach. With the same assumptions, Zhang and Liew [190] analyzed the geometrical nonlinear behaviour of carbon nanotube reinforced composite plates. In many real applications, local phenomena and large cross-sectional deformations occur in particular areas of the structure, for example, in the nearby of external loads or constraint conditions. In such cases, it would be needed to build a model with variable kinematics, namely, capable of refining only the portions of the structure which undergo high deformation or rotation. In this way, the accuracy is still guaranteed, with a drastic decrease in the number of degrees of freedom and, subsequently, of the computational cost.

When models with different kinematics have to be coupled, the continuity of the displacements between the two regions has to be guaranteed. The issue of coupling incompatible structural models was widely investigated in the modern scientific literature. The Arlequin method was proposed by Biscani *et al.* [19, 20]. Wenzel [185] proposed an exhaustive state-of-the-art about this topic. For instance, the compatibility between different domains can be reached making use of the Lagrange multipliers, see for instance the work by Prager [151]. Another solution to this problem is the adoption of the global-local technique. Basically, this method consists of a multistep procedure, where, at first, a "global" analysis is carried out using a coarse mathematical model of the structure. Then, a refined FE model is applied separately in specific and more deformable subregions, and the compatibility is ensured by enforcing the continuity of the displacement in the interfacial or overlapping zones. Noor [137] proposed a review on the global-local approaches for the nonlinear analysis of composite panels. The global-local approach found application in many engineering fields. For instance, Hanganu *et al.* [74] applied this method in the analysis of civil structures, for an accurate evaluation of the damage within the structure.

The present Chapter intends to assess the benefits of adopting variable kinematics on composite beam structures in the geometrical nonlinear analysis. The proposed solution is the adoption of the Node-Dependent Kinematics (NDK) in a FE framework based on the Carrera Unified Formulation (CUF) [33, 29]. Thanks to the scalable nature of CUF, any arbitrary expansion of the FE unknowns can be used to achieve the desired theory of structures. In other words, the primary unknowns of a given problem (that, for a 1D problem, are the displacement along the beam axis), are expanded using arbitrary cross-section functions. The novelty of the NDK approach consists in adopting different expansion functions over the beam length for the kinematic description of the cross-sections. Since the Finite Element Method (FEM) is used for the beam axis approximation, no problems about coupling different expansion functions arise. NDK was used and validated in the past years by Carrera and

Zappino [37] and applied to composite structures [38, 117], 2D plate [34, 189] and shell problems [116].

6.3 Unified laminated beam element with node-dependent kinematics

Consider a generic one-dimensional (1D) laminated structure, as depicted in Fig. 6.1. A Cartesian coordinate system is adopted, in a way that x and z are the coordinates of the cross-section (in red) and y is orthogonal and lays along the beam axis (in blue). The three-dimensional (3D) displacement field $\mathbf{u}(x,y,z) = \left\{u_x\ u_y\ u_z\right\}^T$ as well as its variation (denoted by δ), is expressed in the framework of the Carrera Unified Formulation (CUF) and it is:

$$\begin{aligned} \mathbf{u}(x,y,z) &= F_\tau(x,z)\,\mathbf{u}_\tau(y), \qquad \tau = 1,2,....,M \\ \delta\mathbf{u}(x,y,z) &= F_s(x,z)\,\delta\mathbf{u}_s(y), \qquad s = 1,2,....,M \end{aligned} \tag{6.1}$$

where F_τ and F_s are the expansion functions of order M of the cross-section with coordinate x and z and $\mathbf{u}_s$ are the generalized displacement vector. The choice of F_τ and F_s and M is arbitrary and it is according to the theory adopted to model the structure. Many options are available for the expansion functions, i.e. Taylor polynomials [32], Chebyshev polynomials [64], Lagrange expansion [36] and Legendre polynomials [30], among the others. In this thesis both Lagrange and Taylor polynomials are adopted to discretize the displacement field over the cross-section and they allows the empolyment of the Layer-Wise (LW) and Equivalent Single Layer (ESL) approaches, respectively, as shown in Fig. 6.1.

6.3.1 Finite element approximation

As far as the displacements along the beam axis are concerned, the Finite Element Method (FEM) is adopted to approximate the vector $\mathbf{u}_\tau(y)$ and its variation $\delta\mathbf{u}_s(y)$, as follows:

$$\begin{aligned} \mathbf{u}_\tau(y) &= N_i(y)\mathbf{q}_{\tau i} \qquad i = 1,2,\ldots,N_n \\ \delta\mathbf{u}_s(y) &= N_j(y)\delta\mathbf{q}_{sj} \qquad j = 1,2,\ldots,N_n \end{aligned} \tag{6.2}$$

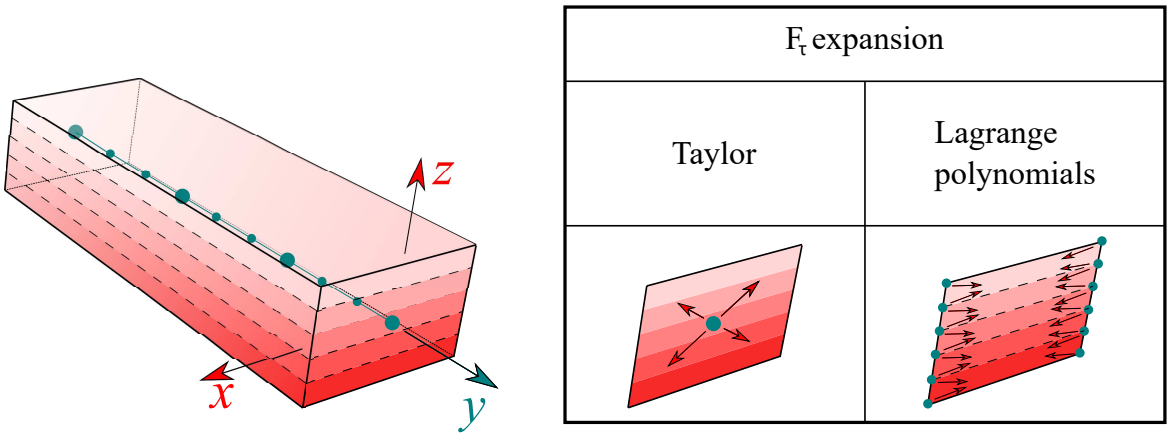

Fig. 6.1 Generic composite structure with equivalent single layer (Taylor) and layerwise (Lagrange polynomials) approaches.

where $N_i(y)$ and $N_j(y)$ stand for the i,j-th 1D shape function, N_n is the number of the structural nodes, i indicates summation and $\mathbf{q}_{\tau i}$ is the vector of the FE nodal parameters $\left\{ \begin{array}{ccc} q_{x_{\tau i}} & q_{y_{\tau i}} & q_{z_{\tau i}} \end{array} \right\}^T$. Interested readers can refer to Bathe [14] and to Carrera *et al.* [29] for the complete form of the shape functions N_j. In this Chapter, classical 1D FEs with four nodes (B4) are adopted, i.e. a cubic approximation along the y axis is considered. Finally, introducing the Eq. (6.2) into Eq. (6.1), the explicit form of the 3D displacement field can be obtained:

$$\begin{aligned} \mathbf{u}(x,y,z) &= F_\tau(x,z)N_i(y)\mathbf{q}_{\tau i} \\ \delta\mathbf{u}(x,y,z) &= F_\tau(x,z)N_i(y)\delta\mathbf{q}_{\tau i} \end{aligned} \tag{6.3}$$

6.3.2 The Node-Dependent Kinematics approach

As discussed in the introduction, the possibility to couple local-to-global parts of the FE model can be done in many ways. NDK allows, by definition, to vary the kinematic node-by-node in the same element, by leading to the possibility to refine kinematics without any use of coupling mathematical artifices. The refinement of the adopted kinematic can be taken a step further by assigning a different approximation to each node of an element. Thanks to the scalable nature of the CUF-based displacement models, it is possible to develop a FE with variable kinematic. The basic idea of NDK is to describe the displacement field over

each cross-section of an element with different kinematics. In this way, one can refine the model only over the regions which require a higher-order theory to be accurately described, and associate lower-order theories in the remaining zones of the domain where localized phenomena do not take place, saving computational cost. The F_τ, F_s functions are node-dependent, that is the indexes i, j of the nodes should distinguish the kinematics at each node. Then, Eq. (6.3) becomes:

$$\begin{aligned} \mathbf{u}(x,y,z) = &\quad F_\tau^i(x,z)N_i(y)\mathbf{q}_{\tau i}, \qquad \tau = 1,2,....,M^i \\ \delta\mathbf{u}(x,y,z) = &\quad F_s^j(x,z)N_j(y)\delta\mathbf{q}_{sj}, \qquad s = 1,2,....,M^j \end{aligned} \tag{6.4}$$

where the indexes i, j on M^i, M^j and $F_\tau^i(x,z), F_s^j(x,z)$ underline that the expansion functions are associated to the i, j-th node of the element, rather than to the entire element itself. An example of NDK approach is finally shown in Fig. 6.2, where a composite beam discretized with one single 4-node B4 finite element in the beam axis direction is shown. Figure 6.2(a) shows the case of a uniform LW kinematic adopted for the whole structure, and every cross-section has 33 LP. Then, the number of Degrees Of Freedom (DOFs) is $33 \times 3 \times 4 = 396$. On the other hand, Fig. 6.2(b) proposes a NDK model of the structure. In particular, the node 1 has a TE1 expansion, that is the Eq. (2.12) truncated at linear term and the number of DOFs is 9; the node 2 is expanded with a TE2 (the Eq. (2.12)), with 18 DOFs.; the node 3 and node 4 are approximated with 12 and 33 LP, respectively, so that their DOFs are $12 \times 3 = 36$ and $33 \times 3 = 99$, respectively. The number of the DOFs is the sum of the DOFs of every cross-section, i.e. $9 + 18 + 36 + 99 = 162$.

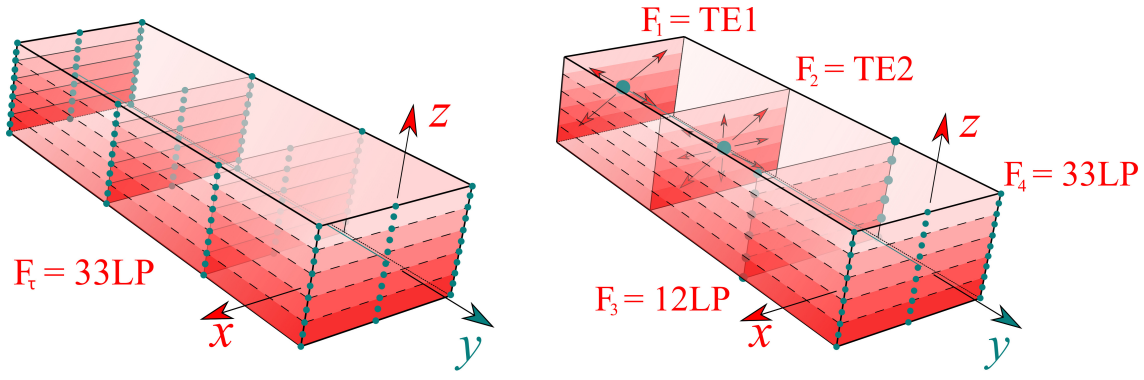

(a) (b)

Fig. 6.2 Composite structure with uniform kinematic (a) and NDK approach (b). Expansion functions (in red) associated individually to each node. The structure is modeled with 4 structural nodes. The uniform kinematic model has 33LP, so that the number of DOFs is $33 \times 3 \times 4 = 396$. The NDK model is approximated with a TE1, TE2, 12LP and 365LP, respectively. Then, the number of the DOFs is $9 + 18 + 12 \times 3 + 33 \times 3 = 162$.

Many examples will be discussed in the numerical results section.

6.3.3 Nonlinear governing equations

The principle of virtual work is hereafter recalled for the derivation of the nonlinear FE governing equations. It states that the virtual work from the internal strain energy (δL_{int}) is equal to the one made by the external loads (δL_{ext}). The strain vector can be written in algebraic form as follows:

$$\varepsilon = (\mathbf{B}_l^{\tau i} + \mathbf{B}_{nl}^{\tau i})\mathbf{q}_{\tau i} \tag{6.5}$$

where $\mathbf{B}_l^{\tau i}$ and $\mathbf{B}_{nl}^{\tau i}$ are the linear and nonlinear algebraic matrices with CUF and FEM formulations. For the sake of completeness, these operators are given below.

$$\mathbf{B}_l^{\tau i} = \begin{bmatrix} F^i_{\tau,x}N_i & 0 & 0 \\ 0 & F^i_{\tau}N_{i,y} & 0 \\ 0 & 0 & F^i_{\tau,z}N_i \\ F^i_{\tau,z}N_i & 0 & F^i_{\tau,x}N_i \\ 0 & F^i_{\tau,z}N_i & F^i_{\tau}N_{i,y} \\ F^i_{\tau}N_{i,y} & F^i_{\tau,x}N_i & 0 \end{bmatrix} \tag{6.6}$$

and

$$\mathbf{B}_{nl}^{\tau i} = \frac{1}{2}\begin{bmatrix} u_{x,x}F^i_{\tau,x}N_i & u_{y,x}F^i_{\tau,x}N_i & u_{z,x}F^i_{\tau,x}N_i \\ u_{x,y}F^i_{\tau}N_{i,y} & u_{y,y}F^i_{\tau}N_{i,y} & u_{z,y}F^i_{\tau}N_{i,y} \\ u_{x,z}F^i_{\tau,z}N_i & u_{y,z}F^i_{\tau,z}N_i & u_{z,z}F^i_{\tau,z}N_i \\ u_{x,x}F^i_{\tau,z}N_i + u_{x,z}F^i_{\tau,x}N_i & u_{y,x}F^i_{\tau,z}N_i + u_{y,z}F^i_{\tau,x}N_i & u_{z,x}F^i_{\tau,z}N_i + u_{z,z}F^i_{\tau,x}N_i \\ u_{x,y}F^i_{\tau,z}N_i + u_{x,z}F^i_{\tau}N_{i,y} & u_{y,y}F^i_{\tau,z}N_i + u_{y,z}F^i_{\tau}N_{i,y} & u_{z,y}F^i_{\tau,z}N_i + u_{z,z}F^i_{\tau}N_{i,y} \\ u_{x,x}F^i_{\tau}N_{i,y} + u_{x,y}F^i_{\tau,x}N_i & u_{y,x}F^i_{\tau}N_{i,y} + u_{y,y}F^i_{\tau,x}N_i & u_{z,x}F^i_{\tau}N_{i,y} + u_{z,y}F^i_{\tau,x}N_i \end{bmatrix} \tag{6.7}$$

The evaluation of the stiffness matrices is, then, the same as described in the previous chapters.

6.4 Examples

6.4.1 Stress distribution on compressed asymmetric compact beams

The first analysis case deals with asymmetric laminated cantilever beams with compact cross-section. The geometric, boundary and material conditions are shown in Fig. 9.2, with L/b = 9, h/b = 0.6, E_1 = 144.8 GPa, $E_2 = E_3$ = 9.65 GPa, ν = 0.3, $G_{12} = G_{13}$ = 4.14 GPa and G_{23} = 3.45 GPa. The considered stacking sequences are [0°/90°] and [0°/45°], as depicted in the figure, where the red lines show the direction of the fibers. 20B4 are employed for the approximation of the beam axis.

Figure 6.4 reports the nonlinear equilibrium curves of the [0°/90°] case using a uniform

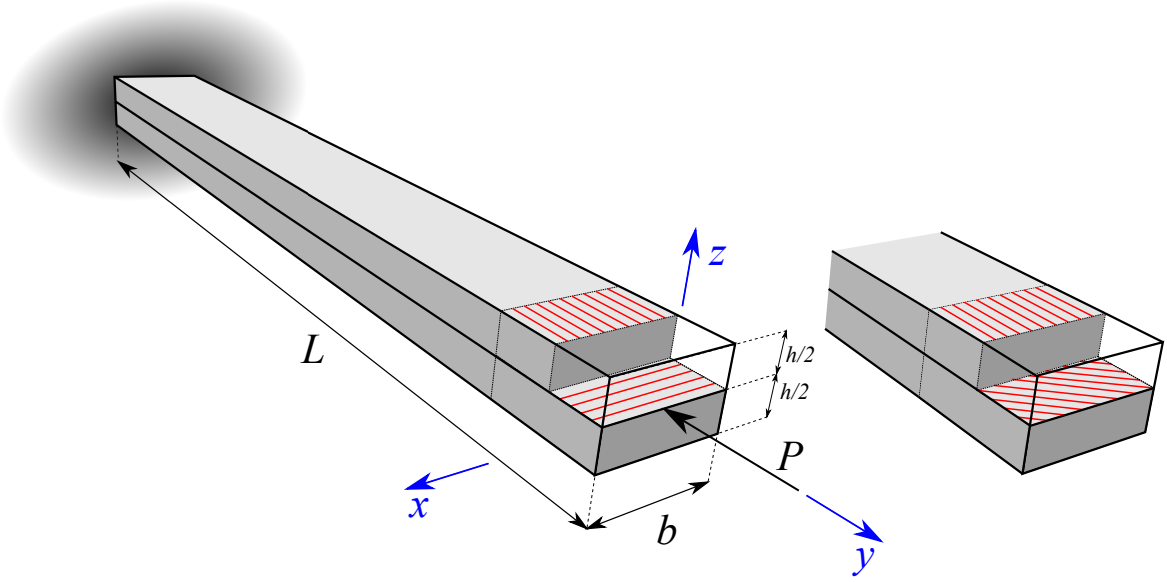

Fig. 6.3 Geometic properties and loading case of the asymmetric beam with compact cross-section subjected to compressive loading.

kinematics. Lower-order and refined theories are employed and, clearly, they lead to the same results. Then, it is evident that the NDK approach is useless for the displacement evaluation of the selected case, since every kinematic is able to predict the displacement field. However, this is not true if one wants to accurately evaluate the stress distribution within the structure. In fact, as shown in Figs. 6.5, 6.6 and 6.7 the stress distribution changes according to the adopted theory. Clearly, the L9, TE2 and TE2 kinematics can not describe the quadratic trend of the shear stress component, whereas the L16 can. On the contrary, this difference is not evident for the axial component, which distribution is linear.

Since only the L16 kinematic model is able to accurately predict the distribution of stress components, the NDK approach is suitable for building a model with less DOFs capable to

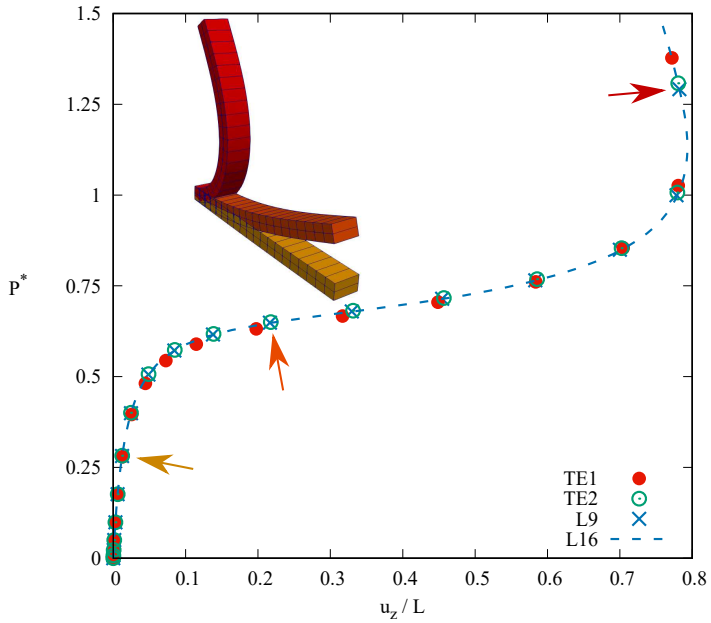

Fig. 6.4 Equilibrium curve of the [0°/90°] composite beam subjected to compression loading. TE1 DOFs = 549, TE2 DOFs = 1098, L9 DOFs = 2745, L16 DOFs = 5124.

describe the stress trend on a given part of the structure. As an example, we consider the stress distribution (axial and shear components) on y = 0.2 L. The NDK approach allows to build a model refined in the selected zone, and gradually less refined as we get further from it. The mathematical model for the selected example is reported in Fig. 6.8, where a L16-TE8-TE5-TE1 model is shown. As reported in the same figure, the stress distribution are the same as those calculated with a heavier uniform higher-order kinematic model, with a significant loss of DOFs (from 5124 to 3579).

The [0°/45°] stacking sequence was further analyzed. The nonlinear static equilibrium curves adopting uniform kinematics are shown in Fig. 6.9. In this case, due to the torsional-bending coupling, the uniform TE1 kinematic leads to wrong results, compared to more reliable TE2, L9 and L16. For this reason, the NDK approach can be useful to describe the displacement field with lower DOFs, mixing TE1 and higher-order theory (the selected one for this example is L9). Figure 6.10 reports the equilibrium curves using various NDK TE1-L9 models (depicted and described in the figure). The figure demonstrates several interesting aspects.

- The four NDK models are built with the same number of DOFs (1655), but the results are different. The distribution of the DOFs is a crucial point when dealing with NDK models.

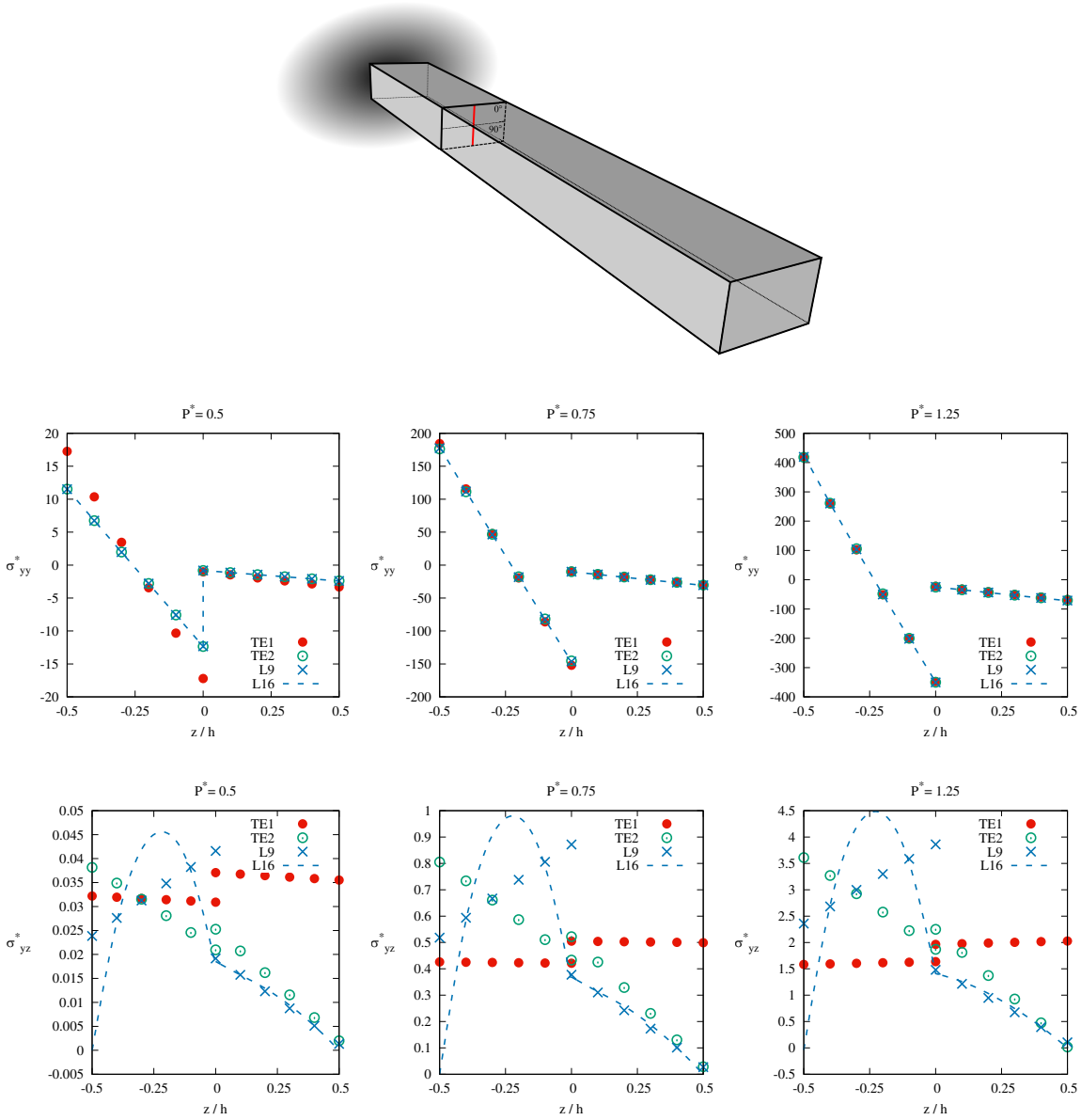

Fig. 6.5 Axial and shear through-the-thickness stress distribution of the [0°/90°] composite beam subjected to compression loading, evaluated at y = 0.2 L (red line). $\sigma^*_{yy} = \dfrac{\sigma_{yy}\, b\, h}{P}$ and $\sigma^*_{yz} = \dfrac{\sigma_{yz}\, b\, h}{P}$. TE1 DOFs = 549, TE2 DOFs = 1098, L9 DOFs = 2745, L16 DOFs = 5124.

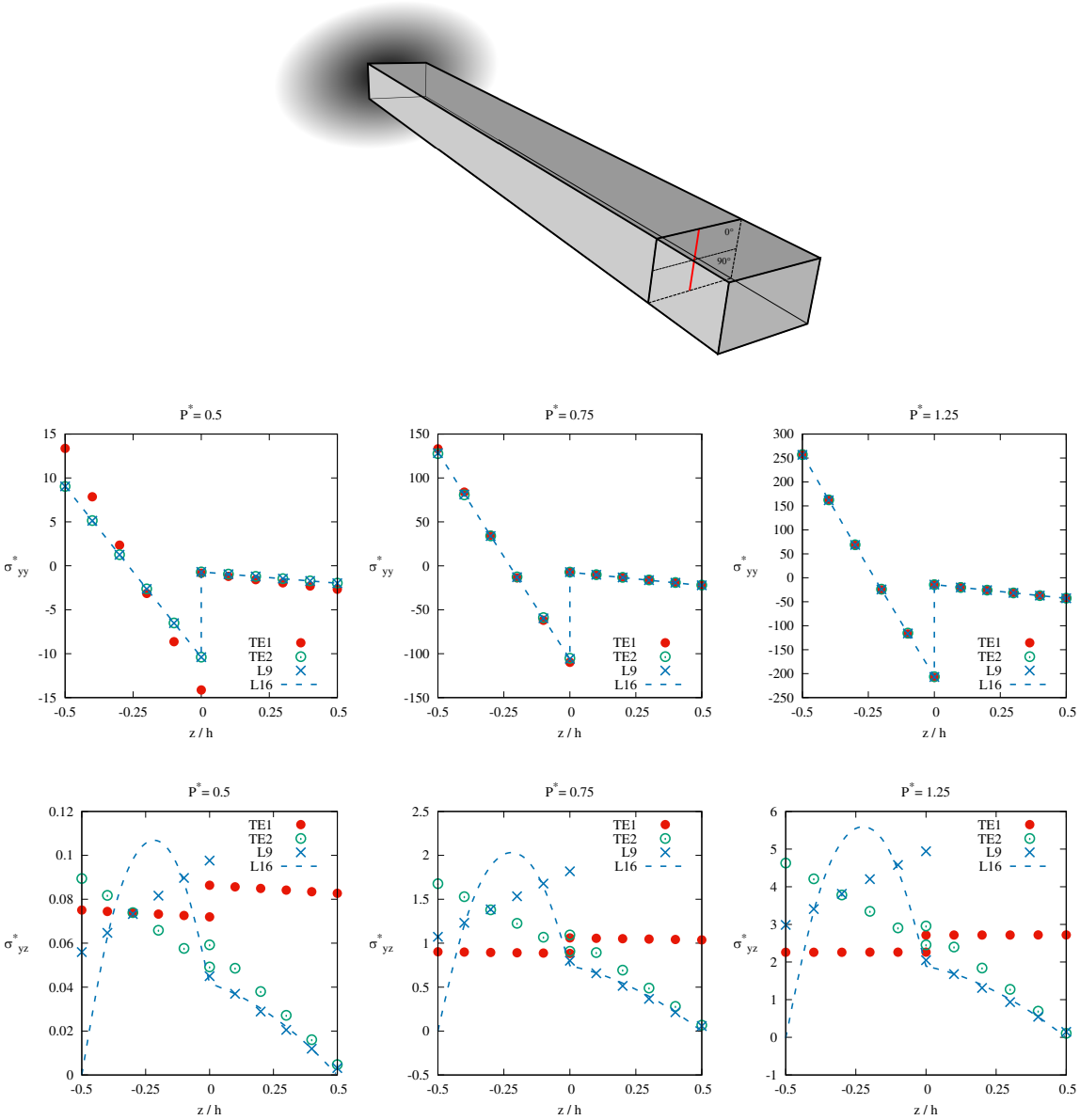

Fig. 6.6 Axial and shear through-the-thickness stress distribution of the [0°/90°] composite beam subjected to compression loading, evaluated at y = 0.5 L (red line). $\sigma^*_{yy} = \dfrac{\sigma_{yy}\, b\, h}{P}$ and $\sigma^*_{yz} = \dfrac{\sigma_{yz}\, b\, h}{P}$. TE1 DOFs = 549, TE2 DOFs = 1098, L9 DOFs = 2745, L16 DOFs = 5124.

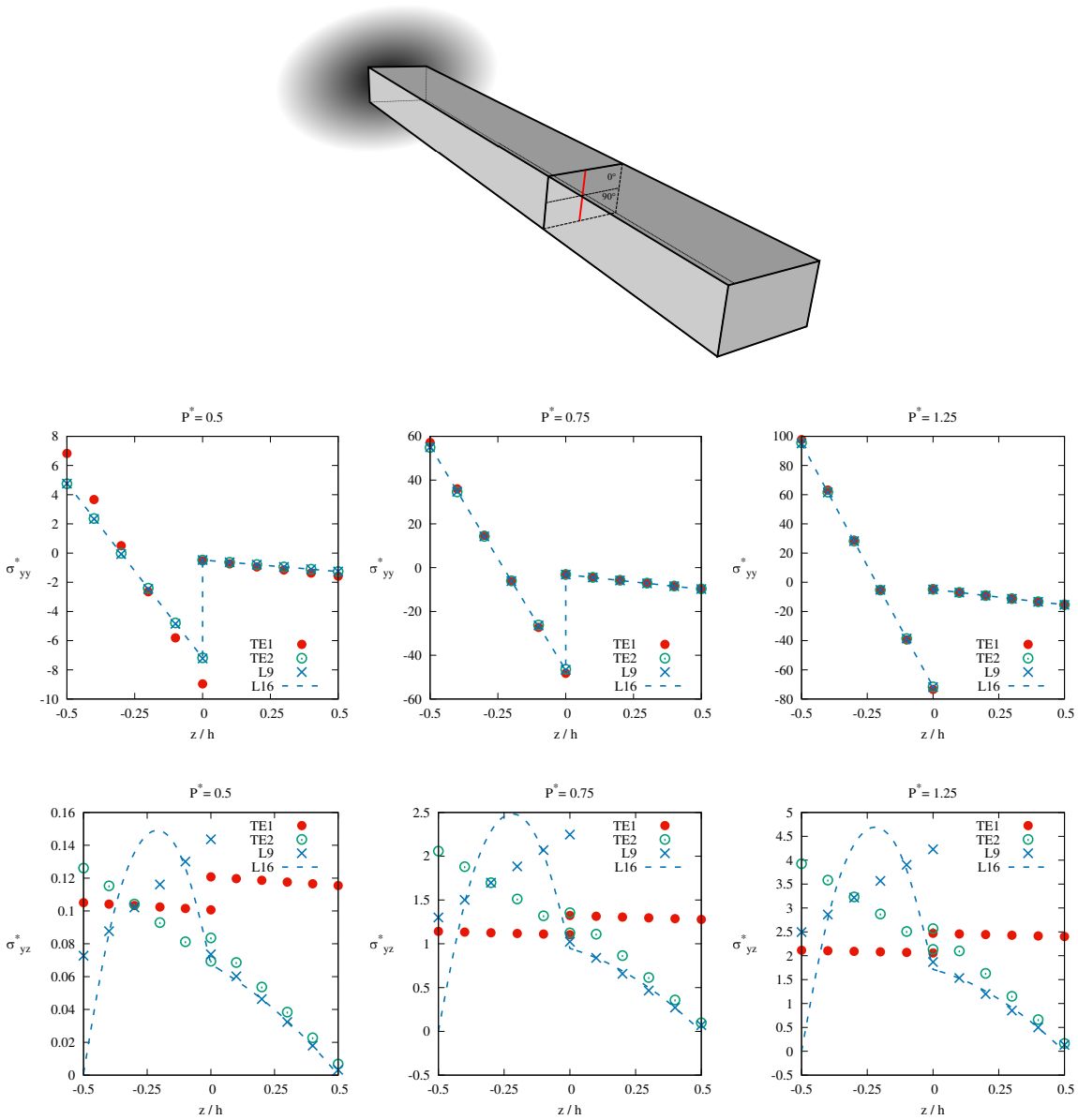

Fig. 6.7 Axial and shear through-the-thickness stress distribution of the [0°/90°] composite beam subjected to compression loading, evaluated at y = 0.8 L (red line). $\sigma^*_{yy} = \dfrac{\sigma_{yy}\, b\, h}{P}$ and $\sigma^*_{yz} = \dfrac{\sigma_{yz}\, b\, h}{P}$. TE1 DOFs = 549, TE2 DOFs = 1098, L9 DOFs = 2745, L16 DOFs = 5124.

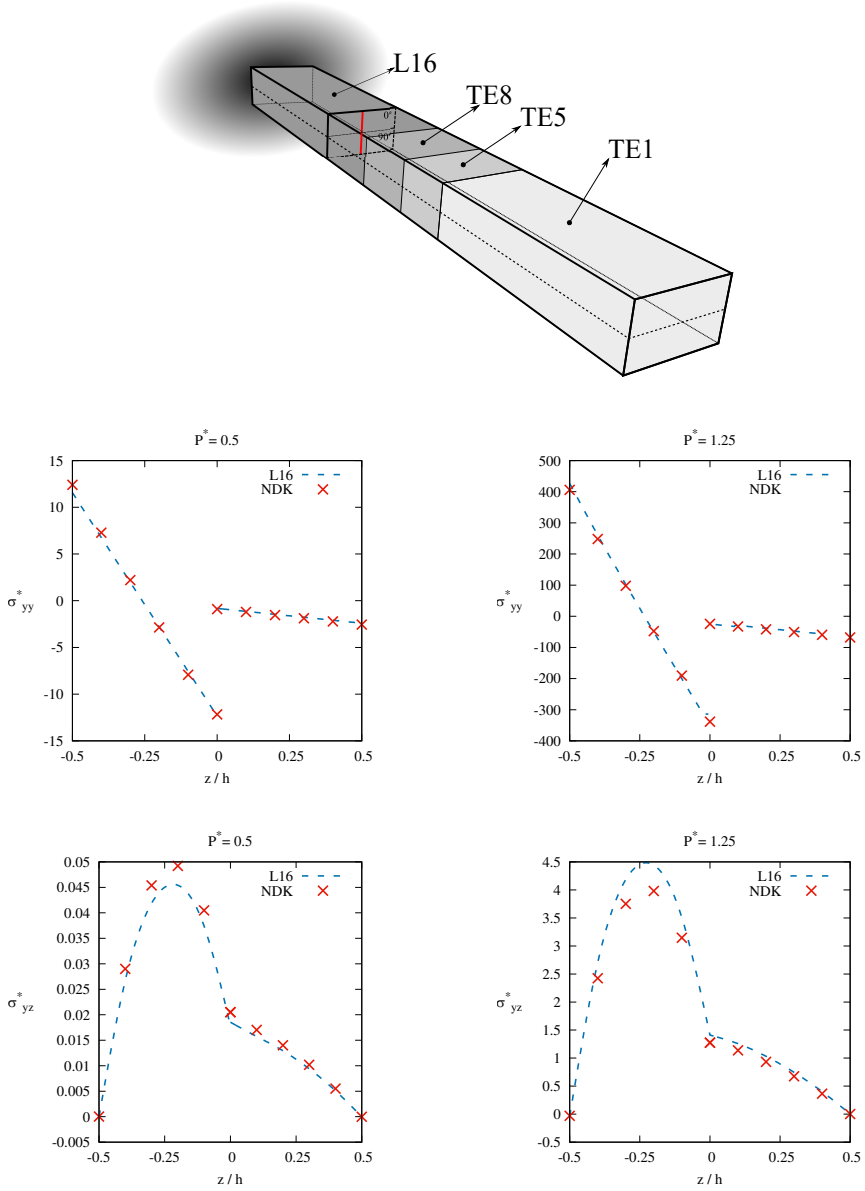

Fig. 6.8 Axial and shear through-the-thickness stress distribution of the [0°/90°] composite beam subjected to compression loading, evaluated at y = 0.2 L (red line) with a NDK model. $\sigma^*_{yy} = \dfrac{\sigma_{yy}\, b\, h}{P}$ and $\sigma^*_{yz} = \dfrac{\sigma_{yz}\, b\, h}{P}$. L16 DOFs = 5124, NDK DOFs = 3579.

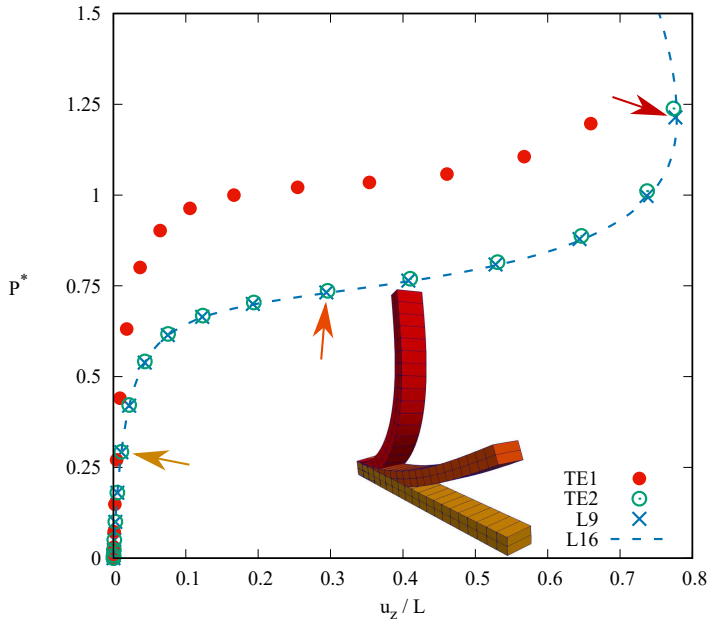

Fig. 6.9 Equilibrium curve of the [0°/45°] composite beam subjected to compression loading. TE1 DOFs = 549, TE2 DOFs = 1098, L9 DOFs = 2745, L16 DOFs = 5124.

- The distribution which, in this case, leads to more accurate results is the one which assignes more DOFs (a more refined model) to the clamped zone.

Stress distributions are considered as well. The same NDK models as those presented in Figs. 6.10, 6.11 and 6.12 are used herein (although the more refined L16 theory is used instead of L9 to catch the parabolic distribution of shear stress). Clearly, significant differences are evident when the stress distriution is evaluated in the TE1 portion of the structure. In fact, the most reliable NDK model (number 1, as demonstrated in Fig. 6.10) is able to merely describe the stress distribution in the L16 zone (Fig. 6.10), whereas it fails when moving in the TE1 part (Fig. 6.11 and Fig. 6.12). Finally, it can be pointed out that, in order to catch the correct stress values, it is not enough to have an accurately refined model in that portion of the structure. In fact, from a mathemacal point of view, the NDK model number 2 would be able to catch the stress components for y = 0.5 L (Fig. 6.11) and y = 0.8 L (Fig. 6.12). However, the distribution is very far from the uniform L16 solution and the reason is that, as demonstrated before, from a physical point of view, the clamped zone needs to be described with a refined model, whereas number 2 assignes only TE1 kinematic to that part of the structure.

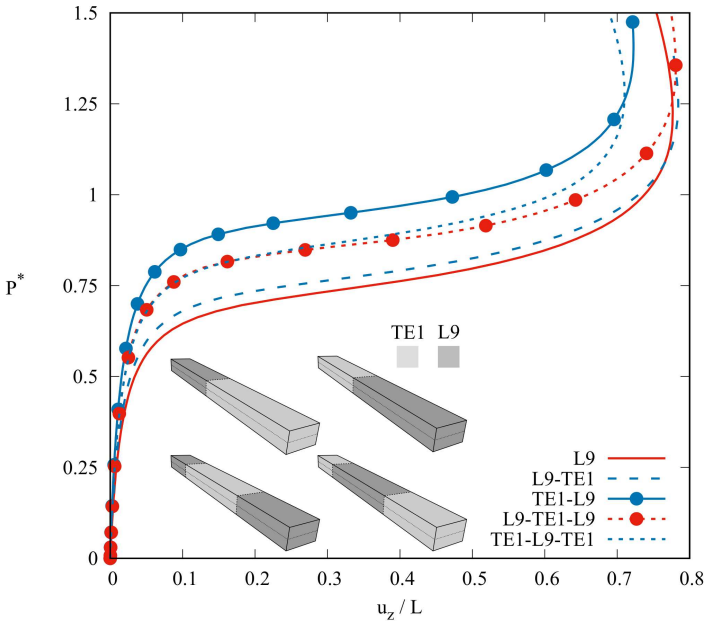

Fig. 6.10 Equilibrium curve of the [0°/45°] composite beam subjected to compression loading with various NDK models. L9 DOFs = 2745, NDK DOFs = 1485.

6.4.2 Stress distribution on laminated box beam

A cantilever laminated box beam undergoing large deflection due to transverse loadings is considered in the following analysis case. The structure is made by two layers, with [0°/90°] stacking sequence on top and bottom and [0°/45°] on the lateral flanges. The considered material is the same as in the previous case. The geometric characteristics and dimensions are shown in Fig. 6.14, with L/b = 10, h = 13.6 mm, h/t = 10. The refined cross-section discretization was made implementing 16L9. This polynomial pattern will be recalled as "LE" in the following analyses. The analysis case was taken from [31]. A preliminary convergence analysis was carried out to enstabilish a FE mesh for the beam axis. Figure 6.15 shows that 10 B4 can be considered a reliable approximation and, therefore, 10 B4 elements are employed for the approximation of the beam axis. Two loading cases are analyzed hereafter, involving a symmetric and unsymmetric transverse loadings, respectively. The nonlinear equilibrium curves using LE as uniform expansion function are shown in Fig. 6.16. In the figure, some deformed configuration are depicted too. It is clear how the clamped portion of the structure undergoes a large cross-sectional deformation, whereas the free tip zone reports a moderate cross-section deformation (Fig. 6.16(a)) and rotation (Fig. 6.16(b)). For this reason the next investigation was made using a refined model in the first portion of the structure, with a lower-order kinematic in the remaining zone, to analyze the static and stress response of the NDK models. As far as the symmetric transverse load case is concerned, the nonlinear static

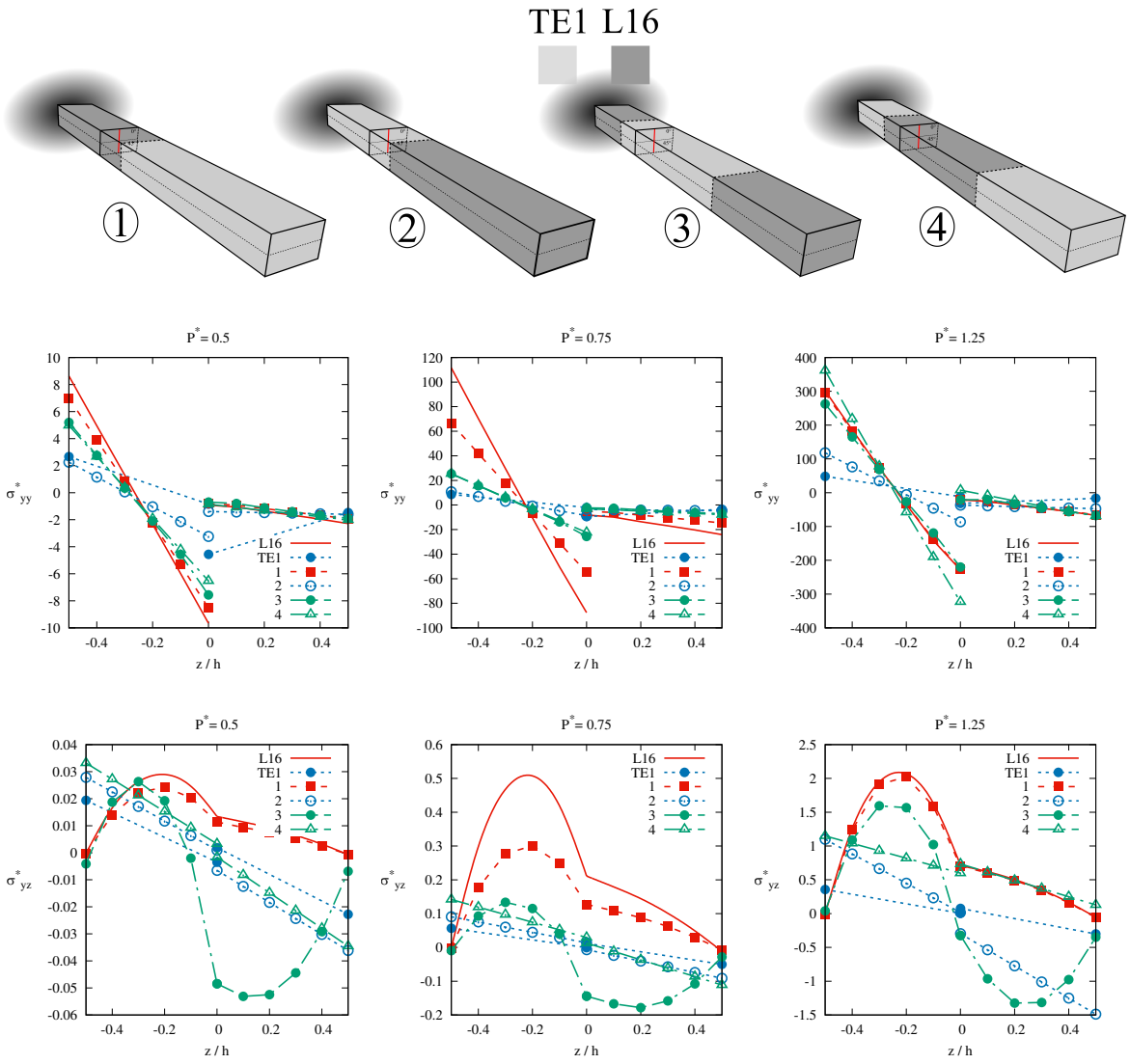

Fig. 6.11 Axial and shear through-the-thickness stress distribution of the [0°/45°] composite beam subjected to compression loading, evaluated at y = 0.2 L (red line) with various NDK models. $\sigma^*_{yy} = \dfrac{\sigma_{yy}\, b\, h}{P}$ and $\sigma^*_{yz} = \dfrac{\sigma_{yz}\, b\, h}{P}$. TE1 DOFs = 549, L16 DOFs = 5124, NDK DOFs = 2694.

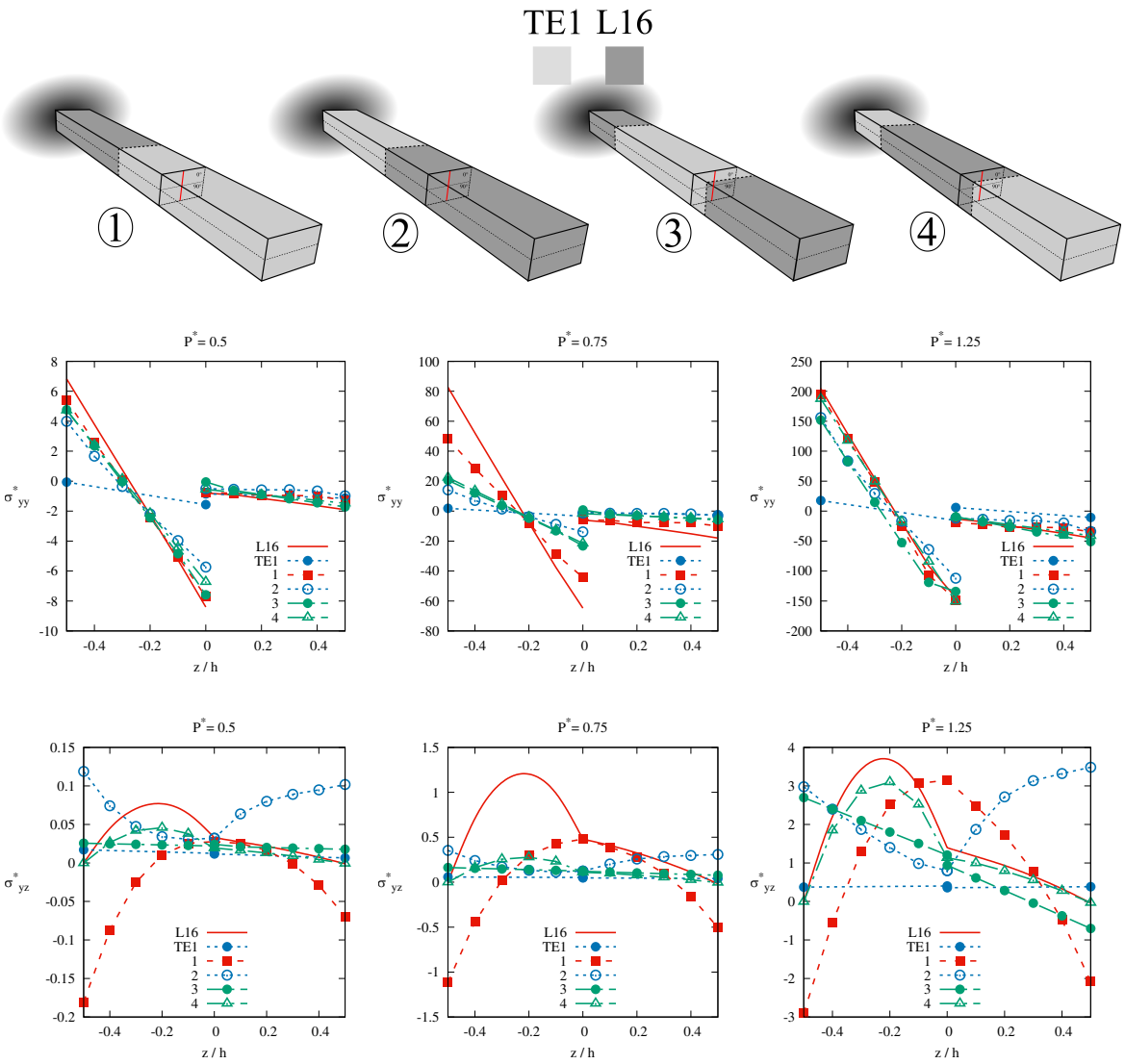

Fig. 6.12 Axial and shear through-the-thickness stress distribution of the [0°/45°] composite beam subjected to compression loading, evaluated at y = 0.5 L (red line) with various NDK models. $\sigma^*_{yy} = \dfrac{\sigma_{yy}\, b\, h}{P}$ and $\sigma^*_{yz} = \dfrac{\sigma_{yz}\, b\, h}{P}$. TE1 DOFs = 549, L16 DOFs = 5124, NDK DOFs = 2694.

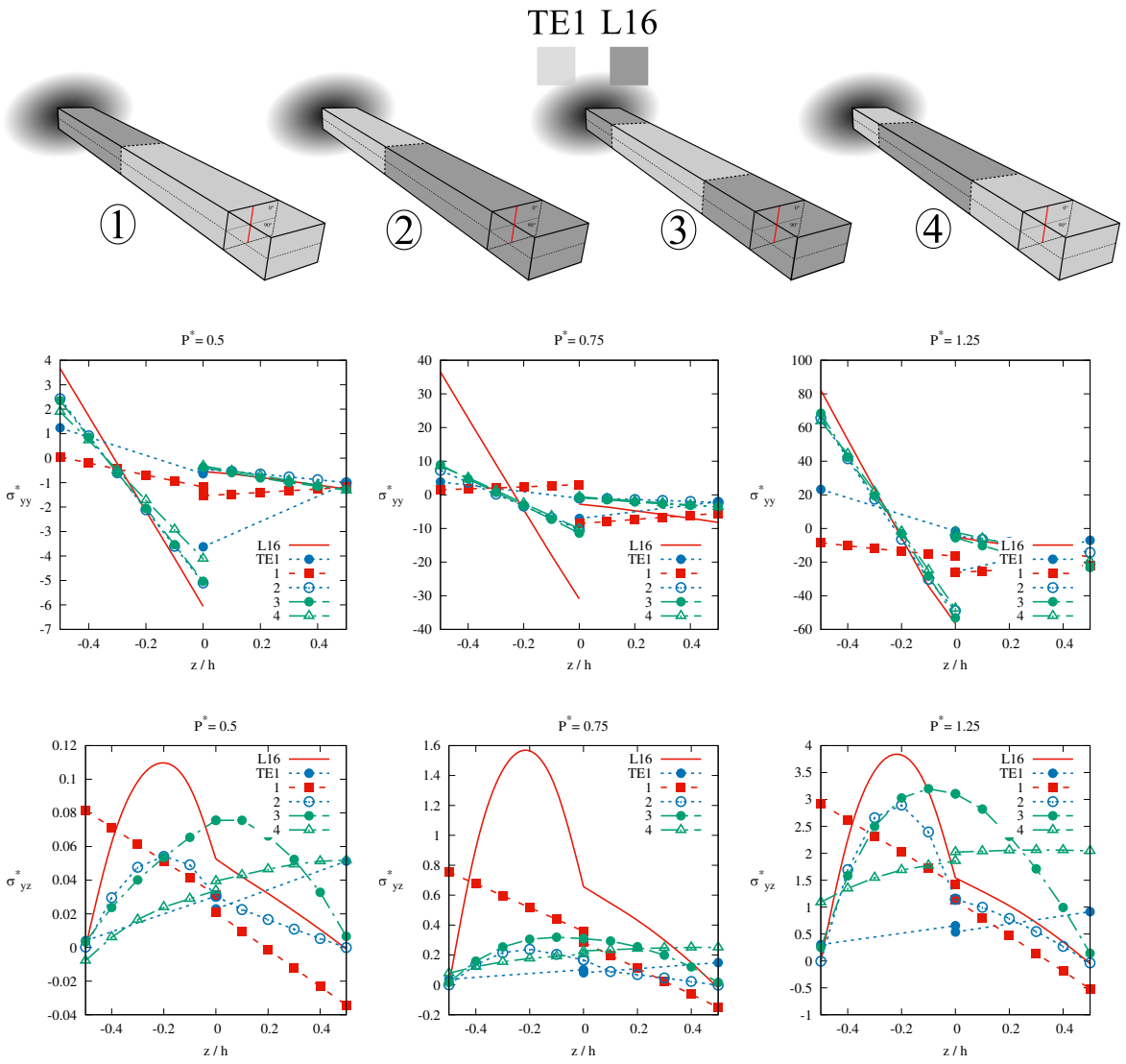

Fig. 6.13 Axial and shear through-the-thickness stress distribution of the [0°/45°] composite beam subjected to compression loading, evaluated at y = 0.8 L (red line) with various NDK models. $\sigma^*_{yy} = \dfrac{\sigma_{yy}\, b\, h}{P}$ and $\sigma^*_{yz} = \dfrac{\sigma_{yz}\, b\, h}{P}$. TE1 DOFs = 549, L16 DOFs = 5124, NDK DOFs = 2694.

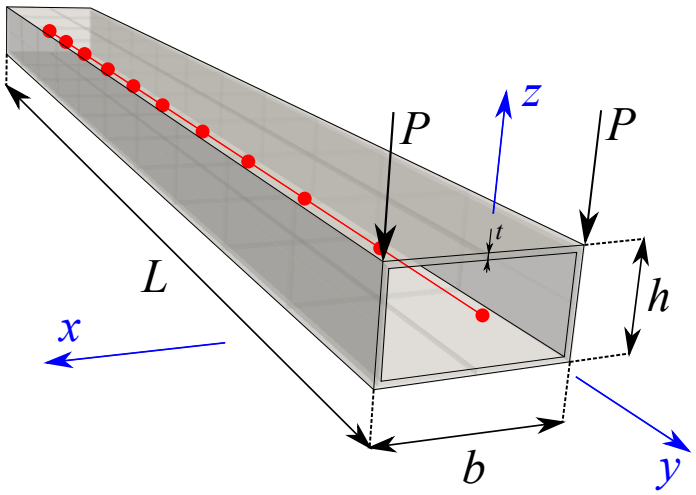

Fig. 6.14 Geometic properties and loading case of the composite box beam subjected to transverse loading.

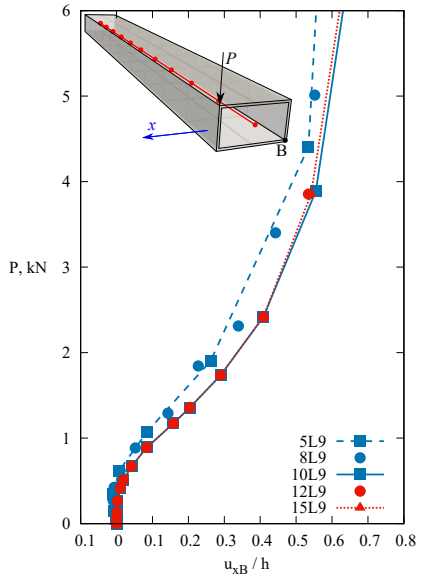

Fig. 6.15 Convergence analysis of the composite box beam subjected to unsymmetric transverse loading.

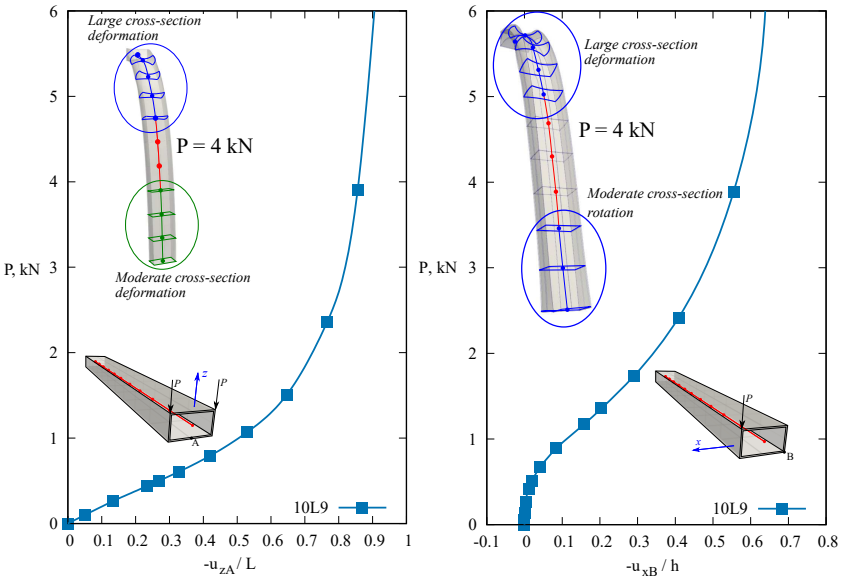

Fig. 6.16 Equilibrium curves of the composite box beam subjected to symmetric transverse loading (a) and unsymmetric transverse loading (b). DOFs = 7440.

curves are presented in Fig. 6.17, along with the adopted NDK models. As stated before, every NDK model involves a higher-order LE kinematic near the clamped zone. Clearly, the results show a great convergence for the displacement evaluation, and only the low-order NDK models TE1, L9-TE1 and TE5-TE1 are far from the reliable solution, provided by a full L9 model. Higher differences can be appreciated looking at stress distributions of Fig. 6.18. It is clear that even the most refined NDK model L9-TE1 fails in correctly evaluating the shear stress distribution (see Fig. 6.18(c)). Regarding the unsymmetric transverse loading, Fig. 6.19 shows the static nonlinear solutions adopting various NDK models, described in the figure. Moreover, the stress distribution of axial and shear components are reported in Fig. 6.20. Clearly, the LE9-TE10 NDK represents a reliable mathematical model, both from the displacement and stress point of view.

6.4.3 Through-the-thickness stresses evaluation of pinched composite cylindrical shell

A clamped composite cylindrical shell subjected to a pinching force is considered as first analysis case. The vertical displacement and the rotation around the β-axis are constrained along its longitudinal edges. The laminated cylindrical shell model, considering stacking sequences $[90°, 0°, 90°]$ and $[45°, 0°, -45°]$, is reported in Fig. 6.21. The investigated model

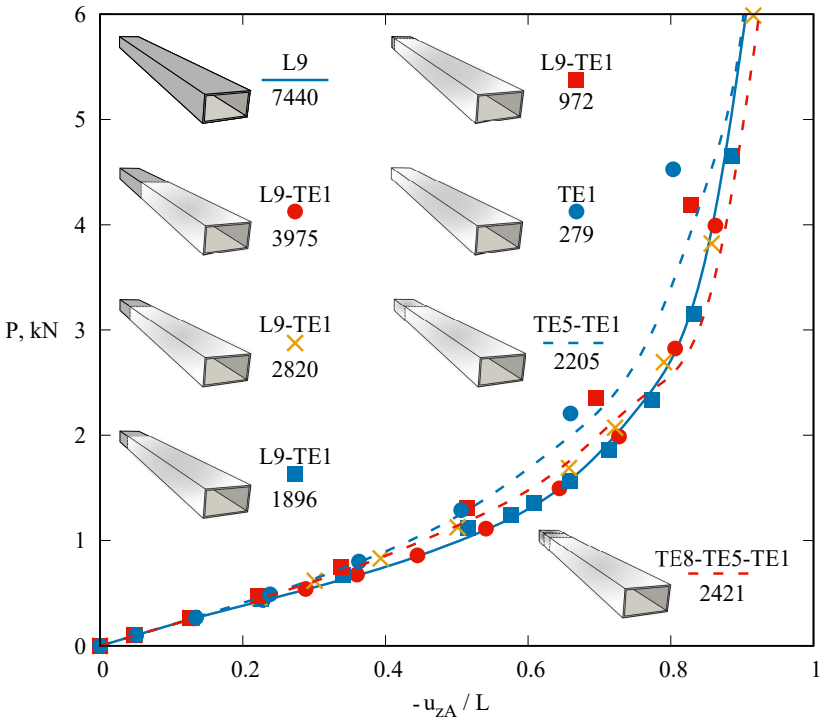

Fig. 6.17 Equilibrium curve of the composite box beam subjected to symmetric transverse loading with various NDK models.

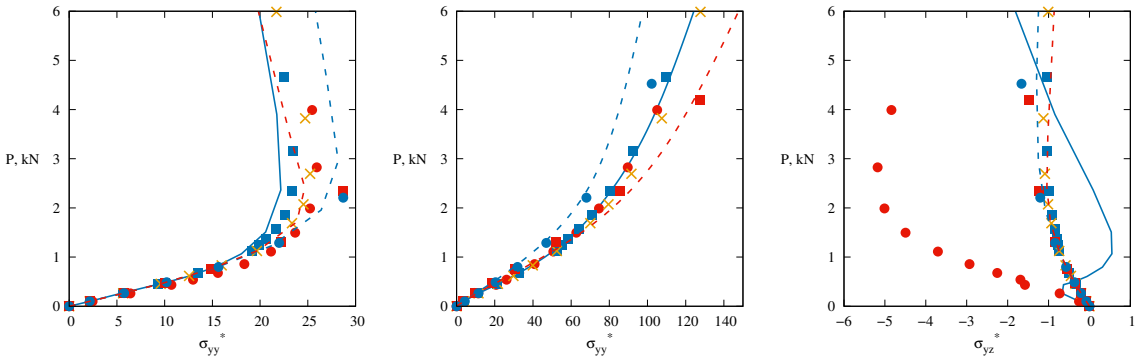

Fig. 6.18 Axial and shear through-the-thickness stress distribution of the composite box beam subjected to symmetric transverse loading with various NDK models. Stress distributions evaluated at $(0, \frac{L}{2}, \frac{h}{2})$ (a), $(0, 0, \frac{h}{2})$ (b) and $(\frac{b}{2}, \frac{L}{2}, \frac{h}{4})$ (c). $\sigma^*_{yy} = \frac{\sigma_{yy}\, b\, h}{P^*}$ and $\sigma^*_{yz} = \frac{\sigma_{yz}\, b\, h}{P^*}$, where $P^* = 6000$ kN.

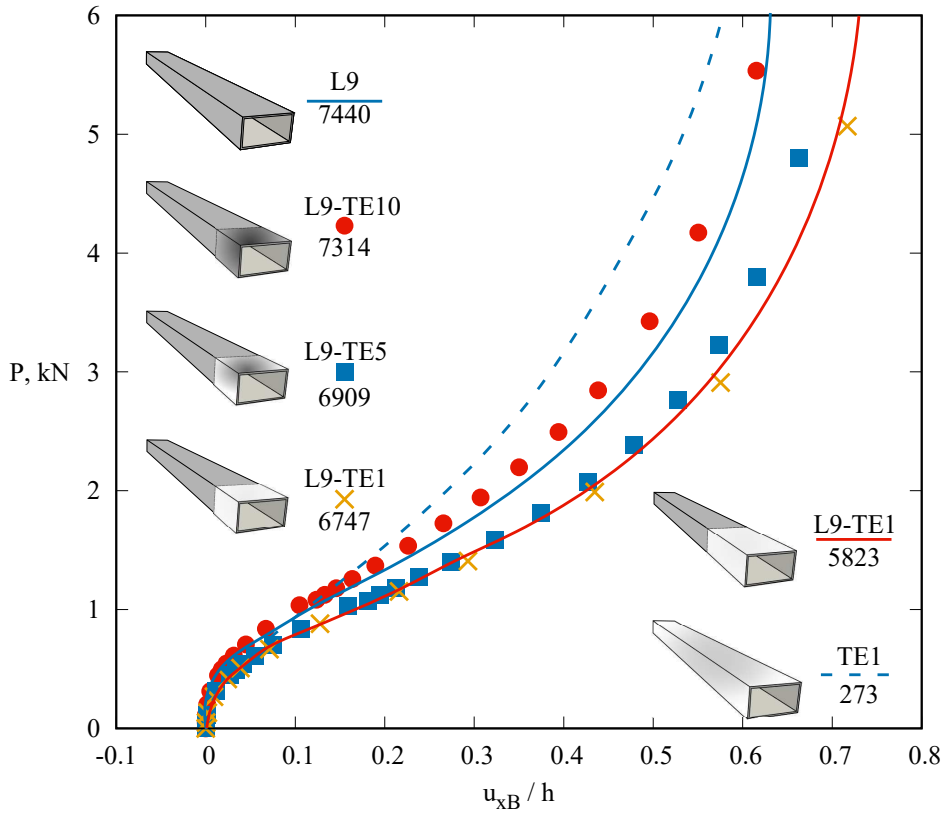

Fig. 6.19 Equilibrium curve of the composite box beam subjected to unsymmetric transverse loading with various NDK models.

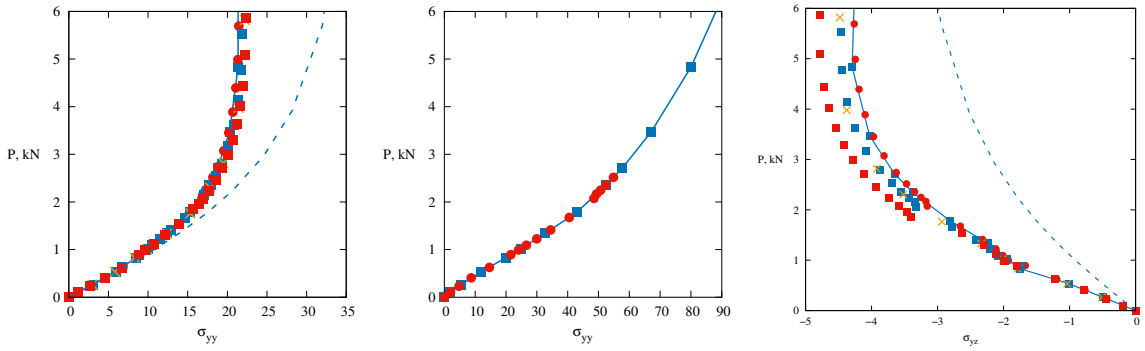

Fig. 6.20 Axial and shear through-the-thickness stress distribution of the composite box beam subjected to unsymmetric transverse loading with various NDK models. Stress distributions evaluated at $(0, \frac{L}{2}, \frac{h}{2})$ (a), $(0, 0, \frac{h}{2})$ (b) and $(\frac{b}{2}, \frac{L}{2}, \frac{h}{4})$ (c). $\sigma^*_{yy} = \frac{\sigma_{yy}\, b\, h}{P^*}$ and $\sigma^*_{yz} = \frac{\sigma_{yz}\, b\, h}{P^*}$, where $P^* = 6000$ kN.

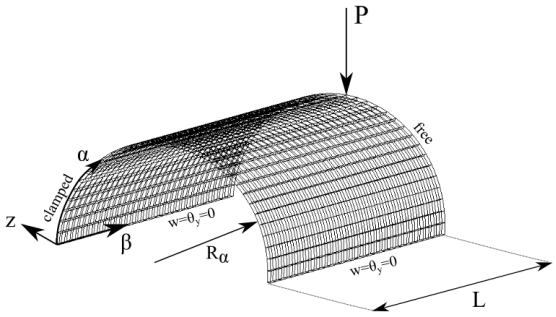

Fig. 6.21 Geometric and loading properties of the pinched cylinder.

has the following characteristics: L= 3.048 m, R_α= 1.016 m, and h=0.03 m. The material has an elastic modulus E_L= 2068.5×10^4 N/m^2, E_T= 517.125×10^4 N/m^2, G_{LT}= 795.6×10^4 N/m^2 and Poisson's ratio ν_{LT}=ν_{TT}= 0.3. The subscripts L and T indicate the longitudinal and transverse (fiber) direction, respectively. This static analysis case was presented by Wu *et al.* [186] and by Sze *et al.* [175]. Nevertheless, no through-the-thickness stress benchmarks were yet described.

First, in order to perform an accurate static analysis, a convergence study on the in-plane finite element mesh is carried out. Figure 6.22 shows the transverse deflection at the load point for different 2D shell models, and from 256Q9 to 1024Q9 FEs are adopted for the surface approximation, whereas one LD2 is used in each layer in the thickness direction. Moreover, Table 6.1 shows the transverse displacement values for different models and loads,

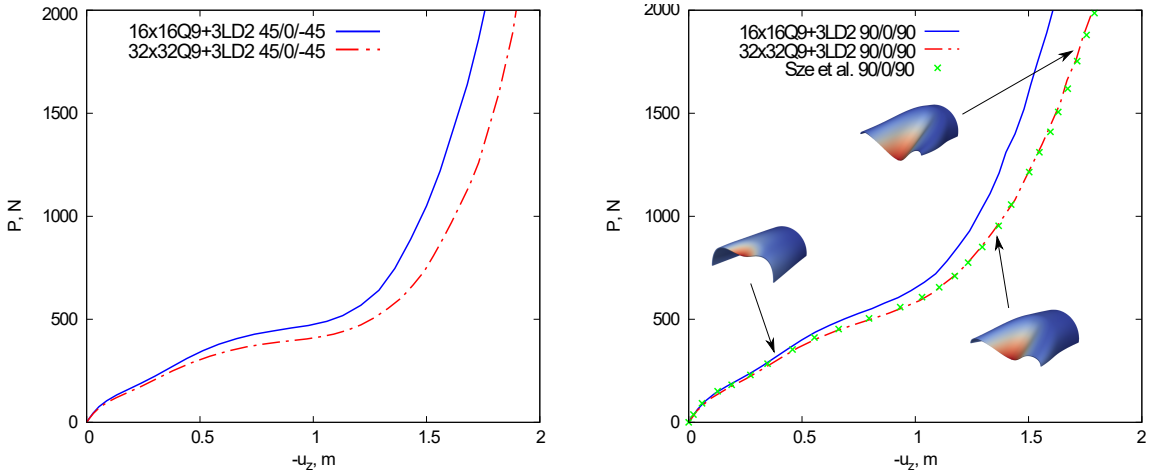

Fig. 6.22 Static convergence analyses of the pinched cylinder: (a) $[45°, 0°, -45°]$, (b) $[90°, 0°, 90°]$.

along with the total degrees of freedom (DOFs). As evident from Fig. 6.22 and Table 6.1, the 32×32Q9 mesh is a reliable approximation for the in-plane description. Then, to perform

Model	DOFs	-u_z [m]			
		$[45°, 0°, -45°]$		$[90°, 0°, 90°]$	
		500 N	1000 N	500 N	1000 N
16 x 16Q9 + 3LD2	22869	1.086	1.481	0.684	1.273
32 x 32Q9 + 3LD2	88725	1.267	1.632	0.807	1.394
Sze *et al*. [175]	-	-	-	0.798	1.393

Table 6.1 Values of transverse displacements of the composite pinhed cylinder. α= 1.596 m, β= 3.048 m and z= 0.015 m.

an accurate stress prediction, different expansion functions in the thickness direction are compared. Both LE and TE functions are considered in this analysis. Figure 6.23 shows the 3D stress distributions, including the circumferential normal stress $S_{\alpha\alpha}$ and the transverse shear stress $S_{\beta z}$ components, for different through-the-thickness kinematic approximations. The corresponding stress values are reported in Table 6.2 for different 2D shell theories and

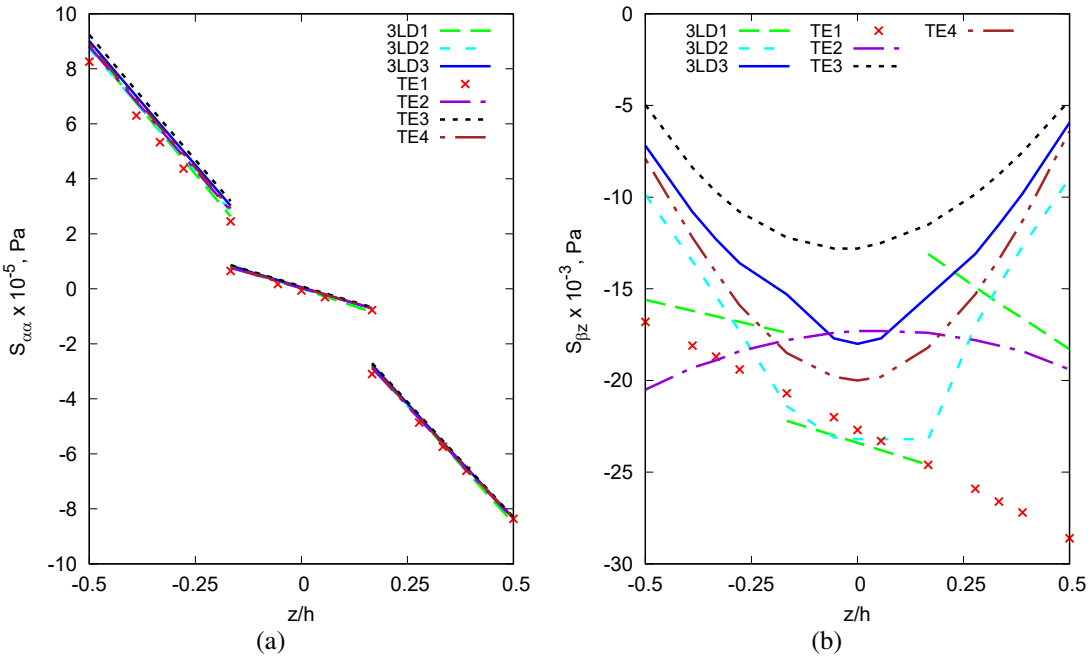

Fig. 6.23 Stress distributions of the pinched cylindrical using various kinematic theories. $[90°, 0°, 90°]$. P= 1000 N. α= 1.596 m and β= 1.524 m.

loads. Clearly, the LW model kinematics should be exploited to accurately predict the stress values, using at least the 3LD3 theory. The results suggest that the ESL model is sufficient to evaluate the circumferential normal stress, whereas it is inadequate to accurately predict the

Theory	DOFs	$[90°, 0°, -90°]$			
		$S_{\alpha\alpha}$ [Pa$\times 10^5$]		$S_{\beta z}$ [Pa$\times 10^3$]	
		500 N	1000 N	500 N	1000 N
TE1	25350	-1.280	-8.356	-1.151	-22.658
TE2	38025	-1.291	-8.375	-1.110	-17.291
TE3	50700	-1.272	-8.298	-1.573	-12.760
TE4	63375	-1.282	-8.344	-1.657	-19.973
3LD1	50700	-1.309	-8.519	-1.622	-23.399
3LD2	88725	-1.289	-8.350	-1.600	-23.185
3LD3	126750	-1.289	-8.350	-1.776	-18.001

Table 6.2 Normal and transverse stresses for various kinematic theories. α= 1.596 m and β= 1.524 m and z= 0.015 m $S_{\alpha\alpha}$ and z= 0 m for $S_{\beta z}$.

transverse shear stress component. Figures 6.24 and 6.25 depict the circumferential normal and transverse shear PK2 stresses in the thickness direction for different loads and for the two laminations using both ESL and LW approaches to highlight the different capabilities. The linear interpolation (*FSDT-like*) provided by the ESL model is, clearly, not enough to catch the transverse shear stress distribution of the laminated pinched cylindrical shell, as shown in Figs. 6.24d and 6.25d.

6.4.4 Through-the-thickness stresses evaluation of pinched composite cylindrical shell

As a second assessment, a hinged composite cylindrical shell under a central transverse force P is considered, as illustrated in Fig. 6.26. This is a well-known nonlinear benchmark and especially popular for the snapping behaviour. The present model has the following geometrical characteristics, L= 508 mm, R_α= 2540 mm, θ= 0.1 rad. The material properties of the laminated hinged cylindrical shell involves E_L= 3300 MPa, E_T= 1100 MPa, G_{LT}= 660 MPa, G_{TT}= 660 MPa and ν_{LT}=ν_{TT}= 0.25. The lamination sequence considered are $[0°, 90°, 0°]$, $[90°, 0°, 90°]$ and $[45°, 0°, -45°]$, and the thickness equals 12.7 mm.
First, in order to perform an accurate static analysis, a convergence study on the in-plane 2D shell model is carried out. Then, a stress evaluation is performed for different expansion orders. Figure 6.27 plots the transverse deflection for different in-plane FE mesh, and the solutions from 25Q9 to 225Q9 are used for the surface discretization, whereas only one LD2 is adopted in each layer in the thickness direction. The nonlinear response curves are divided into the regions A, B and C, as reported in Fig. 6.27c. In addition, transverse

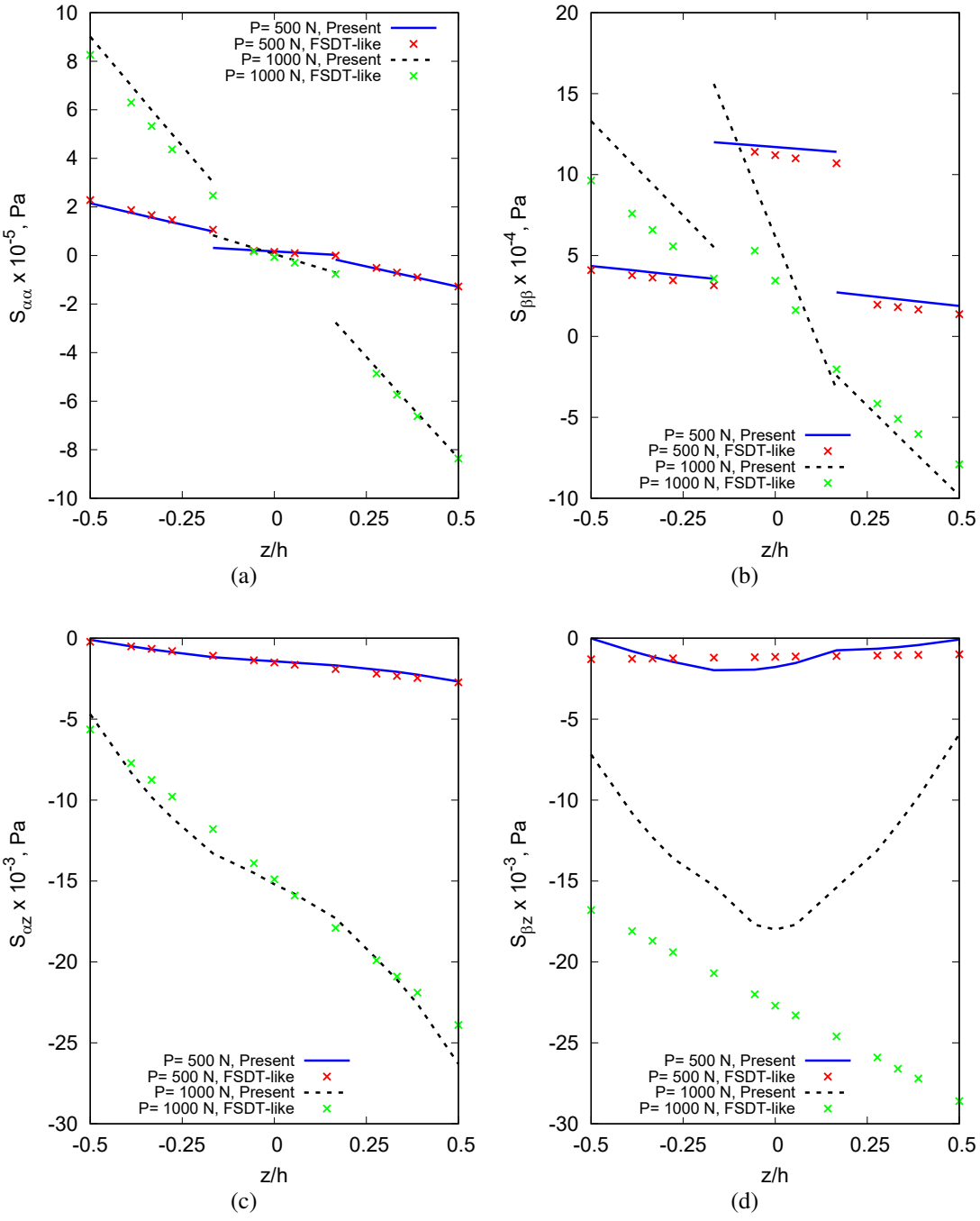

Fig. 6.24 Through-the-thickness transverse stress. α= 1.596 m and β= 1.524 m. $[90°, 0°, 90°]$.

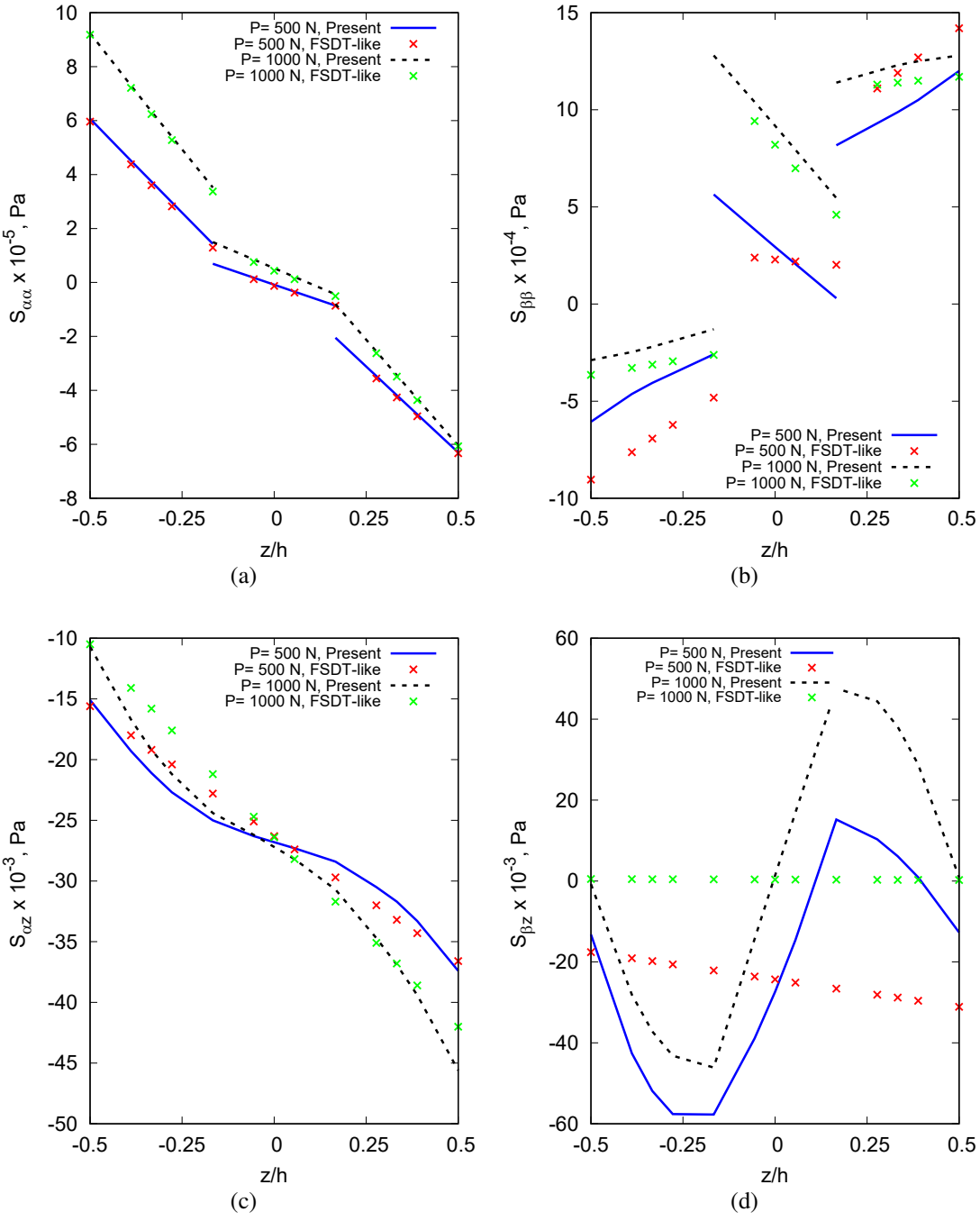

Fig. 6.25 Through-the-thickness transverse stress. α= 1.596 m and β= 1.524 m. $[45°, 0°, 45°]$.

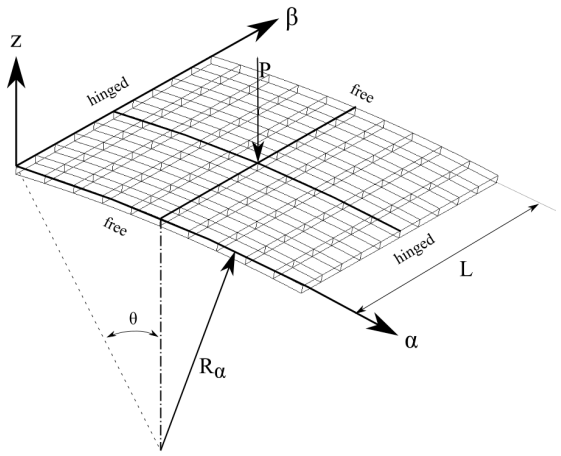

Fig. 6.26 Geometry and loading condition of the hinged cylinder.

displacements values for the three laminations for different in-plane mesh and loads are illustrated in Table 6.3, along with the number of DOFs. Consequently, the 10×10Q9 mesh

Model	DOFs	-u_z [mm]									
		$[0°,90°,0°]$				$[90°,0°,90°]$		$[45°,0°,-45°]$			
		500 N (A)	500 N (B)	500 N (C)	2000 N	500 N	2000 N	500 N (A)	500 N (B)	500 N (C)	2000 N
5 x 5Q9 + 3LD2	2541	2.521	14.629	24.601	29.821	2.125	27.069	2.620	18.074	22.097	29.296
10 x 10Q9 + 3LD2	9261	2.701	15.698	25.092	30.492	2.062	27.701	2.879	17.296	22.691	30.220
15 x 15Q9 + 3LD2	20181	2.702	15.700	25.092	30.495	2.066	27.709	2.883	17.307	22.706	30.221
Sze *et al*. [175]	-	2.697	15.727	25.124	30.506	2.061	27.722	-	-	-	-

Table 6.3 Transverse displacement value in the convergence analyses. Loads at α= 254.0 mm, β= 254.0 mm and z= 6.35 mm.

will be taken as converged discretization and, therefore, it is used for the following stress evaluation. Then, to perform an accurate stress prediction, both ESL and LW models are adopted and compared using different expansion functions in the thickness direction. Figure 6.28 shows the comparison for different kinematic theories for the stress assessment. The corresponding stress values are reported in Table 6.4 for different shell theories. Clearly, the LW model should be exploited to accurately predict the stress values. Results suggest that the ESL model with a low-order model is sufficient to evaluate the circumferential normal stress, whereas it is inaccurate to predict the transverse shear stress component. Figures 6.29, 6.30 and 6.31 depict the circumferential normal and transverse shear stresses in the thickness direction for different loads for the three laminations. As previously reported, the stresses obtained using both ESL and LW models with 4LD3 are plotted to show the different capabilities of the two approaches. According to Fig. 6.29d, ESL models are not able to accurately evaluate the transverse shear stresses.

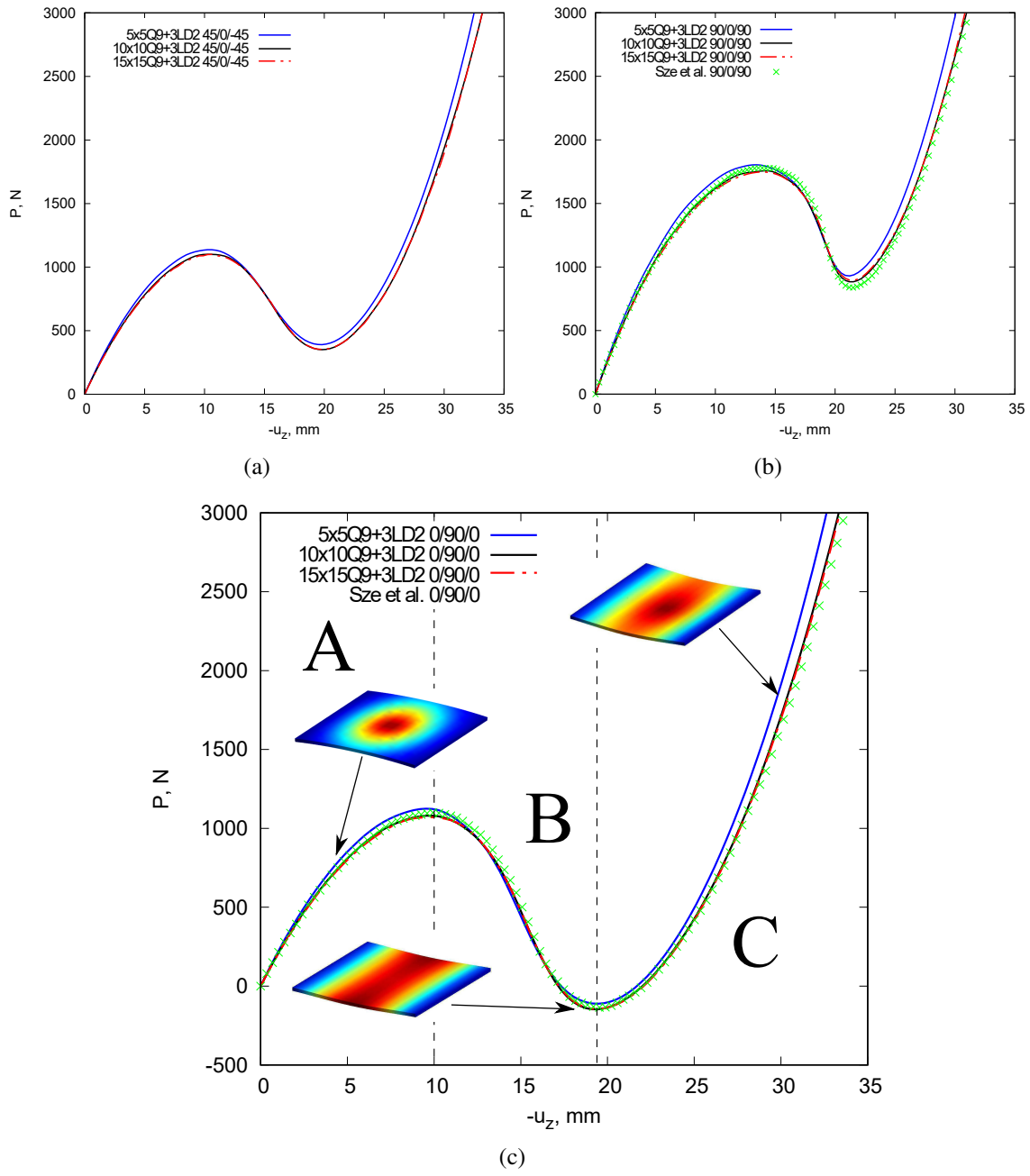

Fig. 6.27 Nonlinear static convergence analyses of the hinged cylindrical shell, using various kinematic theories. Laminations sequence: (a) $[45°,0°,45°]$, (b) $[90°,0°,90°]$, (c) $[0°,90°,0°]$.

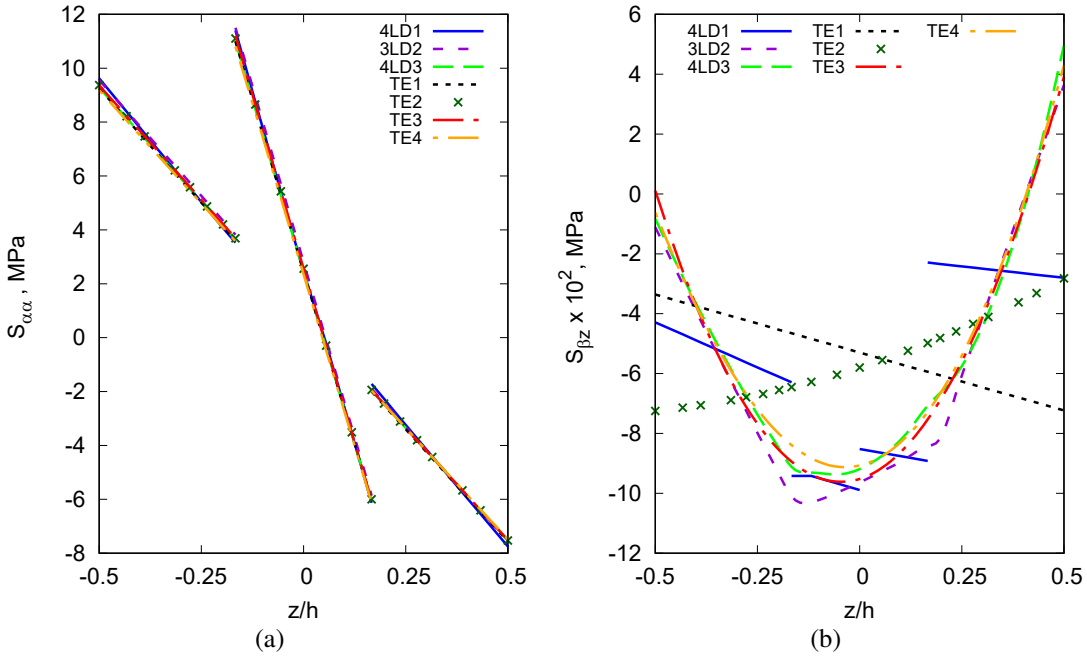

Fig. 6.28 Stress distributions of the hinged cylindrical shell using various kinematic theories. Lamination sequence $[0°, 90°, 0°]$. P= 2000 N.

Theory	DOFs	$[0°, 90°, 0°]$		$[90°, 0°, 90°]$		$[45°, 0°, -45°]$	
		$S_{\alpha\alpha}$ [MPa]	$S_{\beta z}$ [MPa$\times 10^{-2}$]	$S_{\alpha\alpha}$ [MPa]	$S_{\beta z}$ [MPa$\times 10^{-2}$]	$S_{\alpha\alpha}$ [MPa]	$S_{\beta z}$ [MPa$\times 10^{-2}$]
		2000 N	2000 N	2000 N	2000 N	1500 N	1500 N
TE1	2646	-7.563	-5.299	-21.264	-2.135	-11.840	-3.360
TE2	3969	-7.533	-5.802	-21.301	-2.530	-11.817	-3.607
TE3	5292	-7.510	-9.518	-21.214	-4.211	-11.796	-5.919
TE4	6615	-7.480	-9.069	-21.215	-4.231	-11.172	-6.260
4LD1	6615	-7.749	-9.899	-21.470	-3.861	-12.072	-5.932
3LD2	9261	-7.545	-9.635	-21.218	-3.998	-11.857	-5.943
4LD3	17199	-7.05	-9.192	-21.220	-4.157	-11.792	-5.949

Table 6.4 Normal and transvrse stresses for various kinematic theories. loads at α= 254.0 mm, β= 127.0 mm and z= 6.35 mm for $S_{\alpha\alpha}$ and z= 0 mm for $S_{\beta z}$.

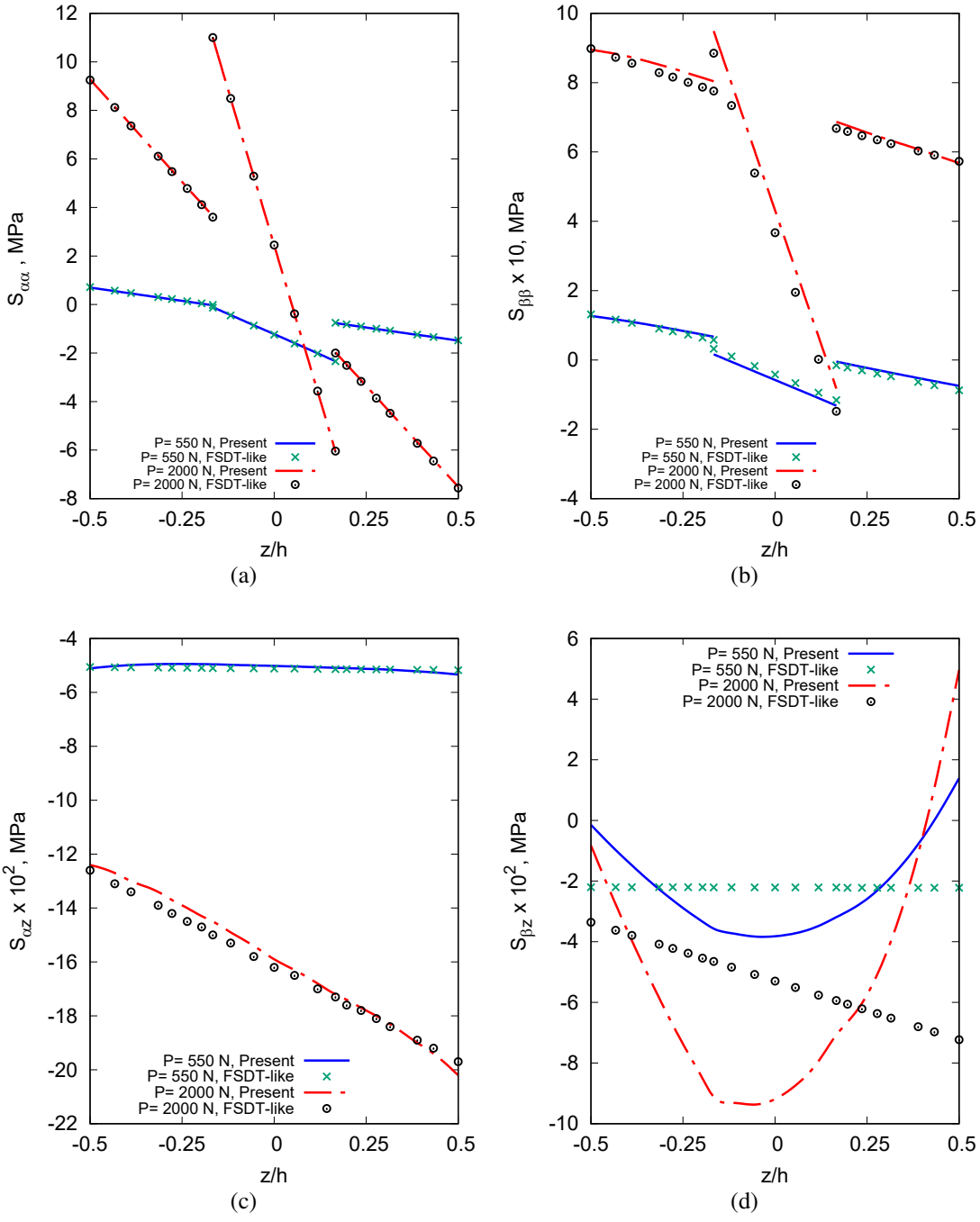

Fig. 6.29 Through-the-thickness transverse stress. α= 254.0 mm and β= 127.0 mm. $[0°, 90°, 0°]$.

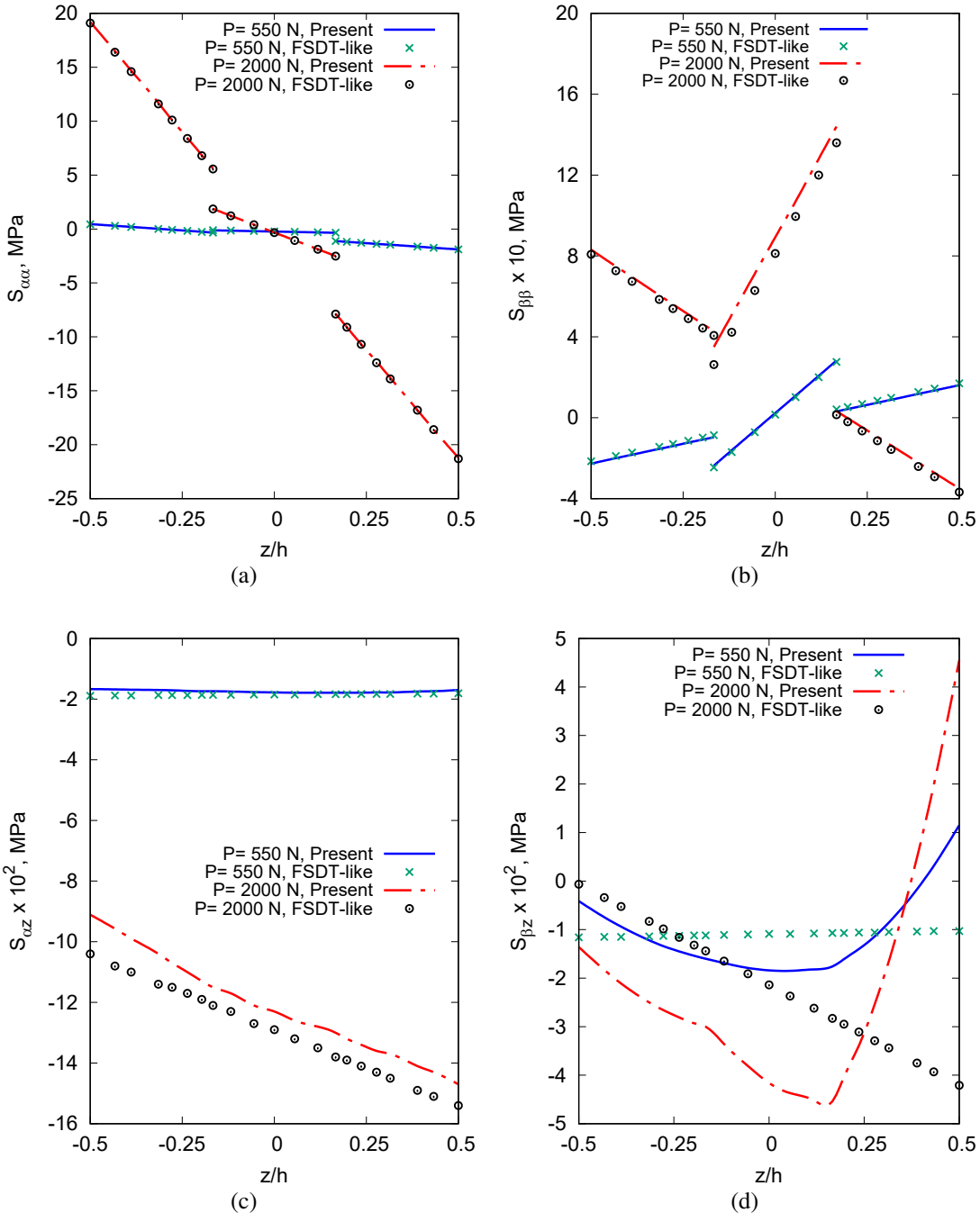

Fig. 6.30 Through-the-thickness transverse stress. α= 254.0 mm and β= 127.0 mm. $[90°, 0°, 90°]$.

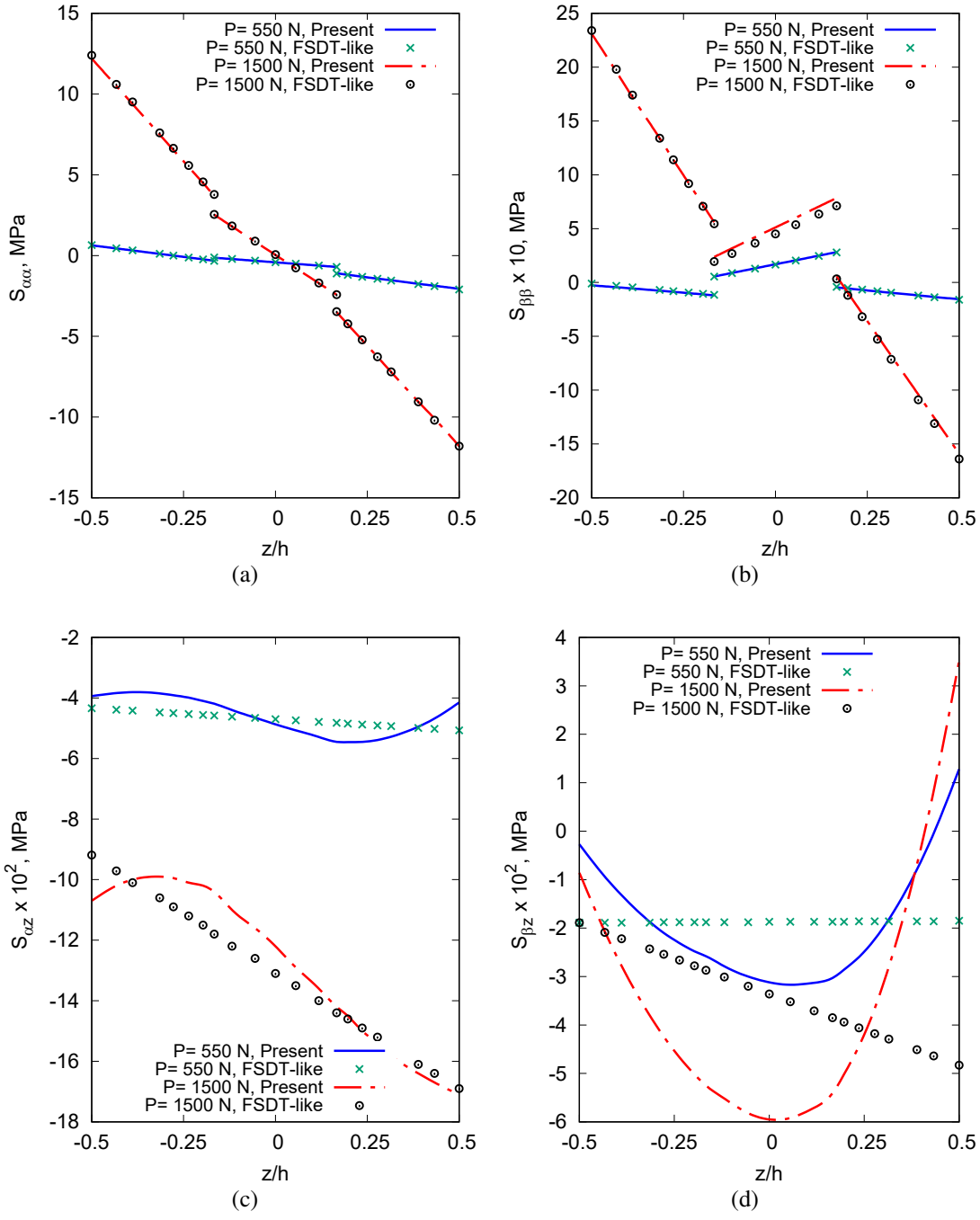

Fig. 6.31 Through-the-thickness transverse stress. α= 254.0 mm and β= 127.0 mm. $[45°, 0°, -45°]$.

Part II

Micropolar mechanics via unified CUF model

Chapter 7

Micropolar theories

7.1 State of the art

When the problem of numerically replicating the process of real scientific and engineering applications arises or when an accurate design of working structures is demanded, the classical continuum mechanics represents the most employed approach. In the previous chapters, the structural theories developed in history were described. Briefly, the classical theories are based on the works by Euler-Bernoulli [62] or Timoshenko [177] for bending models, Coulomb [49] for torsion models and Saint-Venant [54] for the analysis of structures made by arbitrary shape. Every of these theories has its own limitations, but in the respective field of application they provide reliable results. In this thesis, they are recalled as Classical Elasticity (CE). The main assumption made by CE are:

- Within a continuum, the rotations depend on the displacements, and are a direct consequence of them;
- Only translational forces occur between sorrounding points.

Beside its applicability on a large number of applications, CE may be no longer considered as not reliable when particular physical phenomena occur within the structure. In particular, in correspondence of notches and holes large stress gradients may appear, and CE could lack the ability to accurately describe them. This aspect was highligthed by Kennedy [95] in the analysis of plates with notches of elliptical and circular shape, near which a softening behavior occurs. Moreover, in the case of structures which size is comparable to its microstructural representative size, it behaves quite differently from simulation that CE could bring to. For instance, in the case of Nano-Electro Mechanical System (NEMS) and Micro-Electro Mechanical System (MEMS) devises, Li *et al.* [105] stated the need to

develope an appropriate identification of the micromechanical and nanomechanical properties, to investigate the mechanical response of the structure. In fact, as highligthed by Lam et al. [109] and McFarland and Colton [128], an accurate characterization of the material properties at the nano- and micro-level is mandatory.

7.2 Micropolar Elasticity

Several *generalized* continuum theories have been developed in history by scientific researchers to overcome the issues which arise in the mentioned cases, see Kunin [104, 103]. Maugin and Metrikine [127] reported a comprehensive review of such theories. Among these continuum theories, the one this thesis wants to focus on is the Micropolar Elasticity (ME). The main ideas of this *generalized* continuum mechanics appeared in the late 19th century, was discussed in many works. One of the most important pioneering work is represented by Voigt [184]. He proposed that the interactions between adjacent points of a structure are not only by means of translational forces (as in the CE-based theories), but also through the moments. As a natural consequence, a couple stress tensor arise, which is **independent** from the classical force stress one. An important further step was made by the brothers François and Eugène Cosserat [48] who introduced the asymmetry of the force stress and deformation tensors. The contributions by Voigt and Cosserat brothers put the basis for the development of the *generalized* continuum mechanics, including ME. The name *Micropolar Elasticity* was firstly introduced by Eringen [59–61] and Nowacki [140, 139]. In addition, every points of a continuum medium is considered as able to rotate independently by adjacent points. Thus, additional rotational unknowns need to be included in the model in order to describe the motion. As a consequence, each point is represented by six DOFs, three classical translations (related to the macrostructural behavior) and three micro-rotations (related to the microstructure). The identification of the rotational behavior of each particle needs the consideration of additional parameters to be included in the model. Regarding ME, four additional material parameters are added within the mathematical model. The physical meaning of these parameters is the contribution that the microstructural behavior has on the macrostructural one. The evaluation of these parameters is not an easy task, and it is possible by appropriate experimental tests. An important contribution on the experimental researches for this purpose was made by Lakes, on various materials and applications, see for instance the bending and torsion of human bones (Yang and Lakes [187]), polymeric foam (Lakes [187]) and bones with notches and holes (Lakes *et al.* [108]). An additional review of the experiments made for the evaluation of the addiontal paramaters was conducted by Hassanpour [76].

In history, the ME found some application for the analysis of many structures. Coupling CE, the finite element method and ME, Huang *et al.* [81], Ramezani *et al.* [152] and Hassanpour and Heppler [75] analyzed the behavior of beams made by micropolar material. The first introduces an Euler-Bernoulli theory to develop the bending model. The effects of the addional parameters are investgiated as well. The second author adopted the Timoshenko beam model, to add the shear effect to the mathematical model. Finally, the third author introduced a torsional behavior to the model, based on an extended theory of the Duleau torsion model. Higher-order models were introduced to the ME by Zozulya, for curved rods [194] and for plates and shells [195].

7.2.1 Preliminaries

In the ME framework, every point of a given structure is described by means of three translations and three micro-rotations. As a consequence the three dimensional unknwons field $\mathbf{u}(x,y,z)$ can be described as follows:

$$\mathbf{u}(x,y,z) = \left\{ \begin{array}{cccccc} u_x & u_y & u_z & \omega_x & \omega_y & \omega_z \end{array} \right\}^T \tag{7.1}$$

where u are the displacements and ω are the micro-rotations.

The classical force stress σ tensor and strain ε vectors are written in vectorial form. They read as:

$$\begin{aligned} \sigma &= \left\{ \begin{array}{cccccccccc} \sigma_{xx} & \sigma_{yy} & \sigma_{zz} & \sigma_{xy} & \sigma_{yx} & \sigma_{xz} & \sigma_{zx} & \sigma_{yz} & \sigma_{zy} \end{array} \right\}^T \\ \varepsilon &= \left\{ \begin{array}{cccccccccc} \varepsilon_{xx} & \varepsilon_{yy} & \varepsilon_{zz} & \varepsilon_{xy} & \varepsilon_{yx} & \varepsilon_{xz} & \varepsilon_{zx} & \varepsilon_{yz} & \varepsilon_{zy} \end{array} \right\}^T \end{aligned} \tag{7.2}$$

Moreover, the micropolar couple stress μ tensor and the twist χ vectors have to be defined, as follows:

$$\begin{aligned} \mu &= \left\{ \begin{array}{cccccccccc} \mu_{xx} & \mu_{yy} & \mu_{zz} & \mu_{xy} & \mu_{yx} & \mu_{xz} & \mu_{zx} & \mu_{yz} & \mu_{zy} \end{array} \right\}^T \\ \chi &= \left\{ \begin{array}{cccccccccc} \chi_{xx} & \chi_{yy} & \chi_{zz} & \chi_{xy} & \chi_{yx} & \chi_{xz} & \chi_{zx} & \chi_{yz} & \chi_{zy} \end{array} \right\}^T \end{aligned} \tag{7.3}$$

In this thesis, only isotropic linear elastic materials are considered. Thus, two constitutive relations needs to be described, one relating the force stress and the deformation vectors (Eq.

7.2) and the other between the couple stress and twist vectors (Eq. 7.3).

$$\sigma = \lambda(tr\varepsilon)\mathbf{I} + (\mu+\alpha)\varepsilon + (\mu-\alpha)\varepsilon^T, \qquad \mu = \beta(tr\chi)\mathbf{I} + (\gamma+\varepsilon)\chi + (\gamma-\varepsilon)\chi^T \tag{7.4}$$

where α, β, γ and ε are the four additional micropolar elastic constants (see Ref. [195]) and $\mathbf{I}$ is identity matrix. Equation 7.4 can be written in a matricial form, as follows:

$$\sigma = \mathbf{C}\varepsilon, \qquad \mu = \mathbf{A}\chi \tag{7.5}$$

where $\mathbf{C}$ and $\mathbf{A}$ are the two material matrices:

$$\mathbf{C} = \begin{bmatrix} C_{11} & C_{12} & C_{13} & 0 & 0 & 0 & 0 & 0 & 0 \\ C_{12} & C_{22} & C_{23} & 0 & 0 & 0 & 0 & 0 & 0 \\ C_{13} & C_{23} & C_{33} & 0 & 0 & 0 & 0 & 0 & 0 \\ 0 & 0 & 0 & C_{44}^{M} & C_{44}^{MT} & 0 & 0 & 0 & 0 \\ 0 & 0 & 0 & C_{44}^{MT} & C_{44}^{M} & 0 & 0 & 0 & 0 \\ 0 & 0 & 0 & 0 & 0 & C_{55}^{M} & C_{55}^{MT} & 0 & 0 \\ 0 & 0 & 0 & 0 & 0 & C_{55}^{MT} & C_{55}^{M} & 0 & 0 \\ 0 & 0 & 0 & 0 & 0 & 0 & 0 & C_{66}^{M} & C_{66}^{MT} \\ 0 & 0 & 0 & 0 & 0 & 0 & 0 & C_{66}^{MT} & C_{66}^{M} \end{bmatrix} \tag{7.6}$$

and

$$\mathbf{A} = \begin{bmatrix} A_{11} & A_{12} & A_{13} & 0 & 0 & 0 & 0 & 0 & 0 \\ A_{12} & A_{22} & A_{23} & 0 & 0 & 0 & 0 & 0 & 0 \\ A_{13} & A_{23} & A_{33} & 0 & 0 & 0 & 0 & 0 & 0 \\ 0 & 0 & 0 & A_{44}^{M} & A_{44}^{MT} & 0 & 0 & 0 & 0 \\ 0 & 0 & 0 & A_{44}^{MT} & A_{44}^{M} & 0 & 0 & 0 & 0 \\ 0 & 0 & 0 & 0 & 0 & A_{55}^{M} & A_{55}^{MT} & 0 & 0 \\ 0 & 0 & 0 & 0 & 0 & A_{55}^{MT} & A_{55}^{M} & 0 & 0 \\ 0 & 0 & 0 & 0 & 0 & 0 & 0 & A_{66}^{M} & A_{66}^{MT} \\ 0 & 0 & 0 & 0 & 0 & 0 & 0 & A_{66}^{MT} & A_{66}^{M} \end{bmatrix} \tag{7.7}$$

$$\begin{aligned} C_{11} = C_{22} = C_{33} &= \lambda + 2\mu, \\ C_{12} = C_{13} = C_{23} &= \lambda, \\ C_{44}^{M} = C_{55}^{M} = C_{66}^{M} &= \mu + \alpha, \\ C_{44}^{MT} = C_{55}^{MT} = C_{66}^{MT} &= \mu - \alpha \end{aligned} \tag{7.8}$$

$$\begin{aligned} A_{11} = A_{22} = A_{33} &= \beta + 2\gamma, \\ A_{12} = A_{13} = A_{23} &= \beta, \\ A_{44}^{M} = A_{55}^{M} = A_{66}^{M} &= \gamma + \varepsilon, \\ A_{44}^{MT} = A_{55}^{MT} = A_{66}^{MT} &= \gamma - \varepsilon \end{aligned} \tag{7.9}$$

where λ and μ are the Lamé constants of classical elasticity.

Finally, the kinematic relations are formulated as:

$$\varepsilon = (\mathbf{b}_{m1})\mathbf{u}, \qquad \chi = (\mathbf{b}_{m2})\mathbf{u} \tag{7.10}$$

where $\mathbf{b}_{m1}$ and $\mathbf{b}_{m2}$ are the differential operators:

$$\mathbf{b}_{m1} = \begin{bmatrix} \partial_x & 0 & 0 & 0 & 0 & 0 \\ 0 & \partial_y & 0 & 0 & 0 & 0 \\ 0 & 0 & \partial_z & 0 & 0 & 0 \\ \partial_y & 0 & 0 & 0 & 0 & 1 \\ 0 & \partial_x & 0 & 0 & 0 & -1 \\ \partial_z & 0 & 0 & 0 & -1 & 0 \\ 0 & 0 & \partial_x & 0 & 1 & 0 \\ 0 & \partial_z & 0 & 1 & 0 & 0 \\ 0 & 0 & \partial_y & -1 & 0 & 0 \end{bmatrix}, \qquad \mathbf{b}_{m2} = \begin{bmatrix} 0 & 0 & 0 & \partial_x & 0 & 0 \\ 0 & 0 & 0 & 0 & \partial_y & 0 \\ 0 & 0 & 0 & 0 & 0 & \partial_z \\ 0 & 0 & 0 & \partial_y & 0 & 0 \\ 0 & 0 & 0 & 0 & \partial_x & 0 \\ 0 & 0 & 0 & \partial_z & 0 & 0 \\ 0 & 0 & 0 & 0 & 0 & \partial_x \\ 0 & 0 & 0 & 0 & \partial_z & 0 \\ 0 & 0 & 0 & 0 & 0 & \partial_y \end{bmatrix} \tag{7.11}$$

Chapter 8

1D CUF-Micropolar model

8.1 Unified 1D beam model based on Micropolar Elasticity

For the evaluation of a beam model, consider a 1D structure placed in a cartesian reference system, so that the cross-section Ω is on the x,z plane. Consequently, the axis of the beam lays along the y direction and measures L.

CUF approach is used for the evaluation of the three dimensional unknowns field $\mathbf{u}(x,y,z)$. As already described in the previous chapters, it can be expressed as a generic expansion of the beam axis unknowns. Briefly:

$$\mathbf{u}(x,y,z) = F_s(x,z)\mathbf{u}_s(y), \qquad s = 1,2,....,M \tag{8.1}$$

where F_s represent the expansion functions over the cross-section x,z, $\mathbf{u}_s$ is the vector of the *generalized* unknowns which are placed along the beam axis, M is the order of the expansion, and the summation operation is assumed by the repeated subscript s.
In this chapter, Lagrange expansion are employed as expansion functions, which guarantee the adoption of Lagrange polynomials for the approximation of the displacement and micro-rotation fields on the cross-section. The same F_s are used for both translational displacements and micro-rotation.

8.1.1 Finite element formulation

The Finite Element Method is hereafter employed for the discretization of the beam axis. The generalized displacement vector $\mathbf{u}_s(y)$ can be expressed as a function of the nodal unknowns

through opportune shape functions N_j, as follows:

$$\mathbf{u}_s(y) = N_j(y)\mathbf{q}_{sj} \qquad j = 1,2,\ldots,p+1 \tag{8.2}$$

where p and j represent the number of terms used within the shape functions and the summation notation, respectively. $\mathbf{q}_{sj}$ is the vector of the nodal unkwnons, and can be expressed as follows:

$$\mathbf{q}_{sj} = \left\{ \begin{array}{cccccc} q_{u_{x_{sj}}} & q_{u_{y_{sj}}} & q_{u_{z_{sj}}} & \omega_{z_{sj}} & \omega_{z_{sj}} & \omega_{z_{sj}} \end{array} \right\}^T \tag{8.3}$$

In the Micropolar Elasticity approach, the number of terms used for the shape function (i.e. the degree of the beam axis discretization) does not depend from the order of the cross-section expansion function F_s. In this work, classical four-noded finite elements (B4) are employed. They ensure a cubic approximation.

8.1.2 Fundamental Nuclei

For the evaluation of the equilibrium equations, the principle of virtual work is hereafter recalled:

$$\delta L_{\text{int}} = \delta L_{\text{ext}} \tag{8.4}$$

Where the virtual variation of the internal work and the virtual variation of the external work are represented by L_{int} and L_{ext}, respectively. Introducing the force stress, couple stress, strain and twist vectors (σ, μ, ε and χ), the L_{int} can be evaluated as follows:

$$\delta L_{\text{int}} = \int_V \left((\delta\varepsilon^T \sigma) + (\delta\chi^T \mu) \right) \, dV \tag{8.5}$$

where V stands for the volume of the beam structure (i.e. $V = \Omega \times L$). Given the CUF and FEM equation (Eqs. (8.1,8.2)), the relations between strains, twist and unknwons vectors are:

$$\varepsilon = (\mathbf{B}_{m1}^{sj})\mathbf{q}_{sj}, \qquad \chi = (\mathbf{B}_{m2}^{sj})\mathbf{q}_{sj} \tag{8.6}$$

where $\mathbf{B}_{m1}^{sj}$ and $\mathbf{B}_{m2}^{sj}$ are algebraic matrices, which form is the following:

$$
\mathbf{B}_{m1}^{sj} = \mathbf{b}_{m1}(F_s N_j) = \begin{bmatrix}
F_{s,x}N_j & 0 & 0 & 0 & 0 & 0 \\
0 & F_s N_{j,y} & 0 & 0 & 0 & 0 \\
0 & 0 & F_{s,z}N_j & 0 & 0 & 0 \\
F_s N_{j,y} & 0 & 0 & 0 & 0 & F_s N_j \\
0 & F_{s,x}N_j & 0 & 0 & 0 & -F_s N_j \\
F_{s,z}N_j & 0 & 0 & 0 & -F_s N_j & 0 \\
0 & 0 & F_{s,x}N_j & 0 & F_s N_j & 0 \\
0 & F_{s,z}N_j & 0 & F_s N_j & 0 & 0 \\
0 & 0 & F_s N_{j,y} & -F_s N_j & 0 & 0
\end{bmatrix}
$$

$$
\mathbf{B}_{m2}^{sj} = \mathbf{b}_{m2}(F_s N_j) = \begin{bmatrix}
0 & 0 & 0 & F_{s,x}N_j & 0 & 0 \\
0 & 0 & 0 & 0 & F_s N_{j,y} & 0 \\
0 & 0 & 0 & 0 & 0 & F_{s,z}N_j \\
0 & 0 & 0 & F_s N_{j,y} & 0 & 0 \\
0 & 0 & 0 & 0 & F_{s,x}N_j & 0 \\
0 & 0 & 0 & F_{s,z}N_j & 0 & 0 \\
0 & 0 & 0 & 0 & 0 & F_{s,x}N_j \\
0 & 0 & 0 & 0 & F_{s,z}N_j & 0 \\
0 & 0 & 0 & 0 & 0 & F_s N_{j,y}
\end{bmatrix}
\tag{8.7}
$$

Introducing Eq. (8.6) and the constitutive equations:

$$\begin{aligned} \delta L_{\text{int}} &= \delta \mathbf{q}_{\tau i}^T \int \left((\mathbf{B}_{m1}^{\tau i})^T \mathbf{C} (\mathbf{B}_{m1}^{sj}) + (\mathbf{B}_{m2}^{\tau i})^T \mathbf{A} (\mathbf{B}_{m2}^{sj}) \right) dV \ \mathbf{q}_{sj} \\ &= \delta \mathbf{q}_{\tau i}^T \mathbf{K}^{ij\tau s} \mathbf{q}_{sj} \end{aligned} \tag{8.8}$$

where $\mathbf{K}^{ij\tau s}$ represents the stiffness matrix. This matrix is evaluated by means of *fundamental nucleus*, which are 6×6 matrices. They have the same properties of the FNs presented in the previous chapters, so that by an opportune choice of the indexes τ, s, i, j they can be expanded to reach any desiderd structural theory, from low- to higher-order. The complete expression of the matrix is introduced:

$$\mathbf{K}_{uuxx}^{\tau sij} = C_{11} \int_\Omega F_{\tau,x} F_{s,x} d\Omega \int_L N_i N_j dL + C_{55}^M \int_\Omega F_{\tau,z} F_{s,z} d\Omega \int_L N_i N_j dL +$$

$$C_{44}^M \int_\Omega F_\tau F_s d\Omega \int_L N_{i,y} N_{j,y} dL$$

$$\mathbf{K}_{uuxy}^{ij\tau s} = C_{12} \int_\Omega F_\tau F_{s,x} d\Omega \int_L N_{i,y} N_j dL + C_{44}^{MT} \int_\Omega F_{\tau,x} F_s d\Omega \int_L N_i N_{j,y} dL$$

$$\mathbf{K}_{uuxz}^{ij\tau s} = C_{55}^{MT} \int_\Omega F_{\tau,x} F_{s,z} d\Omega \int_L N_i N_j dL + C_{13} \int_\Omega F_{\tau,z} F_{s,x} d\Omega \int_L N_i N_j dL$$

$$\mathbf{K}_{uuyx}^{ij\tau s} = C_{44}^{MT} \int_\Omega F_{\tau,z} F_{s,x} d\Omega \int_L N_{i,y} N_j dL + C_{12} \int_\Omega F_{\tau,x} F_s d\Omega \int_L N_i N_{j,y} dL$$

$$\mathbf{K}_{uuyy}^{\tau sij} = C_{44}^M \int_\Omega F_{\tau,x} F_{s,x} d\Omega \int_L N_i N_j dL + C_{66}^M \int_\Omega F_{\tau,z} F_{s,z} N_i N_j d\Omega \int_L +$$

$$C_{22} \int_\Omega F_\tau F_s d\Omega \int_L N_{i,y} N_{j,y} dL$$

$$\mathbf{K}_{uuyz}^{ij\tau s} = C_{66}^{MT} \int_\Omega F_\tau F_{s,z} d\Omega \int_L N_{i,y} N_j dL + C_{23} \int_\Omega F_{\tau,z} F_s d\Omega \int_L N_i N_{j,y} dL$$

$$\mathbf{K}_{uuzx}^{ij\tau s} = C_{13} \int_\Omega F_{\tau,x} F_{s,z} d\Omega \int_L N_i N_j dL + C_{55}^{MT} \int_\Omega F_{\tau,z} F_{s,x} d\Omega \int_L N_i N_j dL$$

$$\mathbf{K}^{ij\tau s}_{uuzy} = C_{23}\int_{\Omega} F_{\tau}F_{s_{,z}}d\Omega\int_{L} N_{i_{,y}}N_j dL + C^{MT}_{66}\int_{\Omega} F_{\tau_{,z}}F_s d\Omega\int_{L} N_i N_{j_{,y}}dL$$

$$\mathbf{K}^{\tau sij}_{uuzz} = C^{MT}_{55}\int_{\Omega} F_{\tau_{,x}}F_{s_{,x}}d\Omega\int_{L} N_i N_j dL + C_{33}\int_{\Omega} F_{\tau_{,z}}F_{s_{,z}}d\Omega\int_{L} N_i N_j dL +$$

$$C^{MT}_{66}\int_{\Omega} F_{\tau}F_s d\Omega\int_{L} N_{i_{,y}}N_{j_{,y}}dL$$

$$\mathbf{K}^{ij\tau s}_{u\omega xx} = 0$$

$$\mathbf{K}^{ij\tau s}_{u\omega xy} = -C^{M}_{55}\int_{\Omega} F_{\tau}F_{s_{,z}}d\Omega\int_{L} N_i N_j dL + C^{MT}_{55}\int_{\Omega} F_{\tau}F_{s_{,z}}d\Omega\int_{L} N_i N_j dL$$

$$\mathbf{K}^{ij\tau s}_{u\omega xz} = C^{M}_{44}\int_{\Omega} F_{\tau}F_s d\Omega\int_{L} N_i N_{j_{,y}}dL - C^{MT}_{44}\int_{\Omega} F_{\tau}F_s d\Omega\int_{L} N_i N_{j_{,y}}dL$$

$$\mathbf{K}^{ij\tau s}_{u\omega yx} = C^{M}_{66}\int_{\Omega} F_{\tau}F_{s_{,z}}d\Omega\int_{L} N_i N_j dL - C^{MT}_{66}\int_{\Omega} F_{\tau}F_{s_{,z}}d\Omega\int_{L} N_i N_j dL$$

$$\mathbf{K}^{ij\tau s}_{u\omega yy} = 0$$

$$\mathbf{K}^{ij\tau s}_{u\omega yz} = C^{MT}_{44}\int_{\Omega} F_{\tau}F_{s_{,x}}d\Omega\int_{L} N_i N_j dL - C^{M}_{44}\int_{\Omega} F_{\tau}F_{s_{,x}}d\Omega\int_{L} N_i N_j dL$$

$$\mathbf{K}^{ij\tau s}_{u\omega zx} = -C^{M}_{66}\int_{\Omega} F_{\tau}F_s d\Omega\int_{L} N_i N_{j_{,y}}dL + C^{MT}_{66}\int_{\Omega} F_{\tau}F_s d\Omega\int_{L} N_i N_{j_{,y}}dL$$

$$\mathbf{K}^{ij\tau s}_{u\omega zy} = C^{M}_{55}\int_{\Omega} F_{\tau}F_{s_{,x}}d\Omega\int_{L} N_i N_j dL - C^{MT}_{55}\int_{\Omega} F_{\tau}F_{s_{,x}}d\Omega\int_{L} N_i N_j dL$$

$$\mathbf{K}^{ij\tau s}_{u\omega zz} = 0$$

$$\mathbf{K}^{ij\tau s}_{\omega uxx} = 0$$

$$\mathbf{K}^{ij\tau s}_{\omega uxy} = C^{M}_{66}\int_{\Omega} F_s F_{t_{,z}}d\Omega\int_{L} N_i N_j dL - C^{MT}_{66}\int_{\Omega} F_s F_{t_{,z}}d\Omega\int_{L} N_i N_j dL$$

$$\mathbf{K}^{ij\tau s}_{\omega uxz} = -C^{M}_{66}\int_{\Omega} F_s F_t d\Omega\int_{L} N_{i_{,y}}N_j dL + C^{MT}_{66}\int_{\Omega} F_s F_t d\Omega\int_{L} N_{i_{,y}}N_{j_{,y}}dL$$

$$\mathbf{K}^{ij\tau s}_{\omega uyx} = -C^{M}_{55}\int_{\Omega} F_s F_{t,z} d\Omega \int_{L} N_i N_j dL + C^{MT}_{55}\int_{\Omega} F_s F_{t,z} d\Omega \int_{L} N_i N_j dL$$

$$\mathbf{K}^{ij\tau s}_{\omega uyy} = 0$$

$$\mathbf{K}^{ij\tau s}_{\omega uyz} = C^{M}_{55}\int_{\Omega} F_s F_{t,x} d\Omega \int_{L} N_i N_j dL - C^{MT}_{55}\int_{\Omega} F_s F_{t,x} d\Omega \int_{L} N_i N_j dL$$

$$\mathbf{K}^{ij\tau s}_{\omega uzx} = C^{M}_{44}\int_{\Omega} F_s F_t d\Omega \int_{L} N_{i,y} N_j dL - C^{MT}_{44}\int_{\Omega} F_s F_t d\Omega \int_{L} N_{i,y} N_j dL$$

$$\mathbf{K}^{ij\tau s}_{\omega uzy} = -C^{M}_{44}\int_{\Omega} F_s F_{t,x} d\Omega \int_{L} N_i N_j dL + C^{MT}_{44}\int_{\Omega} F_s F_{t,x} d\Omega \int_{L} N_i N_j dL$$

$$\mathbf{K}^{ij\tau s}_{\omega uzz} = 0$$

$$\mathbf{K}^{ij\tau s}_{\omega\omega xx} = 2C^{M}_{66}\int_{\Omega} F_s F_t d\Omega \int_{L} N_i N_j dL - 2C^{MT}_{66}\int_{\Omega} F_s F_t d\Omega \int_{L} N_i N_j dL +$$

$$A_{11}\int_{\Omega} F_{\tau,x} F_{s,x} d\Omega \int_{L} N_i N_j dL + A_{55}\int_{\Omega} F_{\tau,z} F_{s,z} d\Omega \int_{L} N_i N_j dL + A_{44}\int_{\Omega} F_\tau F_s d\Omega \int_{L} N_{i,y} N_{j,y} dL$$

$$\mathbf{K}^{ij\tau s}_{uuxz} = A_{12}\int_{\Omega} F_\tau F_{s,x} d\Omega \int_{L} N_{i,y} N_j dL + A^{MT}_{44}\int_{\Omega} F_{\tau,x} F_s d\Omega \int_{L} N_i N_{j,y} dL$$

$$\mathbf{K}^{ij\tau s}_{uuxz} = A^{MT}_{55}\int_{\Omega} F_{\tau,x} F_{s,z} d\Omega \int_{L} N_i N_j dL + A_{13}\int_{\Omega} F_{\tau,z} F_{s,x} d\Omega \int_{L} N_i N_j dL$$

$$\mathbf{K}^{ij\tau s}_{uuyx} = A^{MT}_{44}\int_{\Omega} F_\tau F_{s,x} d\Omega \int_{L} N_{i,y} N_j dL + A_{12}\int_{\Omega} F_{\tau,x} F_s d\Omega \int_{L} N_i N_{j,y} dL$$

$$\mathbf{K}^{ij\tau s}_{\omega\omega xx} = 2C^{M}_{55}\int_{\Omega} F_s F_t d\Omega \int_{L} N_i N_j dL - 2C^{MT}_{55}\int_{\Omega} F_s F_t d\Omega \int_{L} N_i N_j dL +$$

$$A_{44}\int_{\Omega} F_{\tau,x} F_{s,x} d\Omega \int_{L} N_i N_j dL + A_{66}\int_{\Omega} F_{\tau,z} F_{s,z} d\Omega \int_{L} N_i N_j dL + A_{22}\int_{\Omega} F_\tau F_s d\Omega \int_{L} N_{i,y} N_{j,y} dL$$

$$\mathbf{K}^{ij\tau s}_{uuyz} = A^{MT}_{66}\int_{\Omega} F_\tau F_{s,z} d\Omega \int_{L} N_{i,y} N_j dL + A_{23}\int_{\Omega} F_{\tau,z} F_s d\Omega \int_{L} N_i N_{j,y} dL$$

$$\mathbf{K}^{ij\tau s}_{uuzx} = A_{13}\int_\Omega F_{\tau_{,x}} F_{s_{,z}} d\Omega \int_L N_i N_j dL + A^{MT}_{55}\int_\Omega F_{\tau_{,z}} F_{s_{,x}} d\Omega \int_L N_i N_j dL$$

$$\mathbf{K}^{ij\tau s}_{uuzy} = A^{MT}_{66}\int_\Omega F_{\tau_{,z}} F_s d\Omega \int_L N_i N_{j,y} dL + A_{23}\int_\Omega F_\tau F_{s_{,z}} d\Omega \int_L N_{i,y} N_j dL$$

$$\mathbf{K}^{ij\tau s}_{\omega\omega xx} = 2C^M_{44}\int_\Omega F_s F_t d\Omega \int_L N_i N_j dL - 2C^{MT}_{44}\int_\Omega F_s F_t d\Omega \int_L N_i N_j dL +$$

$$A_{55}\int_\Omega F_{\tau_{,x}} F_{s_{,x}} d\Omega \int_L N_i N_j dL + A_{33}\int_\Omega F_{\tau_{,z}} F_{s_{,z}} d\Omega \int_L N_i N_j dL + A_{66}\int_\Omega F_\tau F_s d\Omega \int_L N_{i,y} N_{j,y} dL$$

8.2 Examples

8.2.1 Comparison with literature results

As a first example, the capability of the present model is highlighted with the bending of a cantilver beam structure. The case study is taken by the work of Ramezani [152]. The geometric properties are shown in Fig. 8.1(a), where a rectangular cross-section is depicted. The length-to-side ratio $L/h = 100$ and the aspect ratio $h/b = 4$. Figure 8.1(b) shows both cross-sectional discretization and loading condition, involving a L9 Lagrange polynomial and a transverse loading. The material is supposed to be isotropic with material parameters Young modulus $E = 20$ GPa, Poisson modulus $\nu = 0.3$, whereas the micropolar additional parameters are $\alpha = \dfrac{G}{40}$, $\beta = 0$ and $\varepsilon = \gamma = \dfrac{G}{10^4}$. Finally, 10 B4 elements are used along the beam axis, as the beam axis discretization. The static results are shown in Fig. 8.2, where the displacements (Fig. 8.1(a)) and the micro-rotations (Fig. 8.1(b)) of point A (see Fig. 8.1(b)) are shown. Clearly, a great agreement between the proposed model and the reference results arise. As far as the micro-rotations are concerned, in the reference paper an oscillatory behavior shown, which is meaningless for the given problem, as stated by Hassanpour and Heppler [75]. Finally, for comparison purpose, the results using CE is illustrated, showing a softening behavior compared to the ME solution, This means that a portion of the external energy is used to make each node rotate. As a second example, the results from Hassanpour and Heppler [75] are taken as reference. The structure is a cantilever beam with square cross-section, so that $\dfrac{L}{\sqrt{\dfrac{I}{A}}} = 10$, with A being the cross-sectional area, see Fig. 8.3(a). The cross-section discretization is given by a L9 polynomial, as depicted

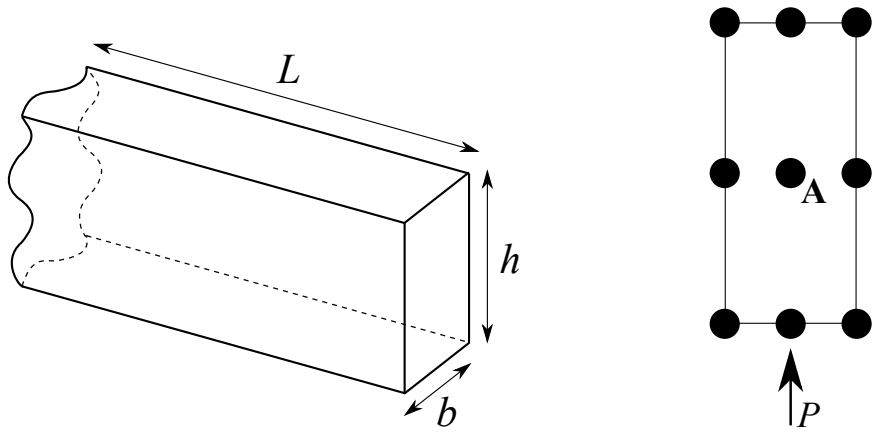

(a) (b)

Fig. 8.1 Geometric conditions (a), loading and LE cross-section approxmation (b) for the cantilever micropolar beam from Ramezani [152].

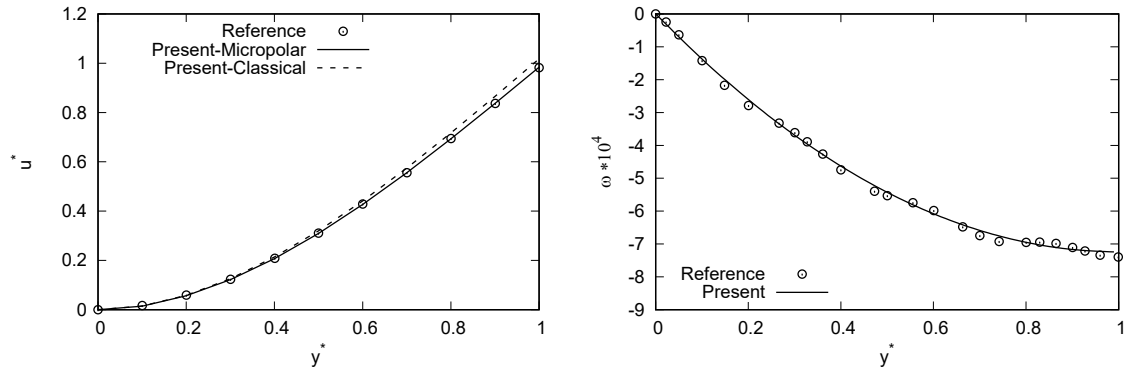

(a) (b)

Fig. 8.2 Displacements (a) and micro-rotations [rad] (b) for the canilever micropolar beam. Reference results come from Ramezani [152]. $u^* = \dfrac{3EIu(y)}{FL^3}$, $y^* = \dfrac{y}{L}$, $\alpha = \dfrac{G}{40}$ and $\varepsilon = \gamma = \dfrac{G}{10^4}$.

in Fig. 8.3(b). In the same figure the transvers loading is reported, so that $\dfrac{P}{EA} = 5 \times 10^{-6}$. Finally, the material properties involve $\dfrac{\alpha}{E} = 10^{-2}$, $\dfrac{\gamma}{E} = \dfrac{\varepsilon}{E} = 2.5 \times 10^{-4}$. Figure 8.4(a) shows the displacements obtained with both CE and ME, which are compared with the reference results. The conclusions are the same as the previous example, including the matching with reference results, which guarantee the accuracy of the proposed mode. The same accuracy is demonstrated by looking at the micro-rotations. The reference results are obtained starting from Timoshenko's assumptions, whereas the present model makes use of

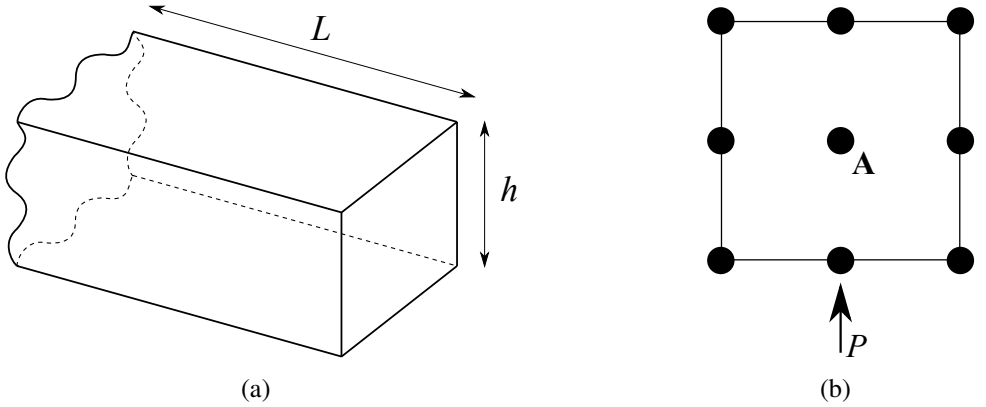

Fig. 8.3 Geometric conditions (a), loading and LE cross-section approximation (b) for the cantilever micropolar beam from Hassanpour and Heppler [75].

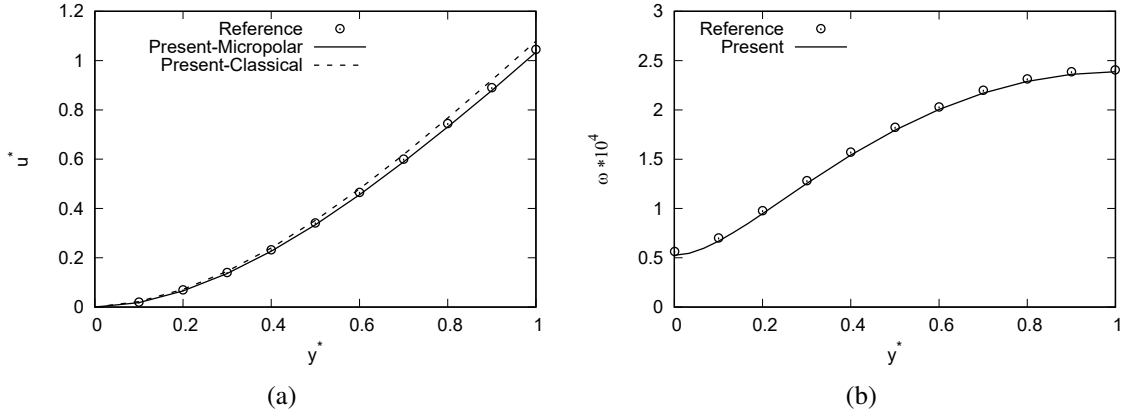

Fig. 8.4 Displacements (a) and micro-rotations [rad] (b) for the cantilever micropolar beam from Hassanpour and Heppler [75]. $u^* = \dfrac{3EILu(y)}{FAL^2}$, $y^* = \dfrac{y}{L}$, $\dfrac{\alpha}{E} = 10^{-2}$, $\dfrac{\gamma}{E} = \dfrac{\varepsilon}{E} = 2.5 \times 10^{-4}$.

refined higher-order theories. This difference between the kinematics models is the reason of the slight discrepancy between the two solutions, but to the cross-section deformation. Given the capability of the present model, the stress distributions are evaluated. The values of $\sigma_{yy}\, h^2/P$ and $\sigma_{yy}\, h^2/P$ are evaluated along the cross-section at three different zones of the beam, at $y = 0.1L$, $y = 0.5L$ and $y = 0.9L$. The values of the yy component are shown in Table 8.1 and the same are depicted in Fig. Fig. 8.5. As already demonstrated by the displacements and micro-rotation results, the results from ME are lower than the CE ones. Figure 8.6 shows the distribution of the shear stress components σ_{YZ} and σ_{ZY} at $y = 0.5L$. For their evaluation a L16 Lagrange polynomial is employed within the cross-section, instead of the L9 used for the displacements, micro-rotations and σ_{YY} (see [36, 28]).

	$\sigma_{YY}\ h^2/P$					
	y=0		y=0.5L		y=L	
z/h	CE	ME	CE	ME	CE	ME
0.500	15.28	14.88	8.663	8.259	1.938	1.841
0.333	10.19	9.920	5.775	5.506	1.292	1.227
0.167	5.090	4.960	2.888	2.735	0.646	0.614
0.000	0.000	0.000	0.000	0.000	0.000	0.000
-0.167	-5.090	-4.960	-2.888	-2.735	-0.646	-0.614
-0.333	-10.19	-9.920	-5.775	-5.506	-1.292	-1.227
-0.500	-15.28	-14.88	-8.663	-8.259	-1.938	-1.841

Table 8.1 CE and ME axial stress $\sigma_{YY}\ h^2/P$ components along the thickness of the beam, adopting L9 model. $\frac{\alpha}{E} = 10^{-2}$, $\frac{\gamma}{E} = \frac{\varepsilon}{E} = 2.5 \times 10^{-4}$.

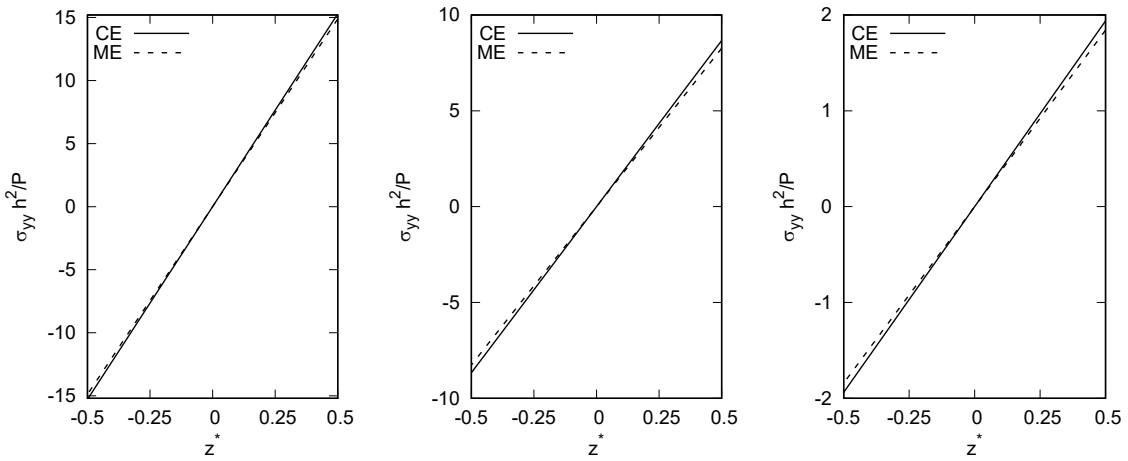

(a) y=0.1L (b) y=0.5L (c) y=0.9L

Fig. 8.5 CE and ME axial stress $\sigma_{YY}\ h^2/P$ components along the thickness of the beam, adopting L9 model. $\frac{\alpha}{E} = 10^{-2}$, $\frac{\gamma}{E} = \frac{\varepsilon}{E} = 2.5 \times 10^{-4}$.

8.2.2 Effects of micropolar mechanical parameters

The influence of the micropolar parameters α, γ and ε in the static behavior of isotropic structures is evaluated. The analysis case is the same as the one in the previous example, and the classical elastic constants E and ν are taken as constant. Instead, the values of the micropolar parameters is varying. In the first analysis, the infleunce of the α parameter is considered, whereas the other material parameters are fixed. The results are shown in Fig. 8.7, where the ratio of the ME (u_M) and the CE (u_C) solutions is reported over the α

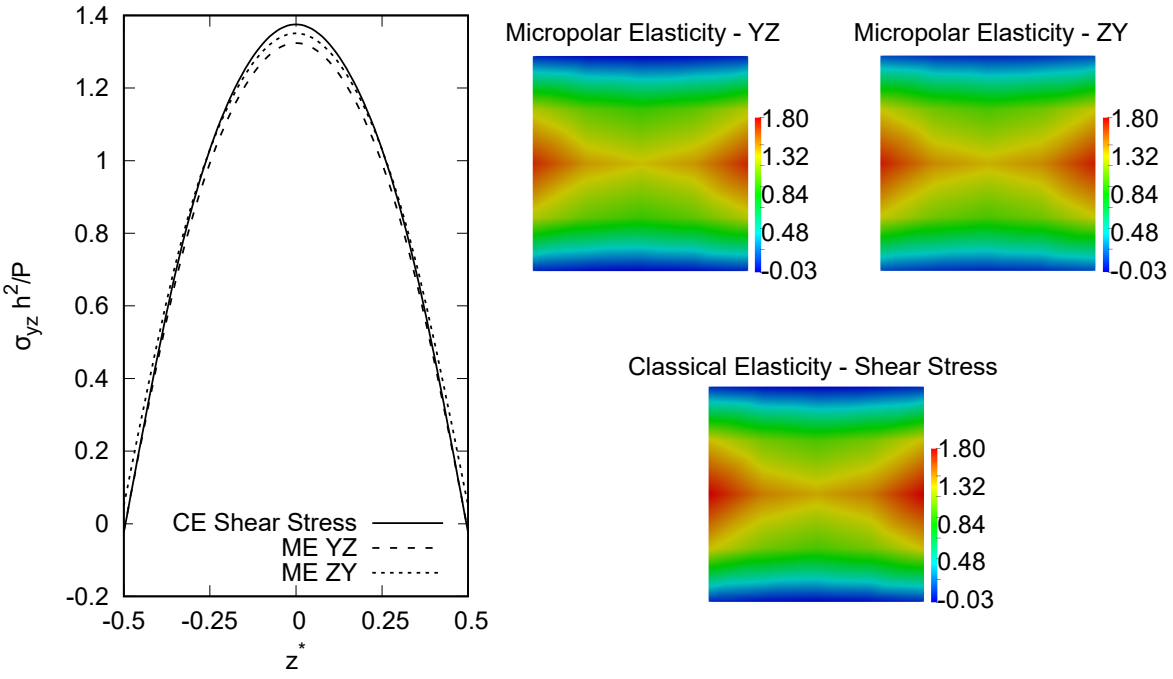

(a) y=0.5L

Fig. 8.6 CE and ME transverse stress $\sigma_{YZ}\, h^2/P$ components along the thickness ($z^* = z/h$), adopting L9 model. $\dfrac{\alpha}{E} = 10^{-2}$, $\dfrac{\gamma}{E} = \dfrac{\varepsilon}{E} = 2.5 \times 10^{-4}$.

material parameter. Clearly, when the value of the parameter decreases, the ME solution gets closer to the CE one. On the contrary, when it increases, the ME solution increases. The

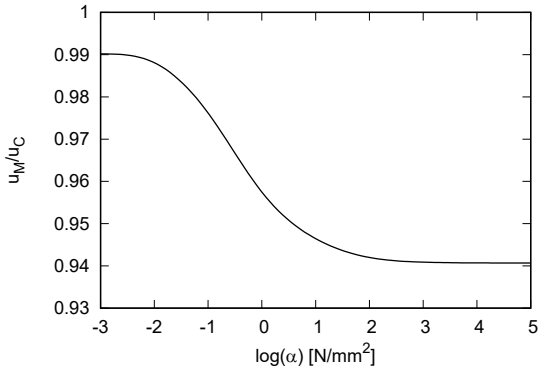

Fig. 8.7 Ratio of the ME (u_M) and the CE (u_C) solutions over the α material parameter.

same approach is employed varying γ and ε. The conclusion are the same as in the previous investigation, but when γ and ε increases, the difference between ME and CE is higher than in the previous example, showing a greater influence than the α parameter. As a final investigation, the length L of the beam is taken as analyzed parameter. The trend is shown in

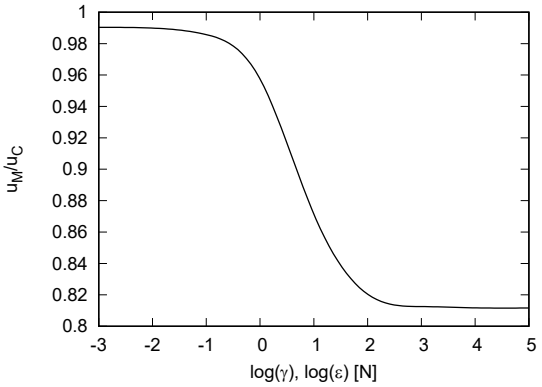

Fig. 8.8 Ratio of the ME (u_M) and the CE (u_C) solutions over the γ and ε material parameters.

Fig. 8.9, where the percentage difference between ME and CE solutions is evaluated over L. The cross-section of the beam changes accordingly to $\dfrac{L}{\sqrt{\dfrac{I}{A}}} = 10$. Clearly, the ME has a stronger influence as the length of the beam gets smaller.

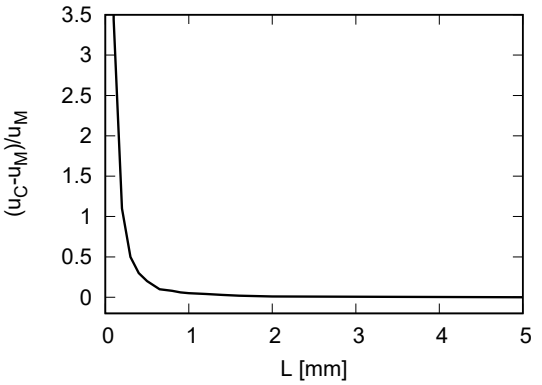

Fig. 8.9 Percentage difference between the ME (u_M) and the CE (u_C) solutions over the length L of the beam.

8.2.3 Human bone specimen

The final analysis case deals with the static analysis of a human bone specimen, supposed to be made of a isotropic micropolar material. The additional micropolar material parameters are taken by the experimental results of Yang and Lakes [187] and Lakes [106]. The human bone is modeled as a cylinder, shown in Fig. 8.10(a) and subjected to a bending loading and d = 7 mm. The structure undergoes clamped-free boundary conditions, and the cross-section is approximated with 12L9, whereas the beam axis, which length is 53.4 mm, is modeled

via 10 B4. The material characteristics are E = 14.1 GPa, G = 4000 GPa, γ = 2487 N, ε = 0 N and α = 7428 N/mm^2. The transverse displacements (adopting both CE and ME) and

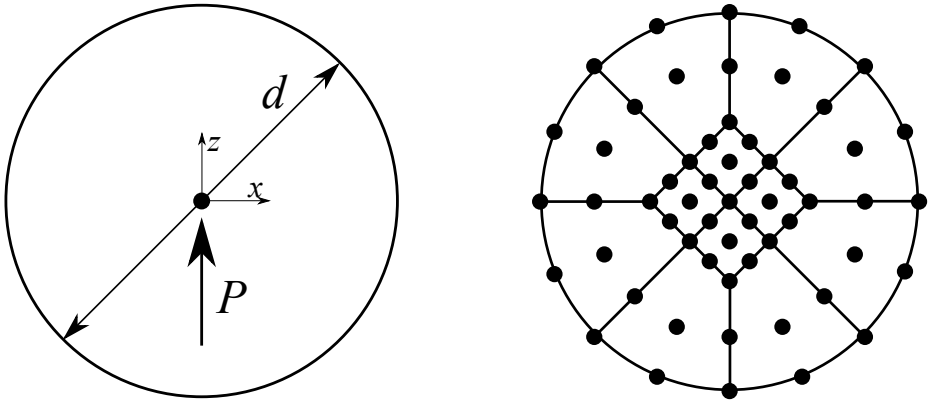

(a) (b)

Fig. 8.10 Modeling properties of the human bone specimen.

micro-rotations are shown in Fig. 8.11. The values are taken at the center of the cross-section. From the comparison between CE and ME it is clear that CE leads to a softening behavior, as described by the previous results. The highest difference between CE and ME occurs at the free tip of the structure and equals 8.2%. The micro-rotation distribution is similar to that reported in previous results.

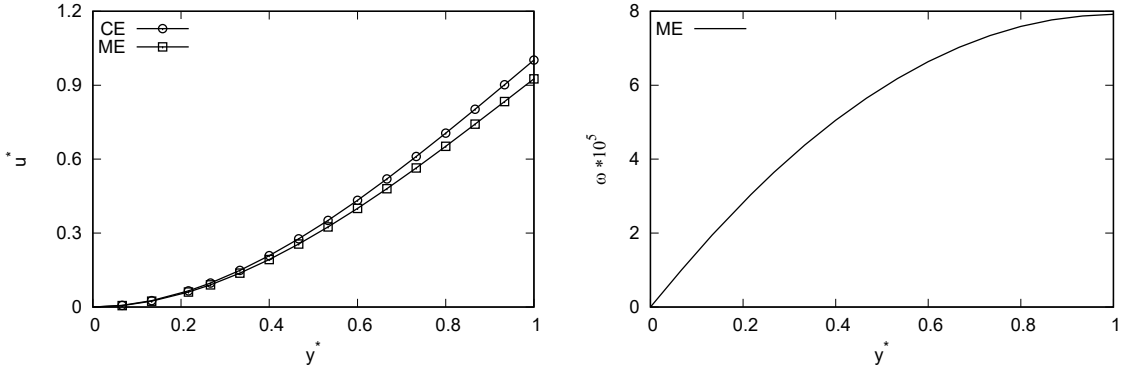

(a) (b)

Fig. 8.11 Displacements (a) and micro-rotations [rad] (b) of the human bone spectimen. Present ME results are compared to the ones using CE. $u^* = \dfrac{3EILu(y)}{FAL^2}$ and $y^* = \dfrac{y}{L}$.

As a final investigation, the $\sigma_{yy}\, h^3/PL$ and $\sigma_{yz}\, h^2/P$ stress distributions are reported in Figs. 8.12 and 8.13. Regarding the σ_{yy} component, its through-the-thickness distribution is evaluated at three different cross-sections, at 0.1 L, 0.5 L and 0.9 L, showing a similar trend

compared to the previous ones. As far as the σ_{YZ} component is concerned, the results show a great difference at the center of the beam, where CE and ME stress values reach the highest amount.

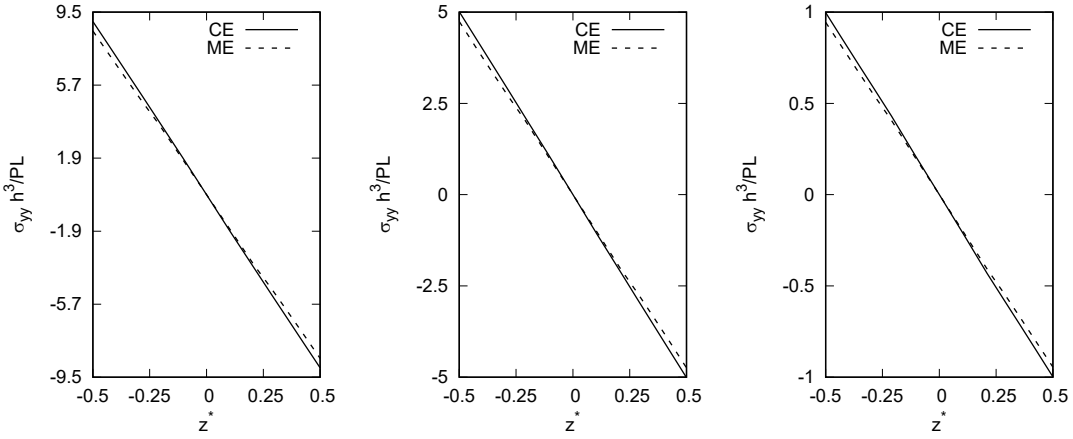

(a) y=0.1L (b) y=0.5L (c) y=0.9L

Fig. 8.12 CE and ME through-the-thickness axial stress $\sigma_{YY}\ h^2/P$.

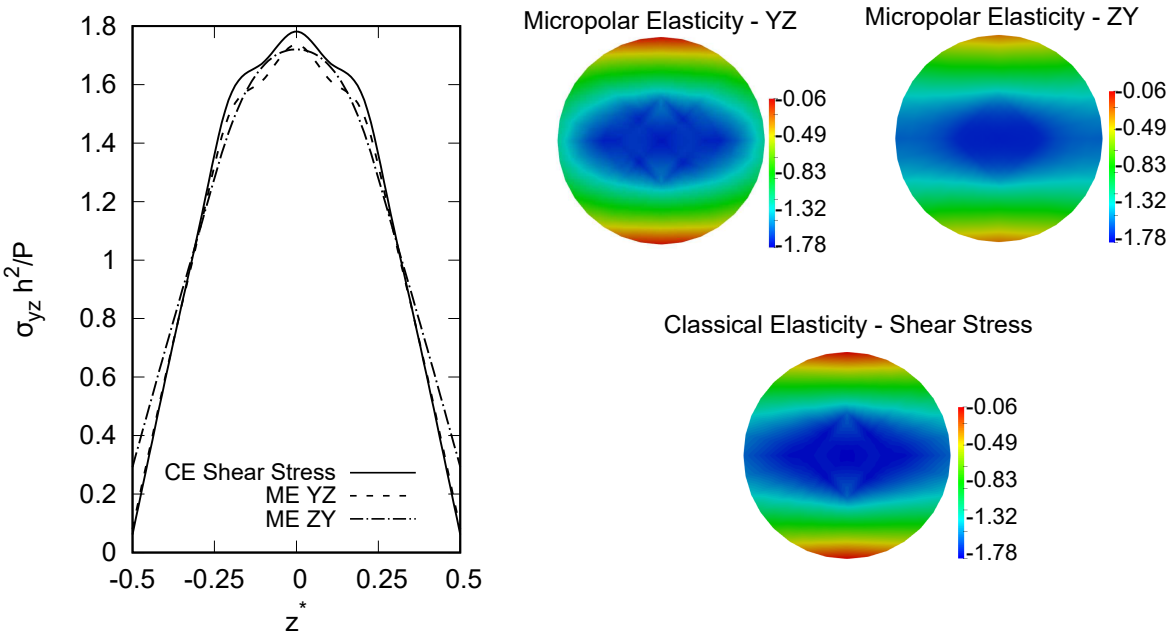

(a) y=0.5L

Fig. 8.13 CE and ME through-the-thickness transverse stress $\sigma_{YZ}\ h^2/P$ component.

Chapter 9

2D CUF-Micropolar model

9.1 Unified 2D plate model based on Micropolar Elasticity

For the evaluation of a plate model, consider a 2D structure placed in a cartesian reference system, so that the thickness h is on the z direction. Consequently, the in-plane coordinates of the surface lay along the x, y directions.

CUF approach is used for the evaluation of the three dimensional unknowns field $\mathbf{u}(x,y,z)$. As already described in the previous chapters, it can be expressed as a generic expansion of the beam axis unknowns. Briefly:

$$\mathbf{u}(x,y,z) = F_s(z)\mathbf{u}_s(x,y), \qquad s = 1,2,....,M \tag{9.1}$$

where F_s represent the expansion functions over the thickness z, $\mathbf{u}_s$ is the vector of the *generalized* unknwons which are placed along the 2D surfcae, M is the order of the expansion, and the summation operation is assumed by the repeated subscript s.
In this chapter, Lagrange expansion are employed as expansion functions, which guarantee the adoption of Lagrange polynomials for the approximation of the displacement and micro-rotation fields. The same F_s are used for both translational displacements and micro-rotation.

9.1.1 Finite element formulation

The Finite Element Method is hereafter employed for the discretization of the beam axis. The generalized displacement vector $\mathbf{u}_s(x,y)$ can be expressed as a function of the nodal unknowns through opportune shape functions N_j, as follows:

$$\mathbf{u}_s(x,y) = N_j(x,y)\mathbf{q}_{sj} \qquad j = 1,2,\ldots,p+1 \tag{9.2}$$

where p and j represent the number of terms used within the shape functions and the summation notation, respectively. $\mathbf{q}_{sj}$ is the same vector of the nodal unkwnons as described in the previous Chapter.

9.1.2 Fundamental Nuclei

As far as the fundamental nuclei are concerned, the main differences from the 1D Micropolar formulation regards the $\mathbf{B}^{sj}_{m1}$ and $\mathbf{B}^{sj}_{m2}$ algebraic matrices. In the case of 2D elements, their form is the following:

$$\mathbf{B}^{sj}_{m1} = \mathbf{b}_{m1}(F_s N_j) = \begin{bmatrix} F_s N_{j,x} & 0 & 0 & 0 & 0 & 0 \\ 0 & F_s N_{j,y} & 0 & 0 & 0 & 0 \\ 0 & 0 & F_{s,z} N_j & 0 & 0 & 0 \\ F_s N_{j,y} & 0 & 0 & 0 & 0 & F_s N_j \\ 0 & F_s N_{j,x} & 0 & 0 & 0 & -F_s N_j \\ F_{s,z} N_j & 0 & 0 & 0 & -F_s N_j & 0 \\ 0 & 0 & F_s N_{j,x} & 0 & F_s N_j & 0 \\ 0 & F_{s,z} N_j & 0 & F_s N_j & 0 & 0 \\ 0 & 0 & F_s N_{j,y} & -F_s N_j & 0 & 0 \end{bmatrix}$$

$$\mathbf{B}^{sj}_{m2} = \mathbf{b}_{m2}(F_s N_j) = \begin{bmatrix} 0 & 0 & 0 & F_s N_{j,x} & 0 & 0 \\ 0 & 0 & 0 & 0 & F_s N_{j,y} & 0 \\ 0 & 0 & 0 & 0 & 0 & F_{s,z} N_j \\ 0 & 0 & 0 & F_s N_{j,y} & 0 & 0 \\ 0 & 0 & 0 & 0 & F_s N_{j,x} & 0 \\ 0 & 0 & 0 & F_{s,z} N_j & 0 & 0 \\ 0 & 0 & 0 & 0 & 0 & F_s N_{j,x} \\ 0 & 0 & 0 & 0 & F_{s,z} N_j & 0 \\ 0 & 0 & 0 & 0 & 0 & F_s N_{j,y} \end{bmatrix} \tag{9.3}$$

Consequently, the complete expression of the matrix is the following ("t" stands for the thickness and "S" for the surface):

$$\mathbf{K}^{\tau sij}_{uuxx} = C_{11} \int_t F_\tau F_{s,x} dt \int_S N_{i,x} N_j dS + C^M_{55} \int_t F_{\tau,z} F_{s,z} dt \int_S N_i N_j dS +$$

$$C^M_{44} \int_t F_\tau F_s dt \int_S N_{i,y} N_{j,y} dS$$

$$\mathbf{K}_{uuxy}^{ij\tau s} = C_{12}\int_t F_\tau F_s dt \int_S N_{i,y} N_{j,x} dS + C_{44}^{MT}\int_t F_\tau F_s dt \int_S N_{i,x} N_{j,y} dS$$

$$\mathbf{K}_{uuxz}^{ij\tau s} = C_{55}^{MT}\int_t F_\tau F_{s,z} dt \int_S N_{i,x} N_j dS + C_{13}\int_t F_{\tau,z} F_s dt \int_S N_i N_{j,x} dS$$

$$\mathbf{K}_{uuyx}^{ij\tau s} = C_{44}^{MT}\int_t F_{\tau,z} F_s dt \int_S N_{i,y} N_{j,x} dS + C_{12}\int_t F_\tau F_s dt \int_S N_{i,x} N_{j,y} dS$$

$$\mathbf{K}_{uuyy}^{\tau sij} = C_{44}^{M}\int_t F_\tau F_{s,x} dt \int_S N_{i,x} N_j dS + C_{66}^{M}\int_t F_{\tau,z} F_{s,z} N_i N_j dt \int_S +$$

$$C_{22}\int_t F_\tau F_s dt \int_S N_{i,y} N_{j,y} dS$$

$$\mathbf{K}_{uuyz}^{ij\tau s} = C_{66}^{MT}\int_t F_\tau F_{s,z} dt \int_S N_{i,y} N_j dS + C_{23}\int_t F_{\tau,z} F_s dt \int_S N_i N_{j,y} dS$$

$$\mathbf{K}_{uuzx}^{ij\tau s} = C_{13}\int_t F_\tau F_{s,z} dt \int_S N_{i,x} N_j dS + C_{55}^{MT}\int_t F_{\tau,z} F_s dt \int_S N_i N_{j,x} dS$$

$$\mathbf{K}_{uuzy}^{ij\tau s} = C_{23}\int_t F_\tau F_{s,z} dt \int_S N_{i,y} N_j dS + C_{66}^{MT}\int_t F_{\tau,z} F_s dt \int_S N_i N_{j,y} dS$$

$$\mathbf{K}_{uuzz}^{\tau sij} = C_{55}^{MT}\int_t F_\tau F_s dt \int_S N_{i,x} N_{j,x} dS + C_{33}\int_t F_{\tau,z} F_{s,z} dt \int_S N_i N_j dS +$$

$$C_{66}^{MT}\int_t F_\tau F_s dt \int_S N_{i,y} N_{j,y} dS$$

$$\mathbf{K}_{utxx}^{ij\tau s} = 0$$

$$\mathbf{K}_{utxy}^{ij\tau s} = -C_{55}^{M}\int_t F_\tau F_{s,z} dt \int_S N_i N_j dS + C_{55}^{MT}\int_t F_\tau F_{s,z} dt \int_S N_i N_j dS$$

$$\mathbf{K}_{utxz}^{ij\tau s} = C_{44}^{M}\int_t F_\tau F_s dt \int_S N_i N_{j,y} dS - C_{44}^{MT}\int_t F_\tau F_s dt \int_S N_i N_{j,y} dS$$

$$\mathbf{K}_{utyx}^{ij\tau s} = C_{66}^{M}\int_t F_\tau F_{s,z} dt \int_S N_i N_j dS - C_{66}^{MT}\int_t F_\tau F_{s,z} dt \int_S N_i N_j dS$$

$$\mathbf{K}_{utyy}^{ij\tau s} = 0$$

$$\mathbf{K}_{utyz}^{ij\tau s} = C_{44}^{MT} \int_t F_\tau F_s dt \int_S N_i N_{j,x} dS - C_{44}^{M} \int_t F_\tau F_s dt \int_S N_i N_{j,x} dS$$

$$\mathbf{K}_{utzx}^{ij\tau s} = -C_{66}^{M} \int_t F_\tau F_s dt \int_S N_i N_{j,y} dS + C_{66}^{MT} \int_t F_\tau F_s dt \int_S N_i N_{j,y} dS$$

$$\mathbf{K}_{utzy}^{ij\tau s} = C_{55}^{M} \int_t F_\tau F_s dt \int_S N_i N_{j,x} dS - C_{55}^{MT} \int_t F_\tau F_s dt \int_S N_i N_{j,x} dS$$

$$\mathbf{K}_{utzz}^{ij\tau s} = 0$$

$$\mathbf{K}_{tuxx}^{ij\tau s} = 0$$

$$\mathbf{K}_{tuxy}^{ij\tau s} = C_{66}^{M} \int_t F_s F_{t,z} dt \int_S N_i N_j dS - C_{66}^{MT} \int_t F_s F_{t,z} dt \int_S N_i N_j dS$$

$$\mathbf{K}_{tuxz}^{ij\tau s} = -C_{66}^{M} \int_t F_s F_t dt \int_S N_{i,y} N_j dS + C_{66}^{MT} \int_t F_s F_t dt \int_S N_{i,y} N_{j,y} dS$$

$$\mathbf{K}_{tuyx}^{ij\tau s} = -C_{55}^{M} \int_t F_s F_{t,z} dt \int_S N_i N_j dS + C_{55}^{MT} \int_t F_s F_{t,z} dt \int_S N_i N_j dS$$

$$\mathbf{K}_{tuyy}^{ij\tau s} = 0$$

$$\mathbf{K}_{tuyz}^{ij\tau s} = C_{55}^{M} \int_t F_s F_t dt \int_S N_{i,x} N_j dS - C_{55}^{MT} \int_t F_s F_t dt \int_S N_{i,x} N_j dS$$

$$\mathbf{K}_{tuzx}^{ij\tau s} = C_{44}^{M} \int_t F_s F_t dt \int_S N_{i,y} N_j dS - C_{44}^{MT} \int_t F_s F_t dt \int_S N_{i,y} N_j dS$$

$$\mathbf{K}_{tuzy}^{ij\tau s} = -C_{44}^{M} \int_t F_s F_t dt \int_S N_{i,x} N_j dS + C_{44}^{MT} \int_t F_s F_t dt \int_S N_{i,x} N_j dS$$

$$\mathbf{K}_{tuzz}^{ij\tau s} = 0$$

$$\mathbf{K}_{ttxx}^{ij\tau s} = 2C_{66}^{M} \int_t F_s F_t dt \int_S N_i N_j dS - 2C_{66}^{MT} \int_t F_s F_t dt \int_S N_i N_j dS +$$

$$A_{11}\int_t F_\tau F_s dt \int_S N_{i,x} N_{j,x} dS + A_{55}\int_t F_{\tau,z} F_{s,z} dt \int_S N_i N_j dS + A_{44}\int_t F_\tau F_s dt \int_S N_{i,y} N_{j,y} dS$$

$$\mathbf{K}^{ij\tau s}_{uuxz} = A_{12}\int_t F_\tau F_s dt \int_S N_{i,y} N_{j,x} dS + A^{MT}_{44}\int_t F_\tau F_s dt \int_S N_{i,x} N_{j,y} dS$$

$$\mathbf{K}^{ij\tau s}_{uuxz} = A^{MT}_{55}\int_t F_\tau F_{s,z} dt \int_S N_{i,x} N_j dS + A_{13}\int_t F_{\tau,z} F_s dt \int_S N_i N_{j,x} dS$$

$$\mathbf{K}^{ij\tau s}_{uuyx} = A^{MT}_{44}\int_t F_\tau F_s dt \int_S N_{i,y} N_{j,x} dS + A_{12}\int_t F_\tau F_s dt \int_S N_{i,x} N_{j,y} dS$$

$$\mathbf{K}^{ij\tau s}_{ttxx} = 2C^{M}_{55}\int_t F_s F_t dt \int_S N_i N_j dS - 2C^{MT}_{55}\int_t F_s F_t dt \int_S N_i N_j dS +$$

$$A_{44}\int_t F_\tau F_s dt \int_S N_{i,x} N_{j,x} dS + A_{66}\int_t F_{\tau,z} F_{s,z} dt \int_S N_i N_j dS + A_{22}\int_t F_\tau F_s dt \int_S N_{i,y} N_{j,y} dS$$

$$\mathbf{K}^{ij\tau s}_{uuyz} = A^{MT}_{66}\int_t F_\tau F_{s,z} dt \int_S N_{i,y} N_j dS + A_{23}\int_t F_{\tau,z} F_s dt \int_S N_i N_{j,y} dS$$

$$\mathbf{K}^{ij\tau s}_{uuzx} = A_{13}\int_t F_\tau F_{s,z} dt \int_S N_{i,x} N_j dS + A^{MT}_{55}\int_t F_{\tau,z} F_s dt \int_S N_i N_{j,x} dS$$

$$\mathbf{K}^{ij\tau s}_{uuzy} = A^{MT}_{66}\int_t F_{\tau,z} F_s dt \int_S N_i N_{j,y} dS + A_{23}\int_t F_\tau F_{s,z} dt \int_S N_{i,y} N_j dS$$

$$\mathbf{K}^{ij\tau s}_{ttxx} = 2C^{M}_{44}\int_t F_s F_t dt \int_S N_i N_j dS - 2C^{MT}_{44}\int_t F_s F_t dt \int_S N_i N_j dS +$$

$$A_{55}\int_t F_\tau F_s dt \int_S N_{i,x} N_{j,x} dS + A_{33}\int_t F_{\tau,z} F_{s,z} dt \int_S N_i N_j dS + A_{66}\int_t F_\tau F_s dt \int_S N_{i,y} N_{j,y} dS$$

9.2 Examples

9.2.1 Comparison with analytical literature results

The capability of the proposed unified theory of two-dimensional (2D) structure based on Micropolar Elasticity (ME) is demonstrated by the comparison with literature results. In

the first analysis case, a square simply-supported plate undergoing a transverse pressure is considered. The reference solution comes from the work by Carrera and Zozulya [39]. The beam is made of polyurethane foam, which material properties are reported in Table 9.1. The values reported in the Table are evaluated through experiments, as reported from Lakes [107, 106]. The geometry of the analyzed square plate is shown in Fig. 9.1(a), with thickness

Parameters	Values
λ	762.6
μ	103.9
E	299.2
ν	0.44
α	4.333
β	-27.76
γ	39.97
ε	5.324

Table 9.1 Experimental data for classical and micropolar material parameters of polyurethane foam. λ, μ, E and α are expressed in MPa, β, γ and ε are expressed in N.

t = 0.1 m. Two different ratios between the thickness and the side L were considered, 1/10 and 1/30. In addition, in Fig. 9.1(a) the load distribution is shown, and it is sinusoidal with the following form:

$$p(x,y) \quad = \quad p_0 \, sin\left(\frac{\pi x}{L}\right)\left(\frac{\pi y}{L}\right) \tag{9.4}$$

where p_0 equals 10^6 N/m^2 and 10^6 N/m^2 for $t/L = 1/10$ and $t/L = 1/30$, respectively. Figure 9.1(b) shows the discretization used for the surface and for the thickness of the structure. Finite Elements (FEs) were employed to approximate the displacement field over the surface of the plate, whereas a Taylor expansion of order 4 was adopted through the thickness within the Carrera Unified Formulation (CUF) [29] framework. Linear static analyses were conducted using different numbers of FEs and the transverse displacement of the middle point of the square plate is evaluated, in order to perform a convergence investigation referring to the results shown in the reference paper [39]. The results of the convergence analyses are shown in Fig. 9.2. In the first figure, the square plate with $t/L = 1/10$ was considered. The need to consider a refined model for the surface of the plate is clear. The convergence is achieved starting from a number of FEs equal to 900, for which value the percentage difference between the static solutions from the proposed model and the reference solution goes below 2%, as reported in the Table 9.2. In contrast, for the $t/L = 1/30$ analysis case, the convergence is obtained for a lower number of FEs. In fact, with 100 FEs, the two solutions are very close. Then, it can be pointed out that when the

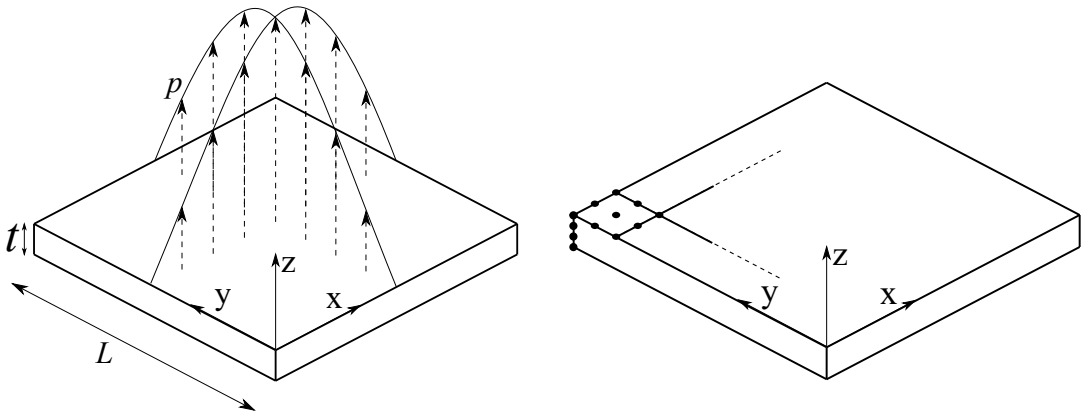

(b)

Fig. 9.1 Geometric properties and loading condition (a) and surface and thickness discretization (b) for the simply-supported square plate.

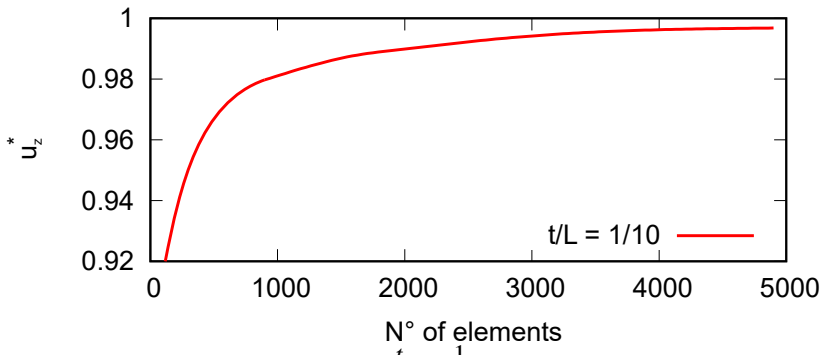

(a) $\frac{t}{L} = \frac{1}{10}$

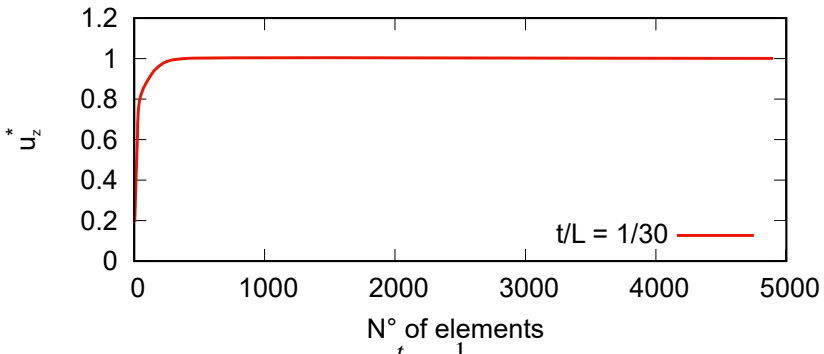

(b) $\frac{t}{L} = \frac{1}{30}$

Fig. 9.2 Convergence analysis of FEs on the non-dimensional transverse displacement in the middle of of the simply-supported square plate. $u_z^* = \dfrac{u_z}{u_{z\,Ref.}}$. analysis case.

size of the 2D structure is small, a higher number of FEs are required to be able to correctly catch micropolar phenomena, whereas, for larger structures, a lower number of elements is enough. These results also prove the accuracy of the proposed model and are used to decide the approximation of the surface of the 2D structures considered in the next analyses.

		$t/L = 1/10$		$t/L = 1/30$	
Mesh	Elements	u_z	$\frac{(u_{z\,Ref.} - u_z)}{u_{z\,Ref.}}$	u_z	$\frac{(u_{z\,Ref.} - u_z)}{u_{z\,Ref.}}$
2x2	4			0.1304	80.71%
5x5	25			0.4174	38.25%
10x10	100	0.08053	8.26%	0.6755	0.07%
20x20	400	0.08454	3.69%	0.6765	-0.07%
30x30	900	0.08597	2.06%	0.6765	-0.08%
40x40	1600	0.08668	1.25%	0.6765	-0.09%
50x50	2500	0.08709	0.79%	0.6766	-0.09%
60x60	3600	0.08735	0.49%		
70x70	4900	0.08753	0.29%		

Table 9.2 Values of the percentage difference between the static solution from the proposed model and those from the reference solution. Reference results from Carrera and Zozulya [39].

Chapter 10

Conclusions

10.1 Concluding remarks

Geometrical nonlinear analyses based con Classical Elasticity (CE) and linear static analyses based on Micropolar Elasticity (ME) have been presented in this thesis work. The adoption of the Carrera Unified Formulation (CUF) allows to easily implement low- to higher-order theories, accounting for the full Green-Lagrange nonlinear strains and the unsymmetrical nature of the force and couple stress tensors of ME models. One-dimensional (1D) and plate/shell two-dimensional (2D) models have been built and adopted for research analyses of structures from real applications.

Main results

During the period of the doctoral research, the following main results have been obtained.

- 1D beam and 2D shell models have been presented and used to perform geometrical nonlinear analysis of isotropic and composite structures. The models are validated with those coming from literature and research activities are conducted to analyze the large-deflection and post-buckling of complicated structures (in terms of stacking sequences and cross-section geometry);
- The nonlinear static behavior of shell-like structures are analyzed using both 1D and 2D models, showing the applicability of both and describing the differences which arise between them;
- The dynamic characteristics of structures during the nonlinear analysis have been exploited. In particular, the mode change in the large deflection field and the mode

aberration in the post-buckling of structure has been demonstrated with numerical examples. Moreover, a reinforced composite panel from a real application is proposed, with the results matching with those from experiments;

- The capability of various popular geometrical nonlinear theories, based on approximations of the full geometrical nonlinear solution, are investigated, as the well-known von Kármán strain assumptions. Both 1D and 2D models have been analyzed for this analysis;
- 1D beam models based on ME are developed. CUF and FEM, presented in the first part of the thesis, are adopted for the analysis of micropolar materials. The capability of the proposed model is validated with literature results, and stress analyses are conducted;
- An analysis of a human bone specimen is conducted, considering it as made of a micropolar material, as suggested by literature research activities, see Lakes [106] and Yang and Lakes [187];
- 2D plate models of ME are developed. The validity of the model is proved with comparison with analytical results coming from the literature;
- The effects of geometrical nonlinearities on the refined kinematic theories are evaluated, and it is demonstrated that an higher-order kinematic theory demands for an accurate nonlinear description;
- Accurate through-the-thickness distributions of stresses are evaluated on isotropic and composite shells;
- An innovative procedure for the analysis of structures made of complex geometry is developed. The geometrical nonlinear behavior can be evaluated integrating just the cross-sectional nonlinearities, saving computational cost.

Future work

Multiple perspective developments of the nonlinear formulation seem to be interesting. The geometrical nonlinear analysis field is vast, and the research lines to be exploited are various. As far as the geometrical structural formulation is concerned, the most promising outlooks appear to be the following:

- Coupling with material nonlinear formulation could provide a complete model for the analysis of real working structures.

- Stress analyses in the large-deflection and, especially, post-buckling field, for the failure index of composite structures.
- Dynamic anaysis in the time domain.

The micropolar modeling framework proposed in this thesis shall be considered as a starting point for subsequent extensions and applications, which could include.

- Modal analysis of micropolar bodies.
- The micropolar elasticity is more efficient when the scale of the structure is small, which could easily exhibit large deflections. Thus, an extension to geometrical nonlinear analysis could be of fundamental importance.

References

[1] Abramovich, H., Govich, D., and Grunwald, A. (2015). Buckling prediction of panels using the vibration correlation technique. *Progress in Aerospace Sciences*, 78:62–73.

[2] Agarwal, S., Chakraborty, A., and Gopalakrishnan, S. (2006). Large deformation analysis for anisotropic and inhomogeneous beams using exact linear static solutions. *Composite Structures*, 72(1):91–104.

[3] Akbarov, S. (2007). Recent investigations on dynamic problems for an elastic body with initial (residual) stresses. *International Applied Mechanics*, 43(12):1305.

[4] Akbarov, S. and Ozisik, M. (2004). Dynamic interaction of a prestressed nonlinear elastic layer and a half-plane. *International Applied Mechanics*, 40(9):1056–1063.

[5] Amabili, M. (2008). *Nonlinear Vibrations and Stability of Shells and Plates*. Cambridge University Press, New York, USA.

[6] Amabili, M. (2015). Non-linearities in rotation and thickness deformation in a new third-order thickness deformation theory for static and dynamic analysis of isotropic and laminated doubly curved shells. *International Journal of Non-linear Mechanics*, 69:109–128.

[7] Amabili, M. (2018). *Nonlinear Mechanics of Shells and Plates in Composite, Soft and Biological materials*. Cambridge University Press.

[8] Amabili, M. and Farhadi, S. (2009). Shear deformable versus classical theories for nonlinear vibrations of rectangular isotropic and laminated composite plates. *Journal of Sound and Vibration*, 320(3):649–667.

[9] Amabili, M. and Reddy, J. (2010). A new non-linear higher-order shear deformation theory for large-amplitude vibrations of laminated doubly curved shells. *International Journal of Non-Linear Mechanics*, 45(4):409–418.

[10] Amabili, M. and Reddy, J. (2020). The nonlinear, third-order thickness and shear deformation theory for statics and dynamics of laminated composite shells. *Composite Structures*, 244:112265.

[11] Ambrosini, R. D., Riera, J. D., and Danesi, R. F. (2000). A modified Vlasov theory for dynamic analysis of thin-walled and variable open section beams. *Engineering Structures*, 22(8):890–900.

[12] Arbelo, M., Kalnins, K., Ozolins, O., Skukis, E., Castro, S., and Degenhardt, R. (2015). Experimental and numerical estimation of buckling load on unstiffened cylindrical shells using a vibration correlation technique. *Thin-Walled Structures*, 94:273–279.

[13] Başar, Y., Ding, Y., and Schultz, R. (1993). Refined shear-deformation models for composite laminates with finite rotations. *International Journal of Solids and Structures*, 30(19):2611–2638.

[14] Bathe, K.-J. (2006). *Finite Element Procedures*. Prencice Hall, New Jersey.

[15] Bathe, K.-J. and Bolourchi, S. (1979). Large displacement analysis of three-dimensional beam structures. *International Journal for Numerical Methods in Engineering*, 14(7):961–986.

[16] Batoz, J.-L. and Dhatt, G. (1979). Incremental displacement algorithms for nonlinear problems. *International Journal for Numerical Methods in Engineering*, 14(8):1262–1267.

[17] Bažant, Z. P. and Cedolin, L. (2010). *Stability of Structures: Elastic, Inelastic, Fracture and Damage Theories*. World Scientific.

[18] Biot, M. (1939). Non-linear theory of elasticity and the linearized case for a body under initial stress. *The London, Edinburgh, and Dublin Philosophical Magazine and Journal of Science*, 27(183):468–489.

[19] Biscani, F., Giunta, G., Belouettar, S., Carrera, E., and Hu, H. (2012a). Variable kinematic plate elements coupled via arlequin method. *International Journal for Numerical Methods in Engineering*, 91(12):1264–1290.

[20] Biscani, F., Nali, P., Belouettar, S., and Carrera, E. (2012b). Coupling of hierarchical piezoelectric plate finite elements via arlequin method. *Journal of intelligent material systems and structures*, 23(7):749–764.

[21] Bisshopp, K. and Drucker, D. (1945). Large deflection of cantilever beams. *Quarterly of Applied Mathematics*, 3(3):272–275.

[22] Boutagouga, D. and Djeghaba, K. (2013). Evaluation of linear and geometrically nonlinear static and dynamic analysis of thin shells by flat shell finite elements. *Proceedings of World Academy of Science, Engineering and Technology*, page 359.

[23] Calladine, C. (1989). *Theory of shell structures*. Cambridge University Press.

[24] Carrera, E. (1994). A study on arc-length-type methods and their operation failures illustrated by a simple model. *Computers & Structures*, 50(2):217–229.

[25] Carrera, E. (1997). C_z^0 requirements—models for the two dimensional analysis of multilayered structures. *Composite Structures*, 37(3-4):373–383.

[26] Carrera, E. (2002). Theories and finite elements for multilayered, anisotropic, composite plates and shells. *Archives of Computational Methods in Engineering*, 9(2):87–140.

[27] Carrera, E. (2003). Historical review of zig-zag theories for multilayered plates and shells. *Applied Mechanics Reviews*, 56(3):287–308.

[28] Carrera, E., Cinefra, M., Petrolo, M., and Zappino, E. (2014a). Comparisons between 1D (beam) and 2D (plate/shell) finite elements to analyze thin walled structures. *Aerotecnica Missili & Spazio*, 93(1-2):3–16.

[29] Carrera, E., Cinefra, M., Petrolo, M., and Zappino, E. (2014b). *Finite Element Analysis of Structures through Unified Formulation*. John Wiley & Sons, New York, USA.

[30] Carrera, E., de Miguel, A., and Pagani, A. (2017a). Hierarchical theories of structures based on Legendre polynomial expansions with finite element applications. *International Journal of Mechanical Sciences*, 120:286–300.

[31] Carrera, E., Filippi, M., Mahato, P. K., and Pagani, A. (2016). Accurate static response of single-and multi-cell laminated box beams. *Composite Structures*, 136:372–383.

[32] Carrera, E. and Giunta, G. (2010). Refined beam theories based on a unified formulation. *International Journal of Applied Mechanics*, 2(1):117–143.

[33] Carrera, E., Giunta, G., and Petrolo, M. (2011). *Beam Structures: Classical and Advanced Theories*. John Wiley & Sons.

[34] Carrera, E., Pagani, A., and Valvano, S. (2017b). Multilayered plate elements accounting for refined theories and node-dependent kinematics. *Composites Part B: Engineering*, 114:189–210.

[35] Carrera, E. and Parisch, H. (1997). An evaluation of geometrical nonlinear effects of thin and moderately thick multilayered composite shells. *Composite Structures*, 40(1):11–24.

[36] Carrera, E. and Petrolo, M. (2012). Refined beam elements with only displacement variables and plate/shell capabilities. *Meccanica*, 47(3):537–556.

[37] Carrera, E. and Zappino, E. (2017). One-dimensional finite element formulation with node-dependent kinematics. *Computers & Structures*, 192:114–125.

[38] Carrera, E., Zappino, E., and Li, G. (2018). Finite element models with node-dependent kinematics for the analysis of composite beam structures. *Composites Part B: Engineering*, 132:35–48.

[39] Carrera, E. and Zozulya, V. V. (2020). Closed-form solution for the micropolar plates: Carrera Unified Formulation (CUF) approach. *Archive of Applied Mechanics*, pages 1–26.

[40] Cauchy, A. (1828). Sur l'equilibre et le mouvement d'une plaque solide. *Exerc. Math.*, 3:328–355.

[41] Chan, S. and Kitipornchai, S. (1987). Geometric nonlinear analysis of asymmetric thin-walled beam-columns. *Engineering Structures*, 9(4):243–254.

[42] Chandrashekhara, K. and Bangera, K. (1992). Free vibration of composite beams using a refined shear flexible beam element. *Computers & Structures*, 43(4):719–727.

[43] Chandrashekhara, K. and Bangera, K. M. (1993). Linear and geometrically nonlinear analysis of composite beams under transverse loading. *Composites Science and Technology*, 47(4):339–347.

[44] Chandrashekhara, K., Krishnamurthy, K., and Roy, S. (1990). Free vibration of composite beams including rotary inertia and shear deformation. *Composite Structures*, 14(4):269–279.

[45] Chia, C.-Y. (1988). Geometrically nonlinear behavior of composite plates: A review. *Applied Mechanics Reviews*, 41(12):439–451.

[46] Cinefra, M. and Carrera, E. (2013). Shell finite elements with different through-the-thickness kinematics for the linear analysis of cylindrical multilayered structures. *International Journal for Numerical Methods in Engineering*, 93(2):160–182.

[47] Cinefra, M. and Valvano, S. (2016). A variable kinematic doubly-curved mitc9 shell element for the analysis of laminated composites. *Mechanics of Advanced Materials and Structures, In Press*, 23(11):1312–1325.

[48] Cosserat, E. and Cosserat, F. (1909). *Théorie des corps déformables*. A. Hermann et fils,.

[49] Coulomb, C. (1784). *Recherches théoriques et expérimentales sur la force de torsion: & sur l'élasticité des fils de métal: application de cette théorie à l'emploi des métaux dans les arts & dans différentes expériences de physique: construction de différentes balances de torsion, pour mesurer les plus petits degrés de force: observations sur les loix de l'élasticité & de la cohérence*.

[50] Crisfield, M. A. (1981). A fast incremental/iterative solution procedure that handles "snap-through". *Computers & Structures*, 13(1):55–62.

[51] Crisfield, M. A. (1983). An arc-length method including line searches and accelerations. *International Journal for Numerical Methods in Engineering*, 19(9):1269–1289.

[52] Crisfield, M. A. (1991). *Non-linear Finite Element Analysis of Solid and Structures*. John Wiley & Sons, Chichester, England.

[53] De Pietro, G. (2019). *Modelling and design of multi-stable composite structures*. PhD thesis, PhD thesis, Politecnico di Torino.

[54] de Saint-Venant, A. (1856). *Mémoire sur la Flexion des Prismes*. Imprimerie Nationale.

[55] Dennis, S. and Palazotto, A. (1989). Transverse shear deformation in orthotropic cylindrical pressure vessels using a higher-order shear theory. *AIAA Journal*, 27(10):1441–1447.

[56] Donders, S., Takahashi, Y., Hadjit, R., Van Langenhove, T., Brughmans, M., Van Genechten, B., and Desmet, W. (2009). A reduced beam and joint concept modeling approach to optimize global vehicle body dynamics. *Finite elements in analysis and design*, 45(6-7):439–455.

[57] El-Sayed, M. (1989). Calculation of joint spring rates using finite element formulation. *Computers & Structures*, 33(4):977–981.

[58] Emam, S. A. (2011). Analysis of shear-deformable composite beams in postbuckling. *Composite Structures*, 94(1):24–30.

[59] Eringen, A. C. (1966). Linear theory of micropolar elasticity. *Journal of Mathematics and Mechanics*, 15(6):909–923.

[60] Eringen, A. C. (1999). *Microcontinuum field theories: I. Foundations and solids*. Springer Science & Business Media.

[61] Eringen, A. C. (2001). *Microcontinuum field theories II: fluent media, 2001*. Springer, New York.

[62] Euler, L. (1744). *De curvis elasticis*. Lausanne and Geneva: Bousquet.

[63] Euler, L. (1952). *Methodus inveniendi lineas curvas maximi minimive proprietate gaudentes sive solutio problematis isoperimetrici latissimo sensu accepti*, volume 1. Springer Science & Business Media.

[64] Filippi, M., Pagani, A., Petrolo, M., Colonna, G., and Carrera, E. (2015). Static and free vibration analysis of laminated beams by refined theory based on chebyshev polynomials. *Composite Structures*, 132:1248–1259.

[65] Fleck, N., Muller, G., Ashby, M., and Hutchinson, J. (1994). Strain gradient plasticity: theory and experiment. *Acta Metallurgica et materialia*, 42(2):475–487.

[66] Flügge, W. (1960). *Stresses in shells*. Springer, Berlin, 2nd edition.

[67] Friberg, P. O. (1985). Beam element matrices derived from Vlasov's theory of open thin-walled elastic beams. *International Journal for Numerical Methods in Engineering*, 21(7):1205–1228.

[68] Frisch-Fay, R. (1962). *Flexible bars*. Butterworths, Washington D.C., USA.

[69] Gol'Denveizer, A. L. (1961). *Theory of Elastic Thin Shells. Solid and Structural Mechanics*. Pergamon Press.

[70] Gorguluarslan, R. M., Gandhi, U. N., Mandapati, R., and Choi, S.-K. (2016). Design and fabrication of periodic lattice-based cellular structures. *Computer-Aided Design and Applications*, 13(1):50–62.

[71] Gruttmann, F., Sauer, R., and Wagner, W. (1998). A geometrical nonlinear eccentric 3d-beam element with arbitrary cross-sections. *Computer Methods in Applied Mechanics and Engineering*, 160(3):383–400.

[72] Gupta, R. K., Gunda, J. B., Janardhan, G. R., and Rao, G. V. (2010). Post-buckling analysis of composite beams: simple and accurate closed-form expressions. *Composite Structures*, 92(8):1947–1956.

[73] Han, S., Tabiei, A., and Park, W. (2008). Geometrically nonlinear analysis of laminated composite thin shells using a modified first-order shear deformable element-based Lagrangian shell element. *Composite Structures*, 82(3):465–474.

[74] Hanganu, A. D., Onate, E., and Barbat, A. H. (2002). A finite element methodology for local/global damage evaluation in civil engineering structures. *Computers & Structures*, 80(20-21):1667–1687.

[75] Hassanpour, S. and Heppler, G. R. (2016). Comprehensive and easy-to-use torsion and bending theories for micropolar beams. *International Journal of Mechanical Sciences*, 114:71–87.

[76] Hassanpour, S. and Heppler, G. R. (2017). Micropolar elasticity theory: a survey of linear isotropic equations, representative notations, and experimental investigations. *Mathematics and Mechanics of Solids*, 22(2):224–242.

[77] Helou, M. and Kara, S. (2018). Design, analysis and manufacturing of lattice structures: an overview. *International Journal of Computer Integrated Manufacturing*, 31(3):243–261.

[78] Herrmann, G. (1956). The influence of initial stress on the dynamic behavior of elastic and viscoelastic plates. *Publications of the International Association for Bridge and Structural Engineering*, 16:275–294.

[79] Hodges, D. (2006). *Nonlinear composite beam theory*. American Institute of Aeronautics and Astronautics.

[80] Hodges, D., Atilgan, A., Fulton, M., and Rehfield, L. (1991). Free-vibration analysis of composite beams. *Journal of the American Helicopter Society*, 36(3):36–47.

[81] Huang, F.-Y., Yan, B.-H., Yan, J.-L., and Yang, D.-U. (2000). Bending analysis of micropolar elastic beam using a 3-d finite element method. *International Journal of Engineering Science*, 38(3):275–286.

[82] Hui, Y. (2019). *Multi-scale modelling and design of composite structures*. PhD thesis, PhD thesis, Politecnico di Torino.

[83] Hui, Y., De Pietro, G., Giunta, G., Belouettar, S., Hu, H., Carrera, E., and Pagani, A. (2018). Geometrically nonlinear analysis of beam structures via hierarchical one-dimensional finite elements. *Mathematical Problems in Engineering*, 2018.

[84] Hui, Y., Giunta, G., Belouettar, S., Hu, H., and Carrera, E. (2019). Multiscale nonlinear analysis of beam structures by means of the carrera unified formulation. In *Advances in Predictive Models and Methodologies for Numerically Efficient Linear and Nonlinear Analysis of Composites*, pages 47–63. Springer.

[85] Ibrahimbegović, A. and Frey, F. (1993). Finite element analysis of linear and non-linear planar deformations of elastic initially curved beams. *International Journal for Numerical Methods in Engineering*, 36(19):3239–3258.

[86] Jang, G., Choi, S. M., and Kim, Y. Y. (2013). Analysis of three thin-walled box beams connected at a joint under out-of-plane bending loads. *Journal of Engineering Mechanics*, 139(10):1350–1361.

[87] Jing, H. and Tzeng, K. (1993). Refined shear deformation theory of laminated shells. *AIAA Journal*, 31(4):765–773.

[88] Kang, Y. J. and Yoo, C. H. (1994). Thin-walled curved beams. I: formulation of nonlinear equations. *Journal of Engineering Mechanics*, 120(10):2072–2101.

[89] Kant, T. and Swaminathan, K. (2001). Analytical solutions for free vibration of laminated composite and sandwich plates based on a higher-order refined theory. *Composite Structures*, 53(1):73–85.

[90] Kapania, R. (1989). A review on the analysis of laminated shells. *ASME. Journal Pressure Vessel Technology*, 111(2):88–96.

[91] Kapania, R. and Raciti, S. (1989a). Recent advances in analysis of laminated beams and plates, Part I: Shear effects and buckling. *AIAA Journal*, 27(7):923–935.

[92] Kapania, R. and Raciti, S. (1989b). Recent advances in analysis of laminated beams and plates, Part II: Vibrations and wave propagation. *AIAA Journal*, 27(7):935–946.

[93] Kapania, R. K. and Raciti, S. (1989c). Nonlinear vibrations of unsymmetrically laminated beams. *AIAA Journal*, 27(2):201–210.

[94] Ke, L.-L., Yang, J., and Kitipornchai, S. (2010). Nonlinear free vibration of functionally graded carbon nanotube-reinforced composite beams. *Composite Structures*, 92(3):676–683.

[95] Kennedy, T. C. (1999). Modeling failure in notched plates with micropolar strain softening. *Composite Structures*, 44(1):71–79.

[96] Kim, D. and Chaudhuri, R. A. (1995). Full and von Kármán geometrically nonlinear analyses of laminated cylindrical panels. *AIAA Journal*, 33(11):2173–2181.

[97] Kim, N.-I. and Lee, J. (2017). Exact solutions for coupled responses of thin-walled fg sandwich beams with non-symmetric cross-sections. *Composites Part B: Engineering*, 122:121–135.

[98] Kirchhoff, G. (1850). Uber da gleichgewicht und die bewegung einer elastischen scheibe. *Journal Für Die Reine und Angewandte Mathematik*, 40:51–88.

[99] Klinkel, S., Gruttmann, F., and Wagner, W. (1999). A continuum based three-dimensional shell element for laminated structures. *Computers & Structures*, 71(1):43–62.

[100] Krawczyk, P., Frey, F., and Zieliński, A. (2007). Large deflections of laminated beams with interlayer slips: Part 1: model development. *Engineering Computations*, 24(1):17–32.

[101] Krawczyk, P. and Rebora, B. (2007a). Large deflections of laminated beams with interlayer slips. *Engineering Computations*.

[102] Krawczyk, P. and Rebora, B. (2007b). Large deflections of laminated beams with interlayer slips: Part 2: finite element development. *Engineering Computations*, 24(1):33–51.

[103] Kunin, I. A. (1983). Elastic media with microstructure ii: Three-dimensional models, vol. 44 of springer series in solid state sciences.

[104] Kunin, I. A. (2012). *Elastic media with microstructure I: one-dimensional models*, volume 26. Springer Science & Business Media.

[105] L., X., Bhushan, B., Takashima, K., Baek, C.-W., and Kim, Y.-K. (2003). Mechanical characterization of micro/nanoscale structures for mems/nems applications using nanoindentation techniques. *Ultramicroscopy*, 97(1-4):481–494.

[106] Lakes, R. (1991). Experimental micro mechanics methods for conventional and negative poisson's ratio cellular solids as cosserat continua. *Journal of Engineering Materials and Technology*, 113(1):148–155.

[107] Lakes, R. S. (1983). Size effects and micromechanics of a porous solid. *Journal of Materials Science*, 18(9):2572–2580.

[108] Lakes, R. S., Nakamura, S., Behiri, J. C., and Bonfield, W. (1990). Fracture mechanics of bone with short cracks. *Journal of Biomechanics*, 23(10):967–975.

[109] Lam, D., Yang, F., Chong, A., Wang, J., and Tong, P. (2003). Experiments and theory in strain gradient elasticity. *Journal of the Mechanics and Physics of Solids*, 51(8):1477–1508.

[110] Lanc, D., Turkalj, G., and Pesic, I. (2014). Global buckling analysis model for thin-walled composite laminated beam type structures. *Composite Structures*, 111:371–380.

[111] Lee, J. (2000). Free vibration analysis of delaminated composite beams. *Computers & Structures*, 74(2):121–129.

[112] Lee, K. and Nikolaidis, E. (1992). A two-dimensional model for joints in vehicle structures. *Computers & Structures*, 45(4):775–784.

[113] Leissa, A. (1973a). The free vibration of rectangular plates. *Journal of Sound and Vibration*, 31(3):257–293.

[114] Leissa, A. (1973b). *Vibration of shells*. Scientific and Technical Information Office, National Aeronautics and Space Administration Washington.

[115] Leissa, A. and Qatu, M. (2011). *Vibrations of Continuous Systems.* McGraw-Hill.

[116] Li, G., Carrera, E., Cinefra, M., de Miguel, A. G., Pagani, A., and Zappino, E. (2019a). An adaptable refinement approach for shell finite element models based on node-dependent kinematics. *Composite Structures*, 210:1–19.

[117] Li, G., de Miguel, A. G., Pagani, A., Zappino, E., and Carrera, E. (2019b). Finite beam elements based on Legendre polynomial expansions and node-dependent kinematics for the global-local analysis of composite structures. *European Journal of Mechanics-A/Solids*, 74:112–123.

[118] Li, Z. and Qiao, P. (2015a). Buckling and postbuckling behavior of shear deformable anisotropic laminated beams with initial geometric imperfections subjected to axial compression. *Engineering Structures*, 85:277–292.

[119] Li, Z. and Qiao, P. (2015b). Thermal postbuckling analysis of anisotropic laminated beams with different boundary conditions resting on two-parameter elastic foundations. *European Journal of Mechanics-A/Solids*, 54:30–43.

[120] Li, Z. and Yang, D. (2016). Thermal postbuckling analysis of anisotropic laminated beams with tubular cross-section based on higher-order theory. *Ocean Engineering*, 115:93–106.

[121] Liew, K., Pan, Z., and Zhang, L. (2019). An overview of layerwise theories for composite laminates and structures: Development, numerical implementation and application. *Composite Structures*.

[122] Love, A. (2013a). Mathematical Theory of Elasticity. *Cambridge University Press*.

[123] Love, A. E. H. (2013b). *A treatise on the mathematical theory of elasticity*. Cambridge University Press, Cambridge, UK.

[124] Lurie, H. (1950). *Lateral vibrations as related to structural stability*. PhD thesis, California Institute of Technology.

[125] Malvern, L. E. (1969). *Introduction to the Mechanics of a Continuous Medium*. Number Monograph. Prentice Hall, Upper Saddle River, New Jersey, USA.

[126] Mashat, D., Carrera, E., Zenkour, A., Al Khateeb, S., and Lamberti, A. (2014). Evaluation of refined theories for multilayered shells via Axiomatic/Asymptotic method. *Journal of Mechanical Science and Technology*, 28(11):4663–4672.

[127] Maugin, G. A. and Metrikine, A. V. (2010). *Mechanics of generalized continua*. Springer.

[128] McFarland, A. W. and Colton, J. S. (2005). Role of material microstructure in plate stiffness with relevance to microcantilever sensors. *Journal of Micromechanics and Microengineering*, 15(5):1060.

[129] Mechab, I., El Meiche, N., and Bernard, F. (2017). Analytical study for the development of a new warping function for high order beam theory. *Composites Part B: Engineering*, 119:18–31.

[130] Mindlin, R. (1951). Influence of rotary inertia and shear flexural motion of isotropic, elastic plates. *Journal of Applied Mechanics*, 18:31–38.

[131] Mohyeddin, A. and Fereidoon, A. (2014). An analytical solution for the large deflection problem of timoshenko beams under three-point bending. *International Journal of Mechanical Sciences*, 78:135–139.

[132] Mororó, L., Melo, A., and Parente Junior, E. (2015). Geometrically nonlinear analysis of thin-walled laminated composite beams. *Latin American Journal of Solids and Structures*, 12(11):2094–2117.

[133] Mucichescu, D. T. (1984). Bounds for stiffness of prismatic beams. *Journal of Structural Engineering*, 110(6):1410–1414.

[134] Mundo, D., Hadjit, R., Donders, S., Brughmans, M., Mas, P., and Desmet, W. (2009). Simplified modelling of joints and beam-like structures for biw optimization in a concept phase of the vehicle design process. *Finite Elements in Analysis and Design*, 45(6-7):456–462.

[135] Niordson, F. (1985). *Shell theory*, volume 29. North-Holland Series in Applied Mathematics and Mechanics.

[136] Noor, A. and Burton, W. (1989). Stress and free vibration analyses of multilayered composite plates. *Composite Structures*, 11(3):183–204.

[137] Noor, A. K. (1986). Global-local methodologies and their application to nonlinear analysis. *Finite Elements in Analysis and Design*, 2(4):333–346.

[138] Novozhilov, V. (1964). *Thin shell theory*. Noordhoff Ltd., Groningen, The Netherlands.

[139] Nowacki, W. (1972). *Theory of micropolar elasticity*. Number 25. Springer.

[140] Nowacki, W. (1986). Theory of asymmetric elasticity. *Pergamon Press, Headington Hill Hall, Oxford OX 3 0 BW, UK, 1986.*

[141] Obst, A. W. and Kapania, R. K. (1992). Nonlinear static and transient finite element analysis of laminated beams. *Composites Engineering*, 2(5-7):375–389.

[142] Ogden, R. and Roxburgh, D. (1993). The effect of pre-stress on the vibration and stability of elastic plates. *International Journal of Engineering Science*, 31(12):1611–1639.

[143] Pagani, A. and Carrera, E. (2017). Large-deflection and post-buckling analyses of laminated composite beams by carrera unified formulation. *Composite Structures*, 170:40–52.

[144] Pagani, A. and Carrera, E. (2018). Unified formulation of geometrically nonlinear refined beam theories. *Mechanics of Advanced Materials and Structures*, 25(1):15–31.

[145] Pagani, A., Carrera, E., and Augello, R. (2019). Evaluation of various geometrical nonlinearities in the response of beams and shells. *AIAA Journal*, 57(8):3524–3533.

[146] Pai, P. F. (2007). *Highly Flexible Structures: Modeling, Computation, and Experimentation*.

[147] Pai, P. F. and Palazotto, A. N. (1996). Large-deformation analysis of flexible beams. *International Journal of Solids and Structures*, 33(9):1335–1353.

[148] Peres, N., Gonçalves, R., and Camotim, D. (2016). First-order generalised beam theory for curved thin-walled members with circular axis. *Thin-Walled Structures*, 107:345–361.

[149] Petrolo, M. and Carrera, E. (2020). Methods and guidelines for the choice of shell theories. *Acta Mechanica*, pages 1–40.

[150] Poisson, S. (1829). Mémoire sur l'équilibre et le mouvement des corps élastiques. *Mm. Acad. Sci. Instr. Fr.*, 8:357–570.

[151] Prager, W. (1967). Recent progress in applied mechanics. *Almquist and Wiksell, Stockholm*.

[152] Ramezani, S., Naghdabadi, R., and Sohrabpour, S. (2009). Analysis of micropolar elastic beams. *European Journal of Mechanics-A/Solids*, 28(2):202–208.

[153] Reddy, J. (2003). *Mechanics of laminated composite plates and shells: theory and analysis*. CRC press, Florida, USA.

[154] Reddy, J. (2014). *An Introduction to Nonlinear Finite Element Analysis: with applications to heat transfer, fluid mechanics, and solid mechanics*. Oxford University Press, Oxford.

[155] Reddy, J. and Liu, C. (1985). A higher-order shear deformation theory of laminated elastic shells. *International Journal of Engineering Science*, 23(3):319–330.

[156] Reddy, J. N. and Robbins, D. H. (1994). Theories and computational models for composite laminates. *Applied Mechanics Review*, 47:147–165.

[157] Reissner, E. (1945). The effect of transverse shear deformation on the bending of elastic plates. *Journal of Applied Mechanics*, 12:69–76.

[158] Reissner, E. (1972). On one-dimensional finite-strain beam theory: the plane problem. *Zeitschrift für angewandte Mathematik und Physik ZAMP*, 23(5):795–804.

[159] Reissner, E. (1973). On one-dimensional large-displacement finite-strain beam theory. *Studies in Applied Mathematics*, 52(2):87–95.

[160] Reissner, E. (1979). Some considerations on the problem of torsion and flexure of prismatical beams. *International Journal of Solids and Structures*, 15(1):41–53.

[161] Reissner, E. (1983). Further considerations on the problem of torsion and flexure of prismatical beams. *International Journal of Solids and Structures*, 19(5):385–392.

[162] Rivera, M., Reddy, J., and Amabili, M. (2016). A new twelve-parameter spectral/hp shell finite element for large deformation analysis of composite shells. *Composite Structures*, 151:183–196.

[163] Schardt, R. (1966). Eeine erweiterung der technischen biegetheorie zur berechnung prismatischer faltwerke. *Der Stahlbau*, 35:161–171.

[164] Shu, X. (1997). A refined theory of laminated shells with higher-order transverse shear deformation. *International Journal of Solids and Structures*, 34(6):673–683.

[165] Silvestre, N. (2007). Generalised beam theory to analyse the buckling behaviour of circular cylindrical shells and tubes. *Thin-Walled Structures*, 45(2):185–198.

[166] Silvestre, N. and Camotim, D. (2002a). First-order generalised beam theory for arbitrary orthotropic materials. *Thin-Walled Structures*, 40(9):755–789.

[167] Silvestre, N. and Camotim, D. (2002b). Second-order generalised beam theory for arbitrary orthotropic materials. *Thin-Walled Structures*, 40(9):791–820.

[168] Simo, J. C. and Vu-Quoc, L. (1991). A geometrically-exact rod model incorporating shear and torsion-warping deformation. *International Journal of Solids and Structures*, 27(3):371–393.

[169] Singh, G., Rao, G. V., and Iyengar, N. (1992). Nonlinear bending of thin and thick unsymmetrically laminated composite beams using refined finite element model. *Computers & Structures*, 42(4):471–479.

[170] Singh, G.and Rao, G. V. and Iyengar, N. G. R. (1992). Nonlinear bending of thin and thick unsymmetrically laminated composite beams using refined finite element model. *Computers & Structures*, 42(4):471–479.

[171] Song, O. and Librescu, L. (1993). Free vibration of anisotropic composite thin-walled beams of closed cross-section contour. *Journal of Sound and Vibration*, 167(1):129–147.

[172] Stephen, N. and Levinson, M. (1979). A second order beam theory. *Journal of Sound and Vibration*, 67(3):293–305.

[173] Stölken, J. S. and Evans, A. G. (1998). A microbend test method for measuring the plasticity length scale. *Acta Materialia*, 46(14):5109–5115.

[174] Sun, C. and Whitney, J. (1976). Dynamic response of laminated composite plates under initial stress. *AIAA Journal*, 14(2):268–270.

[175] Sze, K., Liu, X., and Lo, S. (2004). Popular benchmark problems for geometric nonlinear analysis of shells. *Finite Elements in Analysis and Design*, 40:1551–1569.

[176] Timoshenko, S. P. (1922a). On the transverse vibrations of bars of uniform cross section. *Philosophical Magazine*, 43:125–131.

[177] Timoshenko, S. P. (1922b). On the transverse vibrations of bars of uniform cross-section. *The London, Edinburgh, and Dublin Philosophical Magazine and Journal of Science*, 43(253):125–131.

[178] Timoshenko, S. P. and Gere, J. M. (1961). *Theory of elastic stability*. Tokyo.

[179] Varadan, T. K. and Bhaskar, K. (1997). Review of different theories for the analysis of composites. *Journal of Aerospace Society of India*, 49:202–208.

[180] Vidal, P. and Polit, O. (2008). A family of sinus finite elements for the analysis of rectangular laminated beams. *Composite Structures*, 84:56–72.

[181] Vidal, P. and Polit, O. (2009). Assessment of the refined sinus model for the non-linear analysis of composite beams. *Composite Structures*, 87(4):370–381.

[182] Virgin, L. (2007). *Vibration of axially-loaded structures*. Cambridge University Press, Cambridge, UK.

[183] Vlasov, V. Z. (1961). *Thin-walled elastic beams*. National Science Foundation, Washington.

[184] Voigt, W. (1887). *Theoretische studien über die elasticitätsverhältnisse der krystalle*. Königliche Gesellschaft der Wissenschaften zu Göttingen.

[185] Wenzel, C. (2014). *Local FEM analysis of composite beams and plates: free-edge effect and incompatible kinematics coupling*. PhD thesis, Politecnico di Torino.

[186] Wu, B., Pagani, A., Chen, W. Q., and Carrera, E. (2019). Geometrically nonlinear refined shell theories by carrera unified formulation. *Mechanics of Advanced Materials and Structures*, pages 1–21.

[187] Yang, J. F. C. and Lakes, R. S. (1982). Experimental study of micropolar and couple stress elasticity in compact bone in bending. *Journal of Biomechanics*, 15(2):91–98.

[188] Yu, W., Hodges, D. H., Volovoi, V. V., and Fuchs, E. D. (2005). A generalized Vlasov theory for composite beams. *Thin-Walled Structures*, 43(9):1493–1511.

[189] Zappino, E., Li, G., Pagani, A., Carrera, E., and de Miguel, A. G. (2018). Use of higher-order Legendre polynomials for multilayered plate elements with node-dependent kinematics. *Composite Structures*, 202:222–232.

[190] Zhang, L. and Liew, K. (2015). Geometrically nonlinear large deformation analysis of functionally graded carbon nanotube reinforced composite straight-sided quadrilateral plates. *Computer Methods in Applied Mechanics and Engineering*, 295:219–239.

[191] Zhang, Y. and Kim, K. (2006). Geometrically nonlinear analysis of laminated composite plates by two new displacement-based quadrilateral plate elements. *Composite Structures*, 72(3):301–310.

[192] Zhu, P., Lei, Z., and Liew, K. (2012). Static and free vibration analyses of carbon nanotube-reinforced composite plates using finite element method with first order shear deformation plate theory. *Composite Structures*, 94(4):1450–1460.

[193] Zienkiewicz, O. C. and Taylor, R. L. (2005). *The Finite Element Method for Solid and Structural Mechanics*. Butterworth-Heinemann, Washington, 6th edition.

[194] Zozulya, V. V. (2017). Micropolar curved rods. 2-d, high order, timoshenko's and euler-bernoulli models. *Curved and Layered Structures*, 4(1):104–118.

[195] Zozulya, V. V. (2018). Higher order theory of micropolar plates and shells. *ZAMM-Journal of Applied Mathematics and Mechanics/Zeitschrift für Angewandte Mathematik und Mechanik*, 98(6):886–918.

Appendix A

List of publications

A.1 Journal articles

1. A. Stio, P. Spinolo, E. Carrera, R. Augello (2017), "Analysis of landing mission phases for robotic exploration on Phobos Mars's Moon", Advances in Aircraft and Spacecraft Science, Vol. 4, pp. 529-541.

2. A. Pagani, R. Augello, E. Carrera (2018), "Frequency and mode change in the large deflection and post-buckling of compact and thin walled beams", Journal of Sound and Vibration, Vol. 432, pp. 88-104.

3. A. Pagani, R. Augello, G. Governale, A. Viglietti (2019), "Drop Test Simulations of Composite Leaf Spring Landing Gears", Aerotecnica Missili & Spazio, Vol. 98, pp. 63-74.

4. A. Pagani, E. Carrera, R. Augello (2019), "Evaluation of various geometrical non-linearities in the response of beams and shells", AIAA Journal, Vol. 57 no. 8, pp. 3524-3533.

5. R. Augello, E. Carrera, A. Pagani (2019), "Unified theory of structures based on micropolar elasticity", Meccanica, Vol. 54, pp. 1785-1800.

6. X. Xu, H. Yang, R. Augello, E. Carrera (2019), "Optimized free-form surface modeling of point clouds from laser-based measurement", Mechanics of Advanced Materials and Structures, pp. 1-9.

7. X. Xu, R. Augello, H. Yang (2019), "The generation and validation of a CUF-based FEA model with laser-based experiments", Mechanics of Advanced Materials and Structures pp. 1-8.

8. A. Pagani, R. Azzara, R. Augello, E. Carrera (2020), "Multibody simulation and descent control of a space lander", Advances in Aircraft and Spacecraft Science, Vol. 7 no. 2, pp. 91-113.

9. E. Carrera, A. Pagani, R. Augello, B. Wu (2020), "Popular benchmarks of nonlinear shell analysis solved by 1D and 2D CUF-based finite elements", Mechanics of Advanced Materials and Structures, Vol. 27, pp. 1098-1109.

10. E. Carrera, A. Pagani, R. Augello (2020), "Effect of large displacements on the linearized vibration of composite beams", International Journal of Non-Linear mechanics, Vol. 120, 103390.

11. M.D. Demirbas, X. Xu, E. Carrera, H. Yang, R. Augello (2020), "Evaluation of stress distributions in the geometrical nonlinear regime of functionally graded structures", Composite Structures, Vol. 246, 112385.

12. E. Carrera, A. Pagani, R. Augello (2018), "Evaluation of geometrically nonlinear effects due to large cross-sectional deformations of compact and shell-like structures", Mechanics of Advanced Materials and Structures, Vol. 27, pp. 1269-1277.

13. A. Pagani, R. Azzara, R. Augello, E. Carrera (2020), "Accurate through-the-thickness stress distributions in thin-walled metallic structures subjected to large displacements and large rotations", Vietnam Journal of Mechanics, Vol. 42, pp. 239-254.

14. E. Carrera, A. Pagani, R. Augello (2020), "Large deflection and post-buckling of thin-walled structures by finite elements with node-dependent kinematics", Acta Mechanica, pp. 1-27.

15. E. Carrera, A. Pagani, R. Augello (2020), "On the role of learge cross-sectional deformations in the nonlinear analysis of composite thin-walled structures", Archive of Applied Mechanics, pp. 1-17.

16. A. Pagani, R. Azzara, R. Augello, E. Carrera, B. Wu (2020), "Vibration of metallic and composite shells in geometrical nonlinear equilibrium states", Thin-Walled Structures, Vol. 157, 107131.

17. E. Carrera, A. Pagani, D. Giusa, R. Augello (2021), "Nonlinear analysis of thin-walled beams with highly deformable sections", International Journal of Non-Linear Mechanics, Vol. 128, 103613.

A.2 Conference Proceedings

1. R. Augello, A. Pagani, E. Carrera “Micropolar elasticity by unified theory”, In: *The 15th Jiangsu – Hong Kong Forum on Mechanics and Its Application*, Hong-Kong, China, 13 April, 2019.

2. R. Augello, E. Carrera, W. Chen, M. Filippi, A. Pagani, B. Wu “Effect of in-plane loadings on the free vibration of plates in nonlinear regime”, In: *First International Nonlinear Dynamics Conference (NODYCON 2019)*, Rome, Italy, 17-20 February, 2019.

3. A. Pagani, R. Augello, E. Carrera (2018) “Evaluation of in-plane and out-of-plane stresses in composite structures subjected to large displacements/rotations” and "Virtual vibration correlation technique (VCT) for nonlinear buckling analysis of metallic and composite structures", In: *International Mechanical Engineering Congress and Exposition (IMECE)*, Pittsburgh, Pennsylvania, 9-15 November, 2018.

4. A. Pagani, R. Augello, E. Carrera (2018) “Effects of geometric nonlinearities on refined structural models of laminated beams”, In: *European Solid Mechanics Conference (ESMC2018)*, Bologna, Italy, 2-6 July, 2018.

5. A. Pagani, R. Augello, E. Carrera (2018) “Unified theory of structures based on micropolar elasticity”, In: *International Conference on Mechanics of Advanced Materials and Structures (ICMAMS)*, Torino, Italy, 17-20 June, 2018.

6. A. Pagani, E. Carrera, R. Augello (2017) “Vibrations of structures subjected to prestress states”, In: *talian Association of Aeronautics and Astronautics - XXIV International Conference (AIDAA2017)*, Palermo and Enna, Italy, 18-22 September, 2017.

7. E. Carrera, A. Pagani, R. Augello (2017) “Mode change in nonlinear dynamics of laminated structures”, In: *International Conference on Composite Structure (ICCS20)*, Paris, France, 4-7 September, 2017.

8. A. Stio, P. Spinolo, A. Carluccio, R. Augello (2016) "Cinematic and dynamic analysis with co-simulation between multi body solver and system control software", In: *ATC Altair technological conference Math and system simulation*, Torino, Italy, 29 November, 2017.